DISSERTATION

EXAMINING CHAOTIC CONVECTION WITH SUPER-PARAMETERIZATION ENSEMBLES

Submitted by

Todd R. Jones

Department of Atmospheric Science

In partial fulfillment of the requirements

For the Degree of Doctor of Philosophy

Colorado State University

Fort Collins, Colorado

Spring 2017

Doctoral Committee:

Advisor: David A. Randall

Christian D. Kummerow
Susan C. van den Heever
Russ S. Schumacher
Richard E. Eykholt

ABSTRACT

EXAMINING CHAOTIC CONVECTION WITH SUPER-PARAMETERIZATION ENSEMBLES

This study investigates a variety of features present in a new configuration of the Community Atmosphere Model (CAM) variant, SP-CAM 2.0. The new configuration (multiple-parameterization-CAM, MP-CAM) changes the manner in which the super-parameterization (SP) concept represents physical tendency feedbacks to the large-scale by using the mean of 10 independent two-dimensional cloud-permitting model (CPM) curtains in each global model column instead of the conventional single CPM curtain. The climates of the SP and MP configurations are examined to investigate any significant differences caused by the application of convective physical tendencies that are more deterministic in nature, paying particular attention to extreme precipitation events and large-scale weather systems, such as the Madden-Julian Oscillation (MJO). A number of small but significant changes in the mean state climate are uncovered, and it is found that the new formulation degrades MJO performance. Despite these deficiencies, the ensemble of possible realizations of convective states in the MP configuration allows for analysis of uncertainty in the small-scale solution, lending to examination of those weather regimes and physical mechanisms associated with strong, chaotic convection. Methods of quantifying precipitation predictability are explored, and use of the most reliable of these leads to the conclusion that poor precipitation predictability is most directly related to the proximity of the global climate model column state to atmospheric critical points. Secondarily, the predictability is tied to the availability of potential convective energy, the presence of mesoscale convective organization on the CPM grid, and the directive power of the large-scale.

ACKNOWLEDGEMENTS

I would like to specifically thank David Randall, Mark Branson, Charlotte DeMott, and Brian Medeiros for their help, thoughtful commentary, and for just saying something that spurred an idea.

The 1DD data were provided by the NASA/Goddard Space Flight Center's Mesoscale Atmospheric Processes Laboratory, which develops and computes the 1DD as a contribution to the GEWEX Global Precipitation Climatology Project. The TMPA data were provided by the NASA/Goddard Space Flight Center's Mesoscale Atmospheric Processes Laboratory and PPS, which develop and compute the TMPA as a contribution to TRMM.

This work and a significant portion of my life have been supported by a CIRA Graduate Student Fellowship.

This dissertation is typset in LaTeX using a document class designed by Leif Anderson.

TABLE OF CONTENTS

LIST OF TABLES

LIST OF FIGURES

CHAPTER 1 – INTRODUCTION

Weather prediction skill has advanced steadily and significantly over the past few decades to the point where a five-day forecast of certain features today is typically more skillful than a three-day forecast thirty years ago (Figure 1.1; Bauer et al. 2015), but weather and climate predictions by themselves do not exhibit inherent value. Such value is endowed by their usefulness after the fact that goes beyond common verification measures of a skillful forecast (Roebber and Bosart 1996; Richardson 2012). This is demonstrated by forecasters or end users taking some action based on the forecast at some cost to themselves in order to protect against some loss. Decisions made using valuable, useful forecasts save lives and protect against myriad economic sacrifices, yielding a benefit to cost ratio of 6.2:1 in the United States (Lazo et al. 2009). To achieve a forecast of high value, decision makers must consider not just the predicted variable of interest but also its uncertainty, an important element in how people judge and understand forecasts.

Forecast uncertainty is often quantified using ensemble forecasts, which produce probabilities of occurrence in multiple, slightly differing simulations of a scenario that reveal the range of potential solutions (Figure 1.2; Bauer et al. 2015). The successes of ensemble techniques have been demonstrated many times over the past few decades on multiple scales (Epstein 1969; Leith 1974; Mureau et al. 1993; Palmer et al. 1993; Toth and Kalnay 1993; Tracton and Kalnay 1993; Toth and Kalnay 1997; Molteni et al. 1996; Palmer 2000; Berner et al. 2015; Harnisch and Keil 2015). However, ensembles are not a cure-all. For instance, Clark et al. (2009) demonstrated that sacrificing ensemble members for better resolution can be "highly desirable." Many deficiencies remain due to issues like model biases, initial condition error, and inherent predictability limits; sometimes such poor predictions can be linked to specific conditions and scenarios such as blocking highs and cut-off lows on the large scale (Molteni et al. 1996), though often it is found that

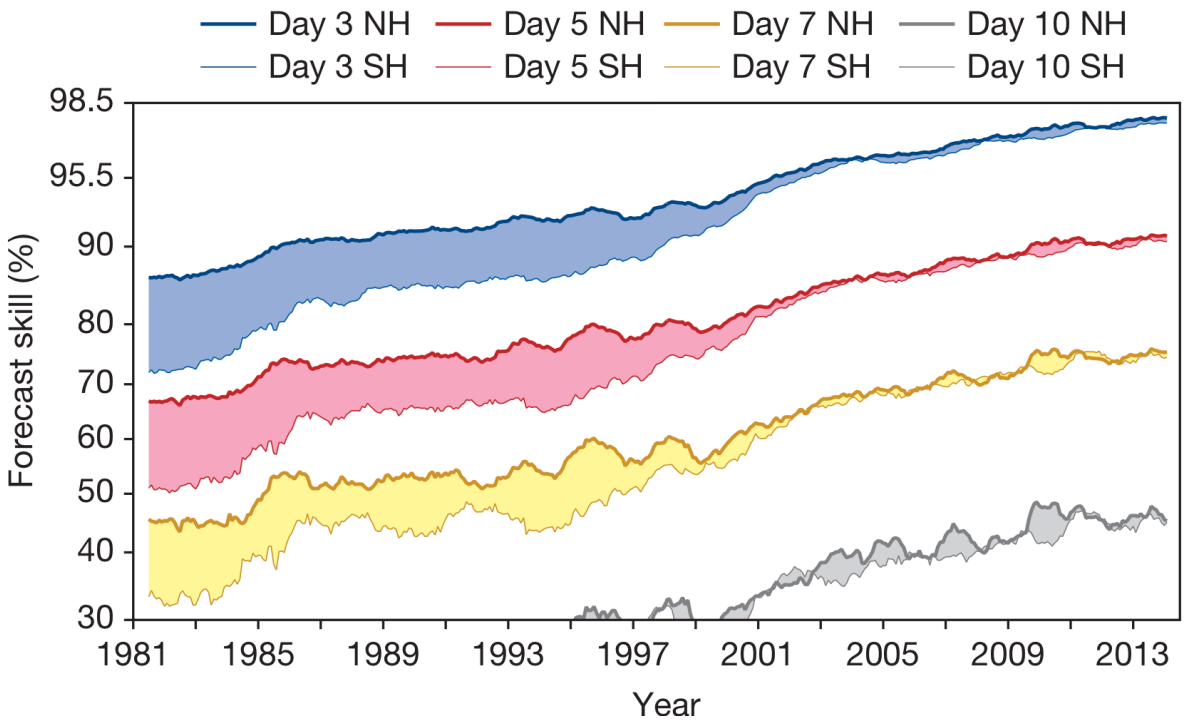

FIGURE 1.1: Caption as in Bauer et al. (2015): Forecast skill is the correlation between the forecasts and the verifying analysis of the height of the 500-hPa level, expressed as the anomaly with respect to the climatological height. Values greater than 60% indicate useful forecasts, while those greater than 80% represent a high degree of accuracy. The convergence of the curves for Northern Hemisphere (NH) and Southern Hemisphere (SH) after 1999 indicates the breakthrough in exploiting satellite data through the use of variational data.

rapid error growth from the small scale is liable (Palmer 2000; Walser et al. 2004). One of the biggest sources of uncertainty coming from global atmospheric models is found in the representation of moist processes below the grid scale (Flato et al. 2013). In particular, there is a high degree of uncertainty involving the interaction between the smaller and larger scales, making research into parameterization of cloud processes an area of prime concern (Stevens and Bony 2013; Jakob 2014).

In representing smaller atmospheric scales, the assumptions used by deterministic convective parameterizations, in particular, those of scale separation, quasi-equilibrium, and robust statistics, have been shown to be problematic. The spectral gap defining scale separation between

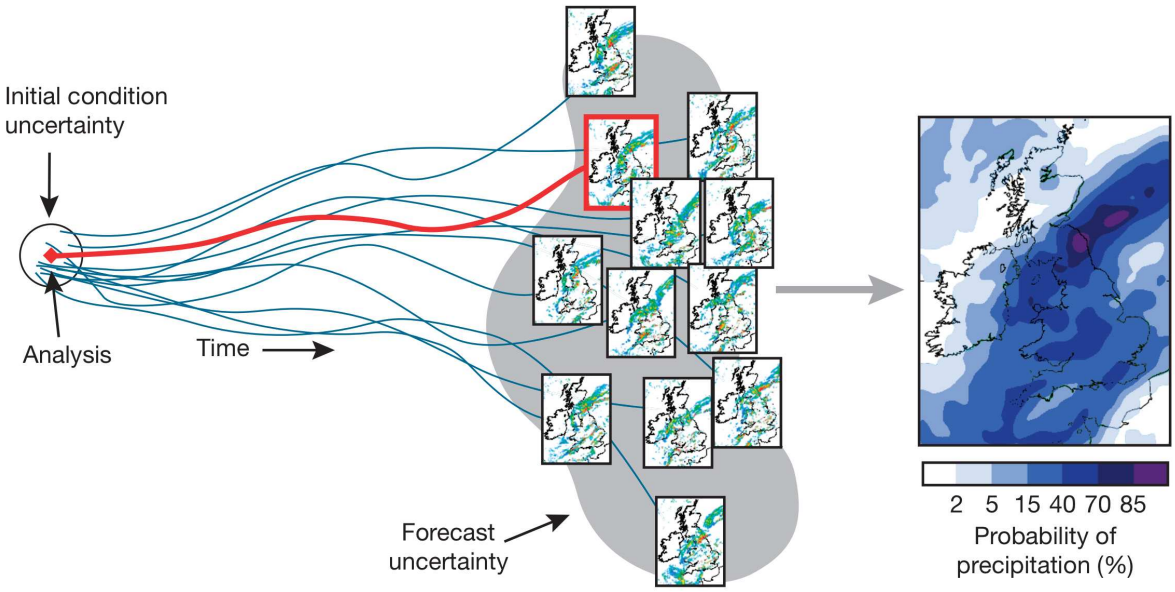

FIGURE 1.2: Caption as in Bauer et al. (2015): A single forecast (red frame, centre) is generated by integrating the model forward in time from the analysis of initial atmospheric state (left). Small perturbations to the analysis, within known analysis uncertainty, provide an ensemble of forecast solutions, which sample the forecast uncertainty (multiple frames). These solutions are combined, including some spatial neighbourhood sampling, to provide a smooth estimate of probability of precipitation (right). Image courtesy of K. Mylne (Met Office).

the large-scale and the convective scale that was described in early work (e.g., Van der Hoven 1957; Vinnichenko 1970) has been shown more recently to be absent in the vast majority of atmospheric fields (e.g., Roy 2009; Moncrieff et al. 2012). This "scale gap" can be thought of as spanning approximately 10-100 km in horizontal scale, a region of the full spectrum populated by organized mesoscale systems that can locally account for more than 50% of rainfall over vast portions of the tropics. The variability of convection that arises from the intrinsically uncertain nature of small-scale motions through sensitive dependence on initial conditions (Lorenz 1969; Arakawa 2004; Hohenegger and Schär 2007) quite often lacks representation in deterministic parameterizations (Randall et al. 1994, 1997; Xu et al. 1992; Xu and Randall 1998; Shutts and Palmer 2007; Jones and Randall 2011). The robust statistics on a given ensemble of clouds in a model grid box become increasingly unreliable as model resolutions are improved and the sample

size decreases (López 1977; Molinari and Dudek 1992; Palmer 1996; Johnson et al. 1999; Jones and Randall 2011). Additionally, with enhanced resolution, finer features are being resolved and are evolving on timescales shorter than the convective adjustment time assumed by a quasi-equilibrium between scales (Molinari and Dudek 1992; Cohen and Craig 2006). This becomes a problem in high-resolution global models that employ deterministic parameterizations (e.g., Bechtold et al. 2008), and diagnostic physical heating and drying tendencies act too quickly, without consideration of the temporally delayed convective response. Raymond and Herman (2011) present a nice review of historical convective quasi-equilibrium thinking along with their analysis demonstrating its differing applicability in the upper versus lower troposphere, a view supported by Lin et al. (2015), who further attribute the problems of convective quasi-equilibrium to its neglect of the second vertical modes associated with shallow convection and stratiform processes. This problem may be remedied in some respects by incorporating a "memory" into the parameterization, thereby making it prognostic (e.g., Pan and Randall 1998; Scinocca and McFarlane 2004; Chikira and Sugiyama 2010; Wagner and Graf 2010).

While convective parameterizations were once deemed reliable if they accurately reproduced the time mean of tropical convection, it has become apparent that the variability of convection also needs to be examined as a metric of parameterization fidelity. In the case of global climate modeling where models run free of the influence of continuing observations, the concern lies with developing statistically appropriate representations of small-scale physical tendencies. That is, the parameterized scales need only provide a likely result, often referred to as the expected value, rather than anything approaching an exact representation of what would occur in the real world. For practical purposes, the spatial resolution in atmospheric general circulation models (GCMs) has been truncated at a point in the spatiotemporal spectrum of atmospheric processes that prohibits the explicit representation of important physical processes from approximately the

mesoscale on down the energy cascade to dissipation. Currently, large-scale atmospheric models necessarily parameterize these processes due to practical limitations, but even after 40 years of development, significant and persistent deficiencies remain in the treatment of clouds, resulting in errors in the predictions of weather and climate (Slingo et al. 1996; Randall et al. 2003; Slingo et al. 2005; Lin et al. 2006; Kim et al. 2009). This is troubling in light of the fact that convection is a primary mover of the evolution of the atmosphere's temperature and moisture structure and the way in which gravity waves form and propagate, potentially giving rise to further errors at the larger scales.

Many researchers have investigated the influence of small-scale variability on large-scale and the ability of deterministic parameterizations to represent this interaction. For example, a comparison of model and observational representations of convective heating variability by Ricciardulli and Garcia (2000) shows significant model underestimation of the high frequency variability for two different convective parameterization schemes. The authors further linked this high-frequency variability discrepancy to problems in the representation of larger-scale processes from Kelvin waves and the Madden-Julian Oscillation (MJO) in the troposphere to the quasi-biennial oscillation (QBO) of zonal winds in the stratosphere. Neelin et al. (2008) also suggest that the realistic representation of convective variability is necessary for a similarly realistic representation of larger-scale weather features like the MJO.

In another study of nine GCMs with various convective parameterization formulations, Horinouchi et al. (2003) also found links between the convective scale variability and the QBO. The models showed a wide range of variability among their precipitation frequency spectra, having different shapes and differing by over an order of magnitude. In particular, they confirmed the results of Ricciardulli and Garcia (2000), showing that certain mass-flux schemes (e.g., Arakawa

and Schubert 1974; Shibata et al. 1999; Zhang and McFarlane 1995) yield less variability compared to the more active or noisy convective schemes such as one using a moist convective adjustment approach to a reference atmospheric profile (Manabe et al. 1965)[1]. Those with greater convective variability, though greater than that in observations, had the ability to simulate the QBO.

It has further been suggested that stochastic fluctuations of convective activity can lead to systematic changes in large-scale weather and climate and that the use of stochastic parameterizations of such activity in atmospheric models can act to ameliorate some deleterious effects of conventional deterministic parameterizations that stem from their lack of knowledge about atmospheric processes at fine spatiotemporal scales. For example, Zhang et al. (2003a) examine these issues through analysis of error growth at various scales in reforecasts of a "surprise" snowstorm over the eastern United States in which initial condition differences between simulations were limited to scales below 100 km. They show that errors below 100 km scales begin with small-scale differences linked to moist convection, errors below 30 km scales begin with differences linked to convective or microphysical parameterizations, and errors below 3 km scales begin with differences linked to the spatiotemporal location of individual convective cells. In each case, errors from the small-scale are shown to place an intrinsic limit on the predictability of larger scales, in these cases manifesting as large-scale discrepancies in areas including the position of the surface low and the distribution of precipitation.

For a set of low-resolution simulations using a single model where the initial conditions differ only at small scales and using deterministic parameterizations of the small-scale physics as direct

[1]Moist convective adjustment schemes can be written as a mass-flux scheme. The lack of variability in these schemes may be related to a specific feature of a given scheme, like relaxation to an equilibrium state. Additional attributes of a mass-flux scheme may make it act with greater variability.

functions of the large scale, the initial differences would be unresolved, resulting in identical forecast solutions lacking potentially significant processes. Without enhancing the model resolution to include the initial small-scale differences, Zhang et al. (2003a) conclude that the parameterizations would have to be stochastic to gain some representation of the true uncertainty in the forecast due to uncertainty inherent in moist processes at the convective scale. The characteristic chaotic behavior exhibited by real cloud systems (e.g., Hohenegger and Schär 2007; Berner et al. 2012) and that will automatically arise from using models of finer resolution needs to be an integral attribute of convective parameterizations.

Not coincidentally, research into implementing stochastic parameterizations to randomly break the deterministic constraints in atmospheric models has been an active area of research for more than a decade and a half. As ensemble prediction aims to alleviate predictability limitations by representation of the potential spread of forecasts, the use of stochastic physics tendencies has been shown to be beneficial (Buizza et al. 1999; Berner et al. 2012), even on top of improvements from ensemble techniques (Mullen and Buizza 2001; Palmer et al. 2005). The concept's use in atmospheric science dates back at least to the 1970s for use in climate models to represent the noise on the scale of daily weather (Hasselmann 1976). Supplying perturbations with a random component allows for noise-induced transitions, whereby noise of the appropriate magnitude permits regime shifts in the overall system or shifts the equilibrium point. The transition can be realized in models as more frequent population of less dominant regimes, like blocking flow patterns in contrast to more dominant westerly flow patterns in midlatitudes. When models lack appropriate representations of this variability, they tend to spend too much time in dominant regimes, a relevant problem in a number of models (Molteni and Tibaldi 1990; Jung 2005; Berner et al. 2009, 2012).

Some very simple stochastic schemes are capable of inducing model improvements. Buizza et al. (1999) applied random multiplicative noise from a uniform distribution to scale the total parameterized tendencies by $\pm 50\%$ and Wilks (2008) add Gaussian white noise to the tendencies. Teixeira and Reynolds (2008) employed random samples from a probability distribution constrained by variability displayed in the deterministic parameterizations in earlier ensemble simulations. Others perturb parameterization input fields or particular components of the parameterizations themselves (Lin and Neelin 2002; Bright and Mullen 2002; Lin and Neelin 2003), the latter tactic being found superior. Another stochastic method involves perturbations to the streamfunction to simulate stochastic kinetic energy backscatter moving upscale from the unresolved flow (Berner et al. 2009) to improve the inertial range power spectrum poorly represented in many global models. Through the stochastic backscatter method, kinetic energy is injected in a stochastic manner as a function of the large-scale flow and kinetic energy dissipation rate to represent kinetic energy release moving upscale from deep convection that is systematically lost in conventional simulation.[2] The significance of this can be inferred from Figure 12 of Malardel and Wedi (2016), which shows an increase of kinetic energy at small scales that is present in the IFS (at equivalent 9- and 5-km resolution) when the convective parameterization is turned off, forcing convection to be represented at the grid scale. Some of this additional energy, particularly in the wavelength range of 1000 to 50 km, is transferred upscale as available potential energy. In many cases, the random components of these schemes are constrained to follow a first-order autoregressive process or are applied identically over certain areas or timespans, giving them some correlation in time and space (Palmer et al. 2009).

Some of these techniques are in use for operational numerical weather prediction (NWP) and have been shown to produce forecast improvements and reduce some systematic biases (Bowler

[2]Use of the term "backscatter" may be inappropriate considering that the convective source is an instability on the small scale rather than a direct result of the energy cascade into the small scale.

et al. 2009; Charron et al. 2010). Weisheimer et al. (2014) describe the combined use of tendency perturbation and kinetic energy backscatter techniques in the European Centre for Medium-Range Weather Forecasts (ECMWF) seasonal forecasting System 4, which couples an ocean model to ECMWF's NWP model, Integrated Forecast System (IFS). The perturbations are constrained by a first-order autoregressive process and characteristics of cloud-resolving model (CRM) simulations that inform the choice of their amplitude. They found bias improvements in a number of convection-related fields as well as near-surface winds that come mainly from the tendency perturbations as opposed to the stochastic backscatter scheme. There was also an improvement in MJO and El Niño-Southern Oscillation (ENSO) characteristics. Similarly, Wang et al. (2016) also show improvements in MJO simulation with the implementation of the stochastic convective parameterization ideas of Plant and Craig (2008). More recently, more emphasis has been placed on the need for developing stochastic elements of parameterizations during model construction (Berner et al. 2012) or providing some physical, empirical basis for their implementation (Plant and Craig 2008; Gottwald et al. 2016; Mewes 2016; Kober and Craig 2016; Wang et al. 2016). Testing of these more-informed stochastic parameterizations is ongoing, and it is expected that they will improve upon their predecessors.

As more informed stochastic parameterizations often derive their guiding statistics from high resolution cloud model simulations, there exists a technique that may be considered the "best-informed" parameterization of cloud-scale processes. Superparameterization (SP) is a modeling technique for use in simulation of global atmospheric circulations by which the traditionally parameterized physics (shallow and deep convection, microphysics, turbulence, surface interactions, etc.) operating in response to individual global grid columns representing large horizontal

areas typically exceeding 1000 km^2 is replaced by the mean response of a much finer resolution, $O(1)$ km, cloud-permitting model (CPM[3]) (Grabowski and Smolarkiewicz 1999; Grabowski 2001; Khairoutdinov and Randall 2001; Khairoutdinov et al. 2005). Typically, one copy of a two-dimensional CPM runs continuously and independently in each GCM column, though other configurations are possible. Microphysics, radiation, and turbulence are all still parameterized, but in this case, it is performed at much finer resolution and with much more detailed information about the cloud structure. More details regarding the SP configuration are presented in Section 2.1.

The SP configuration even allows for memory between time steps and the explicit, high-resolution representation of an inhomogeneous environment with all of the small-scale variations and sensitive dependence on initial conditions inherent with that, all of which are important to appropriate simulation of mesoscale development (e.g., Stensrud and Gao 2010; Sun and Zhang 2008; Schenkman et al. 2011). Because small scale noise arises from the sensitive dependence on initial conditions, no assumptions about the nature of the stochastic effects are required. Following from these characteristics, improvements on a number of features, including the diurnal cycle of convection over land, mesoscale convective systems, African easterly waves, tropical cyclones, monsoon fluctuations, the MJO, ENSO, and the distribution of precipitation intensity, are well documented (DeMott et al. 2007; Benedict and Randall 2007; Pritchard and Somerville 2009; Kim et al. 2009; Stan et al. 2010; DeMott et al. 2011; McCrary et al. 2014; Kooperman et al. 2016; Randall et al. 2016). A much more exhaustive list of examples of the use of the SP model configuration is available online at http://www.cmmap.org/research/pubs-mmf.html.

[3]Demarcating the line between cloud-resolving and cloud-permitting is an issue of ongoing discussion that can sometimes feel little more than pedantic. However, since most previous SP studies, including this one, use embedded domains with grid spacings of about 4 km, which sits on the border between cloud-resolving and cloud system-resolving models, I will refer to this resolution as "cloud-permitting."

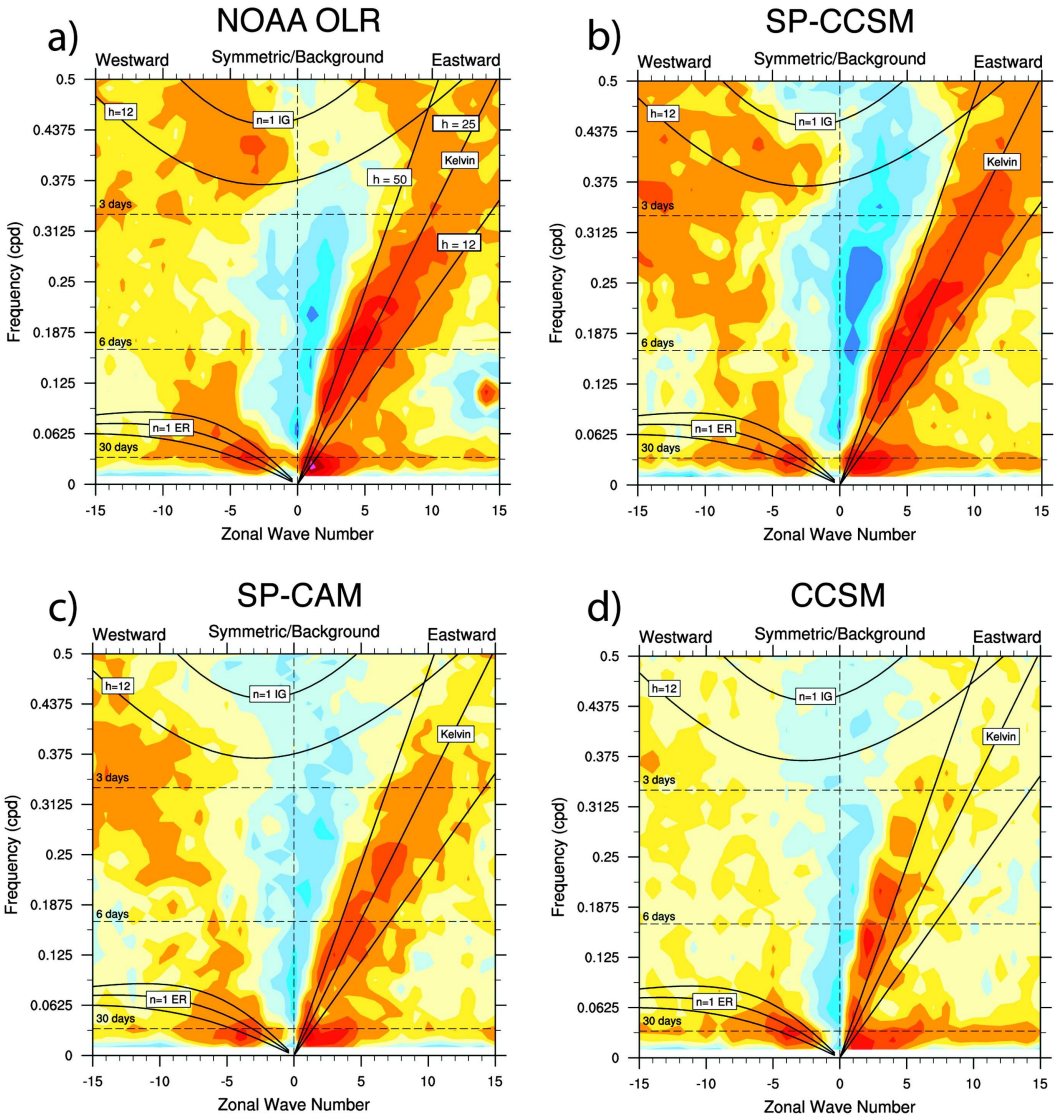

FIGURE 1.3: Caption similar to that in DeMott et al. (2011): Wavenumber vs frequency distribution of spectral-power divided by the background spectra for equatorially symmetric OLR anomalies. Signal-to-noise ratios (SNRs) greater than (less than) one are shaded in yellows and reds (blues). Contour interval is 0.1. Shallow water dispersion relationships for equivalent depths of h = 12, 25, and 50 m are shown for the n = 1 equatorial Rossby, Kelvin, and n = 1 inertio-gravity waves.

This one change in parameterization philosophy appears to be producing rather groundbreaking results.

The differences among deterministic parameterization, stochastic parameterization, and SP classes spring from just conceptual and practical issues. All are born out of the imposition of scale separation caused by the computational difficulty of operating global CPMs, and each has

the equivalent goal of informing the large-scale about the collective effects of cloud processes. In some ways, deterministic parameterizations are holdovers from a time of severe computational limitations. On the other hand, they represent our simplest conceptual model of the interaction across scales, which permits some measure of general understanding. Stochastic parameterizations build on this understanding by contributing the complicating effects of nondeterminism, while keeping computational costs low. SP takes a fundamentally different approach, taking advantage of recent advances in parallel computing capabilities, which are not yet great enough to enable global CPM simulations to become commonplace, and using that power to focus on a more accurate representation of the small-scale. From the perspective of a small-scale stochastic effect on the large-scale model, the effect of SP should be similar to stochastic methods, perhaps better, as the CPM directly simulates the variability of cloud-scale motions while exploring the field's sensitive dependence on initial conditions.

Consider for a moment the most obvious result of convection: precipitation. Lazo et al. (2009) performed a survey of American households asking respondents to rate the importance of different weather forecasts in their daily lives. Six of the top seven responses marked as "extremely" or "very" important (the other being high temperature coming in fifth) were categories related to precipitation (i.e., timing, location, chance, type, and amounts of precipitation). This makes sense in a day-to-day practical sense, as precipitation dictates how we will spend the day, what kind of work can be done outdoors, and whether it's time to water the lawn. This also makes sense on the extreme, longer-term end, as extreme precipitation events can induce dramatic effects in the form of flood and drought. These disasters sit near the top of lists of the most damaging weather-related natural disasters, both in terms of lives lost and financial costs (Smith and Katz 2013; National Centers for Environmental Information cited 2016). Clearly, it is of great importance to simulate precipitation characteristics well.

With the notable exception of an unrealistic double ITCZ, a great majority of models can reproduce broad patterns of precipitation amount and year-to-year variability (Dai 2006; Flato et al. 2013; Mehran et al. 2014). Further buttressing the argument for usefulness of ensembles, Pincus et al. (2008) found a multi-model mean of climate simulations to provide the most consistent and well-matching representation of such large-scale features. Unfortunately, precipitation, and more specifically its extremes, timing, exact spatial distribution, and variability, is one of the more difficult atmospheric phenomena to simulate well. Li et al. (2012) discuss the poor representation of these features as being related to low model resolution and the performance of physics parameterizations as mentioned above. Others have found that many models exhibit a tendency to react too quickly in forming precipitation, not letting the instability build up, and to precipitate too lightly, underestimating heavy precipitation events (Sun et al. 2007; Ma et al. 2012; Rosa and Collins 2013; Garcia-Carreras et al. 2015). Further, Haiden et al. (2012) performed an intercomparison of 24-hour precipitation totals in five global numerical weather prediction models. The models consistently showed tendencies for poorer performance from a measure of skill in the tropics compared to the extratropics and in summer months compared to winter months. Liu et al. (2014) also found significant disagreement in tropical regions and extratropical summer month precipitation among 34 Coupled Model Intercomparison Project Phase 5 (CMIP5) models.

Higher-order precipitation statistics are poor in models using deterministic parameterizations because they tend not to consider the existence of small scale variability. As pointed out by Kooperman et al. (2016), they energetically do not care about the difference between infrequent intense events and frequent weak events because they are more interested in the mean latent heating, which can be the same in both situations. Studies, such as that by Stephens et al. (2010), describe the situation as being quite dire, particularly in light of the fact that model versus observation discrepancies exceed the bounds of error associated with observational or sampling

techniques. They emphasize, as others, far too light precipitation with frequencies up to double that observed, and that this problem tends to vanish in the tropics, and to a lesser extent in the midlatitudes, for models operating at very high resolution, a finding not dissimilar from that of DeMott et al. (2007), who worked with an SP model. Models with stochastic parameterizations are certainly capable of providing an improvement in a number of simulated fields, including the mean, variance, and skewness of convective activity (Gottwald et al. 2016), but such improvements need not be particularly physically based (Buizza et al. 1999). Even their more informed counterparts, like that from Gottwald et al. (2016) who rely solely on observed relationships between convective area fraction and 500 mb vertical velocity, can seem somewhat ad hoc in making the choice as to which components to make stochastic. They tend to be statistics-based first, and process-based second.

Fortunately, the SP configuration does directly account for small-scale processes, with an effect of supplying physical heating and drying tendencies to the large scale that indeed appear more stochastic. In fact, a number of studies (DeMott et al. 2007; Li et al. 2012; Rosa and Collins 2013; Kooperman et al. 2016) demonstrate the vastly superior ability of SP to improve characteristics of precipitation statistics. Figure 1.4 demonstrates SP's superior skill, relative to the Community Atmosphere Model Version 3 (CAM3) with conventional parameterizations, in simulating high-percentile precipitation rates over the continental United States. The results of a similar comparison using global and tropical data by Khairoutdinov and Zhou (2015) are shown in Figure 1.5. Ongoing efforts by Subramanian et al. (2015) examine both stochastic and SP methods in simulations using the ECMWF IFS. They note improved tropical waves and intraseasonal climate variability with SP in long-term simulations and improvements in the modeling of uncertainty in tropical convection, MJO initiation, and tropical cyclone forecasts in SP ensemble forecasts relative to stochastic ensemble forecasts. The extent to which the stochastic nature of SP are

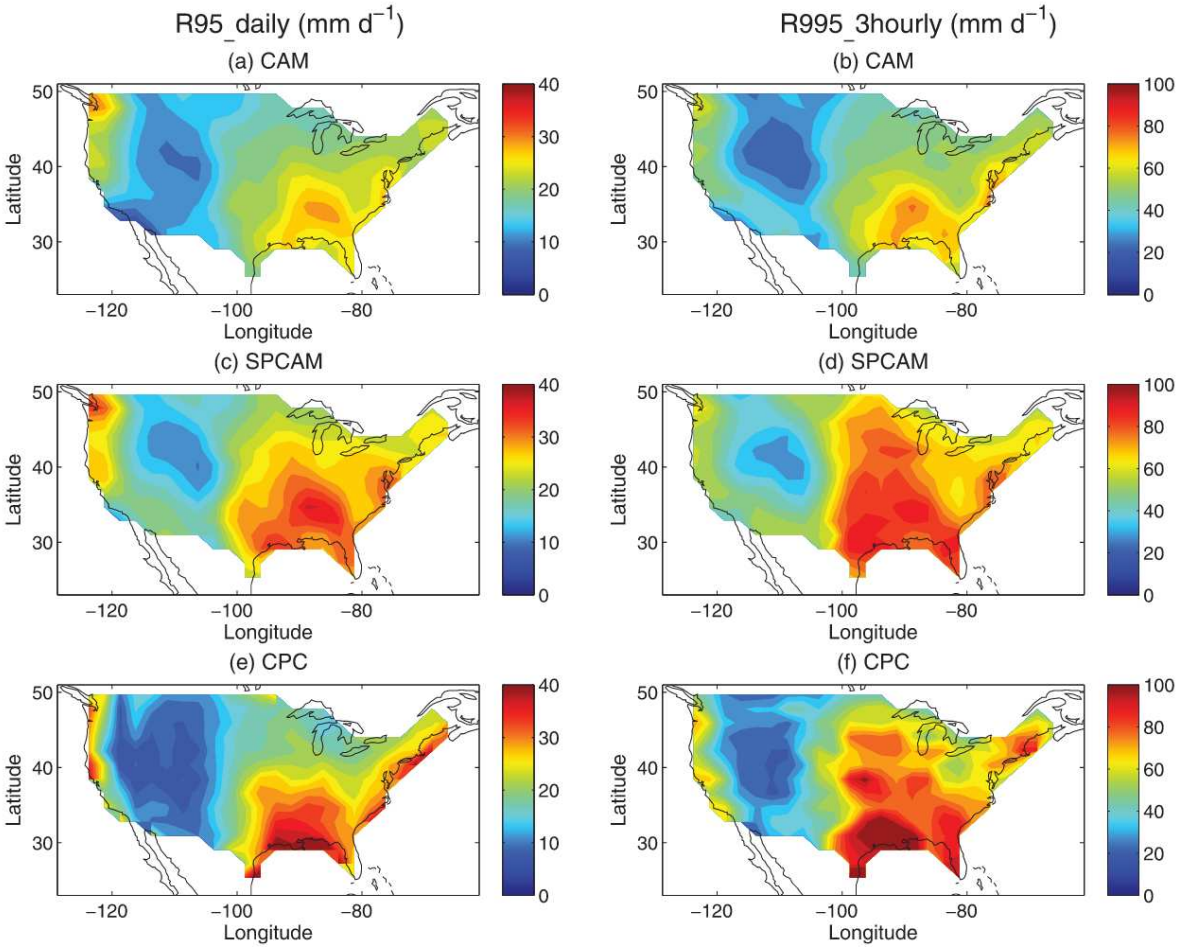

FIGURE 1.4: Caption similar to that presented by Li et al. (2012): Simulated and observed U.S. extreme precipitation: 95th percentile daily precipitation for (a) CAM 3.5.36, (c)SP-CAM, (e) a rain gauge-based observational precipitation dataset from the NOAA Climate Prediction Center (CPC); and 99.5th percentile 3-hourly precipitation for (b) CAM, (d) SP-CAM, (f) CPC.

responsible for the noted improvements remains an open question, but such refined capabilities make the SP configuration ideal for studies of precipitation characteristics.

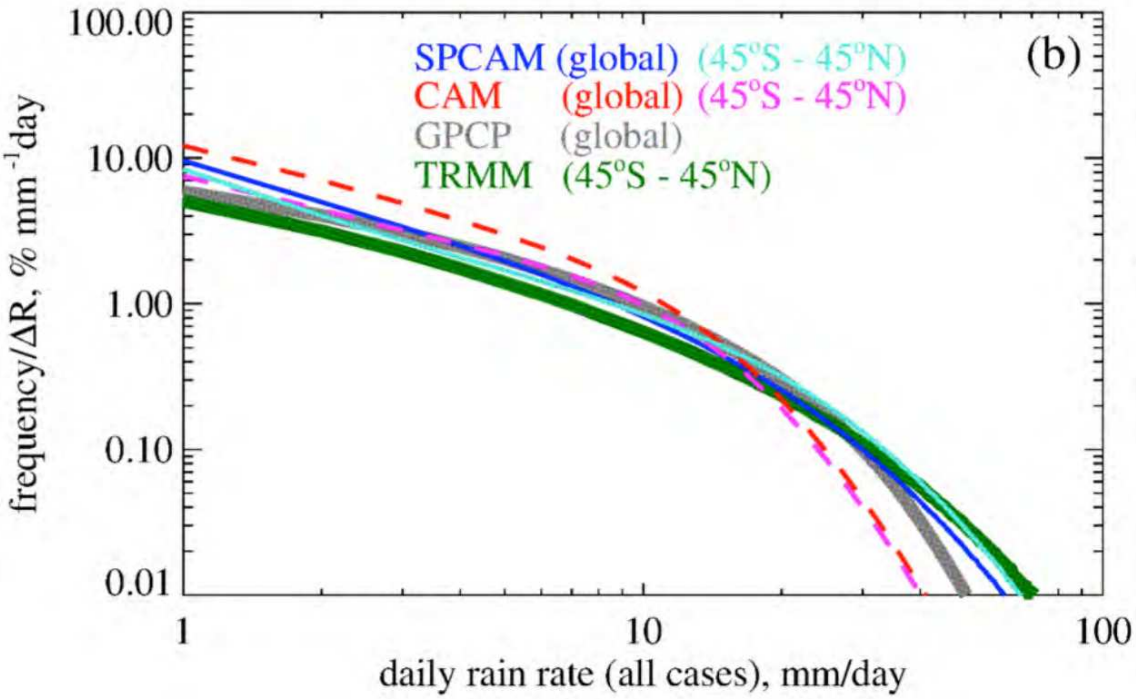

FIGURE 1.5: Caption similar to that presented by Khairoutdinov and Zhou (2015): Color-coded PDFs of daily precipitation rates from T85 CAM 3.5, SP-CAM, Global Precipitation Climatology Project (GPCP), and TRMM over the noted regions.

CHAPTER 2 – EXPERIMENT DESIGN

2.1. SP-CAM DESCRIPTION

Simulations performed in this dissertation begin with the base source code of the special release version of SP-CAM 2.0 (as part of the Community Earth System Model 1.1.1, Randall et al. (2013) available for download at https://svn-ccsm-release.cgd.ucar.edu/model_development_releases/spcam2_0-cesm1_1_1). The underlying atmospheric GCM in SP-CAM 2.0 is Version 5.2 of the CAM (Neale et al. 2012). Here, it is run with the finite volume dynamical core that solves the hydrostatic equations of motion on a $1.9^\circ \times 2.5^\circ$ latitude-longitude grid. The GCM employs 26 levels using a terrain-following hybrid σ-p coordinate, meaning that the levels follow surface elevation in the lower levels and smoothly transition to pressure surfaces aloft. Radiation calculations are performed every GCM time step (15 minutes) using CAM radiation (Neale et al. 2010), and the model includes prognostic bulk aerosols on the GCM grid through the CAM chemistry routines. Sea surface temperatures (SSTs) are prescribed using climatological values, temporally interpolated to the GCM time step; there is no active ocean model in these simulations. Additionally, the model uses the *cam4* physical parameterization package (Neale et al. 2010); this includes moist convective, stratiform cloud, surface, and turbulent processes, which are largely non-interactive when SP is applied.[1] Deep convection is parameterized by a version of the Zhang-McFarlane convective scheme that describes convection in terms of convective plume ensembles that consume convective available potential energy (CAPE) (Zhang and McFarlane 1995), which has been modified to include the plume-diluting effects of entrainment via mixing with the environment (Raymond and Blyth 1992; Neale et al. 2008) and convective

[1]This means that the traditional, deterministic physical parameterizations evaluate the GCM column state and report, but do not apply physical tendencies, cloud and mass flux properties, and precipitation values. These are currently retained for diagnostic purposes but are planned to be bypassed entirely in future releases of SP-CAM.

transport of momentum (Gregory et al. 1997; Richter and Rasch 2008). Parameterization of shallow convection follows that described by Hack (1994), who uses a stability-dependent (based on moist static energy considerations) mass-flux representation of moist convective processes, and large-scale cloud parameterizations include evaporation of convective precipitation following Sundqvist (1988), condensate-vapor phase change effects following Zhang et al. (2003b), and condensate-precipitate conversion effects following Sundqvist (1988) and Rasch and Kristjánsson (1998).

The development of the SP concept arose from the efforts of Grabowski and Smolarkiewicz (1999), Grabowski (2001), Khairoutdinov and Randall (2001), and Khairoutdinov et al. (2005) to provide the most realistic representation of cloud processes in a global model, short of implementing a full global cloud-resolving model (GCRM). In the SP configuration (also often referred to as the multi-scale modeling framework, MMF) of the CAM, conventional physical parameterizations are largely replaced by the use of an embedded, isolated,[2] laterally periodic, two-dimensional (2D) CPM (the System for Atmospheric Modeling, SAM, Version 6.8.2, originally described by Khairoutdinov and Randall (2003)). SAM, as employed here in SP-CAM 2.0, solves the moist nonhydrostatic equations of motion using an anelastic dynamical core, parameterizing microphysics with a bulk, single-moment scheme that produces rain, snow, and graupel and parameterizing turbulence via diagnostic Smagorinsky closure.[3] Each column contains one CPM curtain acting as a detailed sample of convective scale motions, assumed to be representative of the full GCM column. Here, a curtain spans 128 km with 4-km horizontal spacing (32 CPM columns) oriented North-South, with 24 height-coordinate levels in the vertical corresponding to the lowest 24 CAM levels. The areal extent of the CPM domain is not related to the GCM

[2]CPM curtains do not directly interact with each other between GCM grid columns.
[3]Multiple additional options for microphysics and turbulence parameterization are available in SAM and SP-CAM.

grid spacing in much the same way that most conventional parameterizations do not consider the extent of the area they are to represent, and the CPM does not have topography.

The coupling between CAM and SAM has been described by many authors, but was presented most recently and thoroughly by Randall et al. (2016). Here, the qualitative process of the present SP-CAM simulation is described. The simulation is initialized using an internal initialization (i.e., a "cold start") to present climate conditions at the GCM scale. This information is copied over to the CPM as a horizontally uniform profile within each GCM column plus the addition of small, random temperature perturbations over the lowest 5 levels, which act to initiate convection. After the GCM performs its main adiabatic dynamical adjustments resulting in advection of temperature, moisture, and momentum, the "provisional" advected state is compared to the stored CPM mean column state. The differences between the two states act as the large-scale advective forcing of the CPM, in much the same way that stand-alone CRMs can be forced. Representation of atmospheric motions on the convective scale requires much shorter time steps (20 seconds is used in the described configuration), so in order for the CPM to provide a sample of the convective effect that aligns with the GCM time step of 15 minutes, the CPM takes 45 of its own time steps under constant, horizontally uniform forcing from the large-scale. This is sometimes referred to as subcycling, and it is where the model forms and dissipates clouds and precipitation, including features ranging from aggregated systems and squall lines to small-scale turbulent eddies, collectively acting to warm and dry and stabilize the column.

At the conclusion of the CPM integration, the resultant CPM state (and all its natural-looking chaotic components) is averaged horizontally[4] and compared to the initial GCM state. This difference comprises the physical tendencies of temperature, moisture, and condensate due to cloud-scale motions and are qualitatively equivalent to those produced by traditional deterministic parameterizations. These tendencies are then applied to the GCM fields, making the mean column state of the CPM equal to the column state of the GCM, ensuring coherent coupling of the systems as they evolve together. After applying the physical tendencies from the CPM, radiation calculations are performed on the full, detailed CPM state with the radiative tendencies then applied to the GCM column from the CPM horizontal average, generally acting to destabilize the column in the presence of solar forcing. In doing so, the radiation parameterization sees detailed information about fractional cloudiness and overlap. Surface fluxes are computed on the GCM grid. At this point, the whole cycle essentially begins again, with the two models running parallel, continuous simulations.

Some complicating issues arise in this implementation. Perhaps the most obvious is the increase in computational cost, which can be a factor of a hundred in many configurations. Practical simulation, though, is now comfortably possible given high-end supercomputing resources, as it scales well on parallel systems (much more so than a GCRM) and is rather flexible in terms of the fidelity of specific configurations that employ smaller CPM footprints or accelerated CPM simulation (Pritchard et al. 2014; Jones et al. 2015). Other issues are more technical. The previously described vertical coordinates used in the two main components of SP-CAM differ. The hybrid vertical grid of the CAM changes physical position between time steps, and the CPM responds by shifting its height coordinates. However, the previous values of the CPM state are not adjusted. This results in a small spike in the temporal continuity of the CPM integration at

[4]It is also at this point that the full, detailed CPM state is saved to be restarted under new forcing upon the next GCM iteration.

each restart. Potentially, this could be fixed by interpolating to the new grid, but the changes in the hybrid vertical grid are generally so small that the effect is deemed insignificant (Randall et al. 2016). Additionally, the 2D nature of the CPM requires that it feel momentum forcing in only one direction, meridionally in the present configuration. Vertical shear forcing oriented East-West from the GCM, therefore, would not be considered by the GCM, influencing the convective development that may otherwise have initiated organized systems. One might further note that the list of tendencies from the CPM did not include momentum. This is by design, because momentum transport from the 2D CPM is unrealistic according to Khairoutdinov et al. (2005)[5]. Additional details and points of concern are discussed by Randall et al. (2016), who also go on to present potential future developments of the concept.

2.2. MP-CAM DESCRIPTION

A new variation on the SP configuration has been developed, allowing the GCM to interact with the mean feedback of multiple potential realizations of the detailed cloud field produced by multiple two-dimensional CPM curtains. This approach has been dubbed "multiple-parameterization" (MP)[6], and it effectively turns the nondeterministic SP into a deterministic parameterization by using something close to an expected value that may be produced by conventional deterministic parameterizations. In doing so, the physical tendencies from SP that might exhibit strong or sharply varying vertical and temporally stochastic structure would be smoothed by averaging the realizations. How might the climate change with the implementation of the MP configuration? Strong precipitation extremes (including the occurrence of zero precipitation) would surely be reduced, but would the model lose fidelity in large-scale features, like the MJO,

[5]The same authors note that inclusion of the momentum feedback from a three-dimensional CPM alleviates the double Intertropical Convergence Zone (ITCZ) problem common in many GCMs.

[6]As this is a new concept, other names may also be in use. This may also be called multiple-instance superparameterization (MISP).

whose realistic simulation has been attributed to the stochastic nature of the convective scale? The survival of these features with the MP configuration may indicate greater potential for deterministic parameterizations that some have indicated (Zhang 2002; Donner and Phillips 2003; Bechtold et al. 2013). These are among the issues to be addressed in this dissertation.

To accomplish this transformation from SP-CAM into MP-CAM, 10 CPM curtains are run in each GCM column. They are identically configured as in the SP-CAM case. Each curtain is initialized with differing sets of random thermal perturbations, a small difference in initial conditions. After the GCM makes the provisional dynamical adjustment to the large-scale, each member of the CPM ensemble compares its horizontal mean, each applying its own individual large-scale forcing values for the subcycle. The resultant 10 columns of tendencies from the CPMs are then averaged and applied to the GCM state. Radiative tendencies are calculated from the full, detailed states of each member, and their mean is applied to the GCM state. In contrast to the SP-CAM, individual curtains will not have precisely the same mean state as the GCM column after their mean tendency is applied. The ensemble mean, though, would exhibit this constraint, and in this way, the CPMs will stay close to the GCM and one another.

Two important features result from this configuration. First, each member is sees the same large-scale state. But because of their slightly differing initial conditions, they will produce different cloud fields and tendencies. Being less tightly coupled to the GCM than in the SP-CAM case, members will have more freedom to explore potential realizations of convective-scale states possible under the influence of a given large-scale state, effectively modeling the uncertainty inherent at the cloud scale. Recording this information will allow identification of scenarios under which, for the same large-scale forcing and slightly differing cloud-scale scenes, there may be potential for strongly differing results. Perhaps a slight difference means the development of precipitation

in some members, but not others, and in varying intensities. Second, the GCM sees only the effect of the ensemble mean, which should be temporally smoother, and less variable than effect of the single CPM in SP-CAM. In other words, in using a kind of "expected response," the parameterized forcing will be more deterministic and less stochastic. At the same time, the ensemble mean includes the net effect of a quite detailed representation of processes on the convective scale that may still include the beneficial effects produced in SP models.

2.3. Model Simulations

To compare the climates produced by SP-CAM and MP-CAM, multidecadal simulations are performed with each model. SP-CAM was run for 30 years, and MP-CAM was run for just over 23 years[7] on NCAR's Yellowstone supercomputer. Output was recorded as monthly and daily time averages for both models, but evolving needs for certain information and a variety of other complications have yielded a dataset with different availability for different variables. This information has been compiled in tabular format for monthly (Table 2.1) and daily (Table 2.2) data. Timestamps referencing simulation dates follow the YY-MM or YY-MM-DD format. Higher frequency output was also created for January and July subsets of the full MP-CAM simulation. 3-hourly-averaged data was created for model months 07-07 and 08-01 and the period 20-08-01 through 24-04-28, and output every 15 minutes (every GCM time step, with averages only over the CPM subcycle, hereafter ETS) for model days 08-07-02 and 09-01-01. ETS data was also created for SP-CAM on model day 01-01-01. Variables available for the higher frequency output dates correspond to the MP-CAM dates in Table 2.2 with the addition of condensed ice and water and wind components for all CPMs on the global CPM grid for ETS data.

[7]MP-CAM data available as of this writing span the simulation period 01-01 through 24-03 for monthly data and 01-12-31 through 24-04-28, with gaps noted in Tables 2.1 and 2.2

In addition, a 30-year simulation of the standard CAM has been run, using the *cam4* physical parameterization package as described in Section 2.1. It is consistent with the SP-CAM and MP-CAM in terms of grid and initialization. Most[8] of the GCM-level output variables listed in Tables 2.1 and 2.2 for this run as monthly and daily averages for the full simulation period. This simulation provides a deterministic parameterization best-comparison.

Also of note, but not explored here, an SP-CAM ensemble "10-day forecast" simulation was performed; these runs correspond to the first 10 days of January in year 12 of the MP-CAM simulation. The SP-CAM ensemble consists of 10 members using the SP configuration, each initialized from the MP-CAM GCM state and an individual MP-CAM CPM state. This is an ensemble in the traditional sense, with members differing only in initial condition on the CPM grid. Data from each member are available in 3-hourly averages for variables as listed for MP-CAM during year 12 in Table 2.2. For additional comparison, 3-hourly data from the MP-CAM simulation was generated for the same period.

2.4. Observational Datasets

The simulated daily mean outgoing longwave radiation (OLR, also referred to as the upwelling longwave flux at top of model, FLUT in Tables 2.1 and 2.2) from the model simulations is used for comparison with the daily mean NOAA interpolated OLR dataset (Liebmann and Smith 1996). The NOAA OLR dataset is interpolated in time and space from NOAA twice-daily OLR values and averaged to once daily with a spatial resolution of $2.5^\circ \times 2.5^\circ$ latitude-longitude grid. Here, the 30 year record from January 1, 1980 through December 31, 2009 is considered. Thus, this observational dataset is nicely comparable to the simulation datasets in resolution of both time and space. Liebmann and Smith (1996) note that the OLR mapping is accurate to

[8]For instance, no chemical tracer information was saved.

TABLE 2.1: List of monthly-averaged variables produced by the SP and MP simulations that were analyzed from the output NETCDF files. Table footnotes detail a number of data characteristics. A number of additional fields exist but have been omitted for reasons that include quality, relevance, constants, and repetition. Symbolic names are as in the output files. Some long names have been edited from their SP-CAM-coded form for clarity. If not otherwise noted, the values are computed from information available on the GCM grid and span the full simulation times as stated in the text. Simulation dates in the table footnotes are in the YY-MM format.

Symbolic Name	Long Name	Units
ATMEINT	Vertically integrated total atmospheric energy	J m^{-2}
CB1	Black Carbon concentration, hydrophobic (new)	kg kg^{-1}
CB2	Black Carbon concentration, hydrophilic (aged)	kg kg^{-1}
CLDHGH[g]	Vertically-integrated high cloud	fraction
CLDICE	Grid box averaged cloud ice amount	kg kg^{-1}
CLDLIQ	Grid box averaged cloud liquid amount	kg kg^{-1}
CLDLOW[g]	Vertically-integrated low cloud	fraction
CLDMED[g]	Vertically-integrated mid-level cloud	fraction
CLDTOT[g]	Vertically-integrated total cloud	fraction
CLOUD[f]	Cloud fraction	fraction
CLOUDTOP[f]	Cloud Top PDF	fraction
CMFDQ[a]	Water vapor tendency - shallow convection	kg kg^{-1} s^{-1}
CMFDQR[a]	Water vapor tendency - shallow convection, rainout	kg kg^{-1} s^{-1}
CMFDT[a]	Temperature tendency - shallow convection	K s^{-1}
CMFMC[a]	Moist shallow convection mass flux	kg m^{-2} s^{-1}
CMFMCDZM[a]	Convection mass flux - deep convection	kg m^{-2} s^{-1}
CONCLD[a]	Convective cloud cover	fraction
DMS	Dimethyl sulfide, CH_3SCH_3, concentration	mol mol^{-1}
DMSSNK	DMS sink	kg kg^{-1} s^{-1}
DST01[c]	Dust, $AlSiO_5$, mixing ratio	kg kg^{-1}
DST01DD[c]	DST01 dry deposition flux at bottom (grav + turb)	kg m^{-2} s^{-1}
DST01DT[c]	DST01 dry deposition	kg kg^{-1} s^{-1}
DST01DV[c]	DST01 deposition velocity	m s^{-1}
DST01GV[c]	DST01 gravitational dry deposition flux	kg m^{-2} s^{-1}
DST01PP[c]	DST01 wet deposition	kg kg^{-1} s^{-1}
DST01SF[c]	DST01 dust surface emission	kg m^{-2} s^{-1}
DST01TB[c]	DST01 turbulent dry deposition flux	kg m^{-2} s^{-1}
DSTSFDRY	Dust dry deposition flux at surface	kg m^{-2} s^{-1}
DSTSFMBL	Dust mobilization flux at surface	kg m^{-2} s^{-1}
DSTSFWET	Dust wet deposition flux at surface	kg m^{-2} s^{-1}
DTV	Temperature vertical diffusion	K s^{-1}

Continued on next page

TABLE 2.1: *Continued*

Symbolic Name	Long Name	Units
FICE	Fractional ice content within cloud	fraction
FLDS	Downwelling longwave flux at surface	W m^{-2}
FLDSC	Clearsky downwelling longwave flux at surface	W m^{-2}
FLNS	Net longwave flux at surface	W m^{-2}
FLNSC	Clearsky net longwave flux at surface	W m^{-2}
FLNT	Net longwave flux at top of model	W m^{-2}
FLNTC	Clearsky net longwave flux at top of model	W m^{-2}
FLUT	Upwelling longwave flux at top of model	W m^{-2}
FLUTC	Clearsky upwelling longwave flux at top of model	W m^{-2}
FREQSH[a]	Fractional occurrence of shallow convection	fraction
FREQZM[a]	Fractional occurrence of deep convection	fraction
FSDS	Downwelling solar flux at surface	W m^{-2}
FSDSC	Clearsky downwelling solar flux at surface	W m^{-2}
FSDTOA	Downwelling solar flux at top of atmosphere	W m^{-2}
FSNS	Net solar flux at surface	W m^{-2}
FSNSC	Clearsky net solar flux at surface	W m^{-2}
FSNT	Net solar flux at top of model	W m^{-2}
FSNTC	Clearsky net solar flux at top of model	W m^{-2}
FSNTOA	Net solar flux at top of atmosphere	W m^{-2}
FSNTOAC	Clearsky net solar flux at top of atmosphere	W m^{-2}
FSUTOA	Upwelling solar flux at top of atmosphere	W m^{-2}
H2O2	H_2O_2 concentration	mol mol^{-1}
H2O2SNKA	H_2O_2 Sink, aqueous	kg kg^{-1} s^{-1}
H2O2SNKG	H_2O_2 Sink, gas	kg kg^{-1} s^{-1}
H2O2SRC	H_2O_2 Source	kg kg^{-1} s^{-1}
ICIMR[a]	Prognostic in-cloud ice mixing ratio	kg kg^{-1}
ICLDIWP[b,f,l]	In-cloud ice water path	kg m^{-2}
ICLDTWP[b,f,l]	In-cloud cloud total water path (liquid and ice)	kg m^{-2}
ICWMR[a]	Prognostic in-cloud water mixing ratio	kg kg^{-1}
LHFLX	Surface latent heat flux	W m^{-2}
LWCF[d]	Longwave cloud forcing	W m^{-2}
OC1	Organic Carbon concentration, hydrophobic (new)	kg kg^{-1}
OC2	Organic Carbon concentration, hydrophilic (aged)	kg kg^{-1}
OMEGA	Vertical velocity (pressure)	Pa s^{-1}
OMEGAT	Vertical heat flux	K Pa s^{-1}
PBLH	Planetary boundary layer height	m
PCONVB[a]	Deep convection base pressure	Pa
PCONVT[a]	Deep convection top pressure	Pa

Continued on next page

TABLE 2.1: *Continued*

Symbolic Name	Long Name	Units
PHIS	Surface geopotential	$m^2\ s^{-2}$
PRECC[b,f]	Total precipitation rate	$m\ s^{-1}$
PRECCDZM[a]	Deep convection precipitation rate	$m\ s^{-1}$
PRECSC[b,f]	Snow rate (water equivalent)	$m\ s^{-1}$
PRECSH[a]	Shallow Convection precipitation rate	$m\ s^{-1}$
PRECTFREQ[b,e]	Total precipitation frequency	fraction
PS	Surface pressure	Pa
PSL	Sea level pressure	Pa
Q	Specific humidity	$kg\ kg^{-1}$
QC[a]	Water vapor tendency - shallow convection	$kg\ kg^{-1}\ s^{-1}$
QFLX	Surface water flux	$kg\ m^{-2}\ s^{-1}$
QREFHT	2-m height humidity	$kg\ kg^{-1}$
QRL	Longwave heating rate	$K\ s^{-1}$
QRS	Solar heating rate	$K\ s^{-1}$
RELHUM	Relative humidity	percent
RHREFHT	2-m height relative humidity	fraction
SHFLX	Surface sensible heat flux	$W\ m^{-2}$
SO2	SO_2 concentration	$mol\ mol^{-1}$
SO2SRCG	SO_2 Source, total	$kg\ kg^{-1}\ s^{-1}$
SO2SRCG2	SO_2 Source, DMS and OH	$kg\ kg^{-1}\ s^{-1}$
SO4	SO_4 concentration	$kg\ kg^{-1}$
SO4SRC	SO_4 Source, total	$kg\ kg^{-1}\ s^{-1}$
SO4SRCG	SO_4 Source, gas	$kg\ kg^{-1}\ s^{-1}$
SOLIN	Solar insolation	$W\ m^{-2}$
SPBUOY[b,f]	Buoyancy term	$W\ m^{-3}$
SPBUOYSD[b,f]	Standard deviation of the buoyancy term	$W\ m^{-3}$
SPDQ[b]	Water vapor mixing ratio tendency due to CPM	$kg\ kg^{-1}\ s^{-1}$
SPDQC[b]	Cloud water mixing ratio tendency due to CPM	$kg\ kg^{-1}\ s^{-1}$
SPDQI[b]	Cloud ice mixing ratio tendency due to CPM	$kg\ kg^{-1}\ s^{-1}$
SPDT[b]	Temperature tendency due to CPM	$K\ s^{-1}$
SPMC[b,h,k]	Total mass flux	$kg\ m^{-2}\ s^{-1}$
SPMCDN[b,h]	Downdraft mass flux	$kg\ m^{-2}\ s^{-1}$
SPMCUDN[b,h]	Unsaturated downdraft mass flux	$kg\ m^{-2}\ s^{-1}$
SPMCUP[b,h]	Updraft mass flux	$kg\ m^{-2}\ s^{-1}$
SPMCUUP[b,h]	Unsaturated updraft mass flux	$kg\ m^{-2}\ s^{-1}$
SPMSEF[b,h]	Moist static energy flux	$W\ m^{-2}$
SPPFLX[b,f]	Precipitation flux	$m\ s^{-1}$
SPQC[b,f,j]	Cloud water mixing ratio	$kg\ kg^{-1}$

Continued on next page

TABLE 2.1: *Continued*

Symbolic Name	Long Name	Units
SPQG[b,f,j]	Graupel mixing ratio	kg kg^{-1}
SPQI[b,f,j]	Cloud ice mixing ratio	kg kg^{-1}
SPQPEVP[b,f]	Precipitating water evaporation	kg kg^{-1} s^{-1}
SPQPFALL[b,f]	Precipitating water fallout	kg kg^{-1} s^{-1}
SPQPFLX[b,f]	Precipitating water flux	kg m^{-2} s^{-1}
SPQPSRC[b,f]	Precipitating water source	kg kg^{-1} s^{-1}
SPQPTR[b,f]	Precipitating water transport	kg kg^{-1} s^{-1}
SPQR[b,f,j]	Rain mixing ratio	kg kg^{-1}
SPQS[b,f,j]	Snow mixing ratio	kg kg^{-1}
SPQTFLX[b,f]	Non-precipitating water flux	kg m^{-2} s^{-1}
SPQTFLXS[b,f]	Subgrid-scale non-precipitating water flux	kg m^{-2} s^{-1}
SPQTLS[b,f]	Large-scale water vapor tendency (forcing)	kg kg^{-1} s^{-1}
SPQTTR[b,f]	Non-precipitating water transport	kg kg^{-1} s^{-1}
SPQVFLUX[b,f]	Water vapor flux	W m^{-2}
SPTK[b,f]	Subgrid-scale eddy viscosity	m^2 s^{-1}
SPTKE[b,h]	Total turbulent kinetic energy	kg m^{-1} s^{-2}
SPTKES[b,f]	Subgrid-scale turbulent kinetic energy	kg m^{-1} s^{-2}
SPTLS[b,f]	Large-scale liquid-ice water static energy tendency (forcing)	kg kg^{-1} s^{-1}
SPTVFLUX[b,f]	Buoyancy Flux from CPM	W m^{-2}
SRFRAD	Net radiative flux at surface	W m^{-2}
SSLT01[c]	NaCl Prognostic sea salts mixing ratio	kg kg^{-1}
SSLT01DD[c]	SSLT01 dry deposition flux at bottom (grav + turb)	kg m^{-2} s^{-1}
SSLT01DT[c]	SSLT01 dry deposition	kg kg^{-1} s^{-1}
SSLT01DV[c]	SSLT01 deposition velocity	m s^{-1}
SSLT01GV[c]	SSLT01 gravitational dry deposition flux	kg m^{-2} s^{-1}
SSLT01PP[c]	SSLT01 wet deposition	kg kg^{-1} s^{-1}
SSLT01SF[c]	SSLT01 surface emission	kg m^{-2} s^{-1}
SSLT01TB[c]	SSLT01 turbulent dry deposition flux	kg m^{-2} s^{-1}
SSTSFDRY	Dry deposition flux at surface	kg m^{-2} s^{-1}
SSTSFMBL	Mobilization flux at surface	kg m^{-2} s^{-1}
SSTSFWET	Wet deposition flux at surface	kg m^{-2} s^{-1}
SWCF[d]	Shortwave cloud forcing	W m^{-2}
T	Temperature	K
T700	Temperature at 700 mbar pressure surface	K
T850	Temperature at 850 mbar pressure surface	K
TAUX	Zonal surface stress	N m^{-2}
TAUY	Meridional surface stress	N m^{-2}

Continued on next page

TABLE 2.1: *Continued*

Symbolic Name	Long Name	Units
TGCLDCWP[b,g]	Total grid-box cloud water path (liquid and ice)	kg m^{-2}
TGCLDIWP[b,i]	Total grid-box cloud ice water path	kg m^{-2}
TGCLDLWP[b,h]	Total grid-box cloud liquid water path	kg m^{-2}
TMQ	Total (vertically-integrated) precipitable water	kg m^{-2}
TREFHT	2-m height temperature	K
TREFMNAV	Average of TREFHT daily minimum	K
TREFMXAV	Average of TREFHT daily maximum	K
TROP_P	Tropopause pressure	Pa
TROP_T	Tropopause temperature	K
TROP_Z	Tropopause height	m
TS	Surface temperature (radiative)	K
TSMN	Minimum surface temperature	K
TSMX	Maximum surface temperature	K
U	Zonal wind speed	m s^{-1}
U10	10-m wind speed	m s^{-1}
UU	Zonal velocity squared	m^2 s^{-2}
V	Meridional wind speed	m s^{-1}
VD01	Vertical diffusion of water vapor	kg kg^{-1} s^{-1}
VQ	Meridional water transport	m s^{-1}kg kg^{-1}
VT	Meridional heat transport	K m s^{-1}
VU	Meridional flux of zonal momentum	m^2 s^{-2}
VV	Meridional velocity squared	m^2 s^{-2}
Z3	Geopotential height (above sea level)	m

[a] Data is a product of the CAM conventional physical parameterizations.
[b] Data is an average of information on the CPM grid scale.
[c] These variables are reported for four size bins (0.1-1.0, 1.0-2.5, 2.5-5.0, and 5.0-10.0 μm), which are identified by corresponding numerical codes in the symbolic name (01, 02, 03, and 04).
[d] MP-CAM data prior to 16-06 are too high by a factor of 1000.
[e] MP-CAM data prior to 07-11 were computed incorrectly.
[f] MP-CAM data represent information from one CPM member only.
[g] MP-CAM data represent information from one CPM member only through 19-12 and all CPM ensemble members from 20-01.
[h] MP-CAM data represent information from one CPM member only through 06-12 and all CPM ensemble members from 07-01.
[i] MP-CAM data represent information from one CPM member only through 06-12 and all CPM ensemble members from 20-01. Data for this variable do not exist between those months.
[j] MP-CAM data end at 19-12.
[k] MP-CAM data for 06-11 and 06-12 were computed incorrectly.
[l] MP-CAM data prior to 06-11 were computed incorrectly.

TABLE 2.2: List of daily-averaged variables produced by the SP and MP simulations available in NETCDF format. Duplicate fields have been omitted. Table footnotes detail a number of data characteristics. Symbolic names are as in the output files. Availability for the SP or MP simulation is denoted by $\times$. Some long names have been edited from their SP-CAM-coded form for clarity. If not otherwise noted, the values are computed on the CAM grid. SP-CAM output is consistent for its full simulated period. The availability of MP-CAM data is in the YY-MM-DD format.

Symbolic Name	SP	MP	Long Name	Units	MP-CAM Data Range
CAPEP		$\times$	Pseudoadiabatic convective available potential energy	J kg^{-1}	04-01-03 – end
CAPER		$\times$	Moist adiabatic convective available potential energy	J kg^{-1}	04-01-03 – end
CINP		$\times$	Pseudoadiabatic convective inhibition	J kg^{-1}	04-01-03 – end
CINR		$\times$	Moist adiabatic convective inhibition	J kg^{-1}	04-01-03 – end
CLDHGH[a]	$\times$	$\times$	Vertically-integrated high cloud	fraction	04-01-03 – 20-08-01
CLDHGH[b]		$\times$	Vertically-integrated high cloud	fraction	20-08-02 – end
CLDICE	$\times$	$\times$	Grid box averaged cloud ice amount	kg kg^{-1}	06-10-05 – 07-12-31 09-05-26 – end
CLDLIQ	$\times$	$\times$	Grid box averaged cloud liquid amount	kg kg^{-1}	06-10-05 – 07-12-31 09-05-26 – end
CLDLOW[a]	$\times$	$\times$	Vertically-integrated low cloud	fraction	04-01-03 – 20-08-01
CLDLOW[b]		$\times$	Vertically-integrated low cloud	fraction	20-08-02 – end
CLDMED[a]	$\times$	$\times$	Vertically-integrated mid-level cloud	fraction	04-01-03 – 20-08-01
CLDMED[b]		$\times$	Vertically-integrated mid-level cloud	fraction	20-08-02 – end
CLDTOT	$\times$		Vertically-integrated total cloud	fraction	- -
CLOUD	$\times$	$\times$	Cloud fraction	fraction	06-10-05 – 07-12-31 09-05-26 – end
CRM_PREC[c]	$\times$	$\times$	Precipitation rate	m s^{-1}	02-09-12 – 04-01-02 06-10-05 – 07-12-31 09-05-26 – end

Continued on next page

TABLE 2.2: *Continued*

Symbolic Name	SP	MP	Long Name	Units	MP-CAM Data Range
CRM_PREC_ALL[d]		×	Precipitation rate	m s^{-1}	01-12-31 – 02-09-11
CRM_QV_RAD[d]		×	Water vapor mixing ratio	kg kg^{-1}	02-09-27 – 04-01-02 06-02-22 – 07-12-31 09-05-26 – end
CRM_T_ALL[d]		×	Temperature	K	06-02-22 – 07-12-31 09-05-26 – end
CRM_T_RAD[d]		×	Temperature	K	02-09-27 – 04-01-02
FLDS		×	Downwelling longwave flux at surface	W m^{-2}	01-12-31 – 04-01-02
FLNS	×	×	Net longwave flux at surface	W m^{-2}	01-12-31 – end
FLNS_ALL[b]		×	Net longwave flux at surface	W m^{-2}	01-12-31 – 04-01-02
FLNSC	×		Clearsky net longwave flux at surface	W m^{-2}	- -
FLNT	×	×	Net longwave flux at top of model	W m^{-2}	01-12-31 – 04-01-02
FLNTC	×		Clearsky net longwave flux at top of model	W m^{-2}	- -
FLUT	×	×	Upwelling longwave flux at top of model	W m^{-2}	04-01-03 – end
FLUT_ALL[b]		×	Upwelling longwave flux at top of model	W m^{-2}	01-12-31 – 04-01-02
FLUTC	×	×	Clearsky upwelling longwave flux at top of model	W m^{-2}	09-06-19 – end
FSDS	×	×	Downwelling solar flux at surface	W m^{-2}	01-12-31 – 04-01-02
FSDSC	×		Clearsky downwelling solar flux at surface	W m^{-2}	- -
FSDTOA		×	Downwelling solar flux at top of atmosphere	W m^{-2}	09-06-19 – end
FSNS	×	×	Net solar flux at surface	W m^{-2}	01-12-31 – end
FSNS_ALL[b]		×	Net solar flux at surface	W m^{-2}	01-12-31 – 04-01-02
FSNSC	×		Clearsky net solar flux at surface	W m^{-2}	- -

Continued on next page

TABLE 2.2: *Continued*

Symbolic Name	SP	MP	Long Name	Units	MP-CAM Data Range
FSNT	×	×	Net solar flux at top of model	W m^{-2}	01-12-31 – 04-01-02
FSNT_ALL[b]		×	Net solar flux at top of model	W m^{-2}	01-12-31 – 04-01-02
FSNTC	×		Clearsky net solar flux at top of model	W m^{-2}	- -
FSNTOA	×	×	Net solar flux at top of atmosphere	W m^{-2}	09-06-19 – end
FSNTOAC	×	×	Clearsky net solar flux at top of atmosphere	W m^{-2}	09-06-19 – end
FSUTOA	×		Upwelling solar flux at top of atmosphere	W m^{-2}	- -
GCLDLWP[a]		×	Grid-box cloud water path	kg m^{-2}	06-10-05 – 07-01-22
GCLDLWP[b]		×	Grid-box cloud water path	kg m^{-2}	07-01-23 – 07-12-31 09-05-26 – end
LHFLX	×	×	Surface latent heat flux	W m^{-2}	04-01-03 – end
LWCF	×		Longwave cloud forcing	W m^{-2}	- -
OMEGA	×	×	Vertical velocity (pressure)	Pa s^{-1}	04-01-03 – end
PBLH	×	×	Planetary boundary layer height	m	06-10-05 – 07-12-31 09-05-26 – end
PHIS	×		Surface geopotential	m^2 s^{-2}	- -
PRECENMN	×	×	CPM ensemble mean precipitation rate	m s^{-1}	01-12-31 – end
PRECENSD		×	CPM ensemble precipitation standard deviation	m s^{-1}	01-12-31 – end
PRECMN[b]		×	Precipitation rate	m s^{-1}	01-12-31 – end
PRECTFREQ[e]		×	Precipitation frequency (based on PRECENMN)	fraction	01-12-31 – end
PRECTFREQALL[b]		×	Precipitation frequency (based on PRECMN)	fraction	09-05-26 – end
PS	×	×	Surface pressure	Pa	01-12-31 – end
PSL	×		Sea level pressure	Pa	- -

Continued on next page

TABLE 2.2: *Continued*

Symbolic Name	SP	MP	Long Name	Units	MP-CAM Data Range
Q	×	×	Specific humidity	kg kg^{-1}	04-01-03 – end
QRL_ALL[b]	×	×	Longwave heating rate	K s^{-1}	01-12-31 – 04-01-02 06-10-05 – 07-12-31 09-05-26 – end
QRS_ALL[b]	×	×	Solar heating rate	K s^{-1}	01-12-31 – 04-01-02 06-10-05 – 07-12-31 09-05-26 – end
RELHUM	×	×	Relative humidity	percent	06-10-05 – 07-12-31 09-05-26 – end
SHFLX	×	×	Surface sensible heat flux	W m^{-2}	04-01-03 – end
SPDQ_ALL[b]		×	Water vapor tendency due to CPM	kg kg^{-1} s^{-1}	01-12-31 – 04-01-02 06-01-08 – 07-12-31 09-05-26 – end
SPDT_ALL[b]		×	Temperature tendency due to CPM	K s^{-1}	01-12-31 – 04-01-02 06-01-08 – 07-12-31 09-05-26 – end
SPMC[a,f]		×	Total mass flux	kg m^{-2} s^{-1}	06-10-05 – 07-01-22
SPMC[b]		×	Total mass flux	kg m^{-2} s^{-1}	07-01-23 – 07-12-31 09-05-26 – end
SPMCDN[a]		×	Downdraft mass flux	kg m^{-2} s^{-1}	06-10-05 – 07-01-22
SPMCDN[b]		×	Downdraft mass flux	kg m^{-2} s^{-1}	07-01-23 – 07-12-31 09-05-26 – end
SPMCUDN[a]		×	Unsaturated downdraft mass flux	kg m^{-2} s^{-1}	06-10-05 – 07-01-22
SPMCUDN[b]		×	Unsaturated downdraft mass flux	kg m^{-2} s^{-1}	07-01-23 – 07-12-31 09-05-26 – end

Continued on next page

TABLE 2.2: *Continued*

Symbolic Name	SP	MP	Long Name	Units	MP-CAM Data Range
SPMCUP[a]		×	Updraft mass flux	kg m^{-2} s^{-1}	06-10-05 – 07-01-22
SPMCUP[b]		×	Updraft mass flux	kg m^{-2} s^{-1}	07-01-23 – 07-12-31 09-05-26 – end
SPMCUUP[a]		×	Unsaturated updraft mass flux	kg m^{-2} s^{-1}	06-10-05 – 07-01-22
SPMCUUP[b]		×	Unsaturated updraft mass flux	kg m^{-2} s^{-1}	07-01-23 – 07-12-31 09-05-26 – end
SPMSEF[a]		×	Moist static energy flux	W m^{-2}	06-10-05 – 07-01-22
SPMSEF[b]		×	Moist static energy flux	W m^{-2}	07-01-23 – 07-12-31 09-05-26 – end
SPQTLS[a]		×	Large scale water vapor tendency (forcing)	kg kg^{-1} s^{-1}	09-06-19 – end
SPTKE[a]		×	Total turbulent kinetic energy	kg m^{-1} s^{-2}	06-10-05 – 07-01-22
SPTKE[b]		×	Total turbulent kinetic energy	kg m^{-1} s^{-2}	07-01-23 – 07-12-31 09-05-26 – end
SPTLS[a]		×	Large-scale liquid-ice water static energy tendency (forcing)	kg kg^{-1} s^{-1}	09-06-19 – end
SPTVFLUX[a]		×	Buoyancy flux	W m^{-2}	04-01-03 – end
SPWTKE[a]		×	Standard deviation of updraft velocity	m s^{-1}	06-10-05 – 07-12-31 09-05-26 – end
SWCF	×		Shortwave cloud forcing	W m^{-2}	- -
T	×	×	Temperature	K	04-01-03 – end
TAUX	×		Zonal surface stress	N m^{-2}	- -
TAUY	×		Meridional surface stress	N m^{-2}	- -
TGCLDIWP[a]	×	×	Total grid-box cloud ice water path	kg m^{-2}	06-10-05 – 07-01-22

Continued on next page

TABLE 2.2: *Continued*

Symbolic Name	SP	MP	Long Name	Units	MP-CAM Data Range
TGCLDIWP[b]		×	Total grid-box cloud ice water path	kg m^{-2}	07-01-23 – 07-12-31 09-05-26 – end
TGCLDLWP[a]	×	×	Total grid-box cloud liquid water path	kg m^{-2}	06-10-05 – 07-01-22
TGCLDLWP[b]	×	×	Total grid-box cloud liquid water path	kg m^{-2}	07-01-23 – 07-12-31 09-05-26 – end
TMQ	×	×	Total (vertically-integrated) precipitable water	kg m^{-2}	06-10-05 – 07-12-31 09-05-26 – end
TREFHT	×		Reference height temperature	K	- -
TS	×	×	Surface temperature (radiative)	K	04-01-03 – end
U	×	×	Zonal wind	m s^{-1}	04-01-03 – end
U2Z[b]		×	U Covariance,	m^2 s^{-2}	04-01-03 – end
V	×	×	Meridional wind	m s^{-1}	04-01-03 – end
V2Z[b]		×	V Covariance	m^2 s^{-2}	04-01-03 – end
VIBF[b]		×	Vertically-integrated buoyancy flux	W m^{-2}	04-01-03 – end
W2Z[b]		×	W Covariance	m^2 s^{-2}	04-01-03 – end
Z3	×	×	Geopotential height (above sea level)	m	01-12-31 – end

[a] Data for a single CPM member only.
[b] Data for all individual CPM ensemble members.
[c] CPM ensemble mean, output on the global CPM grid.
[d] Output for all CPM members on the global CPM grid.
[e] MP-CAM data prior to 07-10-06 were computed incorrectly.
[f] MP-CAM data were output with incorrect dimensions from 06-11-19 through 07-01-22.

within 6 hours, but because the satellite sampling is performed in 14 swaths per day, anomalous power will appear at that frequency in the course of spectral analysis

Two commonly employed observational precipitation data sets are also introduced for the purposes of statistical comparison to the simulated data. Both were obtained from the National Center for Atmospheric Research's (NCAR) Climate and Global Dynamics (CGD) Laboratory and are available online (ftp://ftp.cgd.ucar.edu/archive/PRECIP)[9]. The first of these is a global product from the Global Precipitation Climatology Project (GPCP, v 1.2), known as the GPCP One-Degree Daily (1DD) Precipitation Data Set (Huffman et al. 2001). As its name suggests, the data are daily estimates of precipitation presented on a global $1^\circ \times 1^\circ$ latitude-longitude grid, representing a complex combination of infrared and microwave satellite-based measurements and surface rain gauge measurements that were originally made at higher temporal resolution. The available data spans 6,878 days, from October 1996 to July 2015.

The second observational precipitation data set comes from the Tropical Rainfall Measuring[10] Mission (TRMM), which provides 3-hourly precipitation rate estimates on a $0.25^\circ \times 0.25^\circ$ latitude-longitude grid with spatial coverage in the latitude band from 50°S to 50°N. The TRMM data used here is derived from a set of satellite-based microwave, visible, infrared, and radar instruments and rain gauges. More specifically, this is known as the TRMM Multi-satellite Precipitation Analysis (TMPA) product 3B42 version 7 compiled by Huffman et al. (2007). The TRMM data obtained from CGD were already averaged to a daily precipitation estimate, spanning 5,844 days, from January 1998 to December 2013. For best comparison to the model data, both observational precipitation data sets were regridded to the CAM grid using conservative interpolation

[9]Data were obtained from this source mainly for convenience. The data can be found in their original form in multiple locations and formats. For example, such GPCP data is available from https://www.ncdc.noaa.gov/wdc/wdcamet-ncdc.html and http://precip.gsfc.nasa.gov/gpcp_daily_comb.html, and such TRMM data is available from http://precip.gsfc.nasa.gov/ and https://pmm.nasa.gov/data-access/downloads/trmm.

[10]This is sometimes found in publications and professional websites as "Measure" or "Measurement."

(Jones 1999) that preserves the spatial integral of the data between the observation and model grids. Though these two data sets both have monthly totals constrained in a similar manner and have similar annual means nearly centered on the range of values provided by many observational and reanalysis systems, they exhibit some significant climatological differences in spatial distribution, frequency distribution, and temporal variability (Gehne et al. 2016; Kooperman et al. 2016), some of which will be shown here.

CHAPTER 3 – ISSUES IN PREDICTABILITY

Clearly, as evidenced by their ability to improve model simulations, the nondeterministic effects of simulating potential individual realizations of cloud effects through stochastic parameterizations and SP is desirable over the expected values produced by deterministic parameterizations. An interesting question remains. Where are these effects having an influence? For example, Kober and Craig (2016), who applied physically based (and notably variable in space and time because of this) stochastic perturbations to physical tendencies in the boundary layer of a regional NWP model, show that the effects of the perturbations were small in the case of convection associated with a cold front but rather consequential in the case of weaker synoptic forcing that relies on CAPE exceeding CIN to begin convection. In the cold front case, there may only be a small range of possible realizations at the cloud scale. In the MP configuration, the ability to examine the parameter space of the individual members of the CPM ensemble may be retained for further study. Low predictability would be indicated when the members produce strongly disparate precipitation rates and physical tendencies, as their mean states each closely match the associated GCM profile with small variations on the small-scale. If those small variations result in large differences, a significant influence of the stochasticity has been located. From there, one can look for associated features on the large-scale that may permit the identification of low-predictability scenarios from a single deterministic forecast on a coarse grid. This kind of predictability information would be useful to forecasters and decision makers for whom precipitation accuracy is a priority, at least as an indication that their forecast might be unreliable. Knowing this, they could act to obtain better information from a higher resolution model over the problem area, perhaps one initialized with targeted observations performed where high

uncertainty lies. Additionally, this information would be useful in the formulation of future stochastic parameterizations, guiding it to the points where greater stochastic effects are likely to be required. The search for these less predictable large-scale conditions will be a focus of this dissertation.

A great many studies have investigated the mechanisms controlling the predictability of convection and the associated precipitation that might provide an advantageous head start in the MP investigation. As Roebber et al. (2004) note in their comparison of high-resolution and ensemble methods to improve prediction, "Since all model forecasts are imperfect, forecasters need to be able to ascertain when and why forecasts are going wrong." One goal of this dissertation is to provide guidance as to the large-scale conditions under which strong precipitation is difficult to predict. The approach in this dissertation is similar of that used by Jankov and Gallus (2004) to link large-scale model fields indicating the strength of the large-scale forcing to the model's ability to predict convective features. Examining simulated mesoscale convective system (MCS) events over the Upper Midwest in the United States, they analyzed the relationship between forcing elements, such as upper-level dynamic forcing, low-level dynamic forcing, and high and low values of convective available potential energy (CAPE), convective inhibition (CIN), relative humidity (RH) averaged in the 1000-500-mb layer, and precipitable water (PW), and the equitable threat score (ETS) as a measure of rainfall forecast accuracy. Overall, they found that greater prediction skill was associated with more strongly forced events[1], and vice versa. More explicitly, strong dynamical forcing, high CAPE, low CIN, and high RH environments tended toward more predictable events, while PW showed little influence on the ETS. The most predictable cases were associated with organizing large-scale features, frequently cold fronts and trailing stratiform

[1]A similar conclusion can be drawn from inspection of Figure 3 in Anber et al. (2014), showing time series of precipitation for various values of surface fluxes and wind shear. Specifically, the higher ratio of variability to the time mean precipitation in the cases of low surface fluxes compared to the cased of higher surface fluxes indicates the predictability difference with forcing.

squall lines, and the least predictable cases were those with elevated convection with low CAPE situated away from frontal structures or those forming nonlinear clusters. The latter cases may be situations where convective triggers would be important in parameterizing the events with some fidelity.

This result is similar to the results of the analysis by Stensrud et al. (2000) that compared the forecasting abilities of an ensemble consisting of members differing only in their initial conditions against an ensemble consisting of members differing only in their physical parameterization schemes. Though the differences between the two ensemble types were small, they found the ETS to be higher for a more strongly forced event.

A caveat of comparing the work of Jankov and Gallus (2004) and Stensrud et al. (2000) to that presented here is that we are considering different spatial scales over which we measure predictability. The ETS measures predictability over some domain, those being approximately 1000 and 2000 km-wide squares, respectively. In the present work, predictability is considered on the order of the GCM grid cell, which is $O(200)$ km.

As demonstrated in a discussion of the Mesoscale Predictability Experiment (MPEX) by Weisman et al. (2015), high-quality representation of convective feedbacks onto the atmospheric environment and of the features acting to direct such convection can significantly improve prediction of convective weather. In their case, the concern lies with their ability to assimilate high-resolution observations into even higher resolution (1-4 km) numerical models, hypothesizing that assimilating enhanced observations targeted at specific points in space and time (represented by points in numerical weather simulation ensembles as exhibiting significant forecast uncertainty) into future forecasts would improve those forecasts. They highlight the studies of Weisman et al. (2008) and Clark et al. (2010a,b) showing that most forecast sensitivity on the 6-48-hour time scale can be traced back to differences in the initial conditions as opposed to other

potential sources of error, such as those from physical parameterization schemes, coarse resolution, or representation of essential elements of storm initiation and development. They further provide a clear example of the wide-ranging 12-hour forecasts stemming from the choice of three different, but all reasonable, initialization data sources employed by otherwise identical model configuration. Neither forecast does a particularly good job of matching the observed atmosphere, nor do they agree well with one another in their representation of the timing, location, or type of mesoscale systems in the forecast. Extending these forecasts further, one can reasonably expect there will be a significant feedback from these mesoscale, and even convective-scale, differences toward influencing significantly different development of the large-scale atmosphere. Subsequent degradation of the weather forecast is inevitable, tending toward chaos as weather forecasts are wont to do. In practice, Weisman et al. (2015) show that improvement of model representation of the mesoscale by way of targeted observations can indeed lead to significant, positive changes in ensemble agreement about timing, position, and type of forecast convective features (e.g., compare their Figures 10 and 13). Similarly, better-simulated convective-scale characteristics were found after spatiotemporal resolution improvements, both in model representation and observations used for initialization, by Brousseau et al. (2016) with the Application of Research to Operations at Mesoscale (AROME-France) convective-scale model.

Some, including Zhang et al. (2003a), whose results were discussed in Chapter 1, point to the potential for moist dynamics to be the source of uncertainty. Walser et al. (2004) employed a limited-area ensemble at 3-km resolution over the European Alps to assess daily precipitation predictability. Their 12 ensemble members, differentiated by initial condition perturbations at the smallest resolvable scale, simulated four different synoptic scenarios. They demonstrate rather clearly, though unsurprisingly, the tendency for greater predictability at larger scales in all cases,

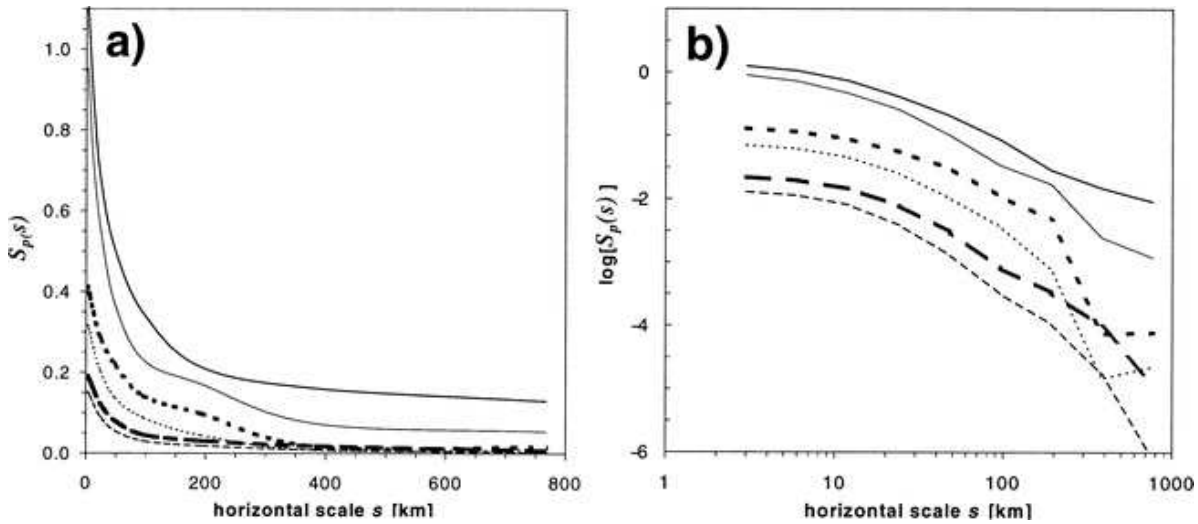

FIGURE 3.1: Caption similar to that presented by Walser et al. (2004): Scale dependence of predictability of precipitation $S_p(s)$ shown in a (a) linear and (b) doubly logarithmic display. The lines show the area-mean normalized spread S_p for three case studies of varying convective characteristics.

precipitously falling off for scales below 200 km (Figure 3.1). Higher predictability was associated with orographic triggering and lower convective activity, and vice versa.

Taraphdar et al. (2014) also found the presence of moist convection to be the source of predictability-limiting error in tropical cyclone simulations. However, the level of convective activity was found in three cases of moderate to strong convective activity by Hohenegger et al. (2006) to be a poor indicator of predictability, even though uncertainty in the temperature field associated with diabatic cloud processes is often coincident with precipitating regions. Instead, further analysis of the group velocity of gravity waves relative to the flow may be a better indicator of predictability. Specifically, propagation against the flow allows localized perturbation growth and poor predictability, whereas propagation with the flow allows perturbations to exit the area and give good predictability.

Clearly there are complicating factors. A training primer on mesoscale convective systems (University Corportation of Atmospheric Research cited 2016) notes, “In the weakly-forced scenarios, which are more difficult for humans to predict, the models also have a much more difficult time.

In these scenarios forecasters must place more emphasis on conceptual models and pattern recognition." In such weakly-forced scenarios with high convective activity, where diurnal heating is the major source of instability, convective initiation is at the whim of features that include gust front lifting, gust front collisions, and orographic lifting (Lima and Wilson 2008). This is an area in which stochastic parameterization has seen some utility in improving the representation of precipitation variability (Groenemeijer and Craig 2012; Keane et al. 2016; Wang et al. 2016). Discussion of this issue by Keane et al. (2016) notes that the convective adjustment timescale can be calculated from model variables to assess the intensity of the forcing as was done by Keil et al. (2014).[2] The convective adjustment timescale estimates how quickly CAPE is used by convective activity and can be determined indirectly from the precipitation rate (Done et al. 2006; Keil et al. 2014) or explicitly from the change in CAPE (Surcel et al. 2015). When synoptic forcing is strong, the timescale is short, $O(1)$ hour, as little barrier (CIN) exists or is easily overcome by the forcing and convective equilibrium is possible, with CAPE being regenerated by large-scale motions. In that case, a deterministic parameterization might do quite well and MP realizations should be in close agreement. In the weakly forced cases, the timescale is long, $O(1)$ day. Longer timescales are associated with high CIN and require local mechanisms to enact convection.

It is possible that areas of low predictability are coincident with areas of intermittent precipitation. Such regions may be mobile and related to large systems. For instance, Tung et al. (2004) computed the fractal dimension spectrum for time series of a deep convection index based on infrared-derived equivalent blackbody temperature. Time series near the edges of the MJO envelope were found to be multifractal, indicative of intermittent convective intensity that manifests as "burst events", whereas central MJO convective time series were monofractal, indicating more continuous behavior. Burst-like behavior on the edges was associated with excitation of

[2] Keane et al. (2016) go on to say that this information may be useful in an adaptive dual-parameterization system, whereby the stochastic parameterization can be used under these weak forcing conditions.

small-scale convectively-coupled waves and disturbances that are linked to the MJO. Similarly, the central, more cohesively forced regions of strong systems might be expected to exhibit greater predictability. In such scenarios, any physical parameterization would be a more constrained slave of the large-scale forcing. As a tangentially related point, Anderson et al. (2016) examined the potential predictability of precipitation variations over the continental United States at long time scales (multiple years). They note enhanced predictability in climatologically wet and dry regions and predictability minima for transitional locations.

One may imagine scenarios in which the small-scale may deviate from some expected result of a given large-scale forcing. In the SP configuration, it is possible that some self-sustaining mesoscale organization develops within the CPM domain that makes the large-scale forcing irrelevant. The source of this mesoscale organization could be many things, such as feedback between the large-scale and small-scale within a large-scale disturbance (Cho 1993), the chance alignment of favorable environmental conditions like wind shear, humidity, CAPE, and CIN or the existence of small-scale disturbances like cold pools (Bluestein and Jain 1985; Bluestein et al. 1987; Del Genio et al. 2012; Houston and Wilhelmson 2011; Feng et al. 2015). In the MP configuration, this may occur in a small subset of the members, allowing significant differences in the resulting precipitation and heating and drying tendencies that could be interpreted as a state of poor predictability. It would be of some use to know whether the existence of mesoscale organization plays a role in the predictability of precipitation since mesoscale systems in the tropics account for approximately 80% of rainfall (Del Genio and Kovari 2002). Further, as few conventional GCM convective parameterizations give some representation of mesoscale updraft and downdraft effects (Donner et al. 2001; Moncrieff 2004; Moncrieff et al. 2012), the SP configuration, being able to give a rather direct representation, is a rather appropriate vehicle for the investigation.

Many GCM convective parameterizations include convective triggers, a condition or set of conditions under which the model allows the initiation of convection. The aforementioned study by Horinouchi et al. (2003) employed convective parameterizations using a variety of convective triggers. Some of those operate on thresholds of buoyancy measures, like positive buoyancy of a parcel above cloud base (Gregory and Rowntree 1990) or the bare minimum for convective activity: the existence some measure of CAPE (Arakawa and Schubert 1974; Zhang and McFarlane 1995). Others consider thresholds of the moisture supply, (Kuo 1974; Tiedtke 1989), measures of stability (Manabe et al. 1965), lifting energy from boundary layer processes (Bretherton et al. 2004a; Grandpeix and Lafore 2010), or vertical velocity (Kain and Fritsch 1989; Donner 1993). A thorough review of some of these common convective trigger functions is given by Suhas and Zhang (2014). They find that the best-performing convective trigger is based on positive entrainment-diluted CAPE generation rates with convection initiating from a level where the relative humidity is greater than 80%. This trigger is basically a rough representation of destabilization from the large-scale environment in moist conditions, which is exactly what SP would detect in a more detailed manner. Though very few parameterizations account for the life cycle of convection and most produce convection too easily, these triggers are all physically and reasonably based on the detection of unstable air. More recently developed methods that account for greater complexity exhibit significant potential for improvement (Roehrig et al. 2013; Couvreux et al. 2015; Romps 2016). In SP, on the other hand, the convective life cycle is already much more realistic. The initiation of convection is based on explicit convective-scale motions. Therefore, when considering an environmental state that is near but exceeding a conventional parameterization threshold for convective initiation, the conventional parameterization model *must* convect, whereas SP convective initiation may or may not occur because the form of the threshold is not assumed. Such ambiguity near deterministic convective trigger thresholds could reasonably

present as MP member convection discrepancies. If so, certain trigger formulations could act as guides toward proxies for poor precipitation predictability.

Observationally, Mecikalski and Bedka (2006) looked for indicators of the likelihood of cumulus evolving into precipitating convective storms within 30-45 minutes following measurements from the Geostationary Operational Environmental Satellite's visible and infrared sensors. Critical values relevant to this study include those for cloud-top height and cooling changes, however the timescales involved are too short to be helpful for much of the MP data.

Another form of threshold behavior that has been proposed for the parameterization of convective precipitation comes from the idea of viewing the phenomenon as phase transition associated with self-organizing criticality (Peters and Neelin 2006; Yano et al. 2012). Here, convection tends to be triggered when column-integrated water vapor (CWV, equivalent to PW, often denoted as w) exceeds a critical value, which appears to be dependent on vertically averaged tropospheric temperature (sometimes presented as some related measure of vertically integrated saturation water vapor), and precipitation rates approach an upper asymptotic limit with continued increases in PW. By way of example, Figure 3.2 provides a depiction of this relationship as measured over the eastern Pacific. This relationship has been reported in monthly mean data from Special Sensor Microwave Imager (SSM/I) and Tropical Rainfall Measurement Mission (TRMM) Microwave Imager (TMI) satellite data (Bretherton et al. 2004b), daily data from the same sources (Peters and Neelin 2006; Bechtold 2008; Neelin et al. 2009), data with sub-daily temporal resolution from Advanced Microwave Scanning Radiometer for Earth Observing System (AMSR-E) and the Atmospheric Infrared Sounder and Advanced Microwave Sounder Unit (AIRS/AMSU) (Masunaga 2012), radiosonde and dropsonde data (Holloway and Neelin 2009; Raymond et al. 2007, 2015; Sentić et al. 2015), CPM data (Posselt et al. 2012; Yano et al. 2012; Sentić et al. 2015), reanalysis data (Tan et al. 2013) and ground radar, TRMM, and merged

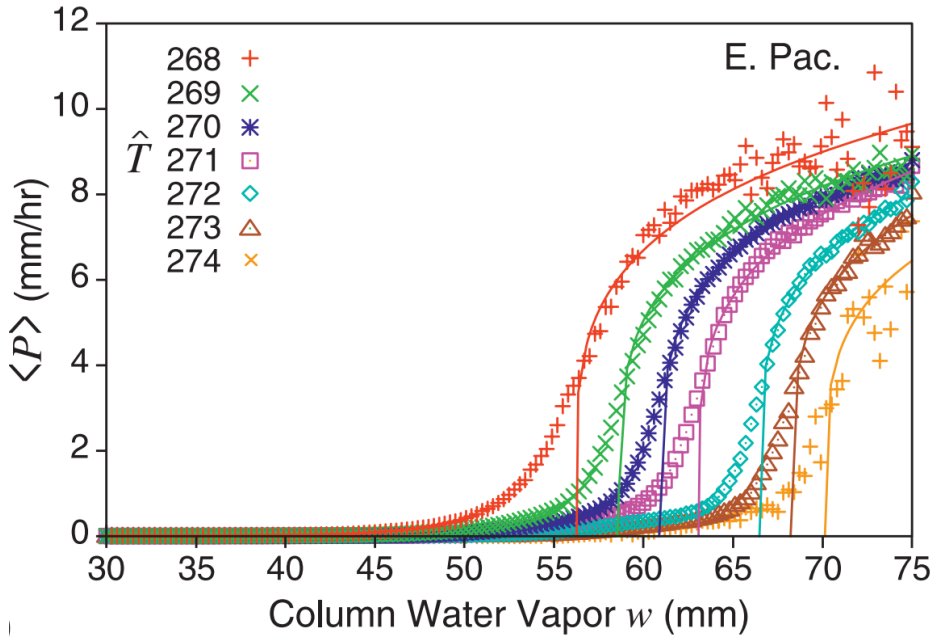

FIGURE 3.2: Caption as in Neelin et al. (2009): Pickup of ensemble average precipitation $\langle P \rangle$, conditionally averaged by 0.3-mm bins of column water vapor w for 1-K bins of the vertically averaged tropospheric temperature $\hat{T}$, for the eastern Pacific.

radiosonde/model data (Ahmed and Schumacher 2015). Most recently, Schiro et al. (2016) extended observation of this relationship to tropical land (Amazonian sites near Manaus, Brazil) using radiosonde, microwave radiometer, Global Positioning System and acoustic rain gauge data. Since the identification of this relationship, new parameterizations incorporating the phenomena have been developed. For example, Hottovy and Stechmann (2015) compare stochastic and deterministic implementations of the precipitation-PW relationship in ways similar to Stechmann and Neelin (2011, 2014). They found that results for the model average of precipitation were identical, but only the stochastic version was allowed for extreme rainfall events, exhibiting greater rainfall duration mean and variance.

Near and above such critical values, we see the highest levels of precipitation variance for a given PW, peaking at the critical value. There also exists a tendency for convective organization on the mesoscale to occur near the critical value (Mapes 1993; Sherwood and Wahrlich 1999; Grabowski and Moncrieff 2004; Mapes et al. 2006; Holloway and Neelin 2009; Posselt et al.

2012; Masunaga 2012). More specifically, Masunaga (2012) found that more organized systems, defined as those greater areal extent, are associated with the presence of greater moisture subsaturation and exhibit a more abrupt transitions (greater variability) in the near-peak growth and decay phases of their life cycles. Similar results were found by Ahmed and Schumacher (2015), who found the strong increase in precipitation near critical PW to be most strongly associated with exponential growth of stratiform precipitation regions and, to a lesser extent, the precipitation rates in convective regions. Therefore, the greater precipitation variability may be linked to processes of mesoscale convective organization.

Also operating near this critical point is the tendency toward homeostasis, whereby convective precipitation acts to keep PW below a threshold like an attractor, a representation of convective quasi-equilibrium's assumption of quick dissipation of instability that underlies many deterministic parameterizations. The fact that the true atmosphere has considerable variance near this point indicates the potential for significant departures from quasi-equilibrium, the cloud-scale variability missing in those deterministic parameterizations. It is of even greater importance upon realization that a large fraction of tropical precipitation occurs for PW values near critical (Neelin et al. 2009). In a way, the old guard, homeostasis and quasi-equilibrium, is giving way to a more nuanced interpretation in which it has been modified as the interacting factors of criticality, organization, and stochasticity. In the words of Schiro et al. (2016), PW "represents a proxy for the impact of free tropospheric humidity on the conditional instability of entraining plumes affecting the transition from shallow to deep convection, and thus ... the statistics quantifying this transition provide a substantial constraint on subgrid scale processes that must be represented in climate models."

Neelin et al. (2008) note that the high variability at the critical point is an intrinsic property of the system that occurs independent of scale and is indicative of the system's extreme sensitivity.

Where these complicating factors arise, there exists the potential for uncertainty, and there we might find the greatest tendency for a difficult prediction of precipitation. They find large and variable CAPE values to be associated with this transition, as well, with CAPE variability to be most strongly a function of water vapor variability in the lower free troposphere above the atmospheric boundary layer. No discernible association with CIN was found. Experimentation with the SP version of the NCAR Community Atmosphere Model (CAM) 3 allows the model to more successfully simulate the observed relationship between tropical precipitation and PW when compared to its standard formulation with deterministic parameterizations (Khairoutdinov et al. 2005; Thayer-Calder and Randall 2009; Zhu et al. 2009). As such, the SP and MP simulations here should provide a good representation of the strong increase in precipitation near critical PW, which may point to conditions for poor precipitation predictability.

On the other hand, Davies et al. (2013) show in data near Darwin, Australia that precipitation intensity is rather variable at all CAPE values, with no apparent association to the PW critical transition point. Instead, they show that such point does appear when comparing against a (to include lower-level mean, rather than specified level, contributions) measure of the K-index, which provides a measure of air mass thunderstorm likelihood based on the magnitude of instability measures. These two features are shown in Figure 3.3. Greatest precipitation variability is seen for K-index values over 30 K, a value that is taken to indicate significant convection and organization potential. Decomposing the K-index into components that measure low-level stability and moisture content and the vertical extent of the moist layer, it was shown that the moisture effects dominate the K-index calculation and therefore may be able to diagnose conditions likely for precipitation uncertainty.

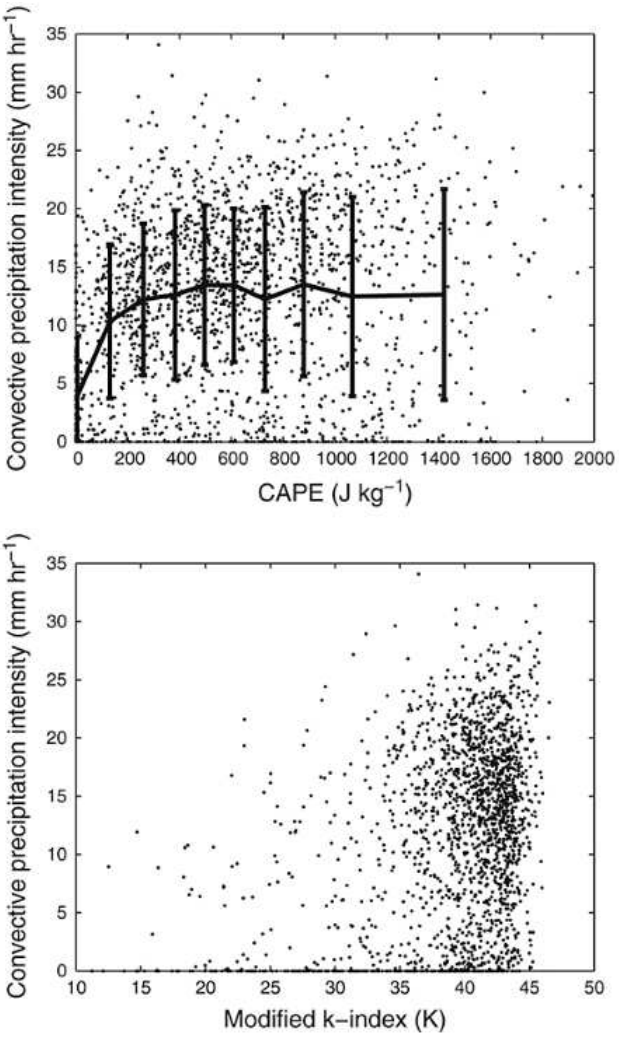

FIGURE 3.3: Caption similar to that presented by Davies et al. (2013): Relationship of (top) CAPE and (bottom) K-index with convective precipitation intensity. In the top panel, also shown are mean and ± 1 standard deviation values for deciles of the data set.

In light of this finding, it may then be fruitful to investigate an array of additional severe storm indices. Zawadzki et al. (1994) made an early attempt to relate the predictability of precipitation to larger-scale meteorological parameters. The analysis was limited to 11 2-4-hour precipitation events near Montreal, Canada as measured by radar, defining predictability in terms of persistence based a spatiotemporal measure of autocorrelation. Testing predictability against several measures of large-scale forcing, significant correlations were found such that increasing CAPE indicated longer predictability times and decreasing values of a bulk Richardson number

formulated on helicity (lower values indicative of the potential for organized storm development) instead of vertical wind shear indicated longer predictability times in exclusively higher-CAPE scenarios. In other words, strongly forced scenarios of high CAPE and organizing winds are more predictable. Considering sample size alone, these results, particularly the latter, which only analyzed five data points, should be taken with a shaker of salt. Persistence of active storms as a measure of predictability differs from measuring a model's difficulty in predicting a feature. Really, what appears to be indicated here is that organized storms with lots of energy behind them have a tendency to last longer after they form, not the probability of slightly differing large-scale conditions prior to storm formation resulting in similar precipitation structures. Nonetheless, the study represents an interesting framework from which to investigate the relationship of precipitation predictability and the large-scale.

There are some possible issues in examining the predictability of precipitation in the MP configuration. One comes from their domain limitations. While SP is immediately more representative across scales, CPM curtains may not bridge the mesoscale spectral gap fully. In this work, the curtains have a horizontal extent of 128 km and the GCM longitude spacing is 2.5°, which is ~275 km at the equator. These distances become more comparable at 60° latitude, but latitudinal spacing is everywhere ~222 km. Therefore, a significant portion of the traditional mesoscale gap remains at every point. Further, for some methods of diagnosing the existence of mesoscale organization, such as the area covered by precipitation, complete coverage of the CPM domain would be ambiguous, as it may be either the formation of a large mesoscale disturbance or part of a larger, synoptic feature.

Another issue comes from the way in which the CPMs are indirectly coupled to one another. If precipitation were to begin in one member, its warming aloft and lower-level drying tendencies

passed to the large-scale would act to stabilize the environment. Without supplementary destabilization from the large-scale, rogue precipitation in one member might actually act to suppress it in the other members. On the other hand, since any one member is only providing on tenth of the parameterized tendencies to the GCM, such a suppression effect would likely be small. In fact, the stabilizing effect could be so small that the precipitating member continues to precipitate for an artificially long period of time.

Given the discussion in this section, we have a number of interesting paths ready for investigation. Predictability may be a function of critical phenomena, instabilities, or even the presence of convective organization. Large-scale state indicators, like CAPE and CIN, may also play important roles. These investigations will be presented in Chapter 5.

CHAPTER 4 – COMPARING SIMULATIONS

> There may, of course, be a wide range of subgrid states that are consistent with the resolved-scale flow, and therefore a deterministic scheme must be regarded conceptually as an attempt to evaluate the ensemble-mean effect of the subgrid states.
>
> *R. S. Plant and G. C. Craig*

This chapter explores various features of the model climatology. First, we examine the way in which MP-CAM is a more deterministic version of SP-CAM. Then differences in various features of the model climatologies are reviewed. Last, we explore differences in the simulation of intraseasonal variability.

4.1. CLOUD REGIMES

Beginning with the work of Jakob and Tselioudis (2003) and Rossow et al. (2005), efforts have been made to identify cloud regimes in complex ways, beyond compositing the cloud data into different dynamic and/or thermodynamic regimes. The more recent efforts have focused on the application of clustering algorithms to joint cloud property distributions (e.g., cloud top pressure, cloud optical depth, albedo, and total cloud fraction). This work was originally undertaken to help understand where climate model failures were located in terms of their combined cloud and dynamical properties in order to make more informed statements about climate change simulations. Williams and Webb (2009) noted that the efforts have shown "that much of the variance in the climate change cloud response across their ensemble of GCMs is due to differences in the present-day simulation of cloud regimes."

A recent benchmark analysis of this type was performed by Tselioudis et al. (2013), who applied a clustering algorithm to a joint histogram of cloud optical thickness and cloud top pressure produced by the International Satellite Cloud Climatology Project (ISCCP). The analysis produced a set of 12 global weather states (GWSs), which are characterized by cloud regimes with distinct distributions of vertical layering and horizontal distribution across the globe. More recently, Jin et al. (2016a) examined the representation of these 12 GWSs (referred to in that paper as cloud regimes, CRs) in 12 fifth Coupled Model Intercomparison Project (CMIP5) models that employed the ISCCP cloud retrieval simulator. A number of model deficiencies, and even potential observational deficiencies were uncovered. Additionally, Jin et al. (2016b), in a companion to the previous paper, develop a new set of CRs based on the covariation of grid-level total cloud fraction, cloud top pressure, and cloud optical thickness. In both analyses, modeled clouds tended to be too optically thick and not as horizontally extensive as in observations.

In the course of producing this dissertation, some of the plots from these papers caught my eye because some of their structures looked similar to patterns in the present work. While we did not run the ISCCP simulator in tandem with the model simulations, it will be useful to refer to these cloud regimes when referencing various features we will encounter. The CR data shown in Figures 4.1 and 4.2 were provided by Daeho Jin (personal communication).

As summarized by Rémillard and Tselioudis (2015),who investigated cloud regime representation over the Azores in models and observations, and with contributions from Tselioudis et al. (2013) and Jin et al. (2016a), the 42-bin ISCCPCRs in Figure 4.1 can be described as listed in Table 4.1. Information about the simplified 3-component CRs in Figure 4.2 is given in Table 4.1. The two sets of CRs organize the clouds in different ways. According to Jin et al. (2016b), " The most important difference is that the new simplified (3-component) method results in four CRs with mean cloud fraction lower than 40% (CR1, CR5, CR8, and CR11) when only one such

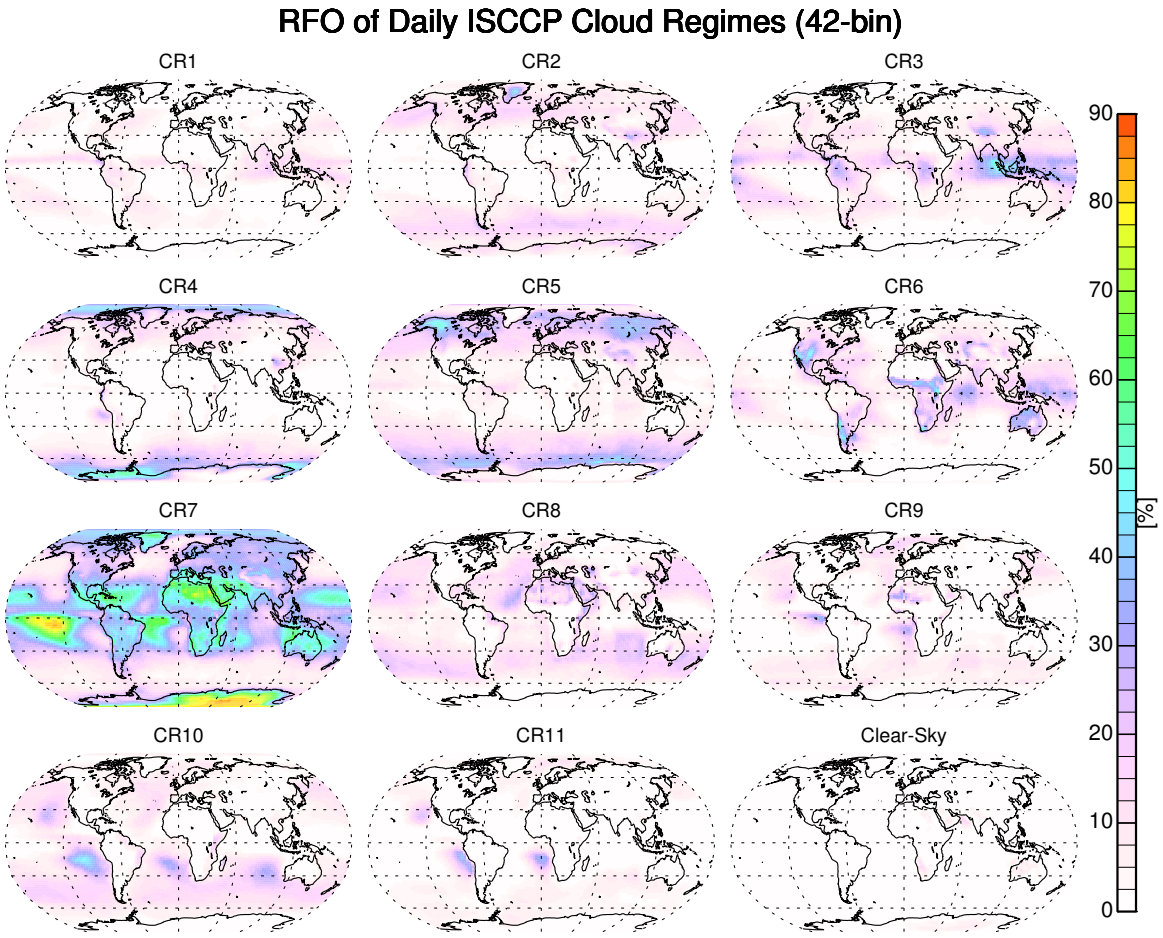

FIGURE 4.1: The geographical distribution of the multi-year mean of relative frequency of occurrence (RFO) of the daily ISCCP 42-bin cloud regimes. The rightmost bottom panel shows the RFO map of completely clear skies at (280 km)^2 scales. This information is also presented by Jin et al. (2016a), which is similar to Tselioudis et al. (2013).

low-CF regime existed in the previous study (GWS7, CR7 in Figure 4.1). The multiple low-CF regimes of our new CR dataset yield a more even distribution of RFO among CRs in contrast to the previous GWS dataset where the 32.5% RFO of WS7 towered over all other GWSs. The end result is that the range of global RFO values in this study extends from 3.4 to 12.5%, compared to a 2.6 to 32.5% range in Tselioudis et al. (2013)." This variety of identified cloud regimes will provide a nice reference to aid in understanding results in this work.

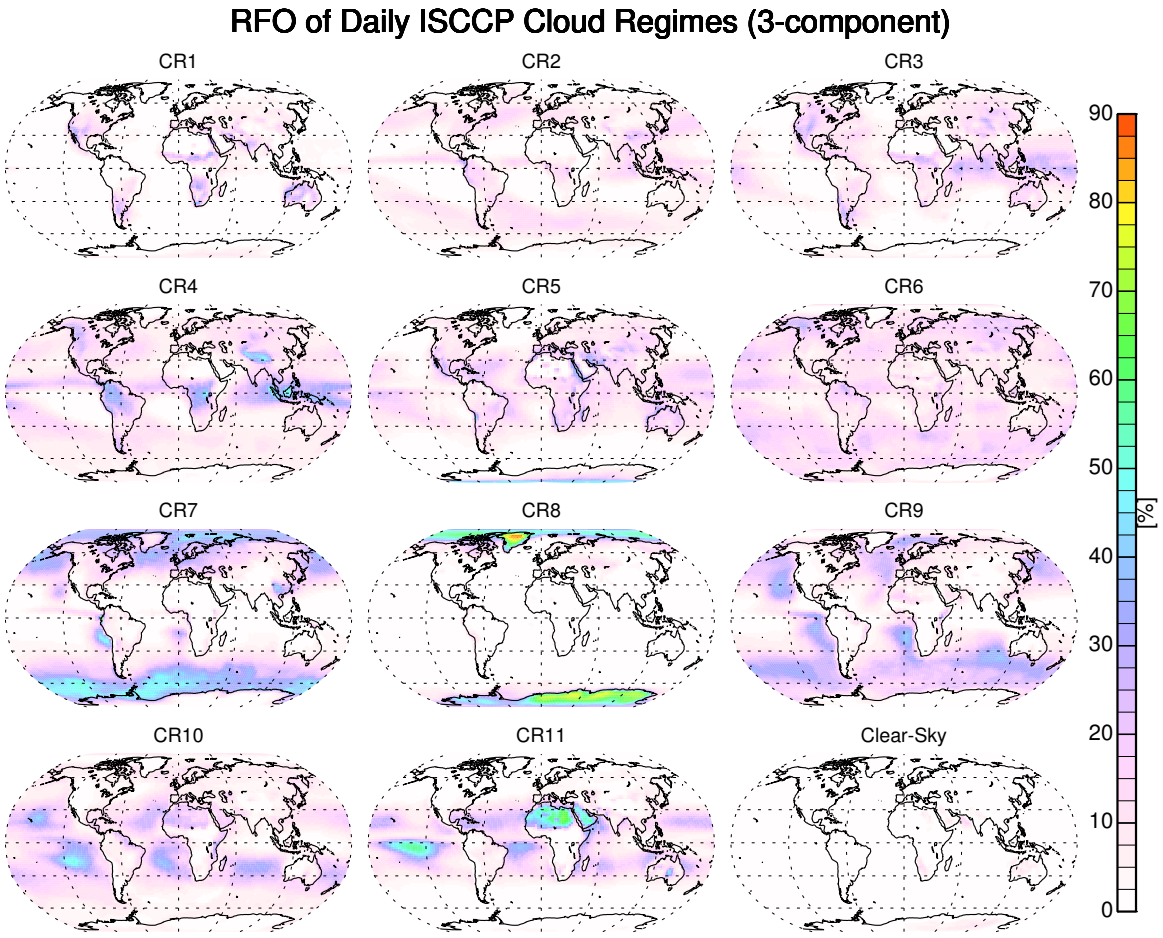

FIGURE 4.2: The geographical distribution of the multi-year mean of relative frequency of occurrence (RFO) of the daily ISCCP 3-component CRs. The right-most bottom panel shows the RFO map of completely clear skies at (280 km)^2 scales. This data is also presented by Jin et al. (2016b).

TABLE 4.1: Descriptions of the 42-bin ISCCP CRs in Figure 4.1 along with their relative frequency of occurrence, typical cloud fraction, cloud top pressure, and cloud optical thickness.

CR	Conditions	RFO [%]	CF [%]	CTP [mb]	τ
1	Deep convection	3.8	97.5	275	12.39
2	Midlatitude storm	6.4	95.4	455	10.97
3	Thick cirrus (anvil)	8.8	89.7	355	3.40
4	Thick midlevel clouds (mostly polar)	6.7	89.4	620	11.16
5	Thin midlevel clouds (mostly storm related)	10.7	84.2	550	3.25
6	Thin cirrus	8.4	71.1	315	1.62
7	Fair weather cumulus	31.6	32.7	600	4.04
8	Shallow cumulus	8.7	62.8	750	2.96
9	Transition stratocumulus	4.2	80.3	825	6.57
10	Marine stratocumulus	7.6	77.6	820	4.95
11	Thick stratocumulus or stratus	1.7	92.3	735	11.35

TABLE 4.2: Descriptions of the simplified 3-component CRs in Figure 4.2 along with their relative frequency of occurrence, typical cloud fraction, cloud top pressure, and cloud optical thickness.

CR	Conditions	RFO [%]	CF [%]	CTP [mb]	τ
1	Thin cirrus	3.4	25	305	0.4
2	Deep convection	6.7	98	356	11.9
3	Thick cirrus	7.4	75	369	1.4
4	Cirrostratus	11.4	92	398	4.2
5	Early/dying convection	9.3	32	561	1.6
6	Thin mid-level	12.2	77	580	2.9
7	Thick mid-level (mostly polar)	12.5	94	634	10.0
8	Arctic	3.9	39	669	12.7
9	Stratocumulus	11.6	85	757	5.0
10	Marine stratocumulus and shallow cumulus	11.6	51	761	3.3
11	Fair weather cumulus	9.7	18	846	2.5

4.2. A MORE DETERMINISTIC MODEL

It was noted in Section 2.2 that an intention of the MP configuration was to create a more deterministic model with regard to convective parameterization. Therefore, the data should be checked to verify that this was accomplished and to what extent. The basic premise of making the model more deterministic is that an average of possible values that may differ due to slight differences in initial condition will give a more constrained "expected value." Since the mean is always between the extremes of a set of values, a data set based on averages will have fewer extremes, making the data set measurably less variable than any individual member of the average. Further, as the sample size increases (more CPMs are used in the MP configuration), the variance of the averaged data becomes smaller, likely approaching the deterministic limit of and expected value.

We can explore this concept using sets of random data, representing some completely non-deterministic system. Consider multiple (n) long time series of random data of length N. The variability of a given time series can be measured by the standard deviation, σ, as given by Equation (4.1), where j is a counter, x_j is an element of the time series, and $\overline{x}$ is the time series mean. For n independent, random time series that have a similar probability distribution, the

standard deviation of their mean time series, $\sigma_{\overline{n}}$, is equal to the standard deviation of any one of the n time series, σ_n (which should all be nearly equal) divided by the square root of n, as related in Equation (4.2). Therefore, in the case of averaging a group of 10 estimates of a system, we may expect to see the standard deviation fall off by $\sqrt{10} \approx 3.16$.

$$\sigma = \sqrt{\frac{1}{N-1} \sum_{j=0}^{N-1} (x_j - \overline{x})^2} \tag{4.1}$$

$$\sigma_{\overline{n}} = \frac{\sigma_n}{\sqrt{n}} \tag{4.2}$$

The use of such random data illustrating this mean-induced σ fall-off is shown in Figure 4.3. Examples are provided for uniform, normal, and gamma distributions of random data, each produced without special consideration for their exact form, i.e., range, mean, standard deviation, skewness, etc. For each type of distribution, 10 sets of one million random points were generated. The black line is a PDF representing one of the 10 sets of data, similar to a single CPM member of MP-CAM. The red line is the PDF of the random points averaged across the 10 sets. In each case, there is a marked reduction in the occurrence of values near the extremes of the original distribution and an increase in the occurrence of values near the mean of the original distribution, as alluded to previously. This is at least qualitatively what we expect to see when comparing, for instance, precipitation, in models using stochastic versus deterministic parameterizations. Stochastic parameterizations have more prevalent extremes.

Below the plot for each distribution are the values for σ_n and $\sigma_{\overline{n}}$. Individually, there is nothing particularly special about these values, but their ratio, representing the factor by which the standard deviation drops following averaging, is notable. Regardless of the underlying original distribution, the ratio is the same for these random distributions, near $\sqrt{10}$. Repeating the same

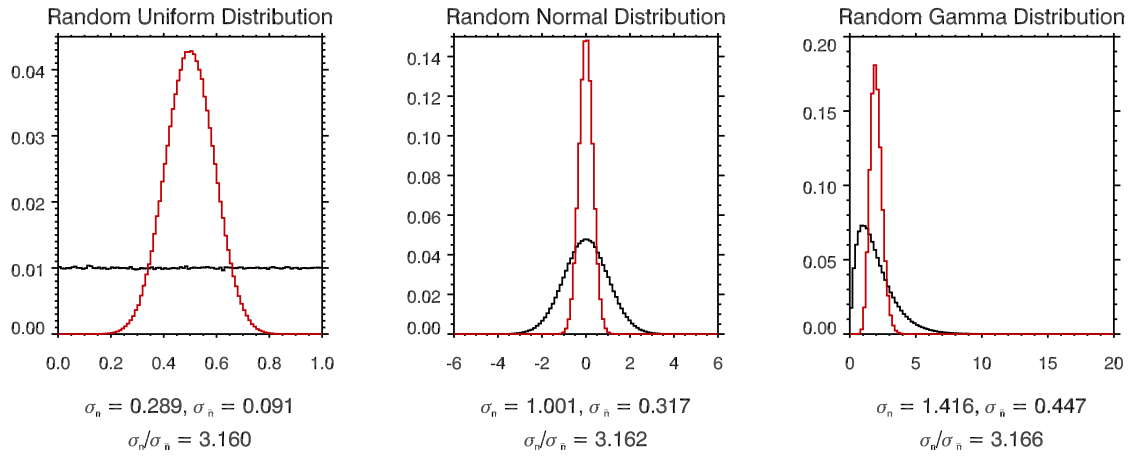

FIGURE 4.3: Probability density functions for data sets based on random (left) uniform, (center) normal, and (right) gamma distributions. Black represents a single original random data set, and red is the result of an average of 10 independent, random data sets. σ_n represents the standard deviation of an original random data set, and $\sigma_{\overline{n}}$ is the standard deviation of the resultant average across 10 independent, random data sets. Refer to the text for more details regarding the construction of this data.

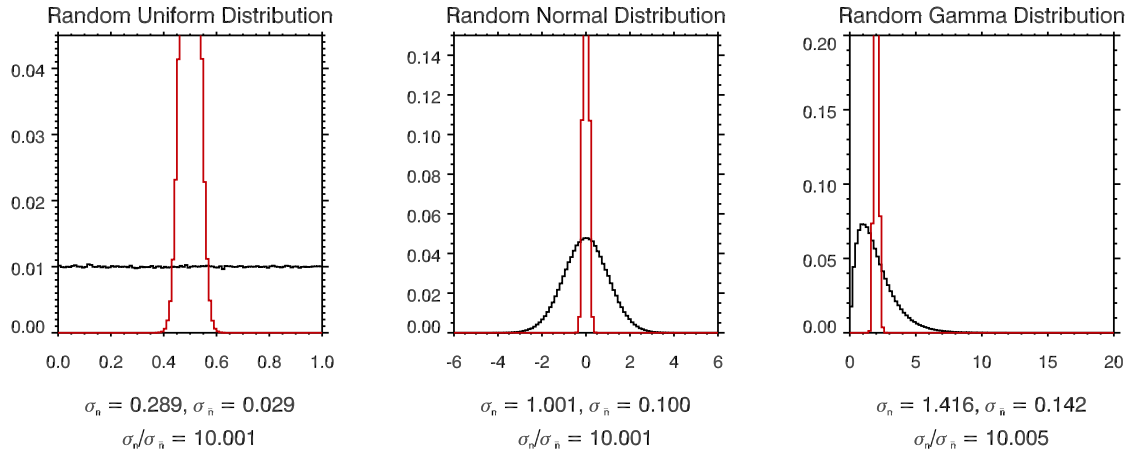

FIGURE 4.4: As in Figure 4.3, but averaging 100 data sets.

analysis for 100 data sets, the same generalizations hold, and the ratio becomes 10 (Figure 4.4) If more samples are used, then the resulting averaged data set becomes less variable and contains fewer extremes. That is a nice confirmation of the underlying theory. However, this investigation does not deal with precisely random data; weather is a convolution of the deterministic and the stochastic. Bearing this in mind, let's attempt a more applicable example.

We begin with the GPCP observational precipitation data set as described in Section 2.4 to examine the effect of randomness on realistic precipitation distributions. From this, three points were selected for comparison based on their temporal standard deviation of daily precipitation. A point with low standard deviation was chosen from the South Atlantic (approximately 16°S, 23.3°W). This point is characterized by generally weak precipitation, with a maximum near 15 mm day^{-1}, 82% dry days (where precipitation is less than 0.1 mm day^{-1}), and a clear seasonal cycle. A point with near average standard deviation was chosen from the western North Atlantic (approximately 39°N, 60°W). This point is characterized by moderate precipitation, with a maximum near 70 mm day^{-1}, 24% dry days, and a muted seasonal cycle. A point with high standard deviation was chosen along the coast of Bangladesh (approximately 22°N, 90°E). Precipitation at this point is characterized by a strong seasonal cycle related to the monsoon, moderate precipitation, with a maximum near 120 mm day^{-1}, and 44% dry days. Perhaps differing climates will yield different results.

Using one of these time series, 10 modified time series were created by adding random noise from a uniform distribution. The random noise at each point in time is scaled to the precipitation magnitude, p, such that random noise denoted as 100% indicates that the additive noise is bounded by $\pm p$. Similarly, random noise at 10% is bounded by $\pm p \times 0.1$. Overall, variability does tend to scale with the mean, and so the proportional noise employed here is a reasonably representative method. As in the case of purely random data, an average of these 10 modified time series should result in a time series with less variability and fewer extreme occurrences.

Figures 4.5 to 4.7 show the PDFs for the three points (low, average, and high temporal standard deviation, respectively) for random noise scaled to 1%, 10%, and 100%. There is not much in the way of a discernible variability difference between the single and averaged data when 1% and 10% noise are added at any of these locations. When the added noise is scaled to 100% of

the precipitation magnitude, the standard deviation-drop ratio becomes notably greater than 1, there is a slight increase in occurrences near the mean of the single distribution, and the extremes become slightly less frequent. This is most visually apparent in Figure 4.6 for the North Atlantic case, where the red curve, showing the PDF of the resultant averaged time series, does not extend as far into the extreme upper values, and there is an increase in intermediate precipitation rates (10-30 mm day^{-1}). By adding noise to the GPCP data, the extreme frequencies are inflated. When adding noise scaled to 100%, the number of dry days in the 10 modified samples (the black line) increases by 2% for the South Atlantic and by 3% for coastal Bangladesh, for example. After averaging, these values are approximately equal to those in the original data.

As a technical note, if the noise were not scaled to the original precipitation, and was instead given a set range in mm day^{-1}, the proportion of dry days could potentially decrease in the noise-modified samples. In fact, dry days decrease from 82% to 50% for a noise maximum of 1 mm day^{-1} and to 81% for a noise maximum of 0.1 mm day^{-1} in the low standard deviation (South Atlantic) case. Neither method is exactly correct on its own, as variability in cases of near zero precipitation is likely to be different from zero, and variability magnitudes are not constant through the spectrum of precipitation rates, but proportional scaling should be a better mimic of reality.

This result shows that not all data sets will show a $\sqrt{n}$ change in standard deviation as a result of averaging n sample data sets. It does indicate, though, that the ratio might increase for higher degrees of randomness. To check this, increasing amounts of random noise were added to the data sets. These results are shown in Figure 4.8. Only after the noise is scaled to greater than 10 times the precipitation magnitude do fall-off ratios saturate to values near[1] $\sqrt{n}$. This is not

[1]The fall-off ratios do not settle down to $\sqrt{n}$ exactly, and in the case of the consecutive integers, it is only chance that this occurs. It turns out that the saturation value is entirely a function of the seed of the random number generator used in the analysis and not the differences in the original data. The reason that such strong differences are possible is that

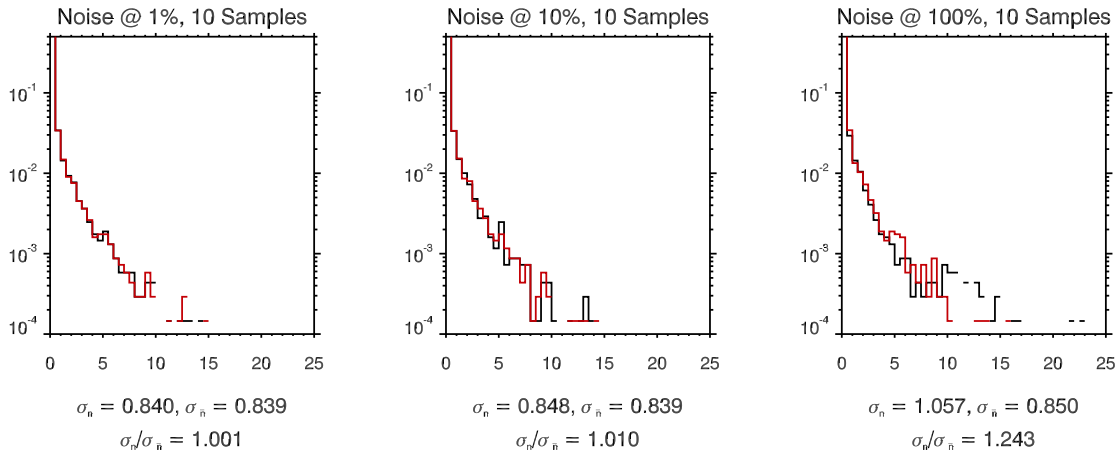

FIGURE 4.5: Similar to Figure 4.3, but for the low temporal precipitation standard deviation (South Atlantic) point in from GPCP modified by adding the noted amount of random noise. Black represents a single modified time series, and red is the result of an average of 10 modified time series.

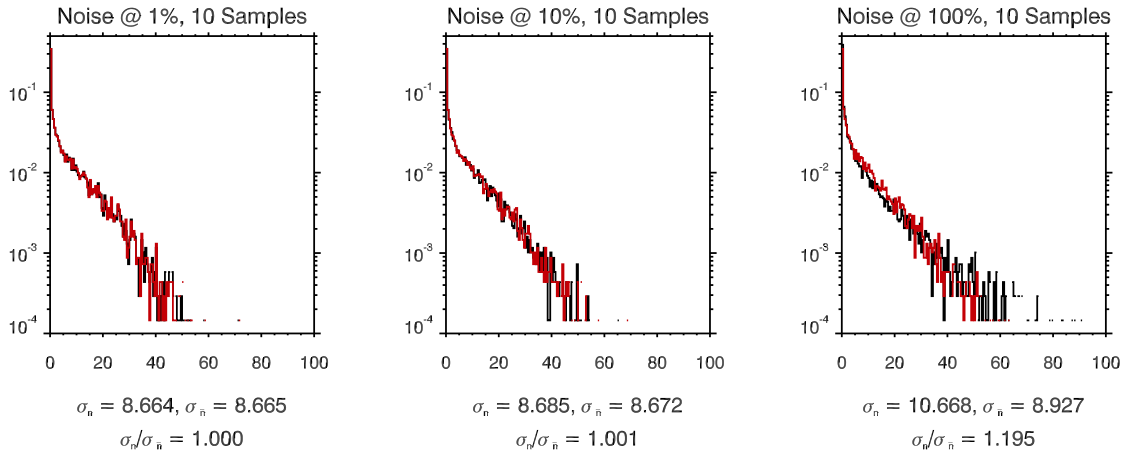

FIGURE 4.6: As in Figure 4.5, but for the near average temporal precipitation standard deviation (western North Atlantic) point from GPCP.

specific to precipitation data; the same analysis for a set of consecutive integers (and other sets not shown) shows the same pattern.

Considering this result with that from the purely random data, we can conclude that the standard deviation fall-off ratio can be used as a measure of randomness in a data set. As such, we can apply this measure to the difference in standard deviation between SP (like our single

we are using a small sample size in this case. If the sample size is increased to 10,000, much closer saturation (to 100) can be achieved.

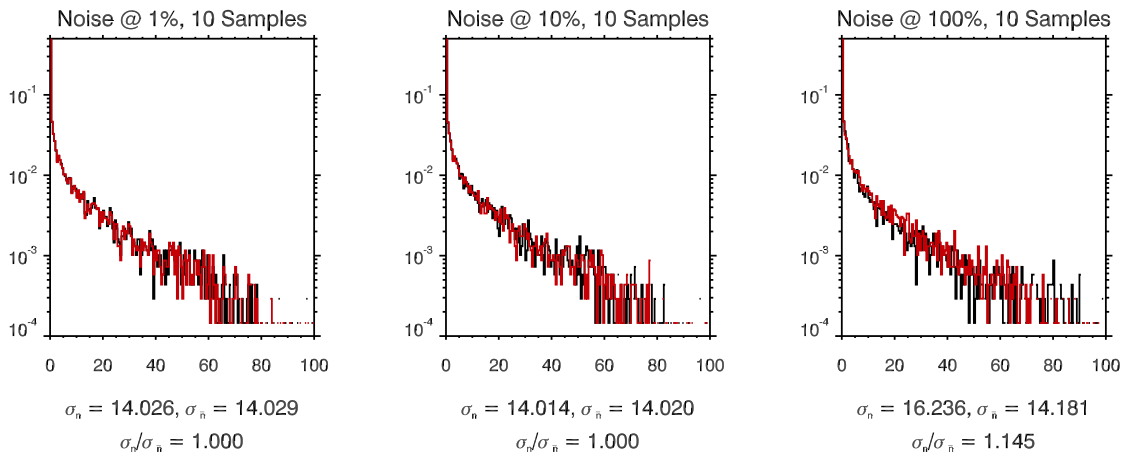

FIGURE 4.7: As in Figure 4.5, but for the high temporal precipitation standard deviation (Bangladesh) point from GPCP.

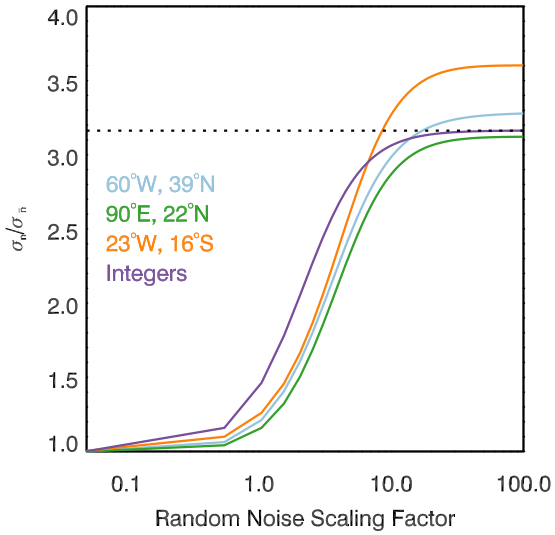

FIGURE 4.8: Precipitation standard deviation fall-off ratio, $\sigma_n/\sigma_{\overline{n}}$, for the noted locations in GPCP data and for a data set containing a list of consecutive integers as a function of random noise. A scaling factor of 1 is equivalent to adding noise at 100% in Figures 4.5 to 4.7. Here, $n = 10$. The black dotted line indicates a fall-off ratio of $\sqrt{10}$.

data set) and MP (like our averaged dataset). With our focus on the nature of convection in these simulations, we will look at how the change in model configuration affects precipitation rate and OLR.

To properly orient the following discussion, Figures 4.9 and 4.10 show maps of the mean and standard deviation of precipitation from TRMM, GPCP, CAM, SP, MP, and MP.1, which refers to the first CPM member of the MP simulation. Statistics comparing the simulations to observations are in Table 4.3. In addition, the differences of those measures from SP are shown in Figures 4.11 and 4.12.

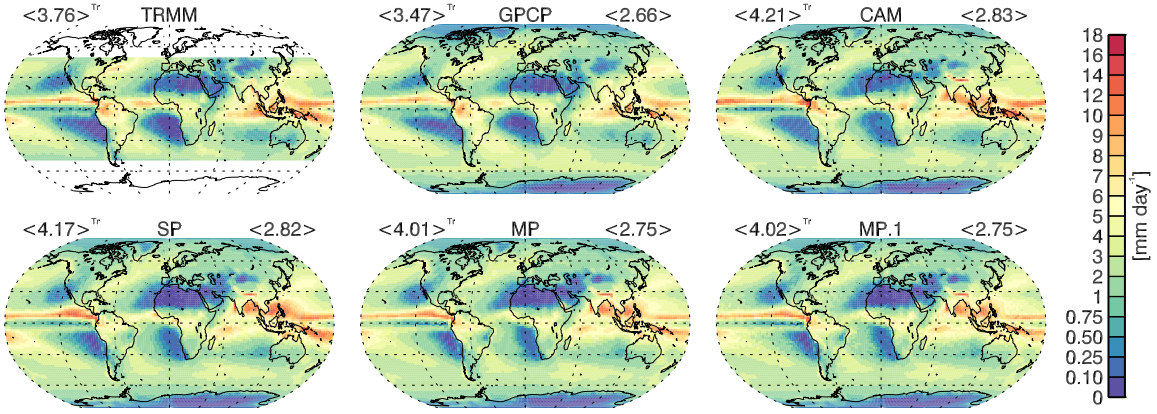

FIGURE 4.9: Annual mean precipitation rate for the full indicated observational and simulated data sets. MP.1 is the first CPM member of the MP simulation. $<x>$ denote spatial averages: the upper left value, denoted with superscript Tr, is an average from 20°S to 20°N, representing tropical values, and the upper right value is the global mean.

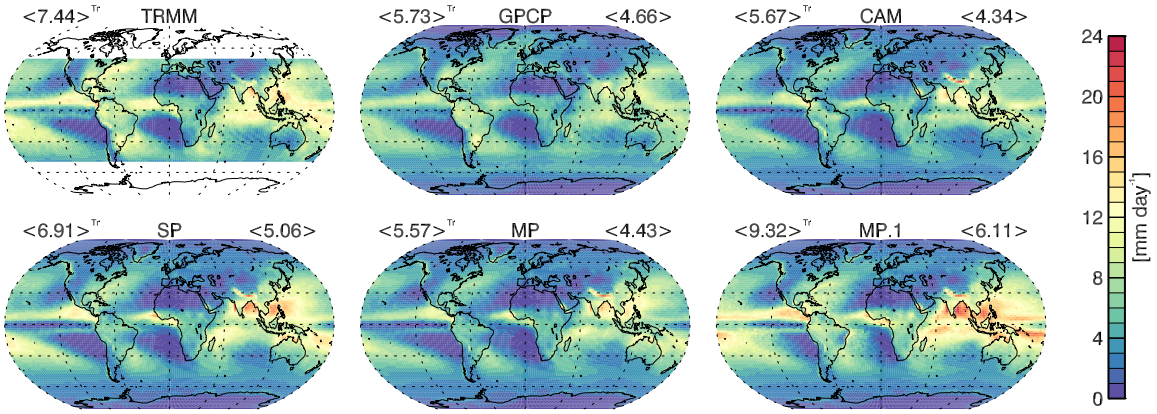

FIGURE 4.10: As in Figure 4.9 but for the temporal standard deviation of the precipitation rate.

Consistent with previous studies (e.g., Kooperman et al. 2016), spatial means from the simulations are each greater than those from observations, though the MP results are closest to GPCP

TABLE 4.3: Global and tropical (^{Tr}) root-mean-square error (RMSE) and spatial correlation (r) of the annual mean precipitation spatial pattern for the model simulations relative to GPCP and TRMM.

	GPCP				TRMM	
Model	**RMSE**	r	**RMSE^{Tr}**	r^{Tr}	**RMSE^{Tr}**	r^{Tr}
CAM	1.126	0.884	1.593	0.869	1.499	0.872
SP	1.219	0.871	1.821	0.816	1.701	0.832
MP	1.144	0.869	1.641	0.812	1.625	0.823
MP.1	1.146	0.868	1.643	0.811	1.631	0.822

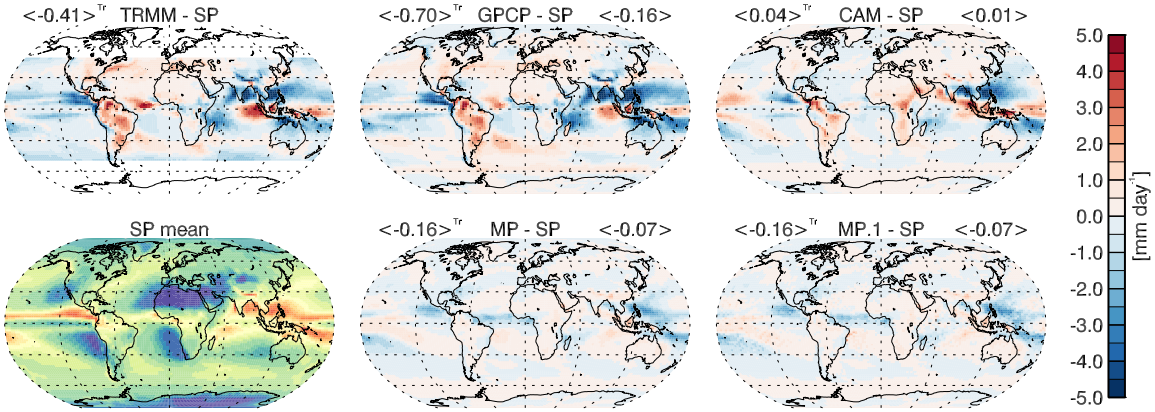

FIGURE 4.11: As in Figure 4.9 but for the difference in mean precipitation rate from SP. The bottom left map is a reproduction from Figure 4.9.

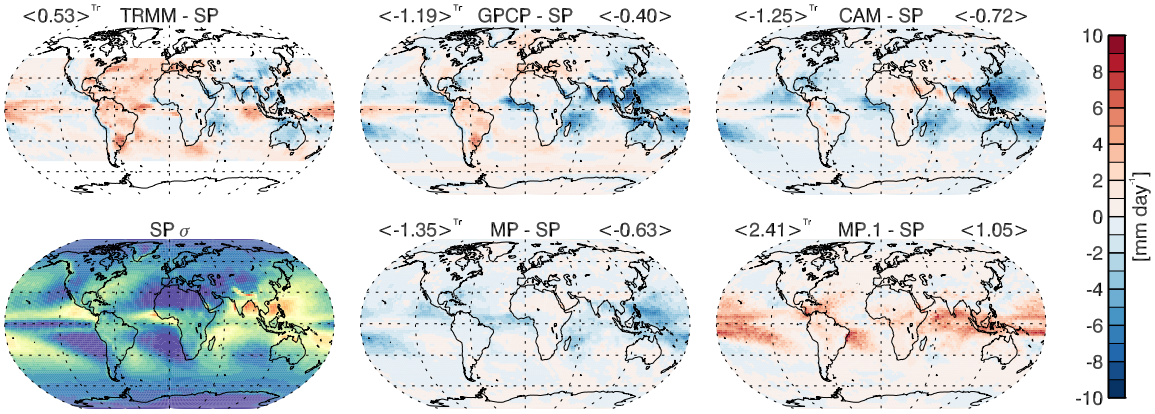

FIGURE 4.12: As in Figure 4.11 but for the difference in temporal standard deviation of the precipitation rate from SP. The bottom left map is a reproduction from Figure 4.10.

and TRMM. The bulk of the simulated difference is found in the Tropics, particularly over wet-biased oceans just off the equator. Conversely, the simulations produce less precipitation over some equatorial land areas, notably South America and the Maritime Continent instead of over Africa. The extent of the disparity in the spatial distribution of the annual mean precipitation is captured in the root-mean-square error (RMSE) and spatial correlation values in Table 4.3. As characterized by lower RMSE and higher spatial correlations both globally and in the Tropics, it is apparent that CAM captures the spatial distribution best. This is largely due to better representations of precipitation over South America, Southeast Asia, and the Maritime Continent. On the other hand, CAM performs more poorly along the Inter-Tropical Convergence Zone (ITCZ) in the Pacific. Here, there is an off-equatorial wet bias in addition to a clear double-ITCZ pattern and elongated South Pacific Convergence Zone (SPCZ). Given its many other improvements over CAM, it is interesting to note that SP performs most poorly with regard to these two aggregate spatial measures. Both SP and MP exhibit somewhat smaller dry regions off the western subtropical coasts of South America and Africa in addition to the strong wet bias in the Asian monsoon region. These are the strongest sources for the poorer pattern matches. Of much smaller extent is a strong wet bias over the Himalayas in each model; this is probably an effect of the topographical representation. Kooperman et al. (2016), and references therein, provide a much more thorough comparison of observations and CAM-variant precipitation.

For the purposes of characterizing MP's level of determinism, we are more interested in the standard deviation information in Figures 4.10 and 4.12. The standard deviation tends to track roughly proportionally to the mean precipitation. Spatial biases in standard deviation similarly follow those in mean precipitation. A notable exception to this is the broad region of low variability in the eastern South Pacific and South Atlantic. By this measure, we see that TRMM, with greater variability than GPCP, is the closest match to SP, whereas standard deviations are mostly

lower than SP in GPCP, CAM, and MP. Also notable is the overall higher standard deviations in MP.1. This is our first indication that a single CPM in MP is not equivalent to SP, as will become more apparent later on.

Encouragingly, there is an overall standard deviation decrease when moving from SP to MP, indicating that the MP case produces precipitation time series with a lesser degree of randomness. In other words, it appears to be more deterministic based on the stated arguments related to standard deviation fall-off. The fall-off ratios are shown in Figure 4.13 and summarized in Figure 4.14. The plot on the right of Figure 4.13 is most analogous to the previous discussion and figures. MP.1 corresponds to a noise-modified sample, and MP very directly corresponds to the mean of the sample data sets.

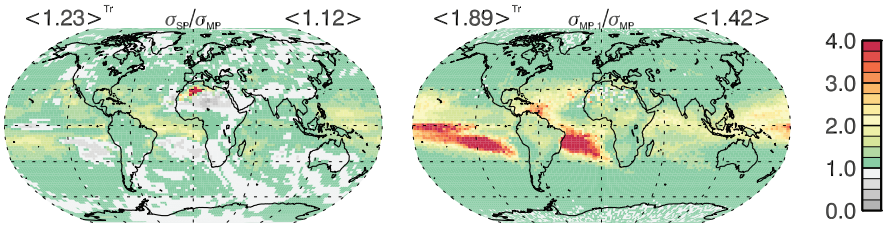

FIGURE 4.13: Precipitation rate temporal standard deviation fall-off ratio for σ_{SP}/σ_{MP} (left) and $\sigma_{MP.1}/\sigma_{MP}$ (right). $<x>$ denote spatial averages: the upper left value, denoted with superscript Tr, is an average from 20°S to 20°N, representing tropical values, and the upper right value is the global mean.

In the global mean, the ratio is 1.42. Referencing Figure 4.8, this is indicative of randomness reduction of a time series that has a random component scaled to 100-200% of the mean. A biasing factor in this value, though, are points where the fall-off is in excess of the estimated purely random fall-off ratio of $\sqrt{10}$. These are indicated by the deep red colors in the southern oceans that account for slightly over 3% of the global surface area. These points are characterized by CPM member (MP.1) precipitation rates most often less than 0.5 mm day^{-1} (Figures 4.15 and 4.16). When averaged, these points more frequently see values up to 3-4 mm day^{-1} due to members with wet outliers, resulting in many fewer dry days at these points in MP than in MP.1.

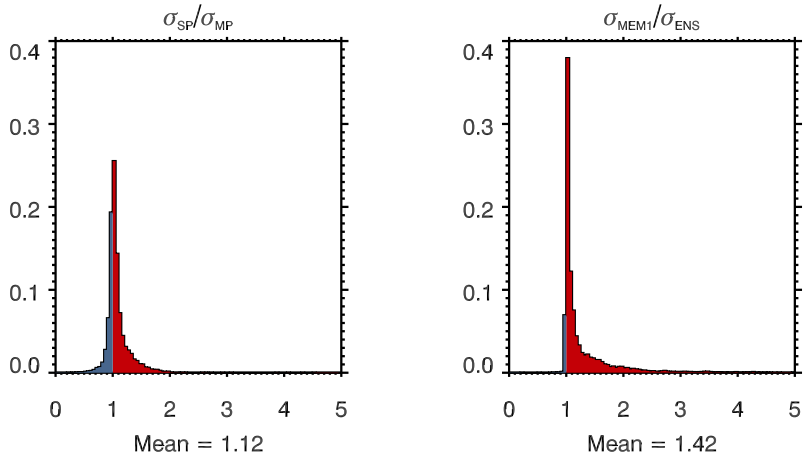

FIGURE 4.14: PDF of the standard deviation fall-off ratio for σ_{SP}/σ_{MP} (left) and $\sigma_{MP.1}/\sigma_{MP}$ (right) as shown in Figure 4.13 with the spatially-weighted global mean.

That is, the process of averaging increases typically low values toward the large outliers. Large outliers further give MP.1 a relatively large standard deviation, but their effects are not apparent in the MP temporal average (Figure 4.10).

The precipitation rate distribution at these points is shown in Figures 4.15 and 4.16. This is another indication that a single MP CPM is not exactly matching what is happening the SP CPM. MP.1 produces much more frequent and greater extremes than SP, CAM, and GPCP at these points. The intention in going from SP to MP was indeed to reduce the frequency of extreme values, perhaps to something like the extent that CAM differs from SP. However, at least in these locations, upper-end MP precipitation extremes have been greatly reduced, and precipitation rates near 1-7 mm day^{-1} occur more frequently than in CAM, which was the previous worst performer in comparison to observations at these locations. This would indicate that MP's CPM ensemble can sometimes be comprised of a large majority of members showing very low precipitation rates and only one or two with very high precipitation rates. In other words, these points often have the potential for strong precipitation, but most commonly, very little is produced. In the context of prediction, one could perpetually forecast light precipitation as indicated by the majority of

members and do quite well, but on occasion, the forecast would be wildly incorrect. Whether that is "good predictability" might be subjective. Interestingly, MP.1 is a close match to GPCP at rates below 5 mm day^{-1}.

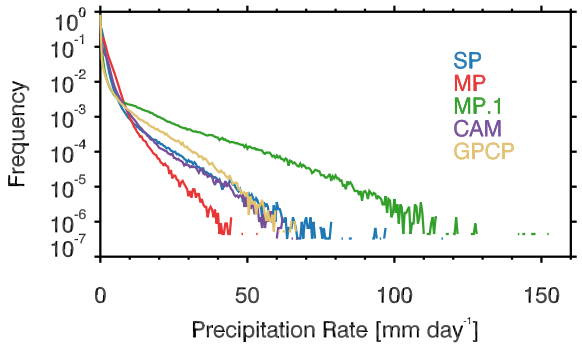

FIGURE 4.15: Precipitation rate PDF for points where the $\sigma_{MP.1}/\sigma_{MP}$ (Figure 4.13) is greater than 3.25.

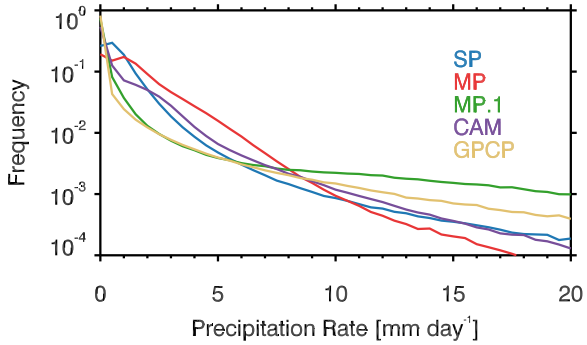

FIGURE 4.16: As in Figure 4.15, but focusing on the lower end of the precipitation rate spectrum.

Turning the attention back to σ_{SP}/σ_{MP} of Figure 4.13, we see more reasonable fall-off ratios (averaging 1.12, globally). This mean randomness reduction corresponds to temporal precipitation noise in SP being closer to 50% of the precipitation magnitude. In this case, large anomalous values are confined to a small region of the Sahara Desert where precipitation is rare. Conversely, there are a few broader regions in which the ratio is less than one, indicating an greater variability in MP. This is surprising as averaging should almost exclusively give a ratio greater than one, but,

again, this highlights that MP CPMs are doing something different than the CPM in SP. The area covered by points where this ratio is less than 0.85 is about 5% of the globe. At these points, the averaging of the MP CPMs does not yield as strong of a reduction in higher precipitation rates (Figures 4.17 and 4.18). Instead, the change puts the PDF of MP more in line with SP, and, in this instance, CAM. The weak change in PDFs (MP.1 to MP) means that more of the CPMs are in better agreement about the precipitation rate more often, perhaps indicating good predictability in these areas. MP is also a closer match to CAM for precipitation less than 5 mm day^{-1}, except for very dry rates, which are less frequent in MP due to the averaging.

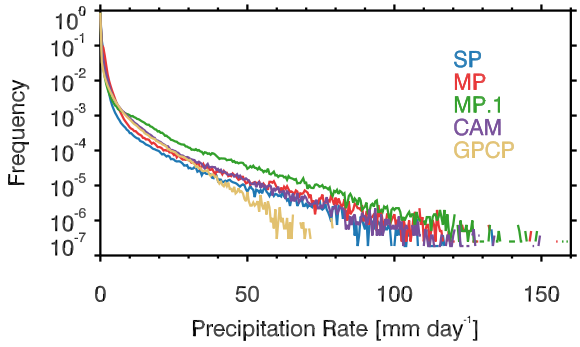

FIGURE 4.17: Precipitation rate PDF for points where the σ_{SP}/σ_{MP} (Figure 4.13) is less than 0.85.

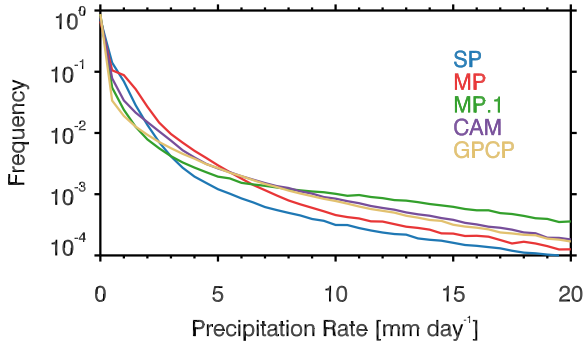

FIGURE 4.18: As in Figure 4.17, but focusing on lower precipitation rates.

The broad majority of points have σ_{SP}/σ_{MP} greater than one. Values near one would indicate places where the variability is unchanged, and by previous arguments, determinism would be

similar. This is the case over most of the globe (Figure 4.14). Areas where the fall-off ratio exceeds the global mean ratio account for 35% of the globe. Areas between 1.5 and 3.25 (yellow to orange colors, indicating significantly greater determinism in MP) account for just over 6% of the globe. In these locations, the MP.1 precipitation distribution is much closer to that of SP for larger precipitation rates (Figures 4.19 and 4.20), and averaging to MP results in an MP distribution that shifts strongly from MP.1 and sits closer to that from CAM, the model with deterministic physics. These points highlight areas where MP is more deterministic than SP, and where MP's CPMs tend to disagree.

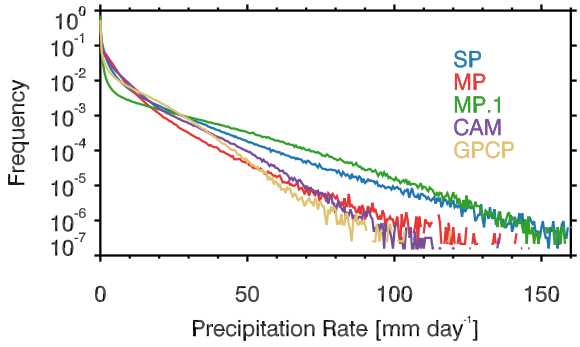

FIGURE 4.19: Precipitation rate PDF for points where the σ_{SP}/σ_{MP} (Figure 4.13) is between 1.5 and 3.25.

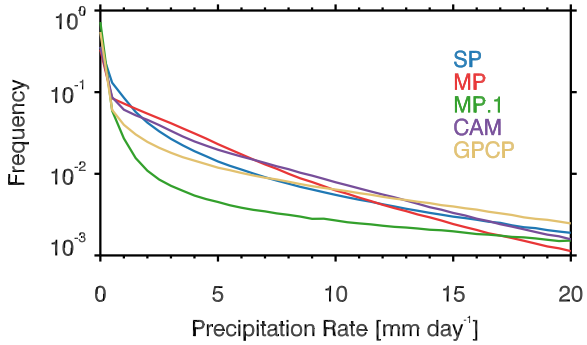

FIGURE 4.20: As in Figure 4.19, but focusing on lower precipitation rates.

Corresponding results of the same analysis for OLR (with NOAA observations, and excluding MP.1 as OLR is not retained for individual ensemble members.) are shown in Figures 4.21

to 4.25. A significant difference in the use of the OLR data is the absence of those dreaded zeros that have a tendency to result in unfortunate statistical anomalies. CAM is a good match to the observations in the global annual mean, whereas SP is a close match in the tropical annual mean and most disparate in the global mean. MP is the poorest match in the tropics, and middling globally. SP and MP tend to show stronger convection (as represented by lower values of OLR) in tropical ocean areas west of Central America, the equatorial Indian Ocean and north of the maritime continent. Conversely, SP shows notably less intense convective activity over equatorial South America, the subtropics of the southern Oceans, and the equatorial Pacific. These tropical differences balance out in the average but are quite strong locally, amounting to an enhancement of local extremes. Moving to MP, we see annual mean values that are almost exclusively lower around the globe, indicating greater convective activity. In some regions, this is an improvement, being closer to observations, but where SP was already making clouds with tops cooler than those in observations, the deficiency is made worse. We saw that MP precipitation was lower than SP, nearer observations, so this result seems to indicate that cloud tops are more frequently cooler, likely deeper than in SP.

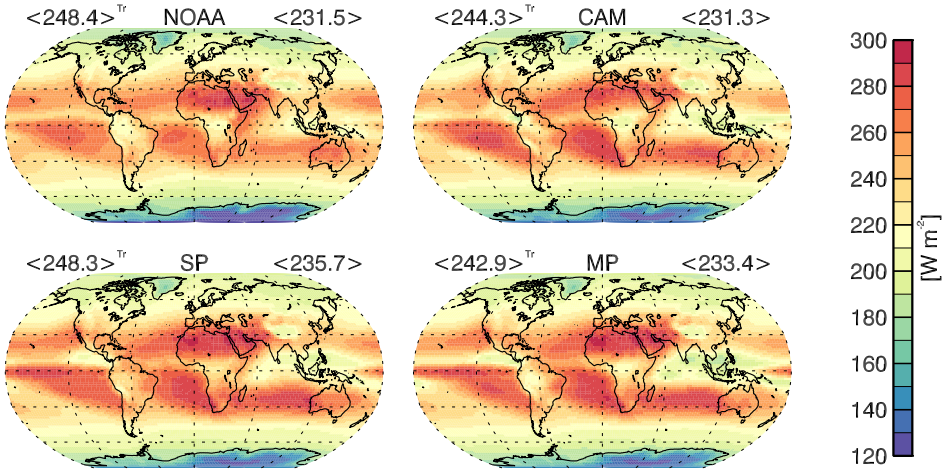

FIGURE 4.21: As in Figure 4.9 but for annual mean OLR.

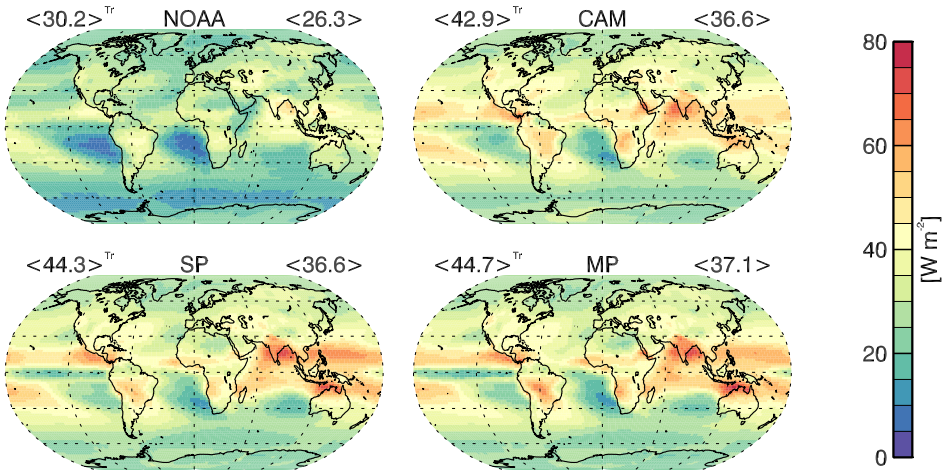

FIGURE 4.22: As in Figure 4.9 but for the temporal standard deviation of OLR.

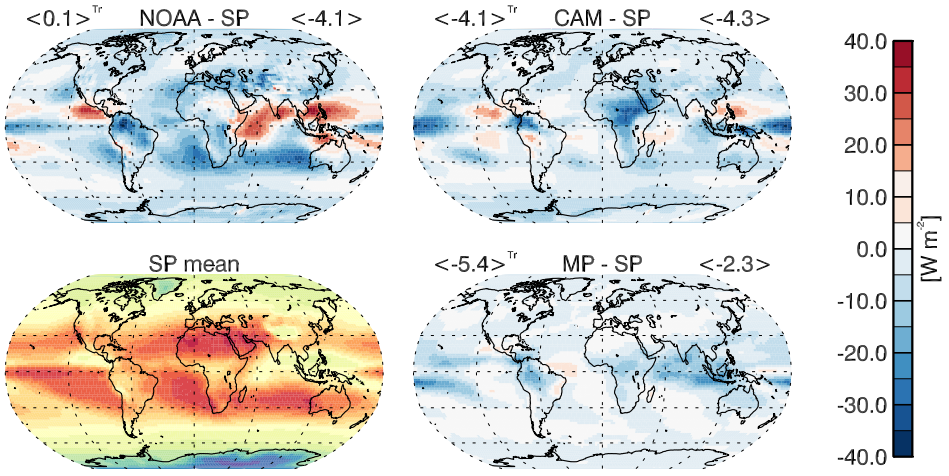

FIGURE 4.23: As in Figure 4.9 but for the difference in annual mean OLR from SP. The bottom left map is a reproduction from Figure 4.21.

The temporal standard deviation of OLR in each model considerably exceeds that in observations, with MP being the most variable of the three in the global average (Figures 4.22 and 4.24). In the tropics, CAM is closest to observations, mainly as a result of a better representation of annual mean OLR near the maritime continent. This strong difference from observations was striking, though not surprising, given the previously mentioned enhancement in the local extremes of OLR.

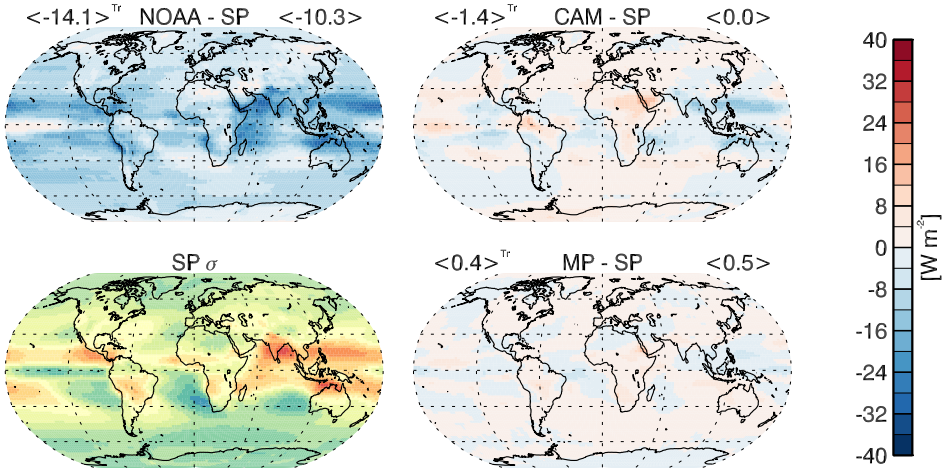

FIGURE 4.24: As in Figure 4.11 but for the difference in temporal standard deviation of OLR from SP. The bottom left map is a reproduction from Figure 4.22.

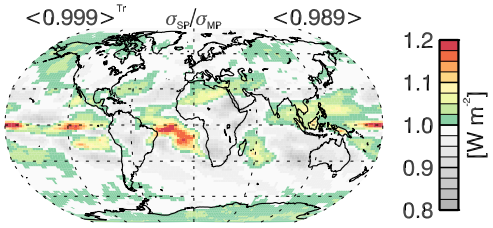

FIGURE 4.25: As in Figure 4.13 but for OLR temporal standard deviation fall-off ratio for σ_{SP}/σ_{MP}.

For OLR, the global mean standard deviation fall-off ratio is neutral, near one(Figure 4.25). As such, increases and decreases in determinism measured this way are local and of low magnitude. The global and tropical means are actually both less than one, a result expected when seeing that the globally averaged standard deviation was higher in MP. Regions where the ratio is greater than one, though, are qualitatively consistent with such regions in the precipitation analysis. As clouds appear to have deepened in MP, the variability reduction due to averaging is not as strong or consistent. As will be clear in a later plot, the regions of highest fall-off values correspond to those where high cloud amount is lower in MP and are therefore unaffected by the potential for the offsetting effects of potentially higher clouds and the associated greater possible range of OLR states. The fact that the standard deviation does not fall off uniformly indicates, once again,

that some MP CRMs are operating in a different phase space than the SP CPM. In particular, some of them are more convectively active.

While the standard deviation fall-off ratio does provide guidance as to the change in determinism, other methods may also prove elucidating. The coefficient of variation (COV, sometimes written as CV or CoV), is defined as the standard deviation divided by the mean, and it gives an indication of the prevalence of noise in a data set in a normalized form that allows for comparison between data sets of widely disparate magnitudes. For COV less than one, the scale of the typical noise is less than the mean, and this could be indicative of a more deterministic, predictable location. Large values of COV, then, could indicate chaotic, unpredictable[2] locations.

Figure 4.26 shows the COV for the present data sets. CAM values are lowest, and we can take that as a confirming measure of its being a deterministic system. Excluding the very high COV values over the Sahara in the superparameterized models, which are mainly a product of there being a great frequency of zero precipitation in those cases (Figures 4.27 and 4.28), TRMM values are the highest, indicating a less deterministic data set. The observations tend to have high COV regions collocated with dry regions (compare with Figure 4.9), indicating relatively large variations about low precipitation values. A common feature in TRMM, CAM, SP, and MP is a local COV minimum in the subtropical southern oceans associated with the climatological position of stratocumulus (Figures 4.1 and 4.2). These are absent in GPCP, and the determination in MP.1 is unclear. Observations, and to a lesser extent MP.1, show equatorial (and slightly south) maxima in the eastern Pacific and Atlantic, areas associated with sparse fair-weather cumuli. This cloud regime is also common over the Saharan and Arabian Deserts. Maxima are also present in the stratus decks off western coasts, though they are considerably weaker in CAM, and over Antarctica.

[2]Here, "unpredictable" is relative to the scale of the mean. For spaces commonly characterized by drizzle, a forecast in the ballpark of drizzle is sufficient for practical purposes, but relative error on the mm day^{-1} scale could be large.

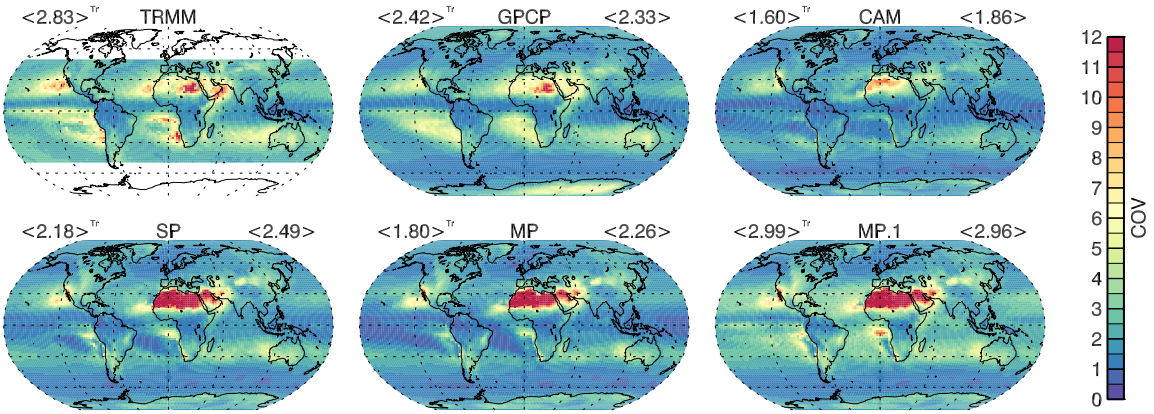

FIGURE 4.26: As in Figure 4.9, but for the coefficient of variation of precipitation rate. Many of the points over the Sahara in the lower plots greatly exceed the color bar maximum, peaking above 45 in each case.

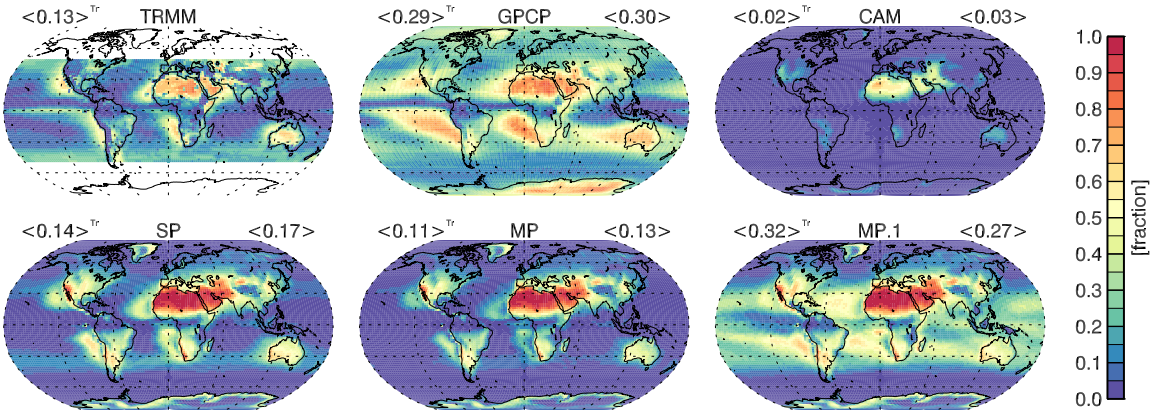

FIGURE 4.27: As in Figure 4.9, but for the fraction of days with exactly zero precipitation.

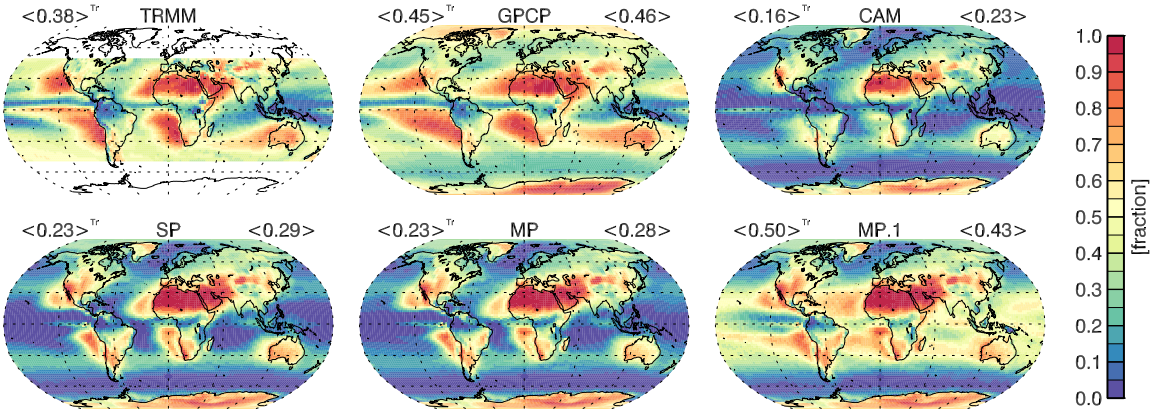

FIGURE 4.28: As in Figure 4.9, but for the fraction of days with precipitation less than 0.1 mm day^{-1}.

COV differences from SP are shown in Figure 4.29. Because of the large positive bias over the desert regions in SP, the tropical means are more meaningful here. TRMM shows larger COV in the aforementioned cumulus humilis and subtropical stratus areas. GPCP shows this feature, as well, but more so in southern the stratocumulus regions than TRMM (Figures 4.1 and 4.2). It is interesting to see MP.1 showing differences that similarly appear in the observations, indicating that MP.1, with greatest variability, is nearer observations than SP or MP.

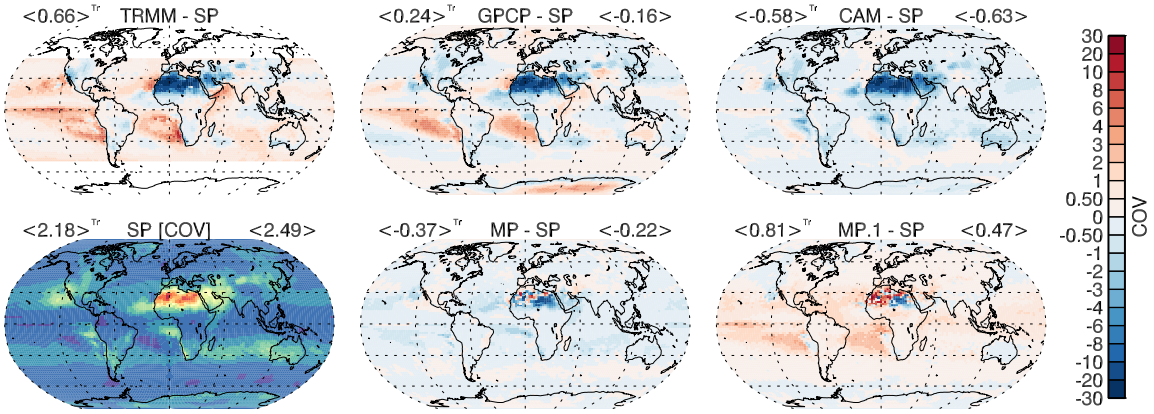

FIGURE 4.29: As in Figure 4.9, but for COV of precipitation rate differences from SP. The bottom left map is a reproduction from Figure 4.26.

The results of the same analysis for the temporal COV of OLR are shown in Figures 4.30 and 4.31. Again the models' greater OLR variability compared to observations is apparent. The great red spots in the COV for precipitation rate are notably absent here, as a result of using a variable without persistent strings of zeros. As in the analysis of OLR standard deviation fall-off, there are a number of regions in which the relative variability of OLR has increased moving from SP to MP, particularly in the tropics. The opposite is true where the occurrence of high cloud has decreased in MP. These are predominantly areas where high cloud was already climatologically infrequent, an exacerbation of existing extremes. It should be noted that this is not a failure of averaging to reduce extremes, as postulated. Instead, it is further indication that we are starting with MP members that are considerably more variable than their SP counterpart. As far as the

COV measures are concerned, precipitation changes indicate the MP is more closely constrained to some expected value, while some shift in its cloud behavior causes OLR to be more widely varying across much of the tropics. The same analysis carried out at 3-hourly temporal resolution (not shown) gives qualitatively similar results.

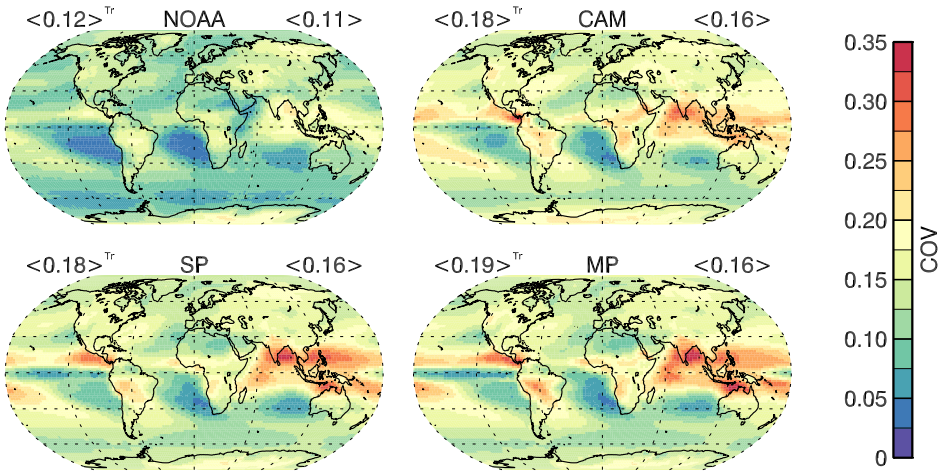

FIGURE 4.30: As in Figure 4.9, but for the coefficient of variation of OLR.

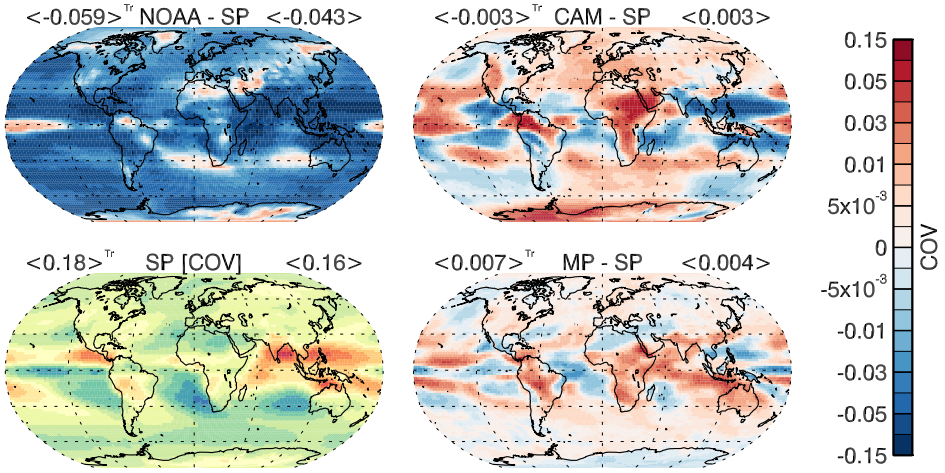

FIGURE 4.31: As in Figure 4.9, but for COV of OLR differences from SP. The bottom left map is a reproduction from Figure 4.26.

While the standard deviation fall-off ratio and the COV changes provide guidance as to the change in determinism, they lack consideration of the sequences of the values in the data. For instance, sets $S_1 = \{50, 50, 25, 25, 0, 0, 0, 0\}$ and $S_2 = \{50, 0, 50, 0, 25, 0, 25, 0\}$ have the same

mean and standard deviation, indicating the same levels of determinism by measures of standard deviation fall-off ratio and COV. However, from the point of view that persistence in time is an indicator of predictability, the predictability of these two sets should be measurably different. A measure that does account for this is the e-folding time of the autocorrelation function. The e-folding measure, the lag time at which the autocorrelation is reduced to $1/e$, looks at linear correlations in each local time series. Larger values mean that the evolution of the data is smooth, making it potentially easier to predict. The results for daily mean precipitation rate and OLR are shown in Figures 4.32 and 4.33 and for 3-hourly MP data in Figures 4.34 and 4.35.

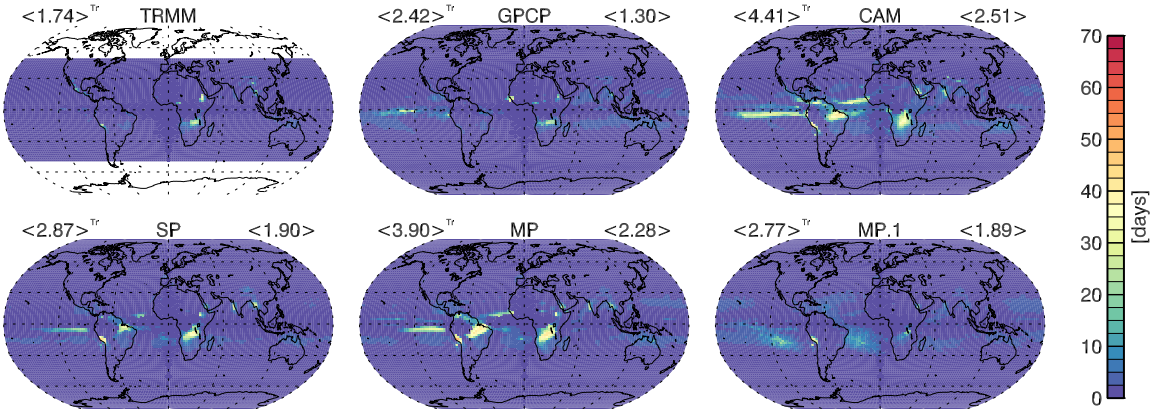

FIGURE 4.32: As in Figure 4.9, but for the e-folding time of the autocorrelation function for daily precipitation rate.

E-folding times for OLR are consistently longer than those for precipitation rate, as OLR is a more smoothly varying feature. Precipitation observations show the shortest e-folding times, and those for CAM and MP are longest. For OLR, which we have noted is significantly more variable in the models, the NOAA spatially averaged e-folding times are longer than those in the models. At the same time, those in MP are longer than those in SP, pointing to greater predictability. The locations at which the e-folding maxima occur are fairly consistent across models (except MP.1) and observations. These appear to be associated with areas of typically low precipitation stratocumulus and shallow cumulus over ocean (Figures 4.1, 4.2 and 4.9). Over southern tropical

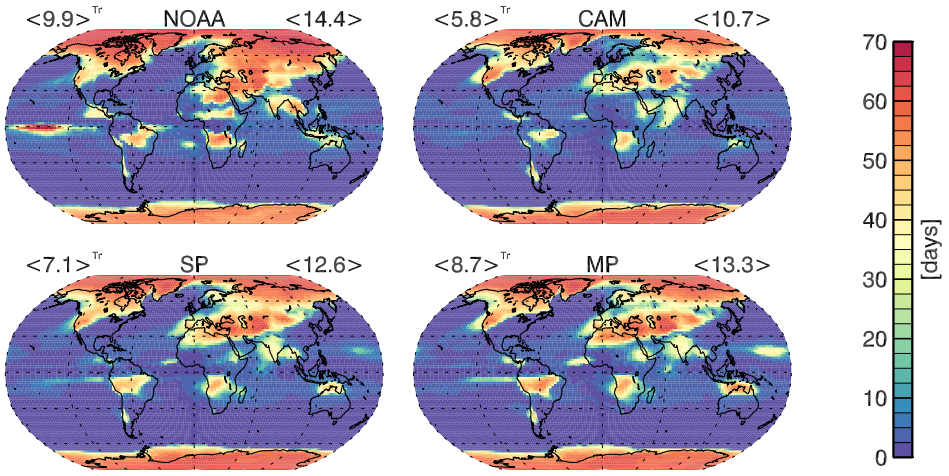

FIGURE 4.33: As in Figure 4.9, but for the e-folding time of the autocorrelation function for daily OLR.

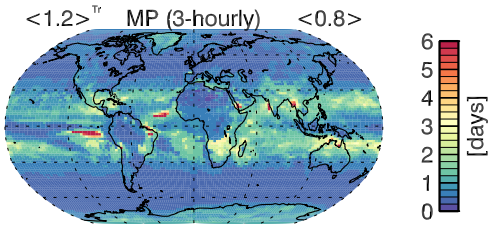

FIGURE 4.34: As in Figure 4.9, but for the e-folding time of the autocorrelation function for 3-hourly precipitation rate.

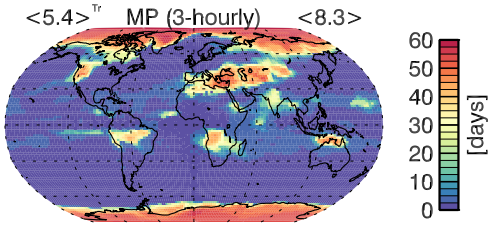

FIGURE 4.35: As in Figure 4.9, but for the e-folding time of the autocorrelation function for 3-hourly OLR.

land, we see maxima over the Amazon, south of the Congo, and from northern Australia to Indonesia, areas with a range of common cloud types. Strong maxima in the OLR e-folding times are also noted over regions that are commonly cloud-free, such as deserts of Africa, the Middle East, and China. Values for OLR are also consistently large over Antarctica and the Arctic, which has persistent drizzle conditions in the SP and MP models. The predictability at the 3-hourly

timescale in MP is considerably less than the daily timescale, as is expected, but the regions of greatest predictability remain similar. Here, much of the tropics show e-folding times above the global mean except for locations nearest the equator.

The e-folding time is helpful, but there are areas where it may be problematic. Consider again the sets, sets S_1 and S_2 or some longer sets with similar structure. Given their long-term trends, autocorrelations may remain large at large lags, while from one point to the next, there may be quite drastic fluctuations. We can further examine the jaggedness of the temporal evolution of the data via a measure that combines elements of the temporal derivative and the root-mean-square-difference. I've never seen this measure before, so I'm naming it "temporal jaggedness," and it is defined by Equation (4.3). Here, N is the number of values (x) in the sequence, indexed by n. J appears to provide a consistent measure of the jaggedness/roughness of a sequence.

$$J = \sqrt{\frac{\sum_{n=0}^{N} \left(\frac{x_{n+1} - x_n}{\delta t}\right)^2}{n-1}} \tag{4.3}$$

Jaggedness daily mean precipitation rate and OLR are shown in Figures 4.32 and 4.33 and for 3-hourly MP data in Figures 4.34 and 4.35. Many of themes of the previous measures are repeated for the temporal jaggedness. This measure is not normalized, and this means that we don't care much about the jaggedness relative to the mean and that strong absolute shifts are given emphasis. If normalized by mean values of the temporal derivative, these plots almost exclusively highlight areas of climatologically low precipitation with high jaggedness (not shown). CAM and MP show lower values, indicating a smoother field and potentially greater determinism. Areas with greatest jaggedness include storm track regions and the ITCZ. Given those features, it would not be surprising to commonly observe changes of large magnitude from one point to the next in the sequence. However, this does not specifically indicate that such changes cannot be predicted. In the case of the storm tracks, for instance, a strong shift in precipitation would

likely be accompanied by a completely foreseeable forcing on the large-scale that would eventually have to be broadly realized even if its exact timing or placement was somewhat questionable. The continental maxima of temporal jaggedness seen in the 3-hourly results would correlate with diurnal convection, which is also more broadly predictable given the regularity of the forcing, but which will also exhibit time derivatives of large magnitude.

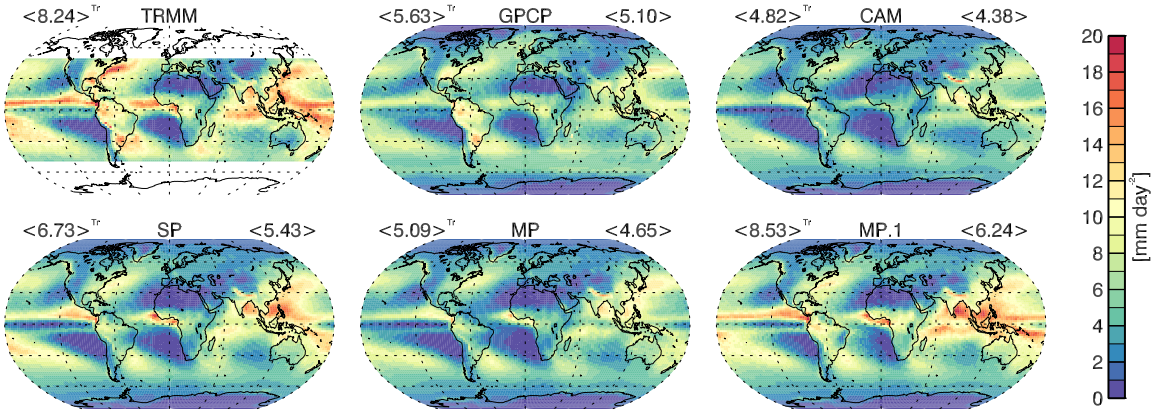

FIGURE 4.36: As in Figure 4.9, but for the temporal jaggedness for daily precipitation rate.

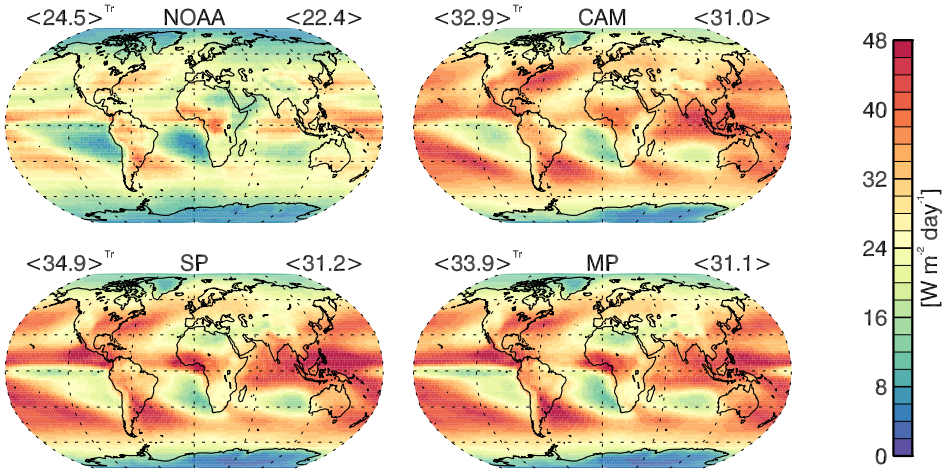

FIGURE 4.37: As in Figure 4.9, but for the temporal jaggedness for daily OLR.

In the final attempt to evaluate whether the formulation of MP is more deterministic than SP, we turn to measures designed to characterize the chaotic nature of a dataset. In general, time

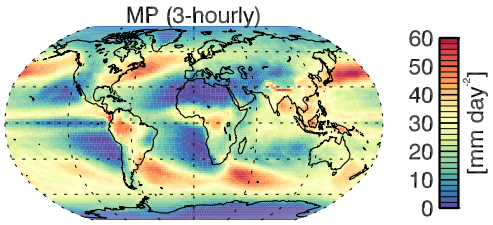

FIGURE 4.38: As in Figure 4.9, but for the temporal jaggedness for 3-hourly precipitation rate.

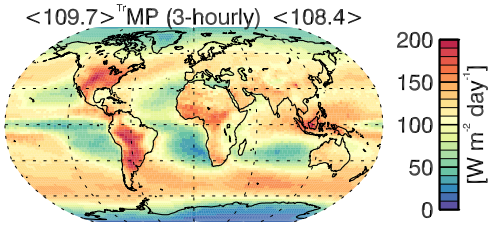

FIGURE 4.39: As in Figure 4.9, but for the temporal jaggedness for 3-hourly OLR.

series data can be analyzed to study predictability from the view of nonlinear error growth dynamics by reconstructing the phase space of a dissipative dynamical system (like the atmosphere) under chaos theory. Such methods date back to Takens (1981) and Grassberger and Procaccia (1983) and have been used to characterize the predictability of various atmospheric parameters for the past few decades. Zeng et al. (1992) examined fractal dimension and predictability of temperature time series at four locations. Chen et al. (2006) and Ding et al. (2008) characterized predictability around the globe in terms of time series of 500 mb geopotential heights. Liu et al. (2016) looked at monthly precipitation predictability over China, and Sivakumar (2001), Millán et al. (2009), and Millán et al. (2011) analyzed predictability of precipitation at a handful of locations at higher temporal resolution. For those with further interest, Sivakumar (2004) provides a review of the use of chaos theory in geophysics[3].

[3]While primarily of interest to mathematicians and physicists, chaos theory has its roots in the work of L.F. Richardson, who pioneered numerical weather prediction in the early 20th century.

The statistical complexity of a dataset can be quantified by its fractal dimension, a typically fractional value commonly used to measure the "strangeness" of chaotic attractors. Further, Lyapunov exponents characterize the degree of chaos. Lyapunov exponents represent the degree to which two very close, but different, initial conditions exponentially diverge or converge with forward integration of the system. A set of these exponents characterizes the whole system, not simply a particular set of similar initial conditions. If a system contains at least one positive Lyapunov exponent, it is defined to be chaotic, and the inverse magnitude of the exponent indicates the timescale on which the system becomes unpredictable. That is, for large exponents, similar initial conditions diverge rapidly and the predictability time is short.

The calculation of the fractal dimension and Lyapunov exponents is not trivial. The calculations are computationally expensive, people have done entire dissertations on individual aspects of their calculation, large datasets (over 10,000 points) are required for sufficient accuracy, and datasets with significant fractions of a repeated value, thereby being quasi-binary, often provide results of poor quality (Zeng et al. 1992; Sivakumar 2001). Being interested with the predictability of precipitation with access to data on the edge of the size requirement, this poses problems. However, we will attempt a not-very-sophisticated calculation of fractal dimensions and Lyapunov exponents for time series of precipitation rate and OLR at each point along three latitude bands (approximately 14°S, 1°S, and 12°N) of our longest datasets. These bands are native model coordinates situated along longitudinally varying features of the earlier potential measures of determinism.

First, we make a determination as to whether the time series presents with an appropriate sampling interval based on the e-folding autocorrelation time as computed above. In the case of precipitation, most points have an e-folding time of 1 day, and the original dataset is appropriately sampled at interval τ_0. In the cases where the e-folding time, τ_d, is longer, the time series

should be subdivided for further analysis with averaging of subsequent results. This is accomplished by creating $s = \tau_d/\tau_0$ new time series from points in the original series that are s apart. Needing to do this may degrade the accuracy of the results, as all the new time series are shorter.

Next, for a time series of length n, we create $n - m$ vectors, where m is referred to as the "embedding dimension," which provides a representation of the reconstructed attractor in an m-dimensional phase space. So for a time series, $\vec{x}$, with $s = 1$, we create $n - m$ vectors, $\vec{y}_n$, each with length m,

$$\begin{aligned} \vec{y}_1 &= (x_1, x_2, x_3, \ldots, x_m) \\ \vec{y}_2 &= (x_2, x_3, x_4, \ldots, x_{m+1}) \\ &\vdots \\ \vec{y}_{n-m} &= (x_{n-m}, x_{n-m+1}, \ldots, x_n)\,. \end{aligned} \tag{4.4}$$

Incorporating, s, we can begin with,

$$\vec{y}_1 = \left(x_1, x_{1+s}, x_{1+2s}, \ldots, x_{1+(m-1)s}\right). \tag{4.5}$$

For a sequence of integers, m, we then calculate the Grassberger-Procaccia dimension, D_{GP} (Grassberger and Procaccia 1983). What m is initially is not terribly important, as long as it is small. It may be wise to start with 1. D_{GP} is defined as,

$$D_{GP} = \lim_{\epsilon \to 0} \frac{\ln C\left(\epsilon\right)}{\ln \epsilon} \tag{4.6}$$

where $C(\epsilon)$ is the correlation integral,

$$C\left(\epsilon\right) = \frac{2}{n\left(n-1\right)} \sum_{i,j\ pairs} \theta\left(\epsilon - |\vec{y}_i - \vec{y}_j|\right), \tag{4.7}$$

ϵ is initially very small relative to the magnitude of the data, and $\theta(x)$ is the Heaviside function,

$$\theta(x) = \begin{cases} 1 & x > 0 \\ 0 & x \leq 0 \end{cases}. \tag{4.8}$$

The sum in Equation (4.7) is over all unique combinations of possible pairs, which can be considerably large. Further, $|\vec{y}_i - \vec{y}_j|$ can be calculated as the "supnorm,"

$$|\vec{y}_i - \vec{y}_j| = \max\left(|\vec{y}_{i_1} - \vec{y}_{j_1}|, |\vec{y}_{i_2} - \vec{y}_{i_2}|, \ldots\right). \tag{4.9}$$

To find the limit in Equation (4.6), the correlation integral is calculated over a range of ϵ covering a few orders of magnitude. Then, D_{GP} is determined by the ratio of $\ln C(\epsilon)$ to $\ln \epsilon$, where the ratio forms a regular linear relationship. I have learned informally that this can be a particularly difficult task to perform rigorously. Here, I have averaged the derivative of the relationship in a region expected to be linear (at larger ϵ) to obtain the slope as D_{GP}.

This process is repeated for subsequent values of m until the result for D_{GP} converges to significant accuracy. In this case accuracy was set to 0.1. The values found using the methods described above are presented in Figures 4.40 and 4.41 for precipitation and OLR. For comparison, Zeng et al. (1992) found in their analysis for surface temperature that the fractal dimension was near 10; these values are mostly considerably lower than that. In the case of precipitation, the model values differ significantly from the observed values, which lie near 1. This is likely due to the fact that GPCP precipitation stands out from the other datasets because of its excess of zero values (Figure 4.27). Model data tends to follow suit, with very low D_{GP} near points of frequent zero precipitation, and maxima over the oceans, where precipitation exhibits few dry days. On average, the fractal dimension was 3.06 in SP and 1.91 in MP. This may indicate a reduction in complexity. Spatial patterns in D_{GP} for OLR are more difficult to discern, as most

are near 5-6 for NOAA, SP, and MP (averaging 6.17 for SP and 5.45 for MP). CAM values more frequently show larger dimension. NOAA OLR fractal dimension shows a few large spikes along the equator. These appear to be associated with land points that exhibited maxima in temporal jaggedness Figure 4.37. One might argue that a similar pattern exists in SP, but it would be to a much lesser extent.

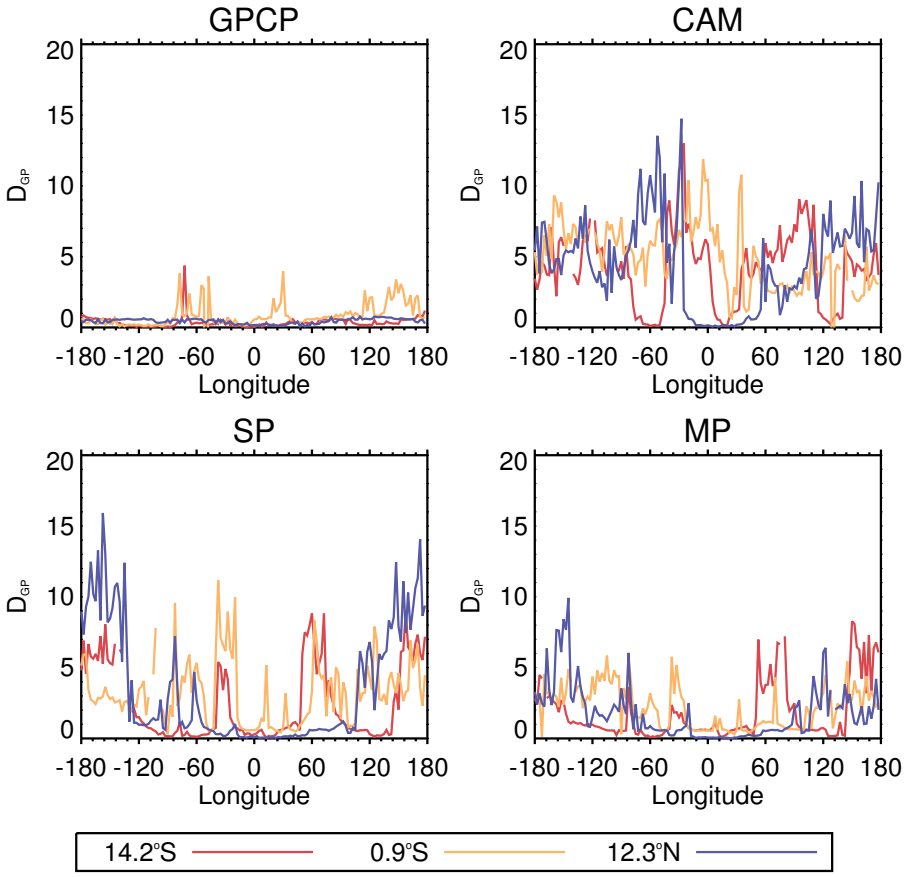

FIGURE 4.40: D_{GP} for daily mean precipitation rates at the noted latitudes.

With fractal dimension in hand, we use $m(D_{GP})$ as the embedding dimension for the determination of the leading Lyapunov exponent[4]. With this embedding dimension we are creating a projection of the attractor in m dimensions as in Equation (4.5). To find the leading Lyapunov exponents, we begin with a search through all vectors, $\vec{y}$, to find nearby pairs, and then we evaluate

[4] m Lyapunov exponents can be obtained, but they are lesser in magnitude and the procedure for finding them is particularly difficult.

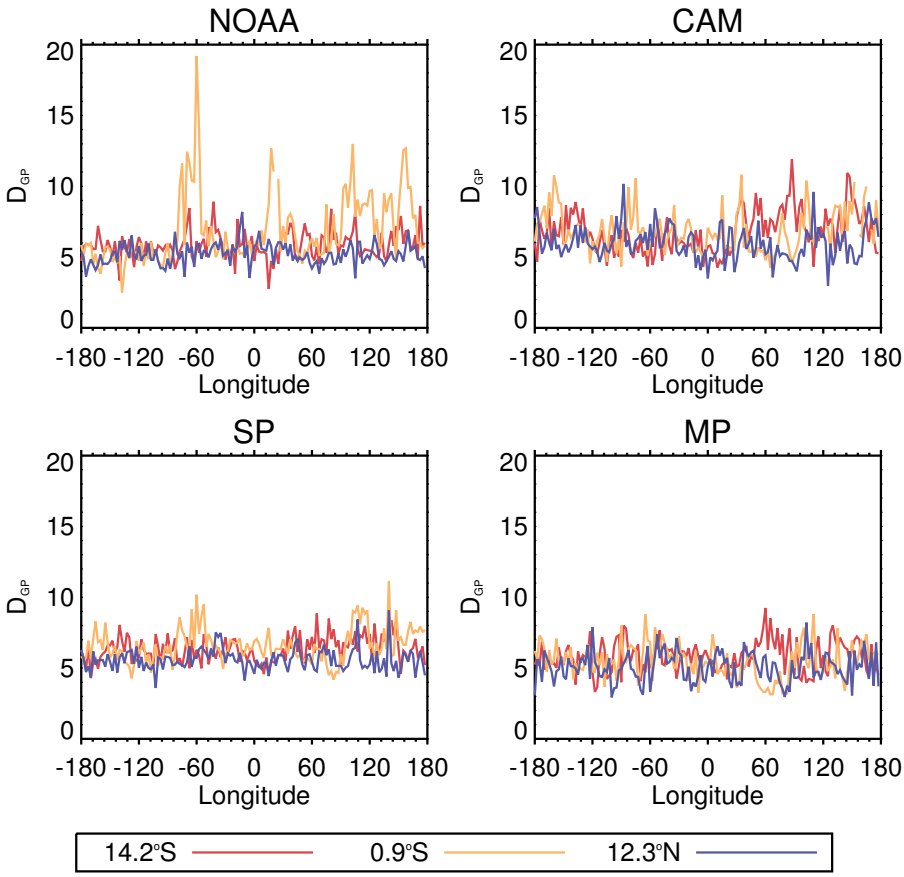

FIGURE 4.41: D_{GP} for daily mean OLR at the noted latitudes.

the way in which evolution of the state from those points evolves in time. For example, if there is a match between $\vec{y}_{10}$ and $\vec{y}_{630}$, we calculate an estimate of the Lyapunov *number*

$$\Lambda \approx \frac{|\vec{y}_{631} - \vec{y}_{11}|}{|\vec{y}_{630} - \vec{y}_{10}|}. \tag{4.10}$$

From this estimate, we can calculate the Lyapunov exponent,

$$\lambda = \ln \Lambda, \tag{4.11}$$

and average λ for each of the similar vector pairs. This average is the largest Lyapunov exponent in which we are interested, and

$$T = \frac{\ln 2}{\lambda} \tag{4.12}$$

is the error-doubling time (Zeng et al. 1992), which can be interpreted as a predictability timescale.

The results of this calculation are shown in Figures 4.42 and 4.43. For comparison, Zeng et al. (1992) found in their analysis for surface temperature that the leading Lyapunov exponents ranged from 0.06 to 0.19, indicating error-doubling times of 7 days over the North Atlantic Ocean and 2-3 days in Fort Collins, Colorado. In the case of daily mean precipitation rate, we can see the havoc caused by the excess of zero values. Nearly all points in the GPCP case are unreliable. At a few points in the models, λ is negative. This means that no positive Lyapunov exponents were found and the system at that point is not chaotic, a result that is spurious given the nature of atmospheric dynamics and the percentage of zeros in the data at these points. Due to the problems already discussed, these values are all deemed to be unreliable, and we are unable to draw conclusions regarding whether precipitation in MP is less chaotic than in SP. In the case of daily mean OLR, the leading Lyapunov exponent values generally appear more reasonable, and their patterns are similar between datasets. Notably, larger values, indicating short predictability times are found over much of the Pacific Ocean, with pronounced minima over land masses along the southern latitude band. On average, OLR error doubling time increased at these points from 3.2 days in SP to 3.7 days in MP, a result reminiscent of the decline in the area-averaged e-folding times shown in Figure 4.33.

Considering the combined results of the standard deviation fall-off, COV, e-folding times, temporal jaggedness, and chaotic analysis, it is reasonable to conclude that the daily mean precipitation rate is more deterministic in MP than in SP, as desired. The nature of the values involved in making this determination has clearly complicated parts of the analysis, but it is clear that

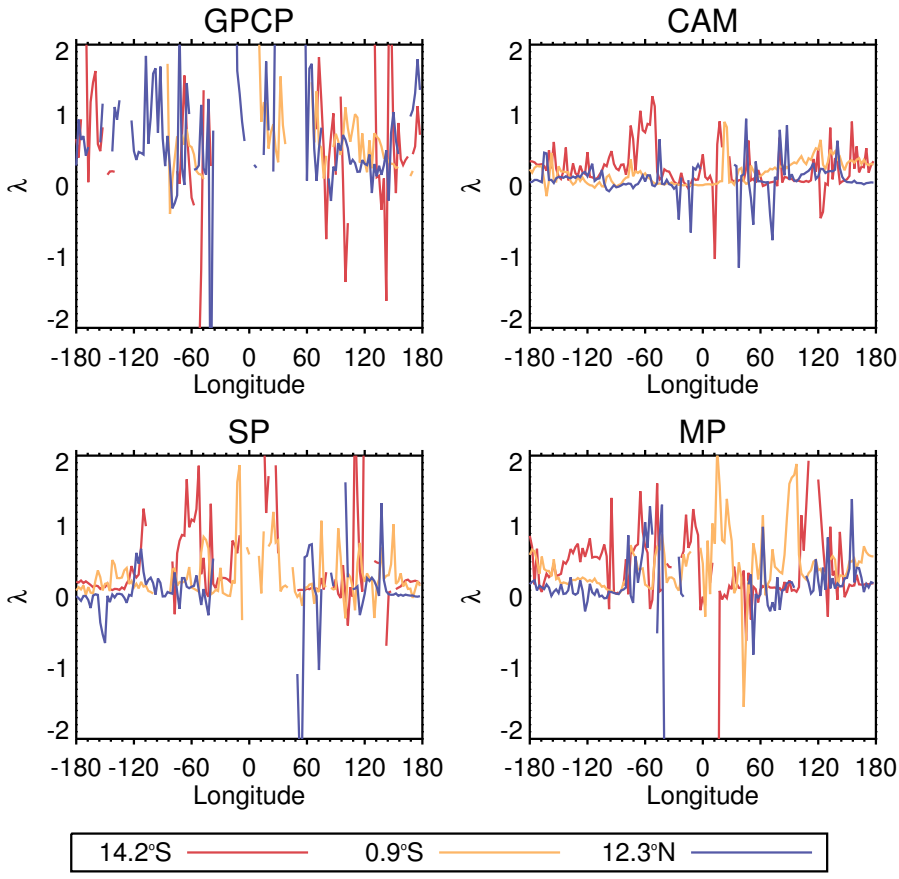

FIGURE 4.42: λ for daily mean precipitation rates at the noted latitudes.

precipitation in MP has mainly shifted to being less variable in time. Additionally, comparing the time-mean *spatial* standard deviations of daily mean precipitation rate in SP and MP, one obtains a fall-off ratio of 1.15, which is greater that what was reported for the global average of the temporal standard deviation fall-off. This is further evidence of a more constrained, and therefore, deterministic, model. Foreshadowing what will be seen in the next section, the analyses for OLR often showed the reverse relationship to be true. That is, greater temporal OLR variability was present in MP. Similarly, comparing the time-mean *spatial* standard deviations of daily mean OLR in SP and MP, one obtains a fall-off ratio of 0.998, indicating an increase in spatial variability. OLR in MP has a greater potential range, resulting in some difference in its climatological mean state that is not present in the precipitation data.

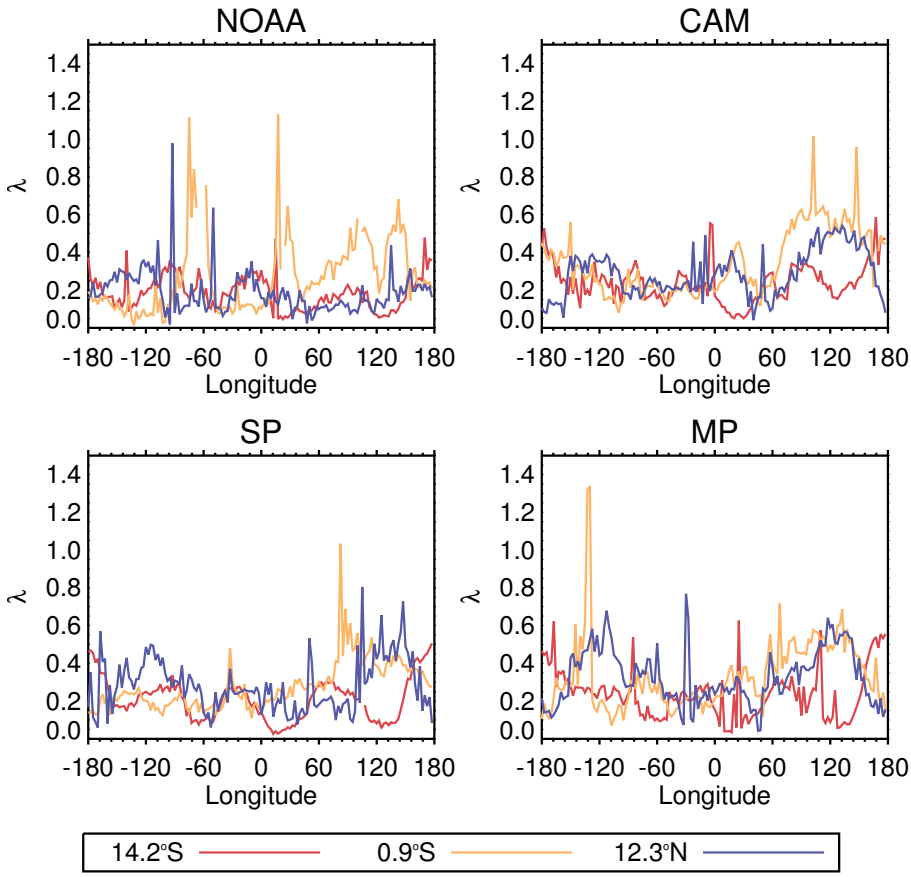

FIGURE 4.43: λ for daily mean OLR at the noted latitudes.

4.3. MODEL CLIMATOLOGIES

The inclusion of stochastic processes, whether through stochastically-enhanced physical parameterizations or superparameterization, in atmospheric models can produce a number of improvements in simulated features of the climate (Chapter 1). The question at present is whether a model which directly incorporates representation of variability at the cloud scale, but which applies such cloud-level influences to the large-scale in a deterministic fashion, can similarly reproduce those improvements. A major test for evaluating this will be how MP simulates the MJO. Before turning to that question, it is important to evaluate the changes that have been produced by implementing the MP framework in order to verify that its climate is reasonable and to ensure awareness of any unintended consequences.

First, we have assumed that the 10 CPMs in MP will be concurrently technically different and still very similar in order to provide a range of likely responses to large-scale forcing from the GCM. Since each member only provides 10% of the influence that will be felt by the GCM, one might reasonably expect the potential for drift, especially considering that the SP CPM is exclusively engaged with the GCM and therefore more tightly coupled in this way. However, because each member sees exactly the same tendencies from the GCM, there should be a substantial element of constraint. We would like to demonstrate the extent of the constraint by way of analyzing the similarity of the CPMs within a given GCM column.

Using data at every GCM time step (15 minutes), the root-mean-square-difference from the MP CPM ensemble mean temperature and specific humidity at the 850, 500, and 300 mb pressure levels were calculated and averaged over sample months of January (Figure 4.44) and July (Figure 4.45). In the case of both variables, notable CPM differences are found mainly in the presence of clouds. The maximum values for differences are on the order of 1 K for temperature at any level and up to about 1 g/kg for specific humidity at low levels. Average global values are about an order of magnitude smaller, with differences in cloudy regions typically being on the order of less than third of the maximum. In a relative sense, average differences are approximately 1% at 300 mb, 0.5% at 500 mb, and 0.3% at 850 mb in the case of specific humidity and less than 0.01% in terms of temperature in K at all levels. Average deviations from daily mean data are approximately two-thirds the magnitude of those at 15-minute resolution, with maxima being half that for 15-minute data (not shown). For more long-term averages of this quantity, spatial patterns mirror features over oceans as in CR7 of Figure 4.1 and CR3 globally.

Overall, the variations within the CPM ensembles are of the appropriate order for the purposes of this investigation, and it is likely that MP CPM precipitation disagreements will be collocated with the CPM domain mean temperature and moisture disagreements. Let's take a

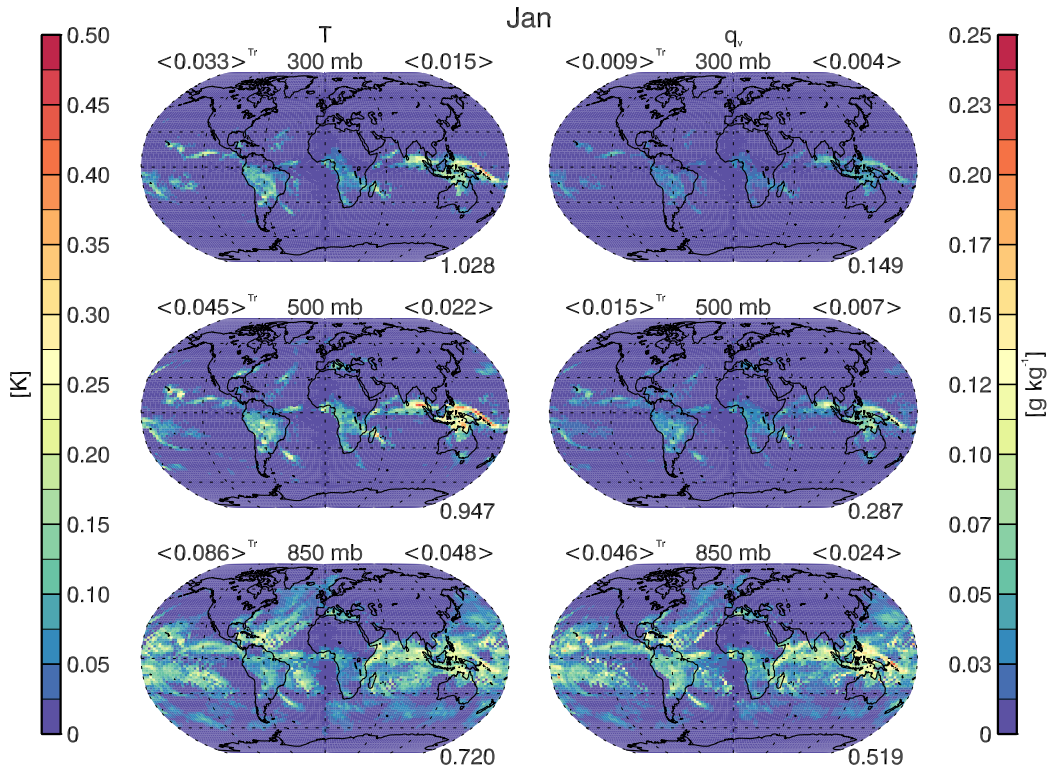

FIGURE 4.44: The root-mean-square-difference from the MP CPM ensemble mean temperature and specific humidity at the 850, 500, and 300 mb pressure levels computed at every GCM time step (15 minutes) and averages over a sample month of January. $<x>$ denote spatial averages: the upper left value, denoted with superscript Tr, is an average from 20°S to 20°N, representing tropical values, and the upper right value is the global mean. The value at the bottom right is the maximum value obtained at that level for the month.

look at how the MP CPMs handle the most basic precipitation prediction: Will it rain, yes or no? Figure 4.46 shows the fraction of occurrence, considering the full MP daily dataset, where MP CPMs unanimously report zero precipitation, unanimously report any amount of precipitation, or are in some proportion in disagreement as to whether there will be any precipitation. The members frequently agree that there will be zero precipitation over deserts and oceanic stratocumulus regions. They frequently agree that there will be any non-zero amount of precipitation over much of the extratropical and polar regions, as well as locations frequently populated by cirrostratus anvils of deep convection. The CPMs have a particular fondness for precipitation over the maritime continent land masses. On the other hand, they tend to have difficulty in finding

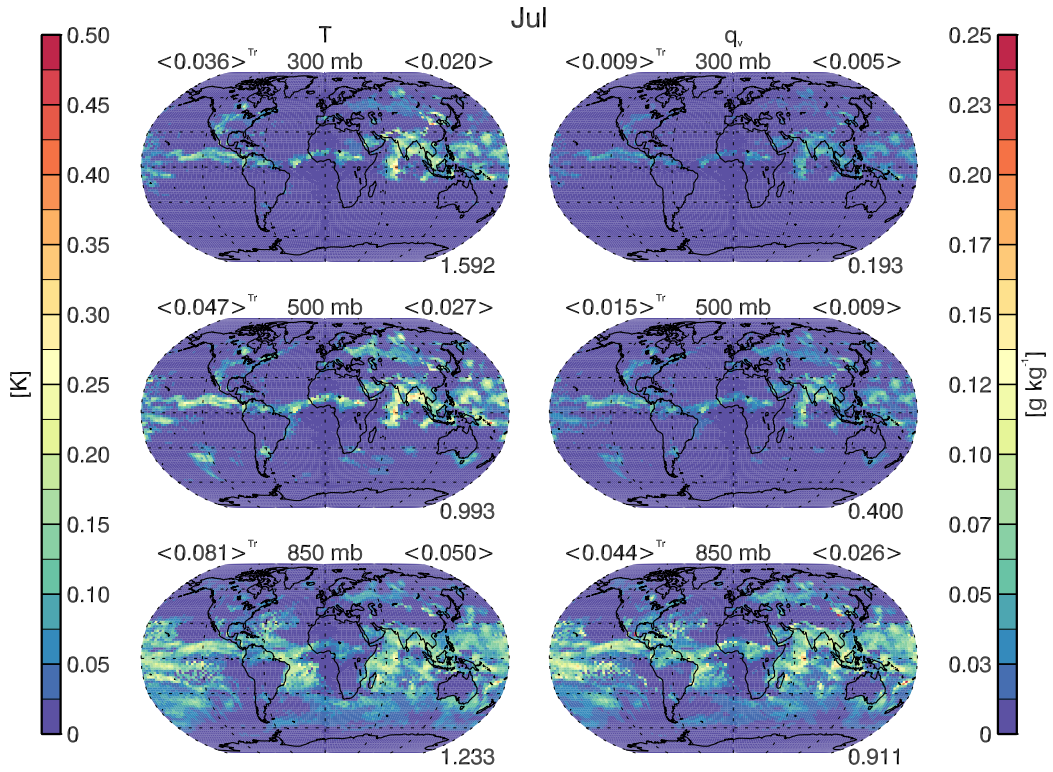

FIGURE 4.45: As in Figure 4.44 but for a sample month of July.

agreement about the occurrence of precipitation in regions frequently populated by fair weather cumuli, which are collocated with annual mean climatological values of precipitation rate in the range of 2-4 mm day^{-1}. These can be characterized as the boundary regions between high and low precipitation, a place where the weather is not extreme and forecasts may appear muddled. Now, perhaps these regions of mixed opinion are difficult to forecast; however, this little analysis has not considered the effects of magnitude of the precipitation rates. It is highly likely that in some of these locations, some CPM in the ensemble is producing trace amounts of precipitation while the others say zero. That scenario fails the "yes or no" test, but is hardly representative of widely divergent forecasts.

As noted before, much of the cloud-scale variability from the CPMs was intended to be removed in the application of physical tendencies to the GCM. In Section 4.2, we saw that temporal variability of precipitation was reduced in MP. Similarly, the fine-scale vertical structure in the

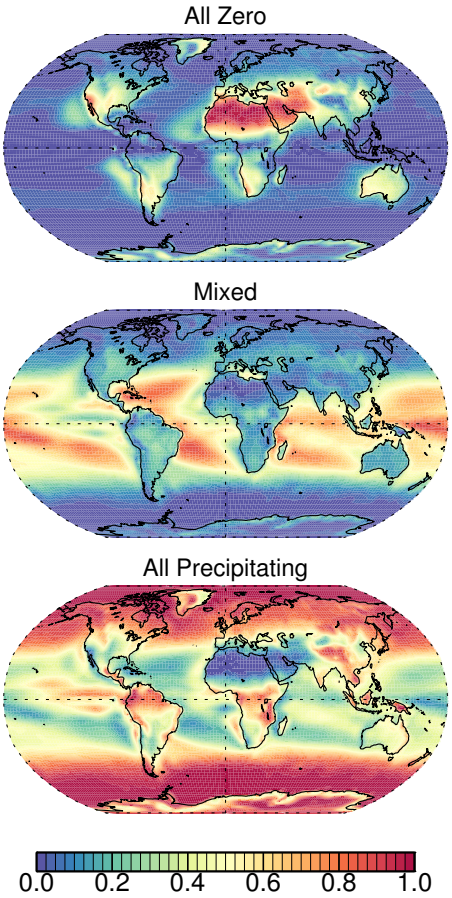

FIGURE 4.46: The fraction of occurrence in the MP simulation where CPM members all agree that the daily mean precipitation will be zero (top), predict both zero or any precipitation (middle), or all agree that there will be some amount of precipitation.

physical tendencies should be reduced. To evaluate whether this goal has been attained, we again employ the jaggedness measure of Equation (4.3), though now, N is the number of points in the vertical, the derivative is with respect to pressure, and the quantities of interest are the temperature and moisture tendencies from the SP single CPM and MP CPM ensemble average. The results of this computation for tendencies at 15-minute intervals over a combined single simulated January are presented in Figure 4.47. By measures of global and tropical spatial averages and global/temporal maxima, the jaggedness of the vertical tendency profiles in MP is less than that in SP. It is by these smoothed profiles that the GCM reacts to the small scale. Will it still be able to produce a reasonable MJO?

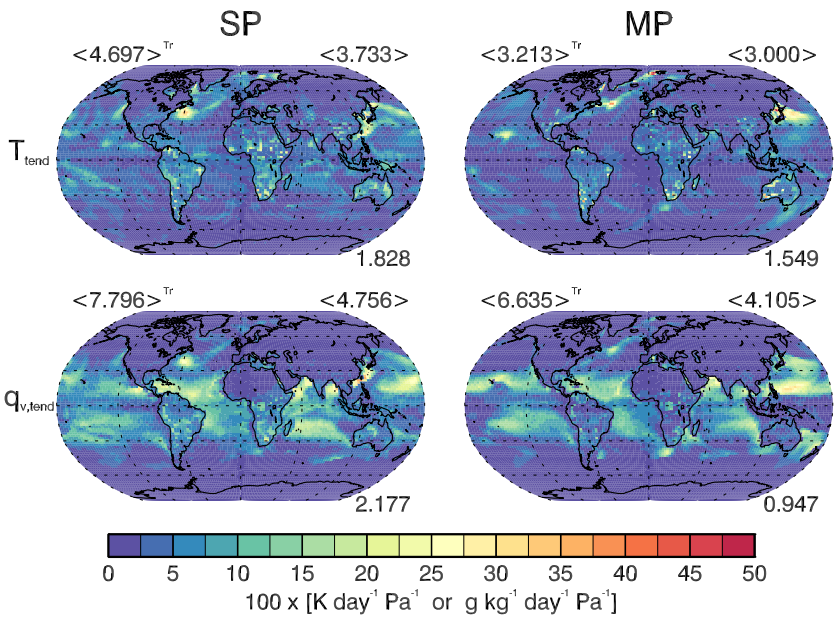

FIGURE 4.47: Time averaged (for one simulated January) jaggedness of the vertical temperature (top row) and specific humidity (bottom row) tendency profiles from the SP single CPM (left column) and MP CPM ensemble average (right column) computed at 15-minute resolution. Numerical values are as described in Figure 4.44.

For the remaining analysis comparing model climates, we focus on model variables in Table 2.1 that are available for both the SP and MP configurations of CAM. For each variable at a selection of pressure levels, the difference between MP and SP were computed annually and seasonally in spatial form. To speed identification of large differences, the root-mean-square-difference normalized by the range of values in SP was used as a guide. These values will not be reported here in full but were very useful in sorting through the many potential model differences. In the case of the spatial comparisons, significant differences (at the 95% confidence level) were calculated based on means testing using a two-sided Student's t-distribution at each location with the assumption of one independent sample per season. This is a rather strict estimation for the number of independent samples, and as such, there is particularly strong confidence in regions identified as being significantly different. Areas meeting this criteria for significant difference in the mean are shaded in subsequent figures.

In addition, global mean time series of the comparable variables were computed and compared. These analyses were subjected to a wider range of tests in order to locate significant differences. The most stringent test assumed one independent sample per year when testing with Student's t-distribution. A consistently less stringent, but likely more accurate, test estimates the effective number of independent samples following the method of Bretherton et al. (1999). This method accounts for the effects of persistence in a time series that would limit the independence of nearby data points. Computation of the effective number of independent samples, n^*, when starting with n data points with a sampling interval of Δt, is based on the lag-1 autocorrelation, r, and is defined in Equation (4.13). These tests were performed comparing the full available data and datasets of equal length where the longer was truncated to match the length of the shorter.

$$n^* = n\frac{1 - r^2\Delta t}{1 + r^2\Delta t} \tag{4.13}$$

Significance tests for differences in the annual mean cycle and for the significance in the correlation of the global mean time series for each variable at a selection of pressure levels and their annual cycles were also performed to investigate potential changed in the timing of the global means. The time series were also compared using the signs test for non-parametric data that do not conform to a normal distribution. Lastly, differences in temporal variance were tested for significance using the F-distribution. More rapid identification of features exhibiting greatest differences was aided by computation of the root-mean-square-difference normalized by the range of values in the SP time series, similar to the process for finding large spatial differences. The data for all of these tests has been retained but is impractical to report in full, as it constitutes greater than 10,000 individual tests.

Even when toying only with the physical parameterizations of a climate model, it is wise to ensure the modifications have not significantly altered the general circulation patterns of the

Earth's atmosphere. With this in mind, the zonal mean of the zonal and meridional flow patterns are compared in Figures 4.48 and 4.49. In most places, the changes in MP zonal wind are a slight magnification and a possible deepening of existing patterns; that is, winds are mostly stronger. The strongest shifts are found at the 100 and 700 mb levels, where they are on the order of 10%. In the global mean (not shown), zonal winds have become more easterly at low levels and more westerly at upper levels. In the case of the meridional wind speed, the changes are less significant in the zonal mean. More significant changes are seen with an enhancement of the low-level inflow and upper-level return flow of the Asian monsoon pattern. While a number of statistically significant changes in the wind patterns were located, the general circulation pattern matches and is stable.

The pattern in zonal wind changes indicates that we should expect to find an enhancement of the equator-to-pole temperature gradient. Indeed, this is the case. Many regions poleward of 60° latitude (especially in the south and near the 200 mb level) are cooler, and significant warming has occurred in the zonal mean at $\pm 15°$ latitude. This is the first figure in which we see some strong model differences at the surface near 60°N; strong differences at this location are present in a number of fields and are the result of a shift in pressure levels over small areas of Siberia and Hudson Bay. They will be ignored as they do not influence any general conclusions in this study and are limited to fields calculated on the 1000 mb level. Temperature increases at 800 mb act to smooth longitudinal variations at the edge of the tropics (Figure 4.51), while increases at 300 mb are more uniform across the whole of the tropics (Figure 4.52), indicating a deepening of the troposphere. This is actually the case, as the global mean tropopause height is about 85 meters higher in MP (Figure 4.53). This difference is not significant with the most stringent test, but it is with all other means tests. Locally, there are increases by as much as 800 meters. Again, the changes are statistically significant, indicative of spatially broad changes, but generally small.

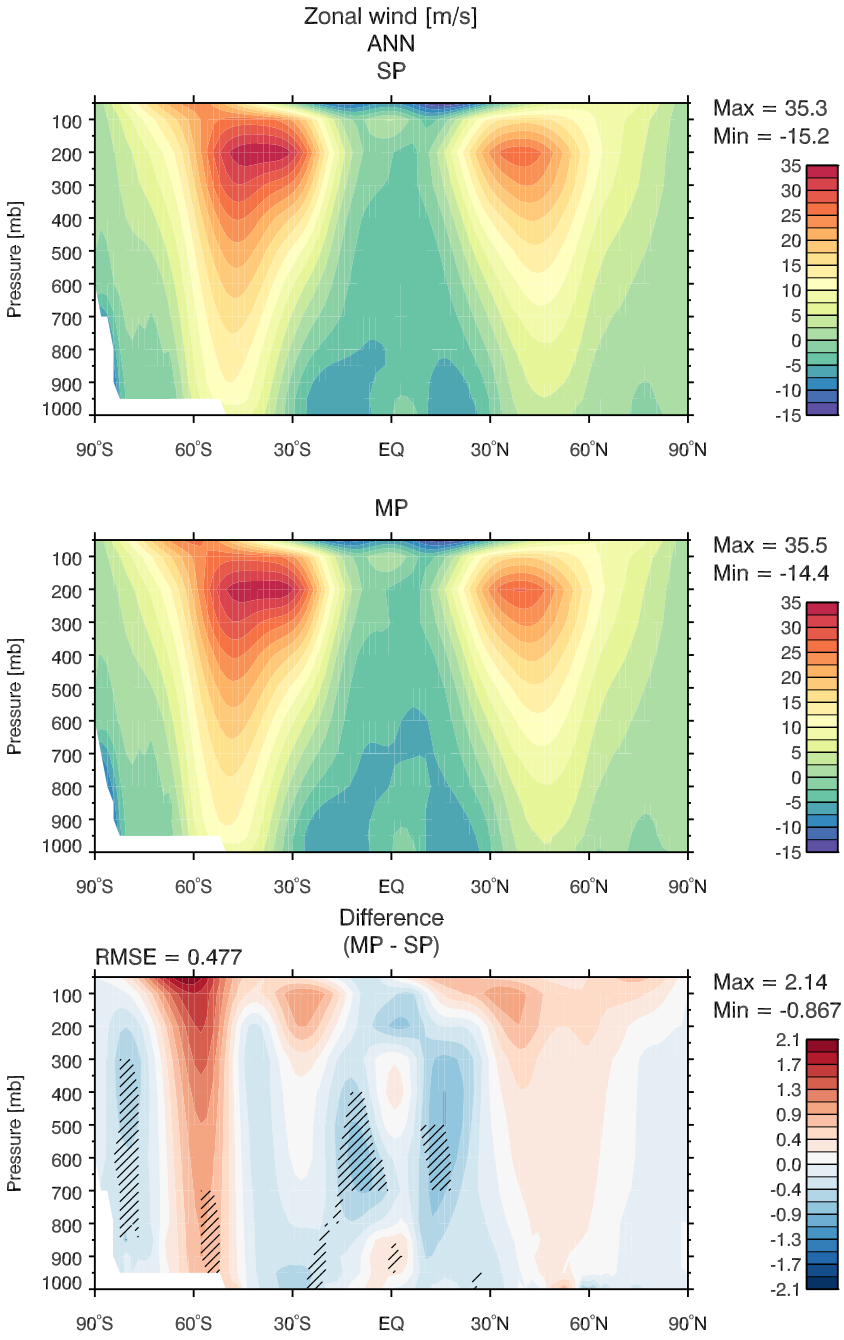

FIGURE 4.48: Annual mean, zonal mean profile of the zonal wind speed for SP (top), MP (middle), and the MP-SP difference (bottom). Diagonal black lines indicate significant differences as described in the text.

Changes in the specific humidity are shown in Figure 4.54. Most of the significant changes are confined to the tropics, with increases at low levels off the equator, decreases aligned above those, and stronger, statistically significant increases above 700 mb. The upper level increases

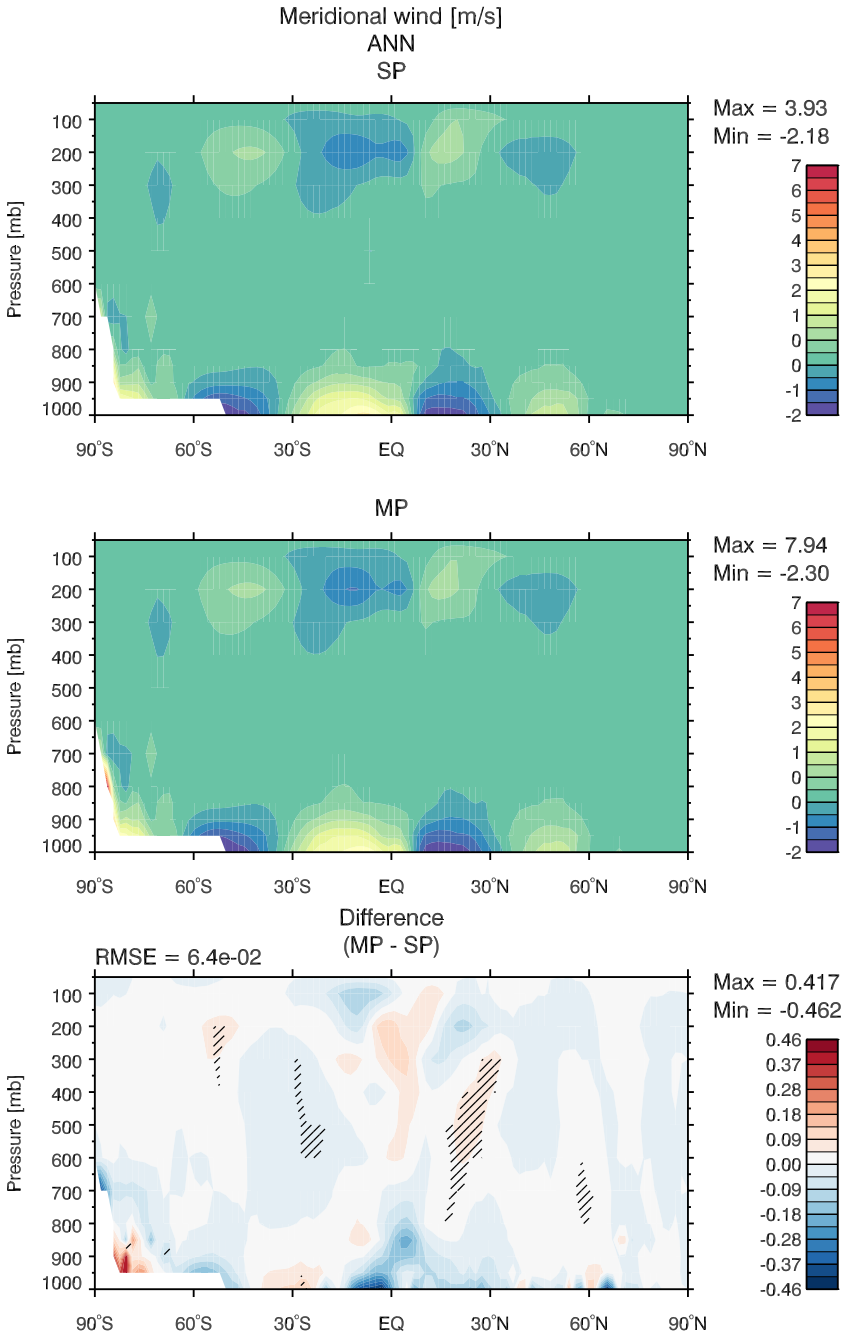

FIGURE 4.49: As in Figure 4.48 but for the meridional wind speed.

appear to track with the previously displayed temperature increases. There is clearly structure to these changes, in agreement with earlier indications of a deepening tropical troposphere. In fact, the changes in the specific humidity make it look as though the change to MP has caused the contents of the atmosphere have been relocated aloft.

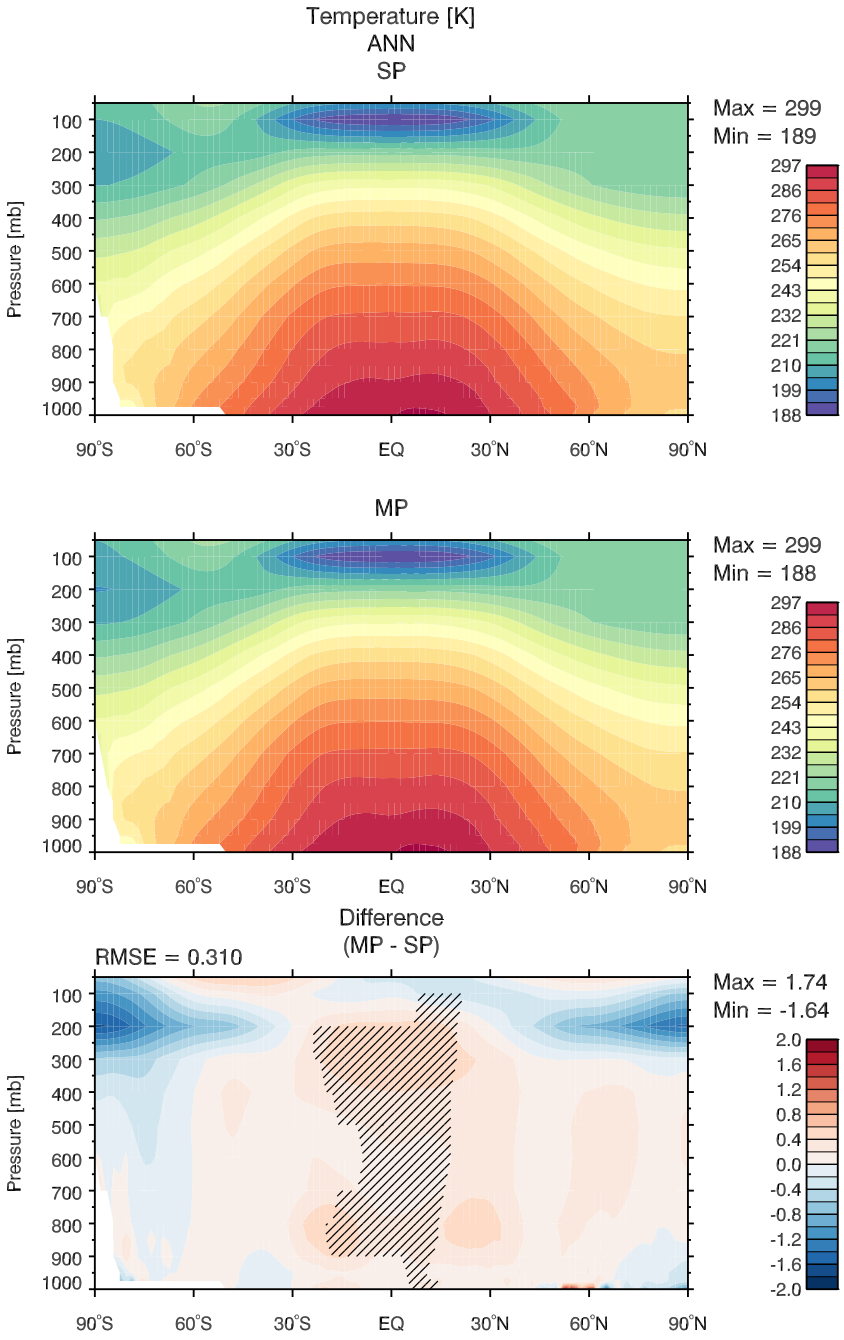

FIGURE 4.50: As in Figure 4.48 but for temperature.

The main interest in this work, though, is what happens to precipitation, and in the case of MP, we are referring to the CPM ensemble mean precipitation. By providing each GCM column with 10 CPMs instead of one, we give the column more chances to produce precipitation. As such, the global mean precipitation frequency increases from 59-64% to 71-76%, a very strong

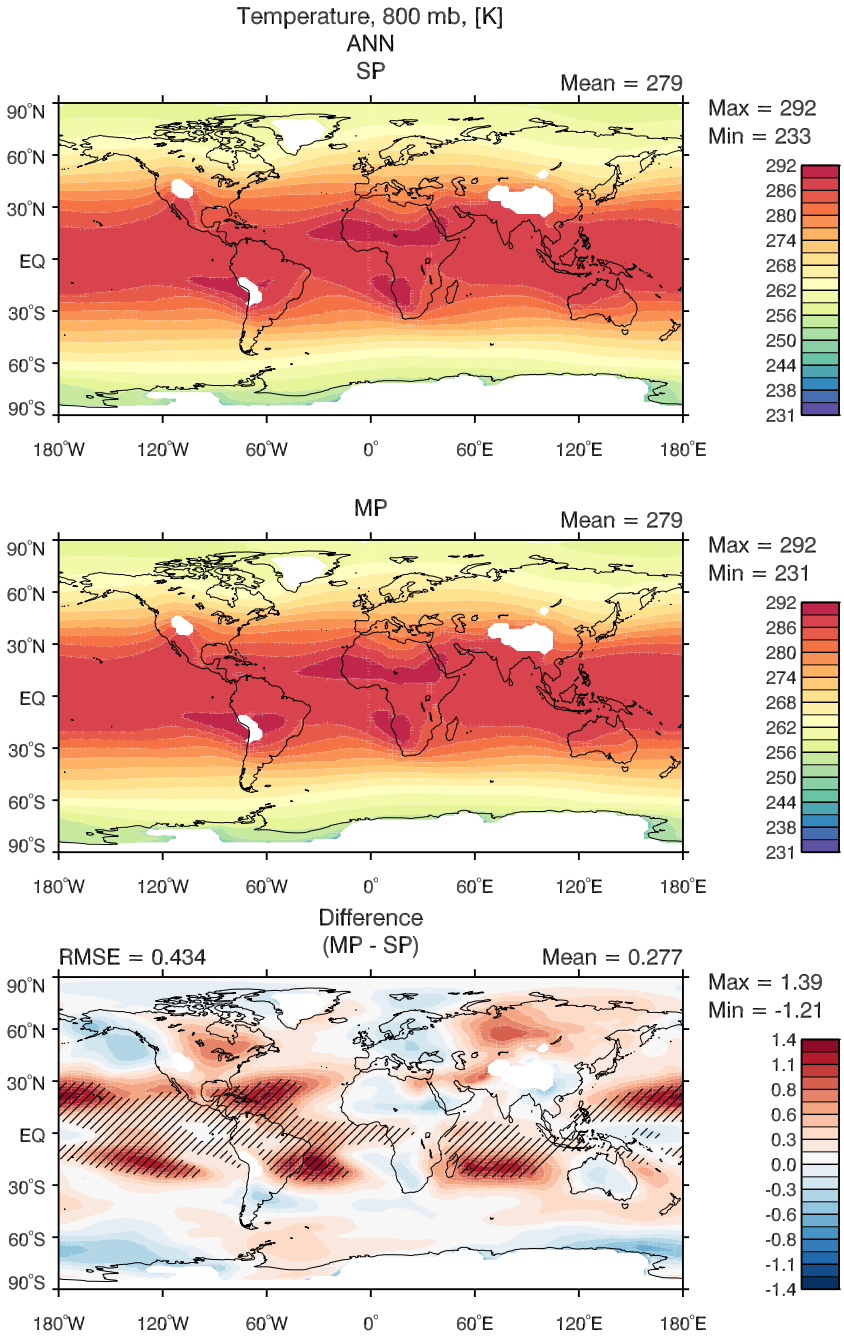

FIGURE 4.51: Annual mean temperature at 800 mb for SP (top), MP (middle), and the SP-MP difference (bottom). Diagonal black lines indicate significant differences as described in the text.

change that is persistent across all seasons and is significant by all measures (Figure 4.55). The increase is generally constant function of latitude with little variation longitudinally. The difference is maximized in the tropics, with nearly zero change in the polar regions (Figure 4.56),

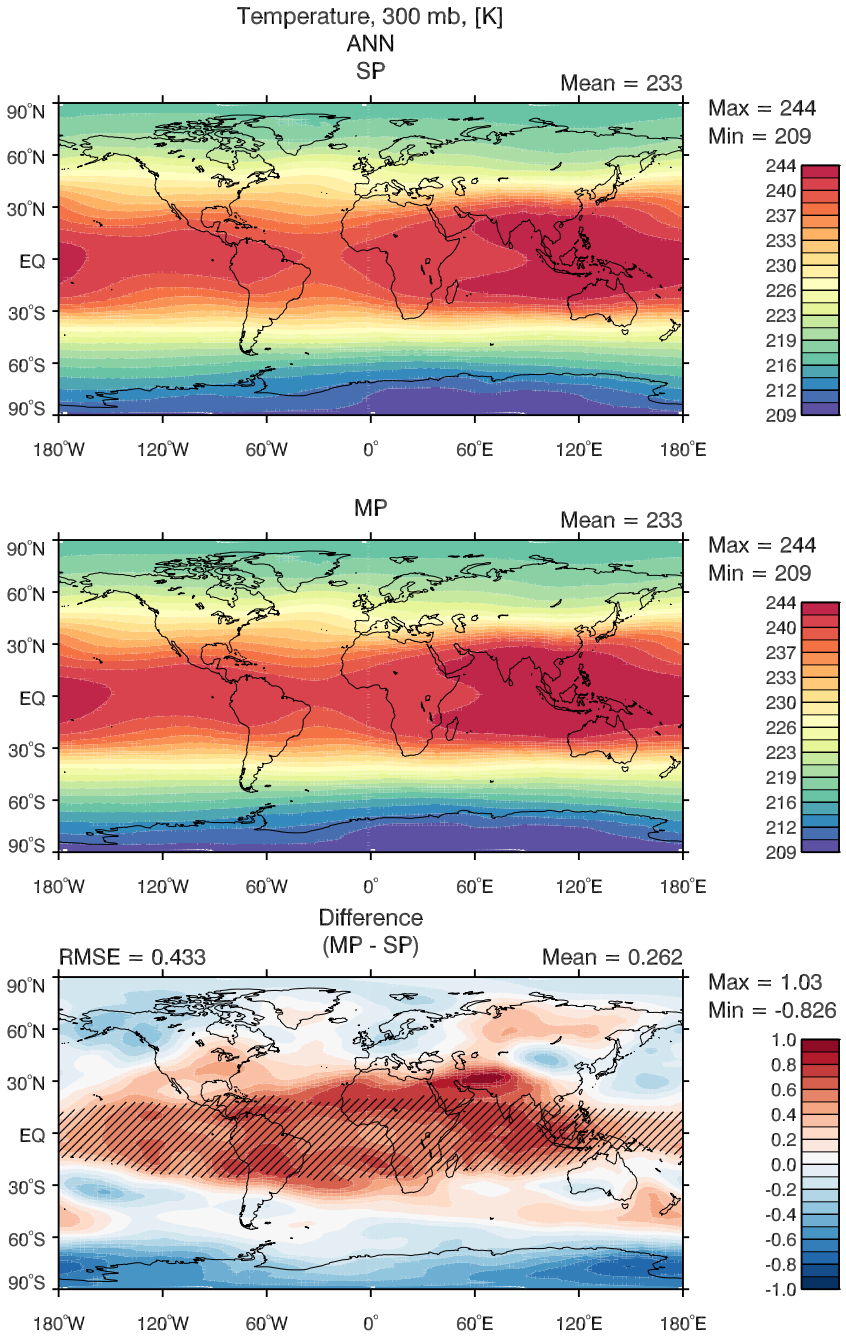

FIGURE 4.52: As in Figure 4.51 but at 300 mb.

where we have already seen the tendency for MP CPMs to most often agree to produce precipitation persistently. The change is hemispherically asymmetric, with the greatest increase occurring near 30°S.

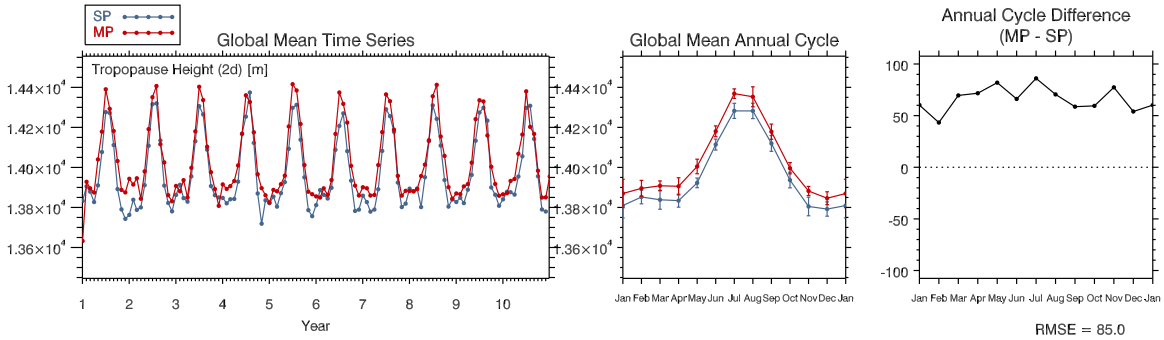

FIGURE 4.53: Global mean statistics for tropopause height as labeled.

Though precipitation falls more frequently, the global mean precipitation is slightly lower (approximately 0.07 mm day^{-1}, or 2%) in MP (Figure 4.57). That difference is statistically significant with all testing measures. Spatially, this small difference is distributed most prominently through the tropical region (Figure 4.58). While to total change is negative (maximum magnitude -3.23 mm day^{-1} in the western Pacific), there are a few weaker regions of precipitation increases (maximum magnitude 2.56 mm day^{-1}), some of which are statistically significant over the central equatorial Pacific. Viewed seasonally, the major decreases follow the ITCZ's deep convection. As an interesting side note, the conventional physics parameterization from CAM runs in the background of the superparameterized simulations, calculating convective responses to changes in the GCM state and writing output without feeding back onto the simulation. With the state as modified going from SP to MP, the Zhang-McFarlane deep convective scheme also suggests a reduction in heavy convective precipitation. In the global mean, the difference is approximately 0.25 mm day^{-1}, and still further reductions are suggested by the shallow convection scheme.

In the previous discussion of standard deviation fall-off ratios, we saw that the process of averaging tends to reduce the frequency of extreme values. Figure 4.59 shows the daily mean precipitation PDFs for the full-length SP and MP datasets in the tropics. There is a clear reduction in the fraction of high precipitation rates in comparison to SP with an increase in the frequency of precipitation between 1 and 10 mm day^{-1}. The reduction in dry days (Table 4.4) that one

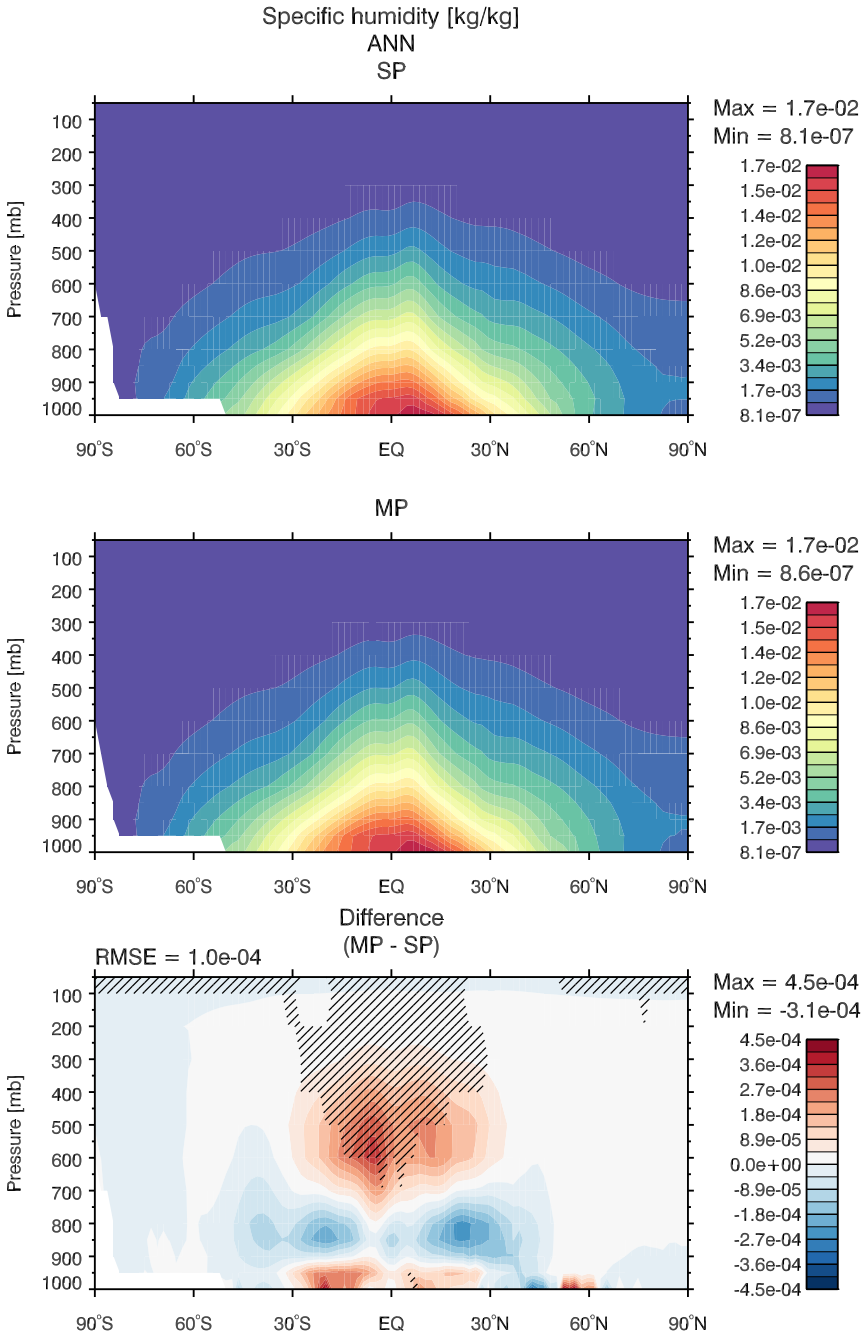

FIGURE 4.54: As in Figure 4.48 but for specific humidity.

might expect is less pronounced, as individual CPMs produce many more such dry days over the tropical oceans than the single SP CPM. The daily mean precipitation PDFs as a function of latitude in TRMM, GPCP, CAM, SP, MP, and MP.1 are shown in Figure 4.60. Here, we can see the way the same differences as in the previous figure, as well as the enhancement of the

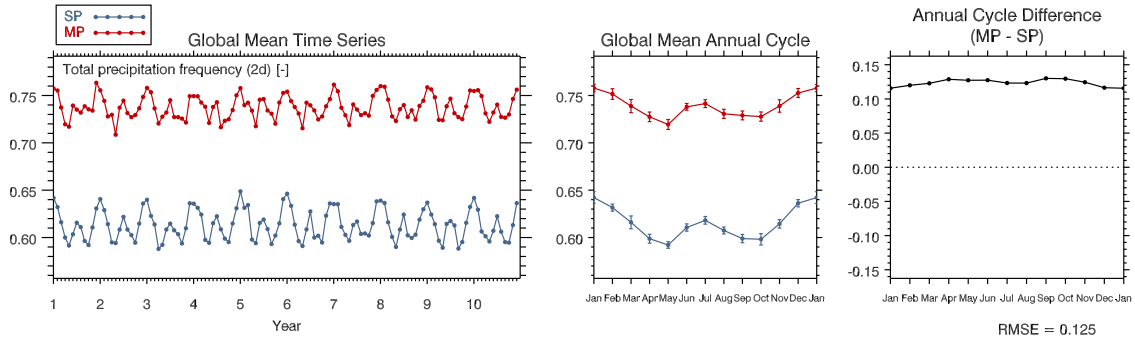

FIGURE 4.55: Global mean statistics for precipitation frequency as labeled.

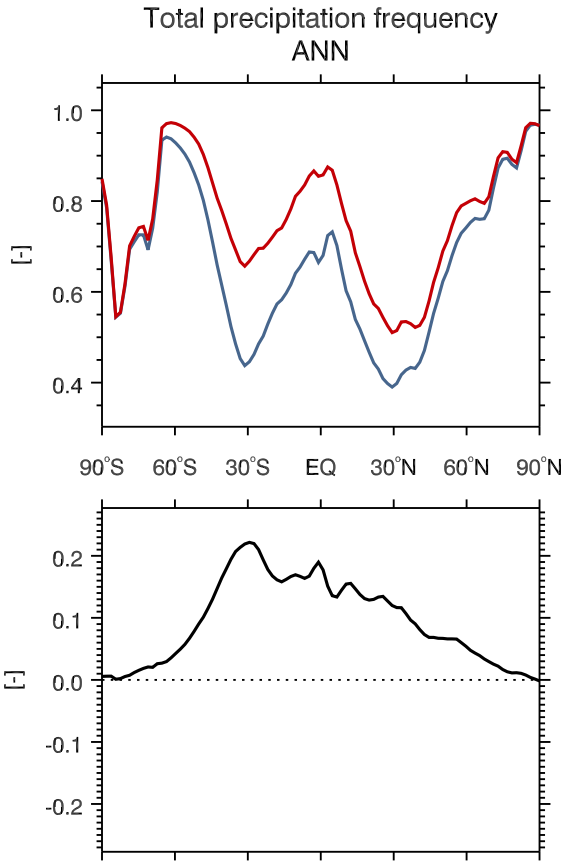

FIGURE 4.56: Zonal mean of the annual mean precipitation frequency for SP (blue) and MP (red) (top) and their difference (bottom).

extreme tropical precipitation values in MP.1. The anomalous-looking spike at about 30°N in the model data is due to excess precipitation over the Himalayas. Figure 4.61 shows how these changes are distributed spatially. Light precipitation areas are mostly concentrated in the tropics

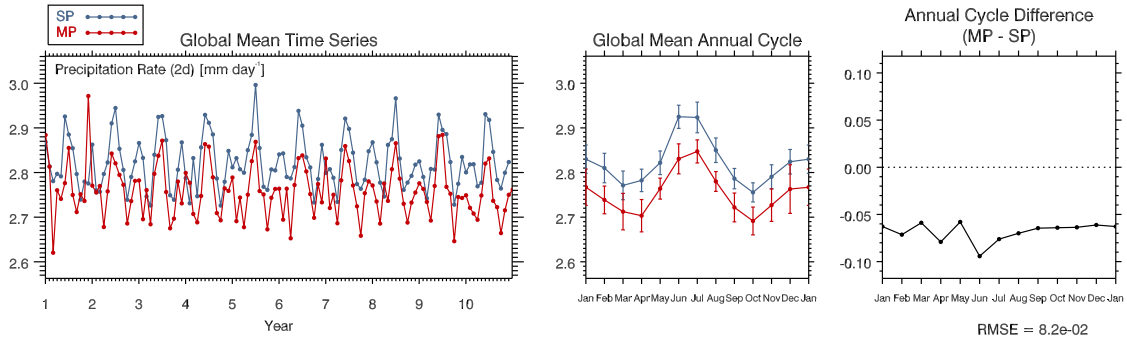

FIGURE 4.57: Global mean statistics for precipitation rate as labeled.

over the Indian Ocean, across the maritime continent and into the central Pacific, with a notable local maximum off the eastern coast of Brazil. The reduction in heavy precipitation is fairly uniform across the whole of the tropics. Despite the noted changes, SP and MP are quite similar in their latitudinal discretization of precipitation PDFs in comparison to the other datasets. In fact, it is a little surprising, given the initial intentions of the MP configuration, that the PDFs do not look more like those from CAM. It is clear from the MP.1 PDFs that the ensemble CPMs are behaving differently than the SP CPM. Specifically, they produce many more extreme values at all latitudes.

TABLE 4.4: Percentage of dry days (precipitation less than 0.1 mm day^{-1}) in each dataset. Data is for the regions: global, Tropical (20°S to 20°N), and TRMM (50°S to 50°N).

	Global	**Tropical**	**TRMM**
TRMM	-	38.4	45.9
GPCP	47.7	45.6	48.2
CAM	25.1	16.1	24.2
SP	30.1	22.9	30.1
MP	30.0	22.8	29.6
MP.1	40.7	49.8	48.4

Next, we will explore cloud features. As the most direct measure of cloud in the model, Figure 4.62 shows the annual zonal mean of grid box averaged cloud liquid and ice. Significant

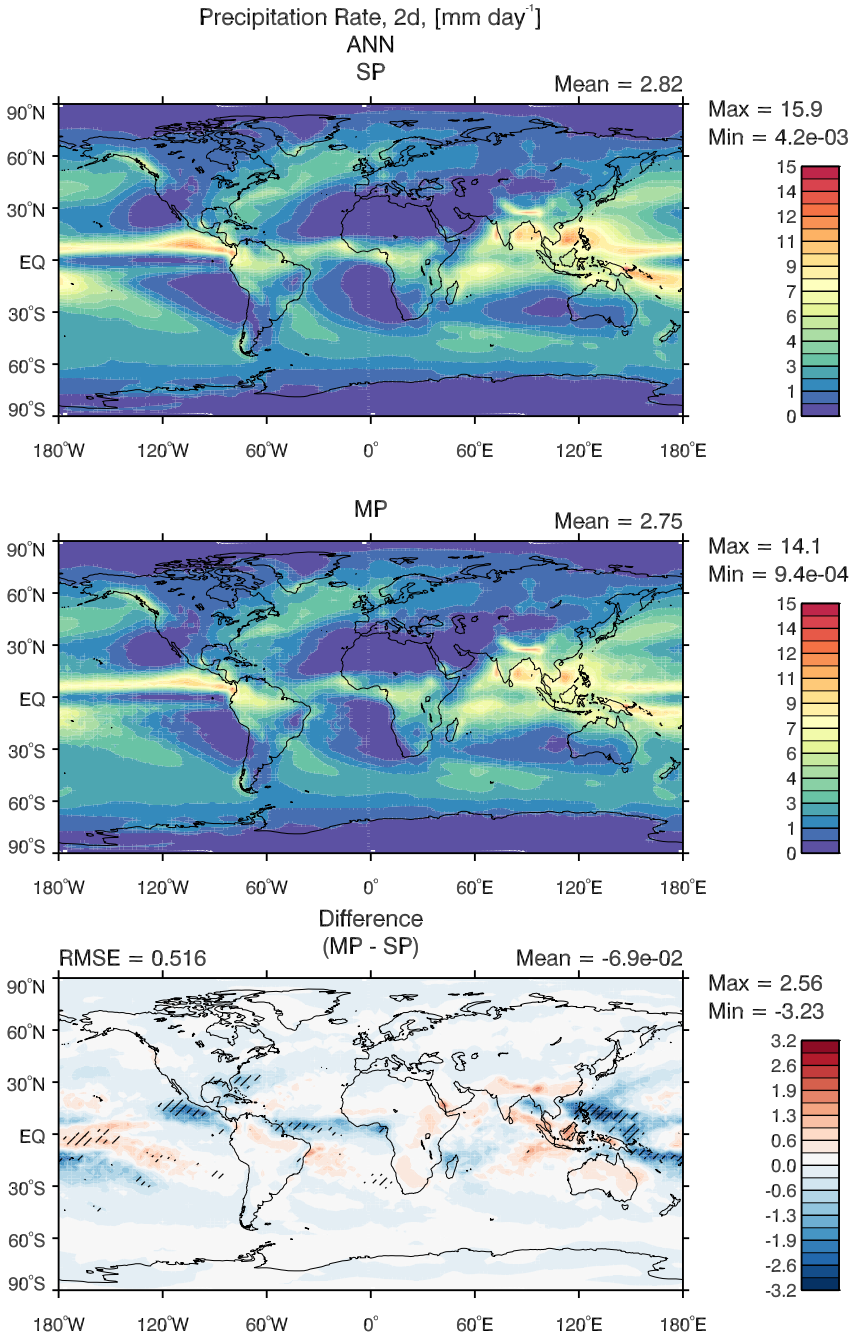

FIGURE 4.58: As in Figure 4.51 but for precipitation rate at the surface.

changes include a reduction in both cloud liquid and ice at lower levels, and an increase in cloud ice above 300 mb, with both of these changes focused in the tropics. The decrease in liquid cloud is slightly stronger in the southern hemisphere than in the north. Additionally, this reduction is strongest and most statistically significant over the oceans. It is mostly absent over land except

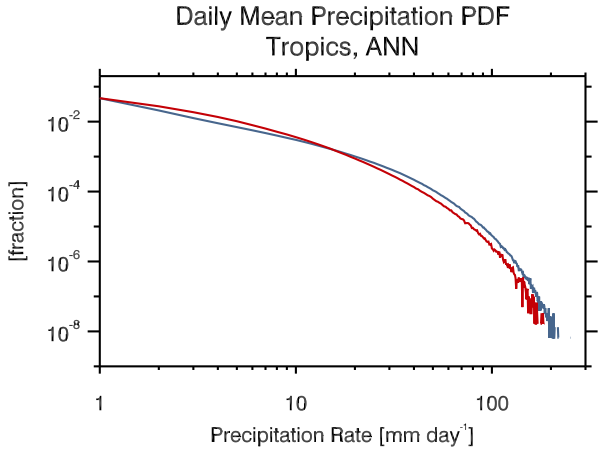

FIGURE 4.59: Daily mean precipitation PDFs for SP (blue) and MP (red).

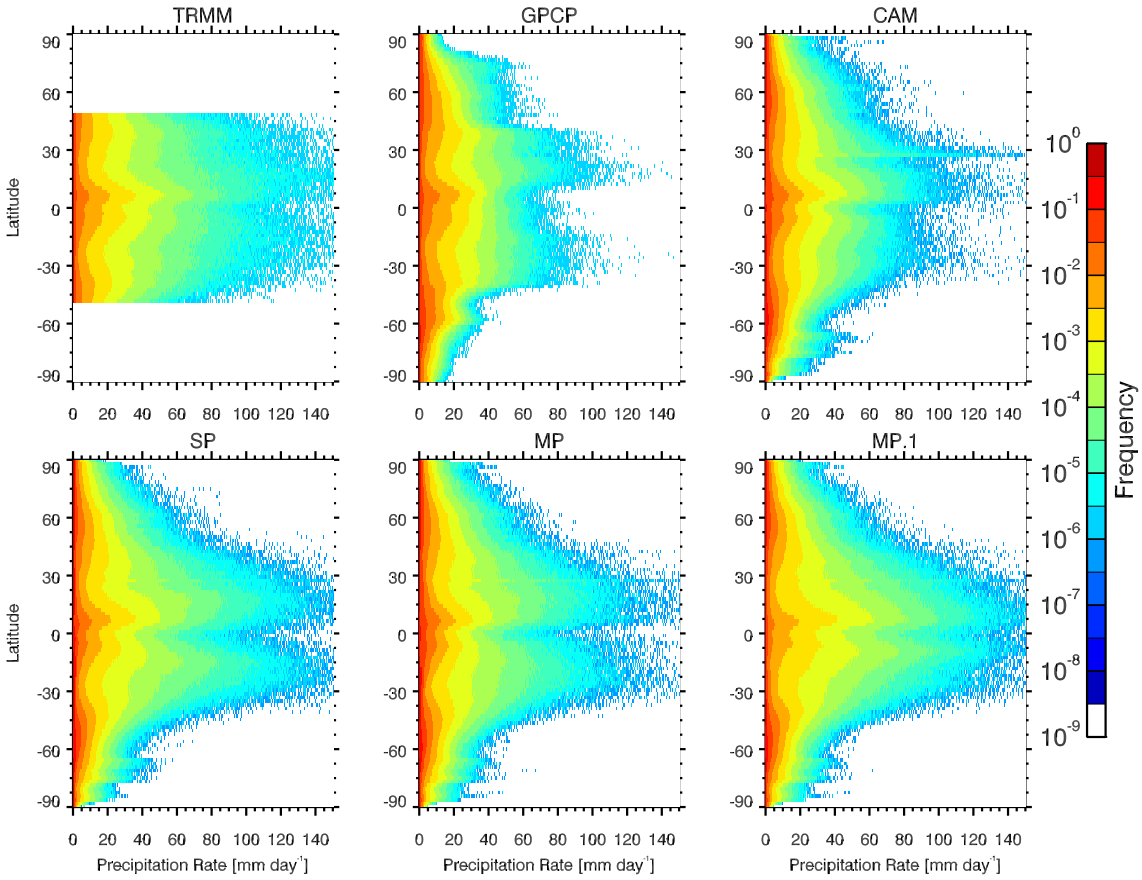

FIGURE 4.60: Daily mean precipitation PDFs as a function of latitude for the noted observational and model datasets.

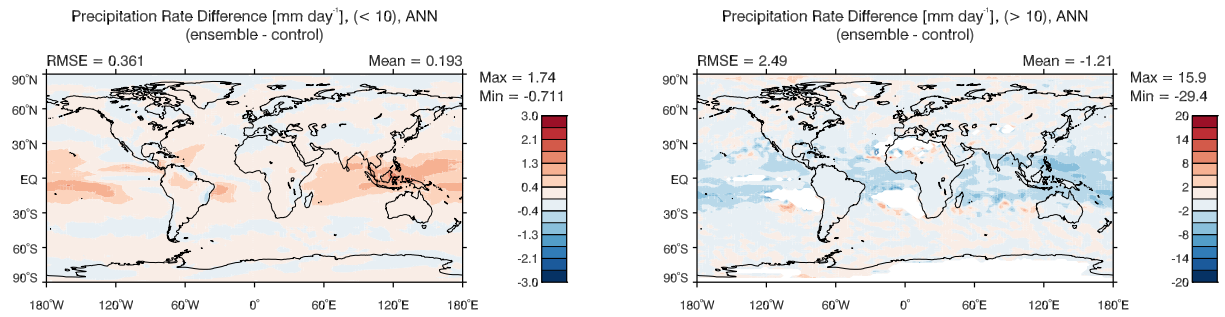

FIGURE 4.61: The precipitation rate difference between MP (ensemble) and SP (control) where rates are less than 10 mm day^{-1} (left) and where rates are greater than 10 mm day^{-1} (right).

for regions with common deep convection and bypasses the coastal stratus decks, as well. Mid-level reductions in cloud ice are mostly significant because there was so little in that location to begin with. Increases in cloud ice are isolated in regions of strongest deep convection over both land and ocean.

Model diagnostics define low, middle, and high cloud for the ranges surface-700 mb, 700-400mb, and above 400 mb, respectively. Mid-level cloud amounts are statistically unchanged in the global mean; however, they do change by up to $\pm 6\%$ along the ITCZ in the annual mean, with decreases across the Atlantic and western Pacific and increases across the Indian Ocean. The annual mean geographic distribution and differences for low and high clouds are shown in Figure 4.63. The difference in the global mean time series for both of these variables is statistically significant according to each testing method. Low cloud amount drops from a global mean of 32% to 30%. Local reductions in low cloud fraction in the tropics, which correspond to the reductions in cloud liquid in Figure 4.62 exceed 10%. Similarly, these are areas common to deep convection and fair weather cumulus and marine stratocumulus away from the coasts. These are areas where low cloud amount is at a relative minimum over the oceans in SP, so this has become more exaggerated in MP. Globally averaged high cloud amount increases in the annual mean from 26.6% to 28.9%, roughly the same fraction change as low cloud amount. Similar to

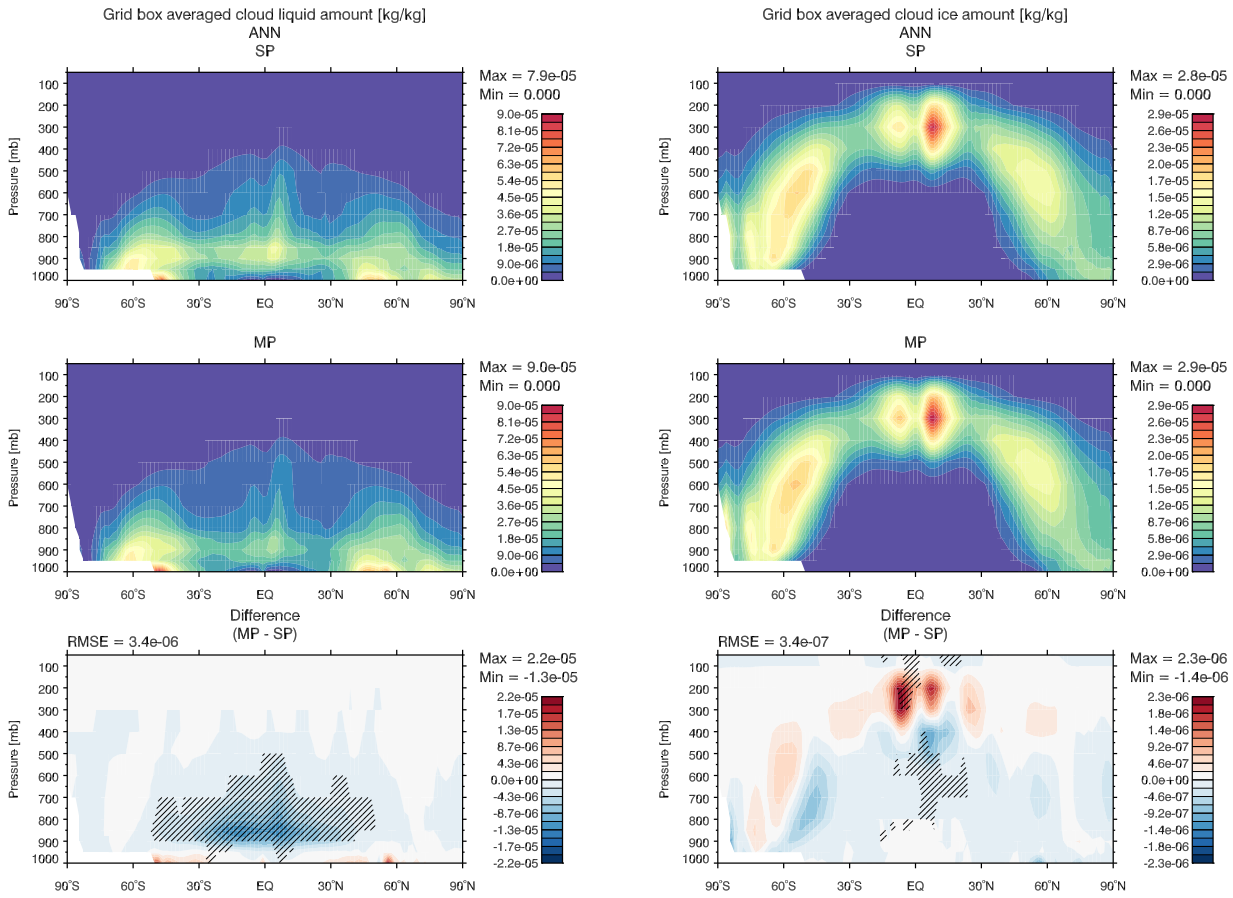

FIGURE 4.62: As in Figure 4.48 but for grid box averaged cloud liquid (left) and ice (right).

the pattern of change in low cloud amount, the high cloud amount tends to increase where high clouds are prevalent in SP, and they decrease, though not as strongly or with particular significance, where high cloud amount in SP displayed local minima. Matching the change in high cloud is the pattern for total precipitable water, which increases very slightly in the global mean, but significantly where there has been an increase in high cloud amount. Cloud water path (liquid and ice), though, follows the loss of low cloud, as liquid water path losses heavily outweigh gains in ice water path, which only barely register as being statistically significant. All of these patterns hold regardless of season. With respect to clouds, we are seeing an another vertical shift in the broad mean state of the atmosphere. Each extreme appears to be just a little more exaggerated,

but the measure of global total cloud fraction is only slightly changed, with only one measure counting statistical significance to the global mean increase of about 0.2%.

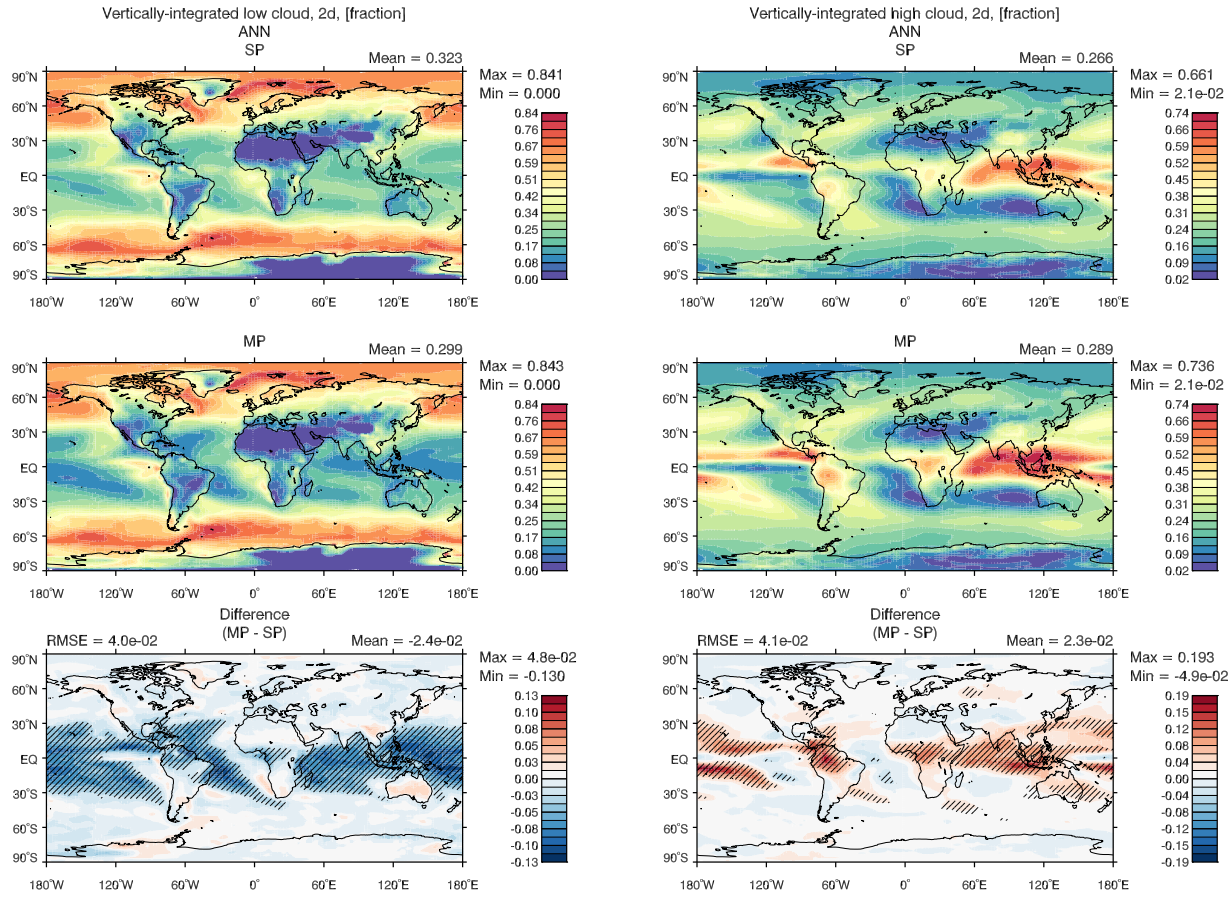

FIGURE 4.63: As in Figure 4.51 but for vertically-integrated low (sfc-700 mb, left) and high (above 400 mb, right) cloud amount.

Since low clouds act radiatively to cool, and high clouds act to warm, the loss of low clouds and gain of high clouds work in the same direction in terms of the cloud radiative effect, the difference between the radiative energy budgets of clear-sky and all-sky conditions. Globally, shortwave cloud forcing increases by about 3 W m^{-2} in association with areas of low cloud loss, and longwave cloud forcing increases by just short of 2 W m^{-2} alongside high cloud increases. Because of these increased radiative effects, the atmosphere is cooling less in MP than in SP. Since atmospheric cooling by radiation will ultimately be balanced by condensational heating

from the formation of precipitation, precipitation must be lower. The decrease in global mean precipitation, then, is a result of the changes in the cloud field. So what caused the change in the cloud field?

Just as we had to consider the effect of ensemble averaging on precipitation in order to understand the changes in the frequency of occurrence in its extremes, the same must be done for the physical tendencies. Not only are they smoother in time and in the vertical, their extremes must be diminished through the ensemble averaging procedure. Figure 4.64 shows the annual zonal mean for the temperature and specific humidity tendencies from the CPM level in SP and MP and their difference. In the simulation average we see the expected form of what physical parameterizations on the cloud scale are designed to do. By creating precipitation in response to an instability, they warm and dry the troposphere via condensation processes and remove thermal and moisture perturbations near the surface. Both SP and MP are accomplishing this task, but since the MP tendencies are derived from an average, there is a complication.

Within the regions where low clouds were most strongly reduced, SP already had few low clouds, and the areas were actually often dominated by high cloud (Figure 4.63). When the CPM ensemble runs in those locations, some members become representative of the high and/or high and low clouds and others are more representative of only the low clouds. In taking the average of their physical tendencies, those aloft are reduced. This can be seen as less drying and heating in Figure 4.64. What cannot well be seen in Figure 4.64, however, is anomalously (compared to SP) drying and heating at the level of the low clouds (Figure 4.65) within these specific regions. This enhanced tendency at low levels spurs low-level convergence that can be seen in annual mean low-level wind and pressure velocity fields.

Further associated with these regions are surprisingly large values of cloud mass flux within the CPMs (Figure 4.66). The peak difference in the annual zonal mean is nearly 25% greater than

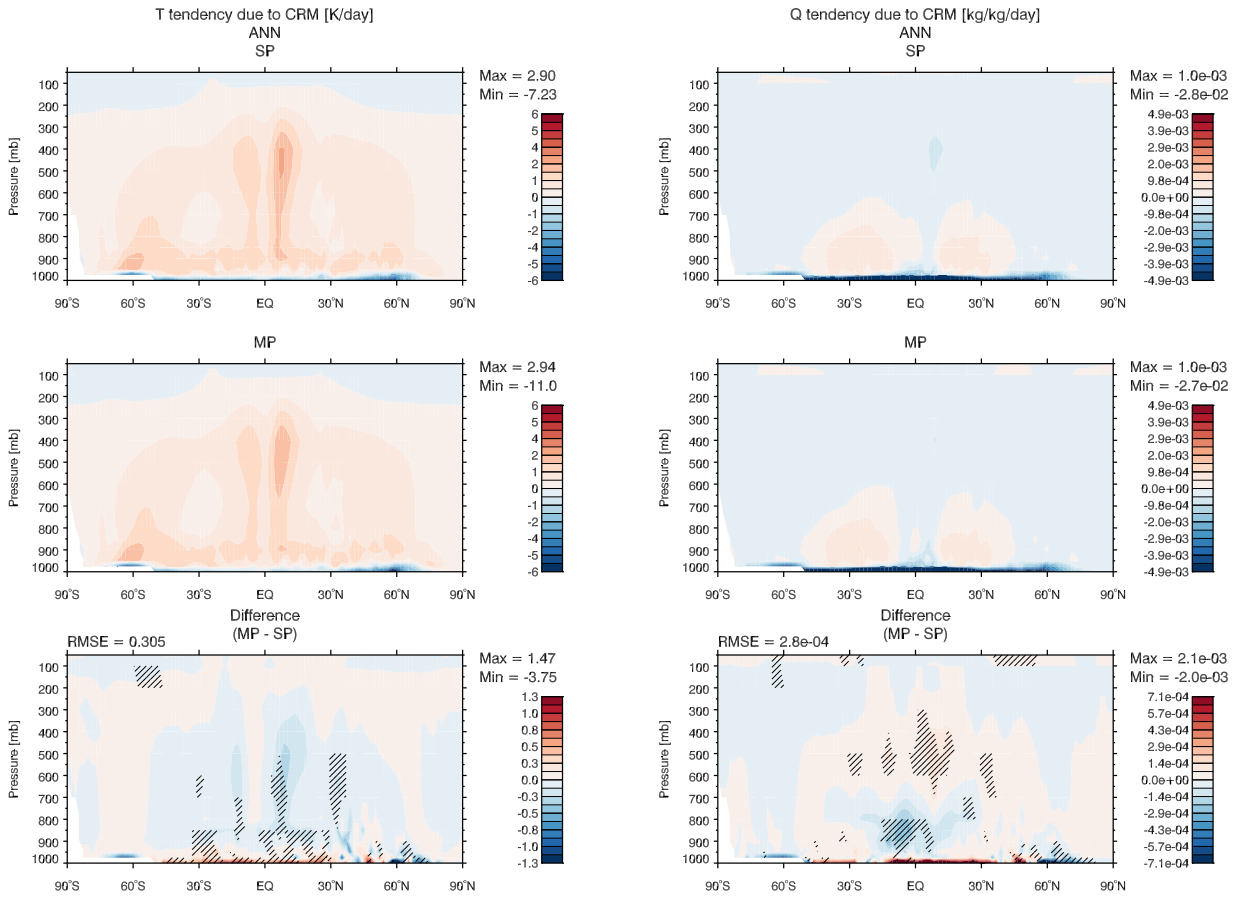

FIGURE 4.64: As in Figure 4.48 but for CPM physical tendencies of temperature (left) and specific humidity (right).

that in SP. This is the strongest relative change in any annual mean, zonal mean variable in the analysis. Relatedly, there is a coincident increase in CPM total kinetic energy at the same locations. The effect of these additional vigorous motions is to mix out the low clouds and strengthen deep convection. Once the low clouds are removed, the regions are subjected to additional surface solar receipt, which aids in sustaining the preexisting deep convection with greater vigor than in SP, giving us the increase in high clouds. Detailed looks at both model runs from equivalent initial conditions shows that these features reach their full climatological differences in under a week's time, with the reduction in low cloud and the increase in high cloud being apparent after two days. As part of the interestingly tangled web, evaluation of the CPM-level data shows that

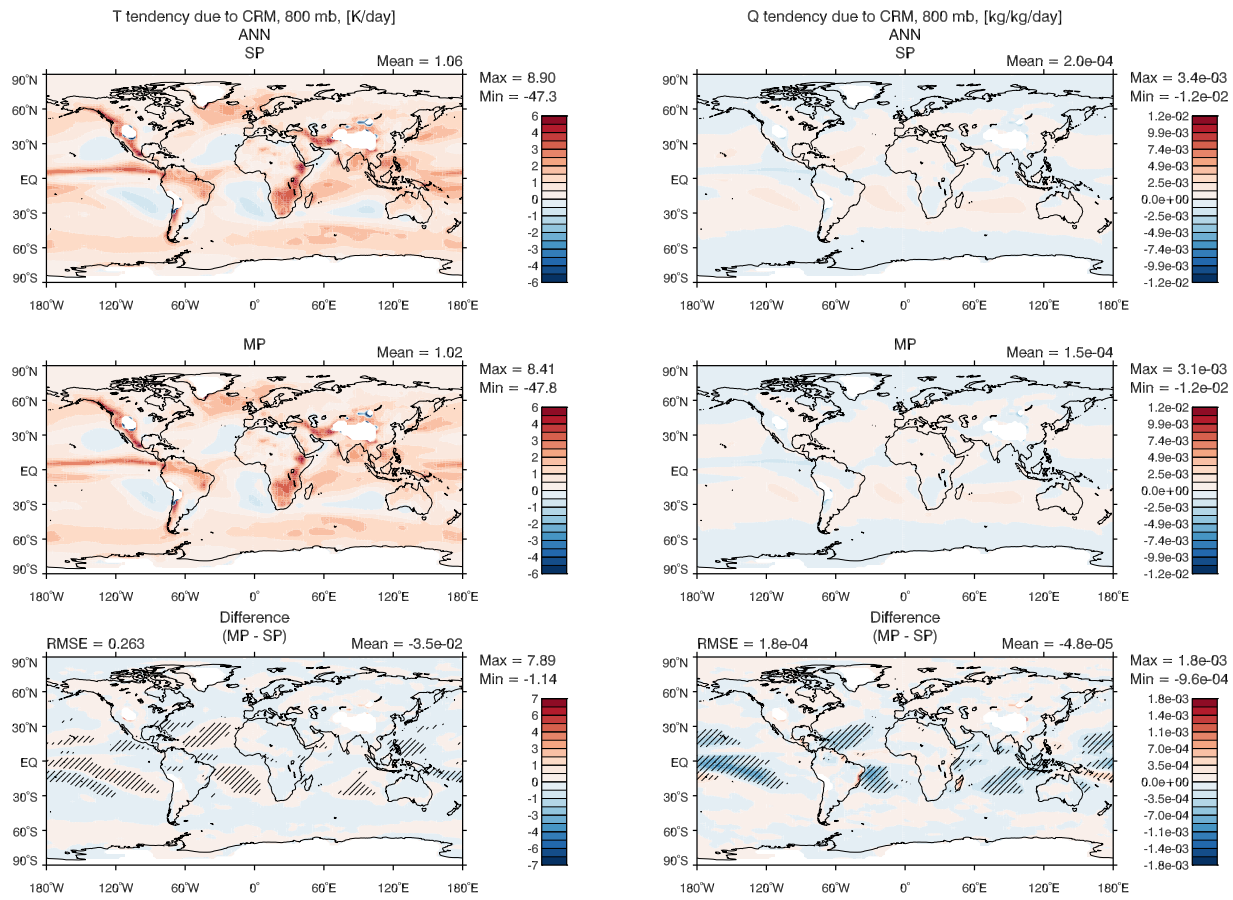

FIGURE 4.65: As in Figure 4.51 but for CPM physical tendencies temperature (left) and specific humidity (right) at the 800 mb level.

nearly all precipitation increases are derived from the deeper clouds, though the mean rates have slowed compared to SP, and nearly all precipitation reductions occur in clouds below 400 mb.

Despite a variety of statistically significant shifts in model climatology following the implementation of the MP framework, the changes do not represent a wild departure from SP or from other models in general. Of particular interest here is that MP shows at least some measurable reduction in variability from the physical parameterization that makes it an arguably more deterministic model than SP, as intended. In addition to the changes in the climatology, we are interested to learn what effect this may have had on known relationships regarding convection and variability.

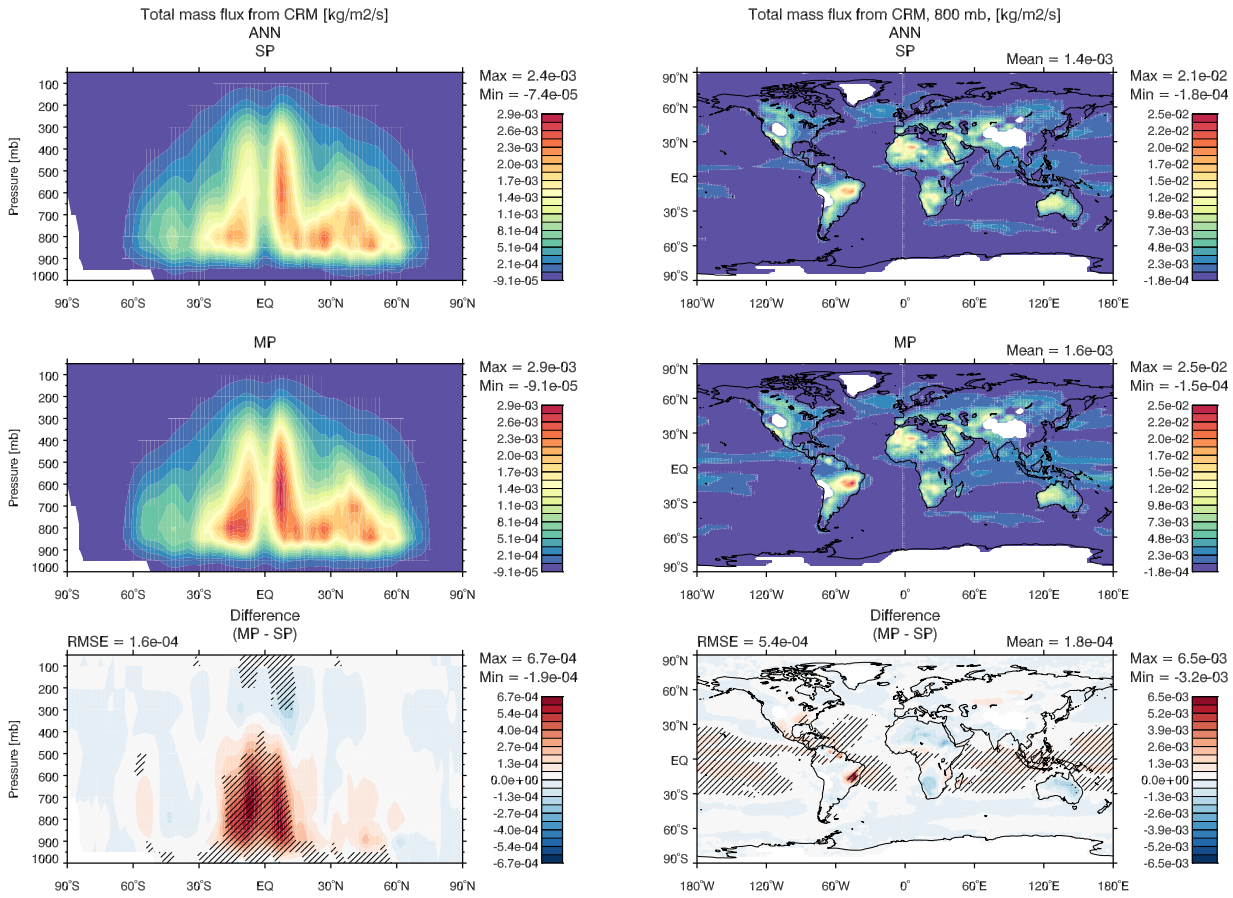

FIGURE 4.66: As in Figures 4.48 and 4.51 but for the zonal annual mean of CPM cloud mass flux (left) and the annual mean at the 800 mb level (right).

While investigating the relationship between the large-scale and convective-scale states in observations and models in the area of Darwin, Australia in order to strengthen foundational assumptions regarding and formulations of convective parameterizations (Peters et al. 2013), the relevant questions revolve around how subgrid-variability should be represented and which large-scale variables should be the input to the convective parameterizations. Peters et al. (2013) and Davies et al. (2013) made note of the fact that the variability of convection scales more slowly than the mean. That is, convection tends to be more variable when forcing from the large scale is weak, a feature also recognized by Jones and Randall (2011). Davies et al. (2013) note

that even the strongest large-scale relationships to convective activity, such as moisture convergence and convective rain area, show considerable scatter in observational data. This results provides confirmation of what is known empirically by tropical forecasters, that tropical convective storms are more easily predicted when embedded into large-scale dynamical features, such as a monsoon pattern or the MJO.

The authors raise concern about this relationship because it is inconsistent with a number of existing physical parameterizations with stochastic elements, which simply use multiplicative noise (Buizza et al. 1999; Teixeira and Reynolds 2008). The implication there is that such stochastic parameterizations may be incorrectly representing this variability. Peters et al. (2013) found a similar relationship and made a similar argument. In fact, Peters et al. (2013) ran tests with a stochastic mulitcloud model and found the convective variability at low forcing to be weaker than observations, though they do suggest that modifications to the formulation of the model, such as making it prognostic or obtaining guidance from observations with higher temporal resolution, may improve the representation of the relationship.

Seeming nearly offended at the accusation, stochastic parameterization enthusiasts Watson et al. (2014) provide an analysis of these relationships in the ECMWF IFS using multiplicative-noise stochastic physics, stating, "Finding that the stochastic scheme used operationally at ECMWF is incapable of representing convective variability would be highly important." By focusing on 500 mb relative humidity and vertical velocity as measures of large-scale forcing, they produced bin-averaged representations of the mean, standard deviation, and their ratio (COV) of precipitation for a wet season over Darwin, much as in Peters et al. (2013). This was performed for the model with deterministic and stochastic parameterizations as well as for variational analysis data (combined observations and model). The results from their Figure 1 are reproduced here in Figure 4.67. The designer of this plot must have had as a basic premise, "Flip everything."

The vertical axis is (1 - relative humidity), and the horizontal axis is negative pressure velocity. Essentially, weak forcing is found toward the upper left, and stronger forcing is found toward the lower right. Color bar choices in the mean and standard deviation panels do not helpfully identify what is shown in the COV panels, which is the variable scaling of the variability with the mean. The authors have shown that both the deterministic and stochastic versions of their model do qualitatively reproduce the relationship found in the variational analysis. They go on to explain that much of the modeled variability arises from nonlinearity within the deterministic part of the convection scheme.

To verify that this relationship is present in MP, the analysis has been reproduced as closely as possible. The results obtained using 3-hourly data near Darwin for single sample months of January and July are presented in Figure 4.68. While all data sources from Watson et al. (2014) are similar to one another, the results from MP most closely match the forms from their variational analysis, especially for the July data. This is particularly encouraging as is shows that for at least one rather specific metric, the MP framework does have the ability to capture important convective relationships. However, we must not take the values here as any broad, supreme authority due to their restricted nature. In fact, expansion of the analysis to the entirety of the tropics yields only qualitatively similar results, with the scaling of variability with forcing being slightly more proportional on average than at Darwin. Unfortunately, data from SP and CAM are not available at the appropriate temporal resolution to repeat this exact analysis.

Of further interest to Davies et al. (2013), Peters et al. (2013), and Watson et al. (2014) were general relationships between precipitation and large-scale energetics and stability parameters, such as CAPE, convective inhibition, convergence, and stability indices. Again, these relationships were explored in order to better formulate convective parameterizations. Davies et al. (2013) noted strong relationships with dynamical variables, such as moisture convergence and

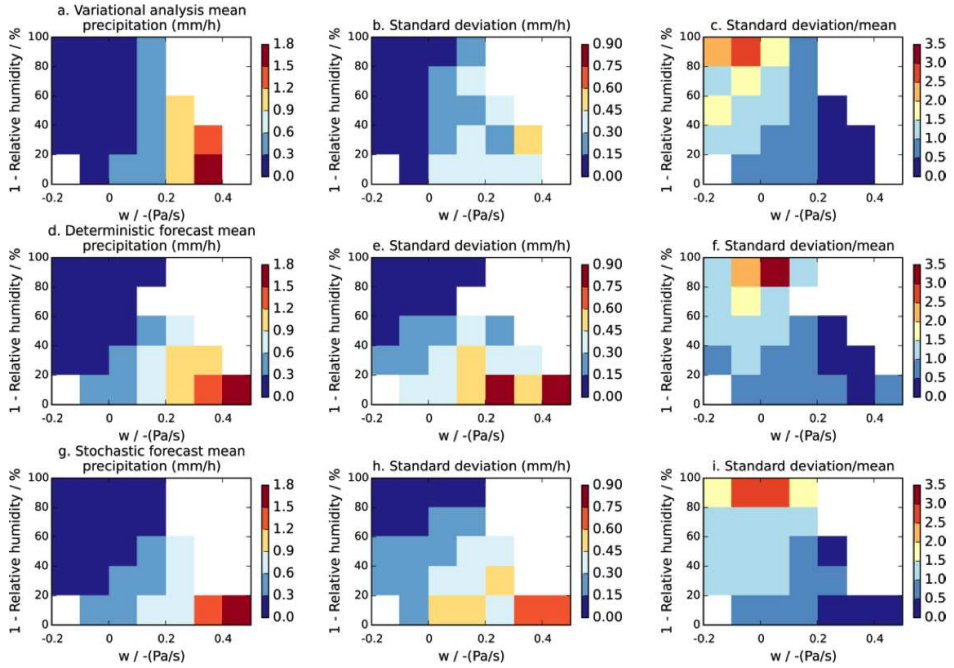

FIGURE 4.67: Caption as in Watson et al. (2014): . (a)-(c) The relationship between Darwin-mean total precipitation and $\overline{w}$ and (1 - $\overline{RH}$) in the variational analysis, (d)-(f) the deterministic control IFS forecasts, and (g)-(i) the stochastic perturbed IFS forecasts. For data binned according to $\overline{w}$ and (1 - $\overline{RH}$) (left) the mean precipitation, (center) the standard deviation of precipitation in each bin, and (right) the ratio of the standard deviation to the mean. Data are plotted only for bins with at least 10 data points. Both types of IFS forecast reproduce the observed relationships well.

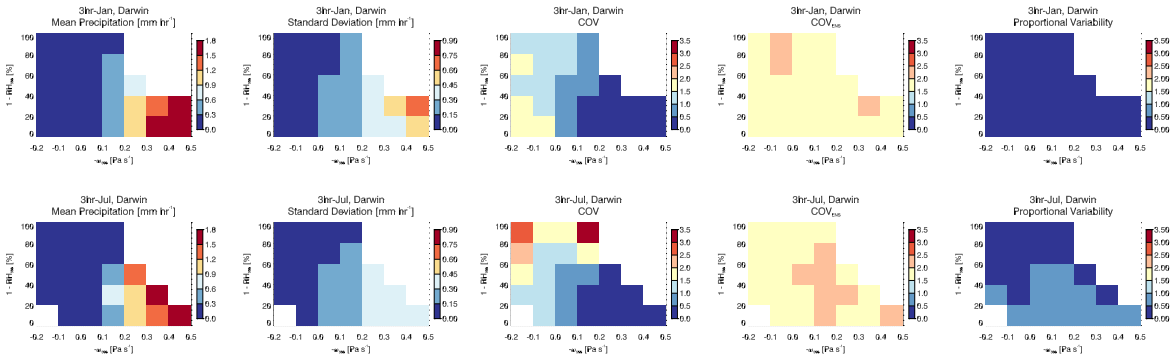

FIGURE 4.68: As in Figure 4.67 (leftmost three panels in each row) but for MP 3-hourly data over Darwin in January (top) and July (bottom). The rightmost two panels in each row represent MP CPM ensemble precipitation spread measures relevant to and described in Chapter 5.

vertical velocity at mid-levels (though there is a chicken-egg issue there), while atmospheric stability measures were not found to have a significant, predictive relationship to the intensity of

precipitation, even though many convective parameterizations have triggers with dependencies on such measures.

Watson et al. (2014) found similar results for their data over Darwin (Figure 4.69). The IFS convection scheme, deep convection is triggered if a test parcel's upward velocity would not reach zero before it reaches its lifting condensation level and if the cloud top, where the parcel's vertical velocity vanishes, is at least 200 hPa above this. The intensity of convection is then proportional to a measure of CAPE. In this way, it would be important to know if this could be empirically justified. A comparison for the MP data is shown in Figure 4.70. A significant difference between these two sources is that the data from MP is not exclusive to instances of deep convection; however, the general relationships are a close match. There is a weak correlation between CAPE and precipitation, even though it is an integral part of the IFS deep convection scheme. In the case of CIN, both datasets show negative correlations, with that from Watson et al. (2014) being stronger. Correlations between precipitation and vertical pressure velocity at 500 mb are remarkably similar. This may be due to convective heating resulting in large scale ascent. Overall, MP does seem to reproduce some basic convective relationships.

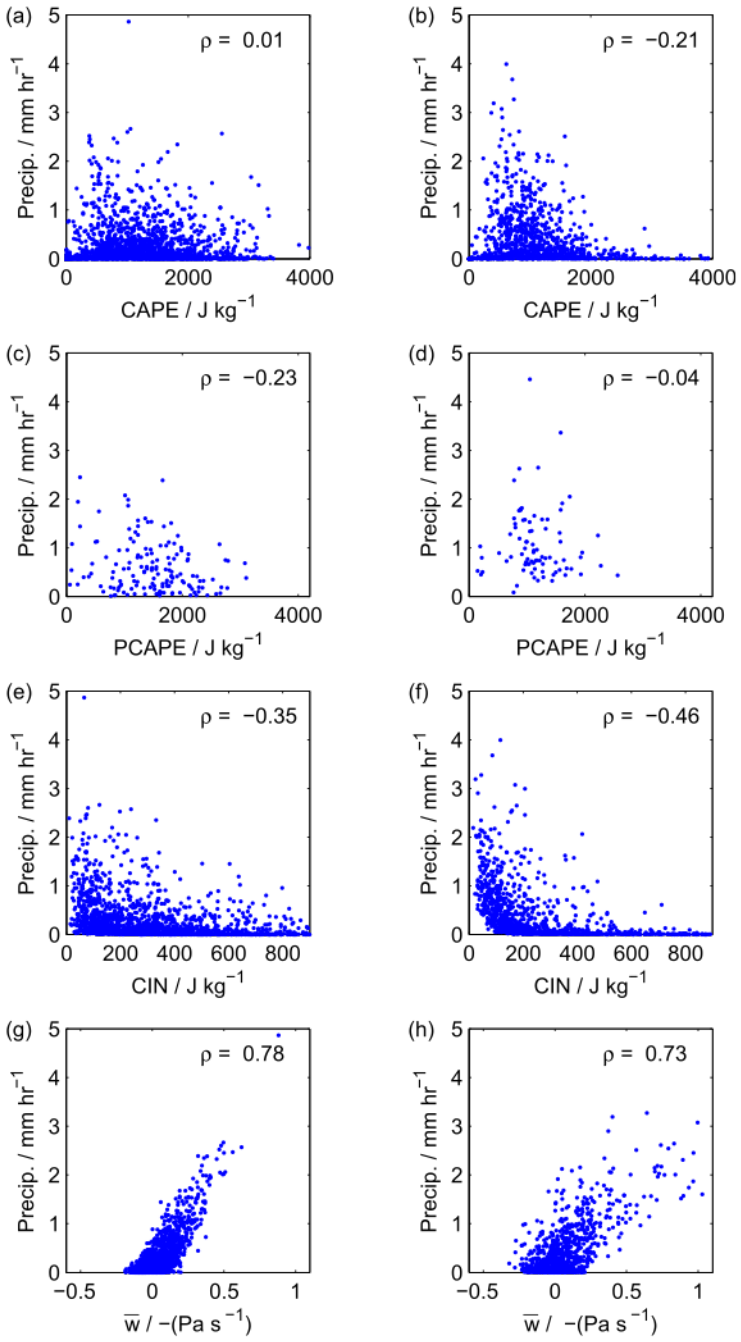

FIGURE 4.69: Caption as in Watson et al. (2014): .The relationship between Darwin-mean total precipitation and important large-scale variables (a),(c),(e),(g) in the variational analysis and (b),(d),(f),(h) in the IFS forecasts. The relationship with (a),(b) CAPE in the VA and the first stochastic forecast ensemble member; (c),(d) PCAPE in the VA and the deterministic forecast when deep convection is identified according to the IFS convection scheme; (e),(f) CIN in the VA and the first stochastic forecast ensemble member; and (g),(h) $\overline{w}$ in the VA and first stochastic forecast member. The correlation for each pair of variables ρ is written in the top-right-hand corner of each panel.

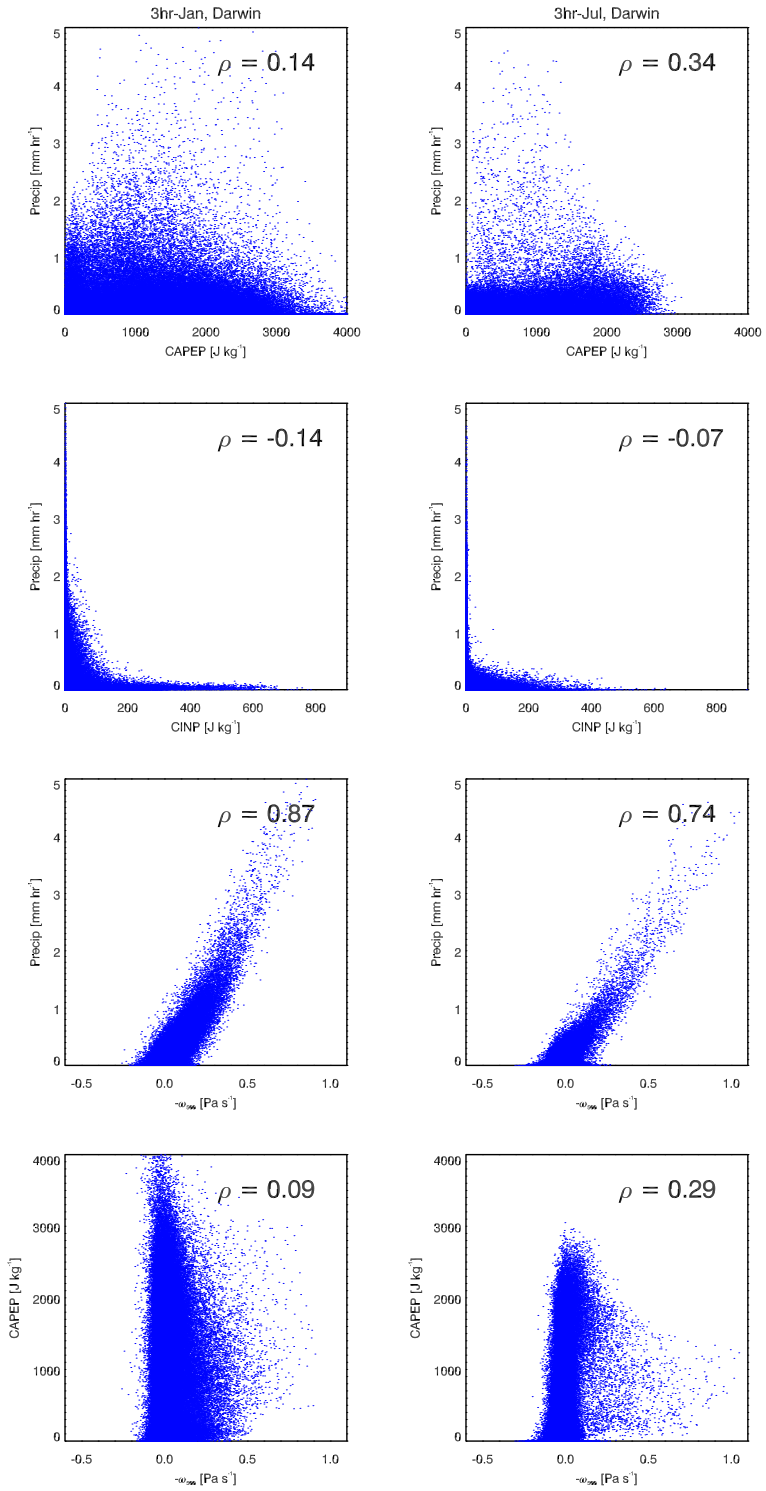

FIGURE 4.70: Similar to Figure 4.69. The relationship between Darwin-mean 3-hourly precipitation and CAPE, CIN, and the vertical pressure velocity at 500 mb and also between CAPE and the pressure velocity for MP single sample months of January (left) and July (right).

4.4. INTRASEASONAL VARIABILITY

The final item to address in this Chapter is the model representations of intraseasonal variability, mainly as represented by the MJO. As mentioned in Chapter 1, there is reason to believe that the presence of stochastic convective variability plays a significant role in a model's ability to produce a realistic MJO. In order to evaluate the MJO in the present models, I have relied heavily on the diagnostic tools provided by WALISER and Coauthors (2009). Relevant variables for the analysis are precipitation rate, OLR, and zonal wind at 850 mb. While each of these variables are available for the entirety of the SP simulation, they only exist in full for MP from year 4 onward. The same reference provides a comprehensive description of the phenomenon. For the purposes of this work, it will suffice to say that it represents the dominant mode of intraseasonal variability in the tropical atmosphere, a large cluster of precipitation and deep clouds that moves from west to east, recurring every 30 to 60 days. While many atmospheric models have had difficulty in accurately simulating the MJO, SP-CAM is one of a handful that has been able to do so. Can its more deterministic offshoot, MP-CAM also produce the general features of the MJO?

Figure 4.71 shows a time versus longitude Hovmöller plot created from 20-80 day band-pass filtered OLR anomalies (with respect to the first four harmonics) meridionally averaged from 10°S to 5°N latitude for a sample of two years. These meridional boundaries have been chosen to include the maximum MJO variance that typically is present during boreal winter. The overall magnitude of the anomalies in these samples is slightly greater in the SP case, but little else of note was found in viewing these kids of diagrams, In fact, very few instances of any eastward propagating anomalies were identified visually in either model.

Perhaps the most iconic way to uncover the MJO signal is through zonal wavenumber-frequency analysis as pioneered by Wheeler and Kiladis (1999). This method reveals distinct tropical wave

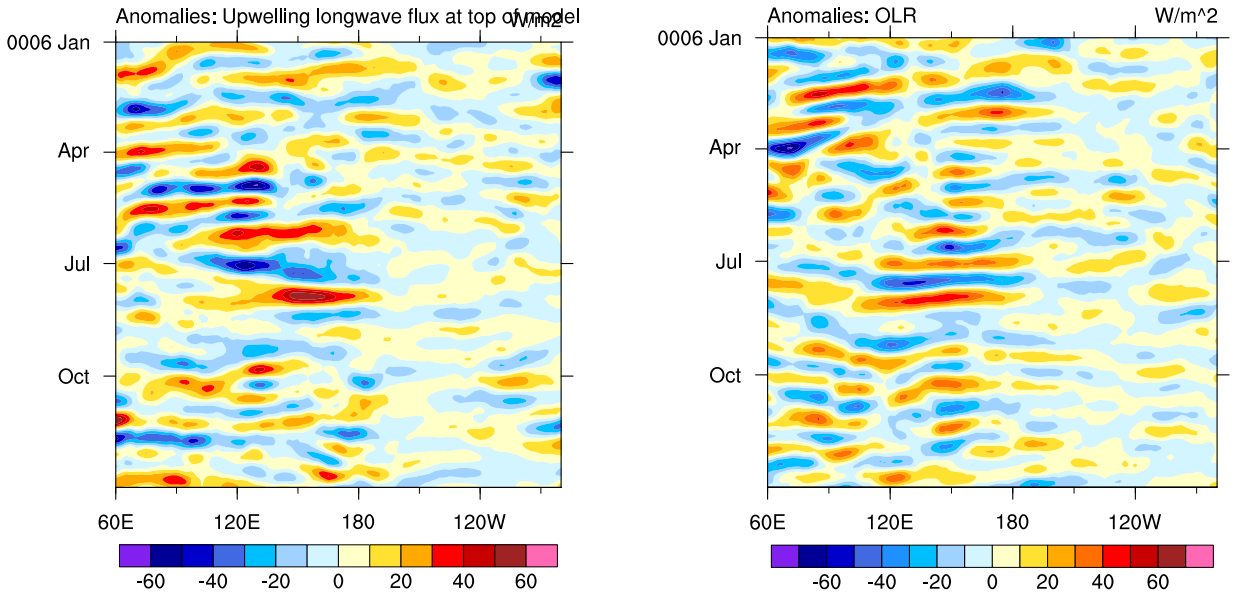

FIGURE 4.71: Time versus longitude Hovmöller plot created from 20-80 day band-pass filtered OLR anomalies for SP (left) and MP (right).

patterns as decomposed into their zonal wavenumber and frequency components. In this case, the frequency spectral bandwidth of 1/96 cycles per day is used with a 65-day temporal segment overlap. Figure 4.72 shows the results of this analysis for waves in the OLR field symmetric about the equator for data within $\pm 15^\circ$ latitude in NOAA observations[5], CAM, SP, and MP. To identify the MJO on these diagrams, we are looking for the region of strong spectral density confined to eastward (positive) zonal wavenumbers 1-2, below the 30-day period dashed lines. Understanding that the background spectra are approximately the same in each case, the first thing to note is that wave activity is generally lower than observations in all cases. CAM actually produces the largest model signal near the MJO; however, much of this peak is placed at incorrect, higher frequencies. CAM is also notably deficient in its representation of Kelvin wave power.

[5]The strong peak near wavenumber 14 and period of about 9 days is due to the sampling frequency of the satellite passes.

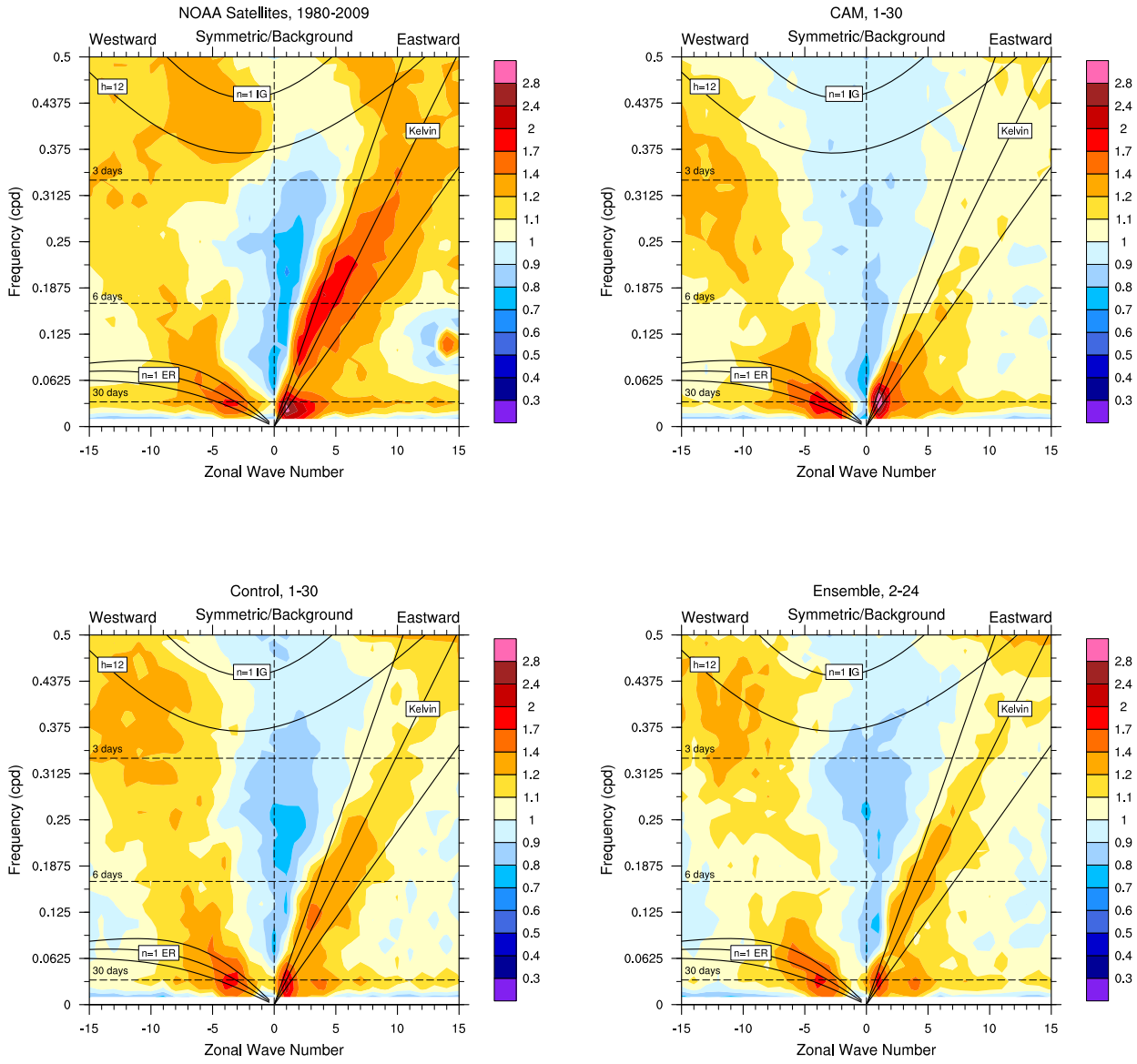

FIGURE 4.72: Ratios of symmetric spectral power to a smoothed background power for OLR for NOAA observations, CAM, SP-CAM (Control), and MP-CAM (Ensemble). Dispersion curves of the linear shallow water equations are shown in solid black for equivalent depths of 12, 25, and 50 meters. Wave types are Equatorial Rossby (ER), inertio-gravity (IG), and Kelvin.

SP and MP appear roughly equivalent at first glance. Both have overall weaker and slightly different signals than the observations, though we should bear in mind that these model runs to not have the advantage of an interactive sea surface, which plays a significant role in modulating

the MJO. Figure 4.73 shows difference plots for the data in Figure 4.72. I have not seen figures like these presented elsewhere, but it seems to provide more conclusive insight than simple comparisons of the original data. In the case of SP (Control) and MP (Ensemble) difference from NOAA OLR observations, We see that the differences are strikingly similar overall. Both appear to lack power in the Kelvin wave and MJO regions of the spectrum, with a more slight deficiency along the inertio-gravity wave dispersion curves. Comparing the results of MP and SP more directly (bottom, left), we confirm that the two models truly are producing a very similar result overall. However, we note that the MP case has a slightly weaker Kelvin wave signal, a difference that may be negligible. More prominent, though is the difference in the MJO signal, which is also weaker in MP, but considerably more so than the Kelvin waves. While SP shows strongest difference form observations at wavenumber 2 with less discrepancy at wavenumber 1, the deficiency in MP is more evenly distributed across both wavenumbers with a stronger deviation at wavenumber 1.

The MP peak difference corresponds to an approximately 10% reduction in the spectral power ratio, which is strong enough to be considered significant. On the other hand, the structure in the power spectra has not changed in any significant way. For instance, the CAM representation of the MJO spectral power signal, while also too tightly confined to the wavenumber 1 position is noticeably shifted to more slowly propagating modes, moving into the Kelvin wave range. By this measure, the MP simulation, with its more smoothed and deterministic physical parameterization from the small-scale, shows only slight degradation in the MJO signal. The caveat here is that these diagnostics are performed on the OLR data, which we have shown to be unexpectedly variable in MP despite the averaging effects of the CPM ensemble due to slight changes in the climatology.

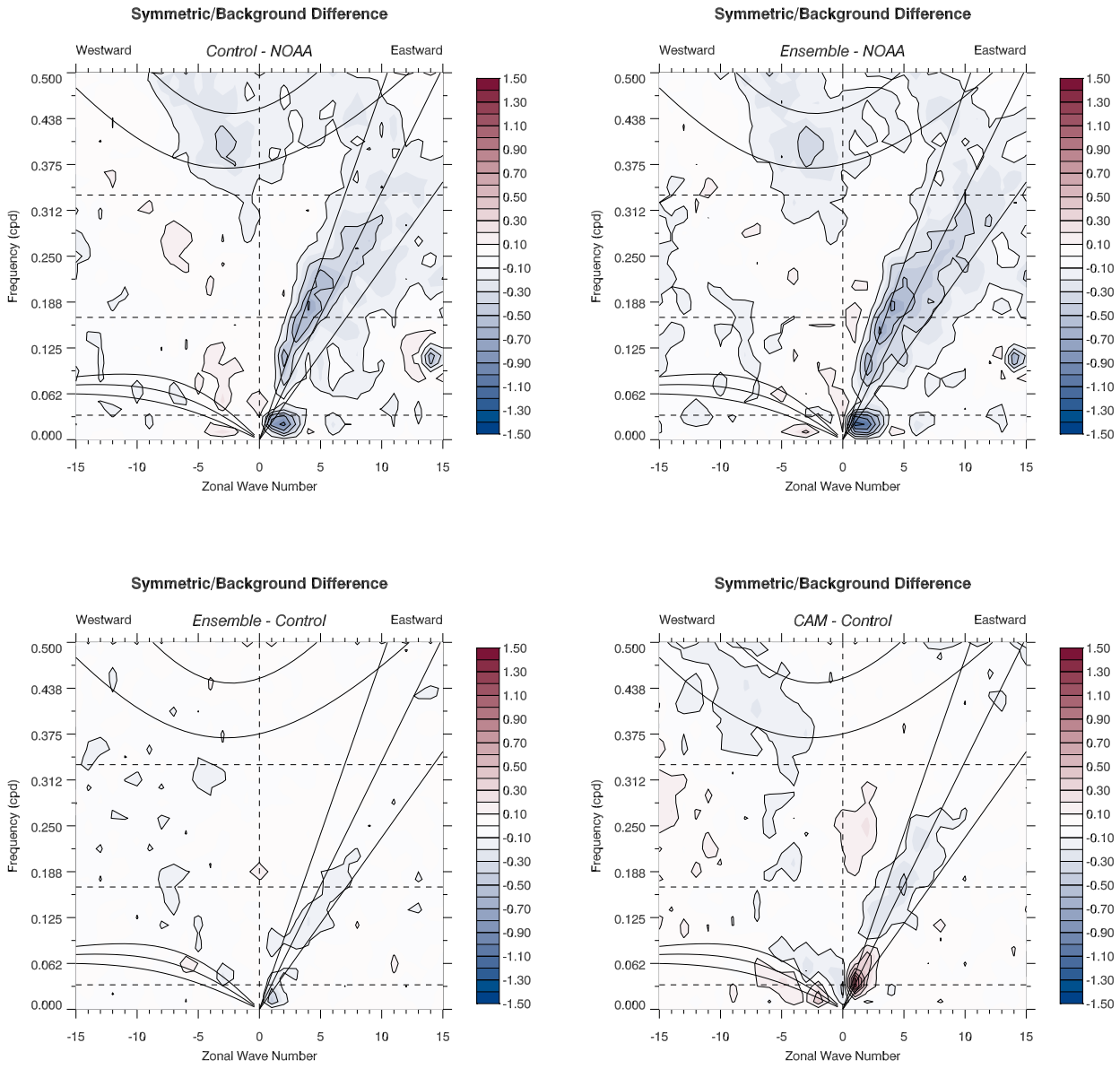

FIGURE 4.73: Differences in the ratios of symmetric spectral power to a smoothed background power for OLR for NOAA observations, CAM, SP-CAM (Control), and MP-CAM (Ensemble) from Figure 4.72 for the labeled pairs.

Last we look at lag correlation diagrams (Figure 4.74), which show the composite motion of the MJO considered from an annual perspective. The lag is with respect to peak precipitation in the central Indian Ocean, the area in which the MJO initiates. This time series is correlated with precipitation and zonal wind anomalies from $\pm 10^{\circ}$ latitude and 80-100° longitude that have

been band pass filtered for the range of 20-100 days. Here the color is precipitation and the line contours are the zonal winds at 850 mb. Motion in the meridional direction appears quite similar in SP and MP, though the MP pattern shows slightly faster propagation of the anomalies from the equator toward the north. For zonal motion, however, there are some clear differences. In MP the disturbance does not propagate as far to the east with as great intensity as SP. The MP precipitation anomalies in that case seem to stop at 120°E, and the trailing anomalies propagate more quickly westward toward the prime meridian than those in SP. Observational anomalies (not shown) closely match the pattern of SP in both directions, though with stronger anomalies. The MP representation of MJO propagation is clearly poorer.

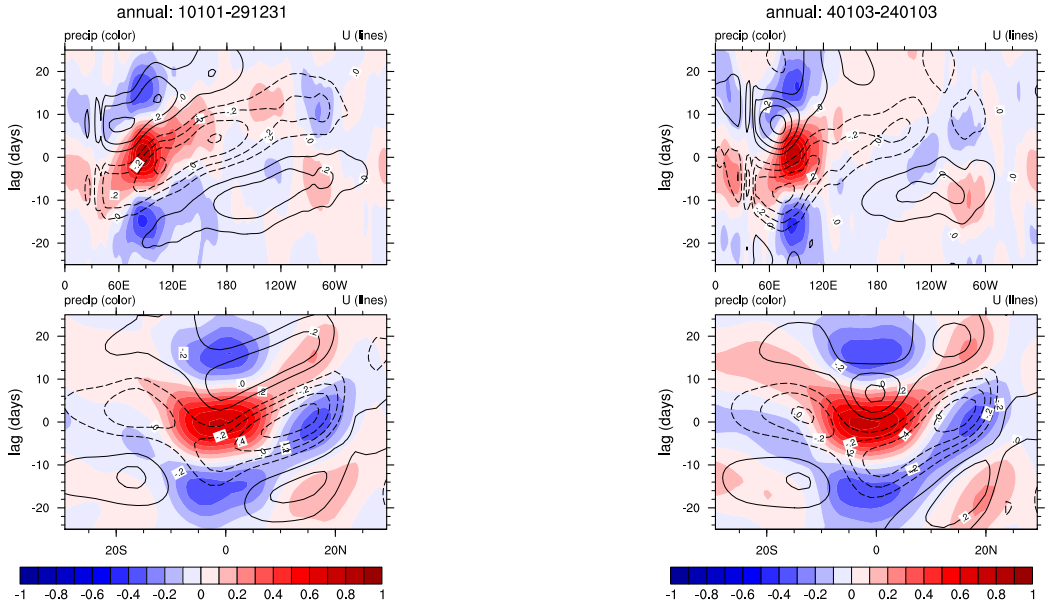

FIGURE 4.74: Lag correlation diagram using filtered daily data, considering the annual precipitation time series for SP (left) and MP (right). Precipitation anomalies are shown in colors, and with 850 mb zonal wind anomalies are contoured in lines.

Through these analyses of the SP and MP simulations, we have learned a number of important pieces of information. I think we can conclusively state that we have created a more deterministic superparameterization with the implementation of the MP framework as shown by a number of metrics regarding the representation of precipitation. Surprisingly, due to unexpected

changes in the cloud climatology, some convective signals, such as OLR, do not see the expected reduction in variability that one might expect from a more deterministic system. Further, the MP simulation was shown to reasonably recreate a number convective relationships in terms of both the scaling of variability with the mean and in relation to features on the large scale. Unfortunately, the changes in model configuration are accompanied by a degradation in the simulation of the MJO in comparison to SP. Namely, its spectral power is slightly reduced, and it appears to have spatially limited and accelerated propagation. While these deficiencies indicate that MP is not an improvement over SP for the accurate simulation of all climate parameters, the model does still perform reasonably well for an individual GCM grid box. In this sense, the framework provides a useful tool to test relationships between the large scale and the convective scale in a great number of samples, as will be done in Chapter 5.

CHAPTER 5 – PREDICTABILITY OF PRECIPITATION

We are interested in assessing the predictability of precipitation (specifically that with a daily mean rate in excess of 5 mm day^{-1}) on the GCM grid and determining those parameters available for analysis on the GCM grid that are strongly associated with low predictability. As discussed in Chapter 3, the initiation of convective precipitation requires the superposition of a number of favorable elements. These may include an appropriate large-scale thermodynamic and kinematic environment, variations or near discontinuities on the meso-scale, the morphology of a meso-scale system (e.g., cellular versus linear squall lines), boundary layer lifting from thermals or topography, or the presence of low-level moisture convergence. Even with a number of these occurrence-indicating elements, there is often considerable additional uncertainty regarding the timing, location, and ultimate magnitude of any potential convection. The eventual outcome may be a result of variations on rather small scales that tend not to be adequately represented in GCMs. Rousseau-Rizzi et al. (2016), in employing cloud resolving simulations with large-scale environments primed for the initiation of convection investigated factors responsible for such sensitivities. They found that the strongest indicator of the peak level of ascent was the initial thermal core size but also that even that strong relationship was modulated by the environment (cores were stronger with higher upper-level humidity) and the relationship became more variable in environments with elements that tended to act against strong convection, including even weak winds aloft.

Because the MP framework presents an ensemble of potential realizations for a given large-scale state, we are able to objectively measure the level of CPM agreement as a measure of predictability. Often in ensemble prediction systems, this is accomplished via some measure of the statistical spread of the ensemble measures and can be as simple as computing the standard

deviation or something similar (Walser et al. 2004). As a general measure of spread, there is no problem with using the standard deviation; even when the underlying distribution of the population may not be normal, it is possible to ascertain a sense of the relative differences in spread among a group of samples. However, when analyzing precipitation, there are a number of potential pitfalls when it comes to statistics, and one must be cognizant of the range of situations in the analysis.

If, for instance, we were interested in predictability in a specific location we might be able to successfully use the standard deviation to assess varying levels of predictability. In our case, though, we do not make any such restriction. We are interested in the predictability of precipitation over the entirety of the globe, where time mean magnitudes can vary greatly from point to point. Consider two sets of precipitation data that may be representative of CPM ensembles at different points. One has a mean of 6.3 mm day^{-1} and the other has a mean of 105.3 mm day^{-1}. No member of either ensemble is exactly the same, indicating imperfect predictability, but by chance every corresponding member is different by exactly 99 mm day^{-1}. This means that both ensembles have the same standard deviation. If that standard deviation happened to be 6.3 mm day^{-1}, one might say that the members of the second ensemble agree quite well, having a spread only 6% of the mean, whereas the first ensemble may be viewed as having rather poor predictability, having spread on the order of the mean. Because of this, initial attempts at quantification of predictability by CPM ensemble spread were the mean-normalized standard deviation, the COV. This is the same measure described in Section 4.2 but applied to the CPM dimension instead of time. For the preceding example ensembles, the first would have COV equal to 1, and the second would have COV equal to 0.06, appropriately making the distinction we desire.

5.1. INSIDE THE MP SIMULATION

Before exploring predictability relationships, we will look at the novel characteristics of the MP simulation. Figure 5.1 shows precipitation rate statistics from the MP run, averaged over five years in the month of April. Over a mean for 5 years, the individual ensemble members produce nearly indistinguishable results, with global mean precipitation rates ranging from 2.67-2.70 mm day^{-1}. If able to look very closely at the top two rows, though, small differences are apparent at the edges of more significantly precipitating regions. This is the first indication in this work that the CPMs are actually creating distinct results. This is even more apparent by investigation of the ensemble standard deviation panel, which shows the time-mean standard deviation in precipitation rate across the ensembles. Maxima in this field tend to be correlated with the locations of mean precipitation maxima, though this is not exclusively true. The bottom right panel shows the COV across the ensemble members averaged over time for points where the ensemble average precipitation rate exceeded 5 mm day^{-1}. Maxima here indicate locations where the CPM standard deviation is large compared to the CPM mean on a regular basis. This situation is most common inside the tropics, peaking near $\pm 15^{\circ}$ latitude. Of particular note is the high prevalence of points with COV values in the range 3.0-3.2. These locations correspond to high RFO values in CR7 and CR10 in Figure 4.1 and in CR5, CR10, and CR11 in Figure 4.2, indicating a potential association with frequent fair weather cumuli, shallow cumulus, incipient or decaying convection, or even some marine stratocumulus. High values of COV across the ensemble members may indicate strong disagreement and poor predictability[1].

[1]The original discovery of these high COV values is credited to David Randall, Mark Branson, and Radha Dutta, an undergraduate summer intern with the CMMAP program at CSU in 2015.

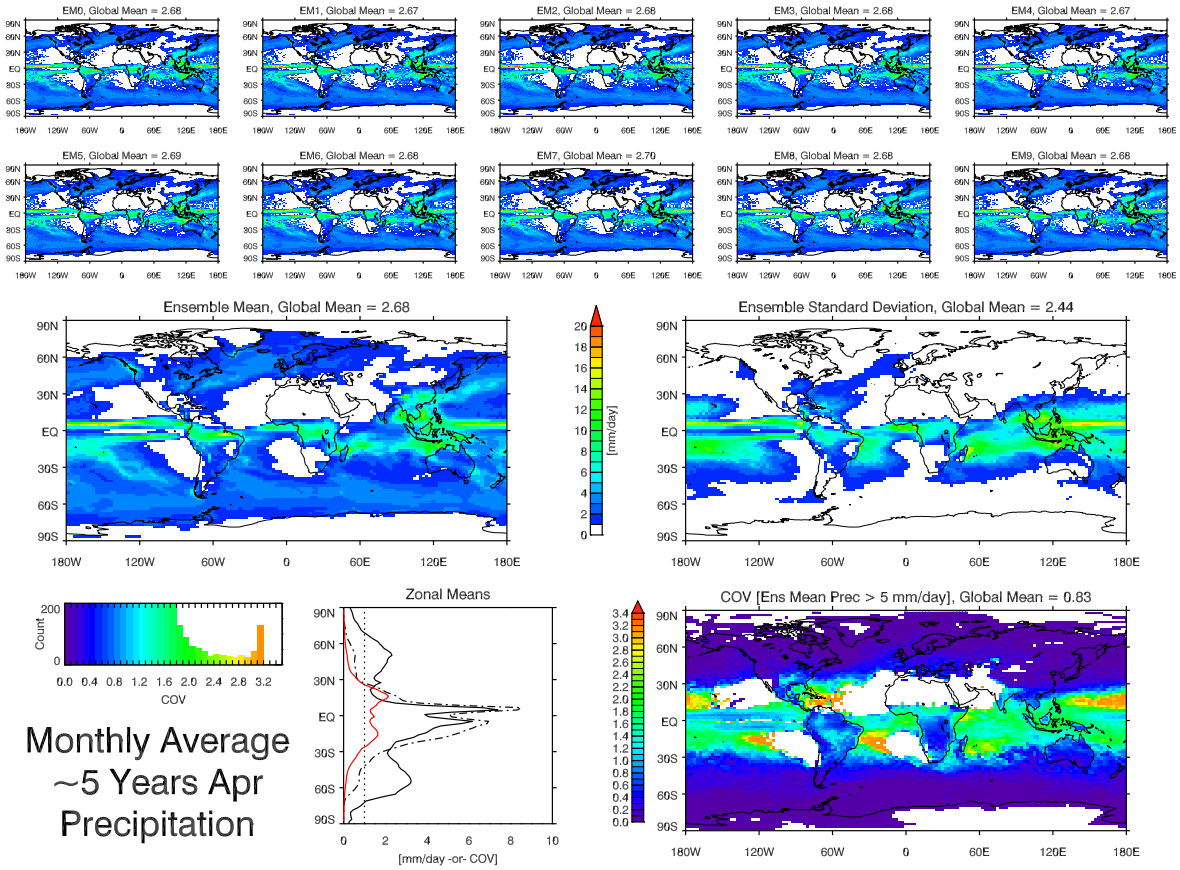

FIGURE 5.1: Precipitation rate statistics from MP-CAM for an average over 5 years of daily data from the month of April. The top two rows show the mean precipitation rate for each of the 10 CPM ensemble members. The center row shows the ensemble-time average of precipitation over this period and the time-averaged standard deviation of the daily precipitation rate across the ensemble members. At the bottom right is the time-averaged COV where the ensemble average precipitation rate was greater than 5 mm day^{-1}. The small histogram at the bottom left shows a count of grid points by COV bin, and the bottom center plot shows zonal means of the ensemble mean (solid black), standard deviation (dot-dash), and COV (red).

Figure 5.2 shows precipitation rate statistics in the same format for just one single day in September of the 5th year of simulation. Here, it is a bit more apparent that the ensemble members are producing different results at certain locations at the daily scale. Even at the daily level, elevated COV values are found in the same tropical locations, with much lower values (indicating CPM agreement) throughout the extratropics and in most locations near the center of horizontally large, intensely precipitating systems. The edges of these systems, where weaker precipitation rates are found do also exhibit somewhat elevated COV, indicating some lack of CPM consensus.

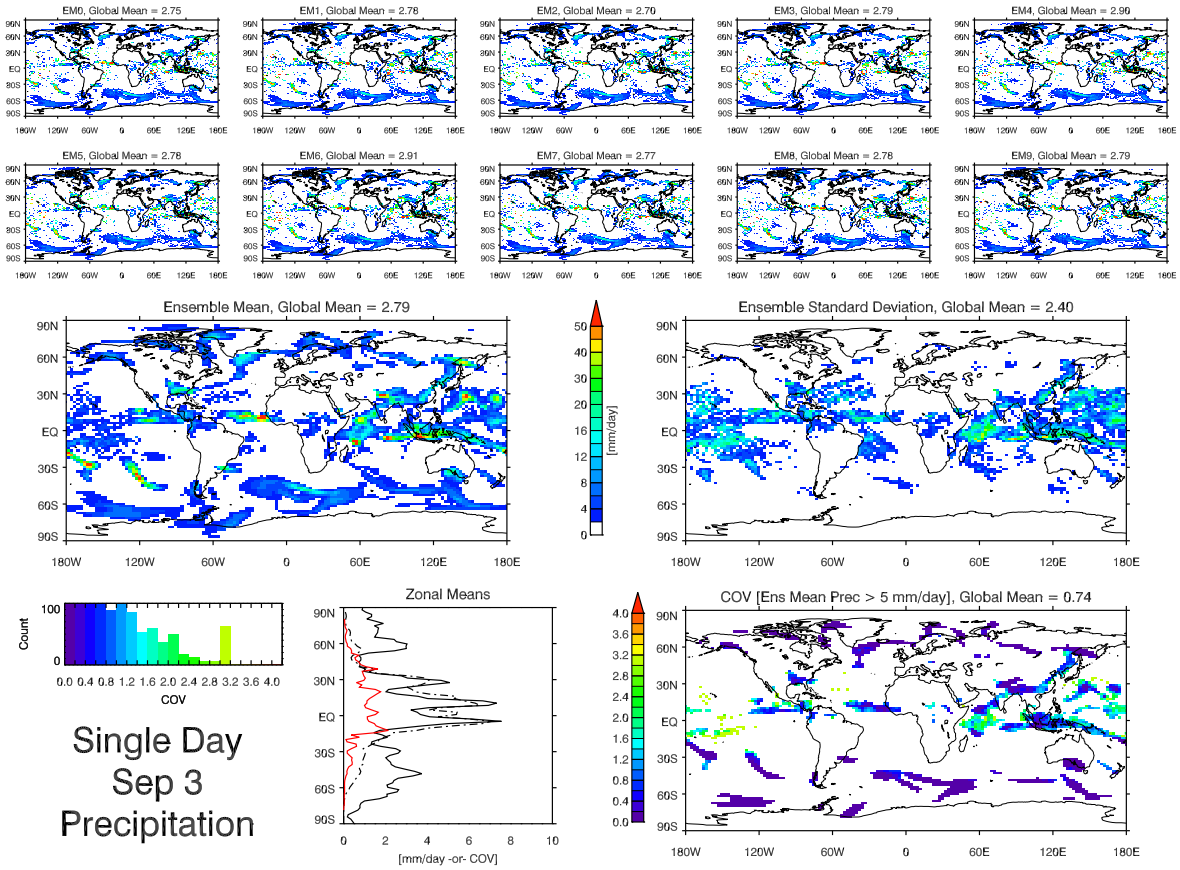

FIGURE 5.2: As in Figure 5.1 but for a single day, the 3rd of September in year 5.

For a more detailed look at what goes on inside the CPM, Figures 5.3 and 5.4 show Hovmöller plots of precipitation rate for each CPM at two different points. This data is obtained as 3-hour averages for the month of July[2] in year 9 of the MP simulation. Translations of individual convective cells are apparent in each case. In the extratropical case, while the details of the precipitation patterns at the CPM level differ, each member shows general agreement as to the domain mean progression. At the equatorial Pacific point, which is associated with the previously mentioned areas of elevated COV, only one member is heavily precipitating at any one time. At first, only member 8 produces any precipitation, and it happens to be a horizontally small, propagating cell of intense convection (Figures 5.5 and 5.6). Note the warm/cold couplet moving from right to

[2]Plus a few days before and after. Seasonal influences aren't very significant here, so all points in time could be shifted by some arbitrary amount without altering the conclusions.

left across the domain. The associated main area of precipitation measures approximately 50-km across and propagates following the surface cold pool. Members 9 and 10 also show evidence of a cold pool-related disturbance, but on a much smaller scale.

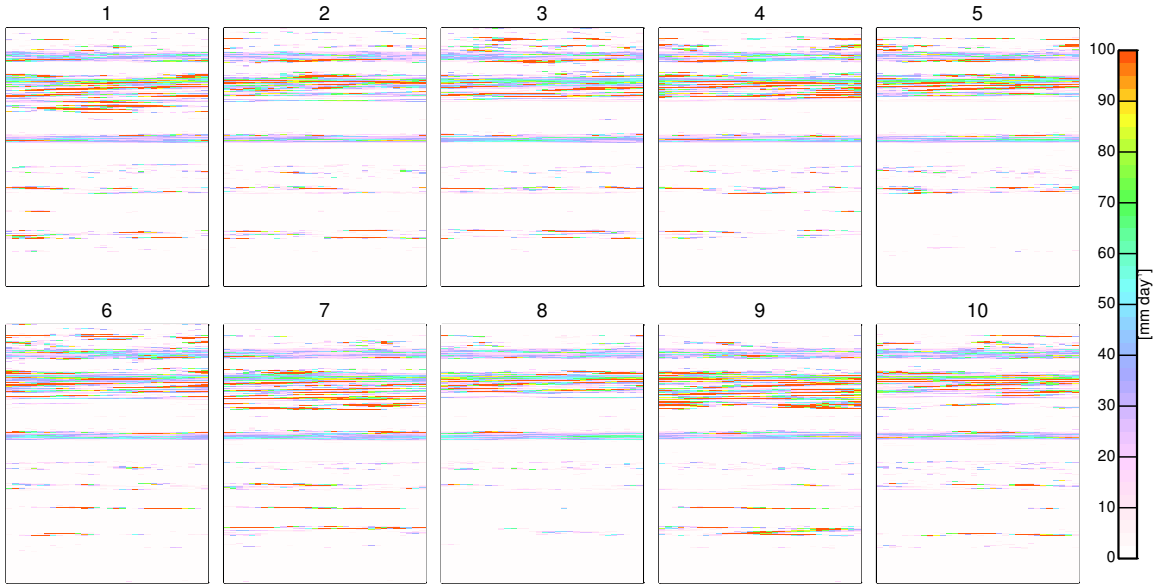

FIGURE 5.3: Hovmöller plots of precipitation rate for each CPM for the month of July of year 9 at a point in the extratropics over eastern Russia (130°E, 44.5°N). The horizontal axis is the horizontal extent of the CPM domain, and the vertical axis is time, increasing upward. Values are 3-hourly.

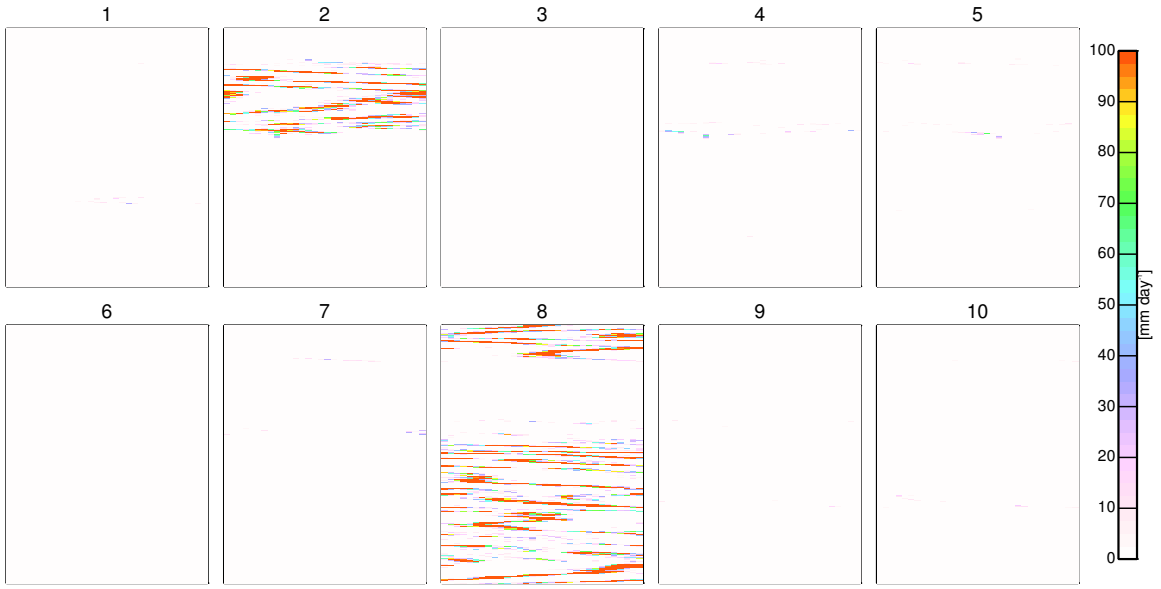

FIGURE 5.4: As in Figure 5.3 but for a point in the equatorial Pacific (132.5°W, 8.5°S, C1).

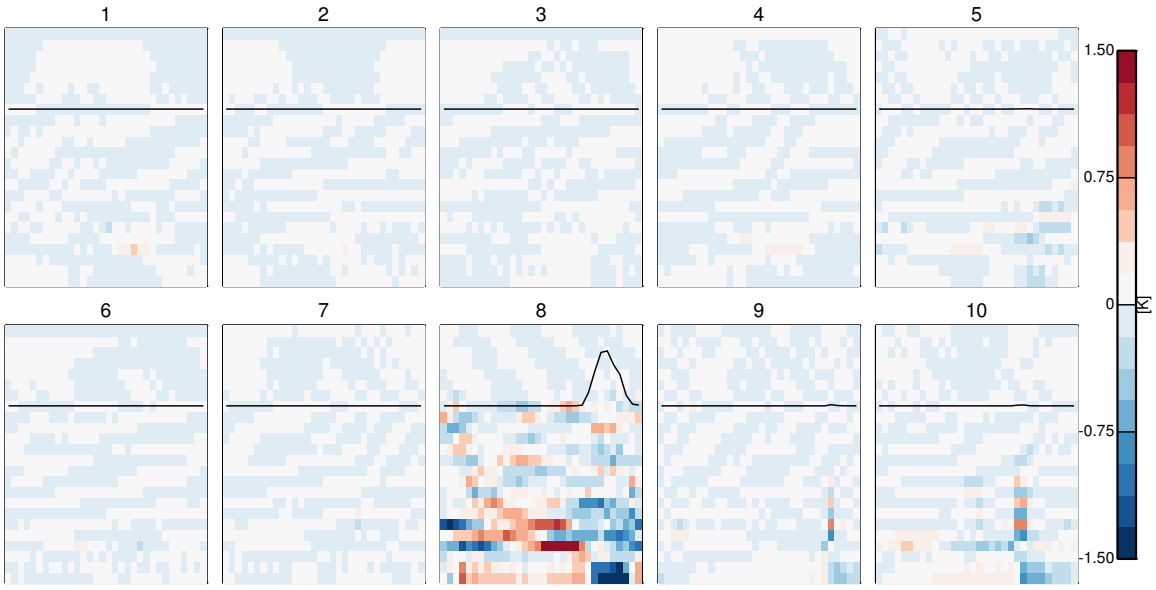

FIGURE 5.5: Temperature deviations from individual CPM domain mean profiles at the time of maximum domain averaged precipitation in member 8 in Figure 5.4. The black line is a representation of precipitation rate. The horizontal axis is the horizontal extent of the CPM domain, and the vertical axis is model vertical levels.

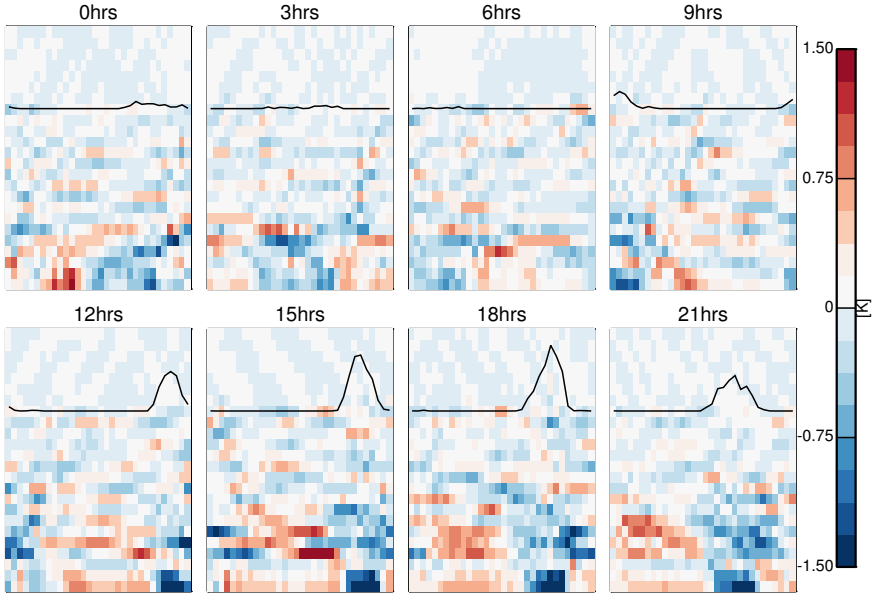

FIGURE 5.6: Temperature deviations from the member 8 domain mean profiles in a sequence of 3-hour intervals near the time of Figure 5.5. The black line is a representation of precipitation rate. The horizontal axis is the horizontal extent of the CPM domain, and the vertical axis is model vertical levels.

Later in the sequence, major precipitation shifts from member 8 to member 2. A snapshot of thermal perturbations in the CPMs during this transition is shown in Figure 5.7. At this point, major activity is decaying in member 8, and new strong perturbations appear in members 2, 4, 5, and 7. After evolving these perturbations for 30 hours, only member 2 has any active precipitation remaining (Figure 5.8). During this transition, very little changed on the large scale (not shown). The convective available potential energy was relatively steady at this transition, increasing slightly as convection in member 8 decayed, though it underwent much more significant oscillations during the periods of single-member domination.

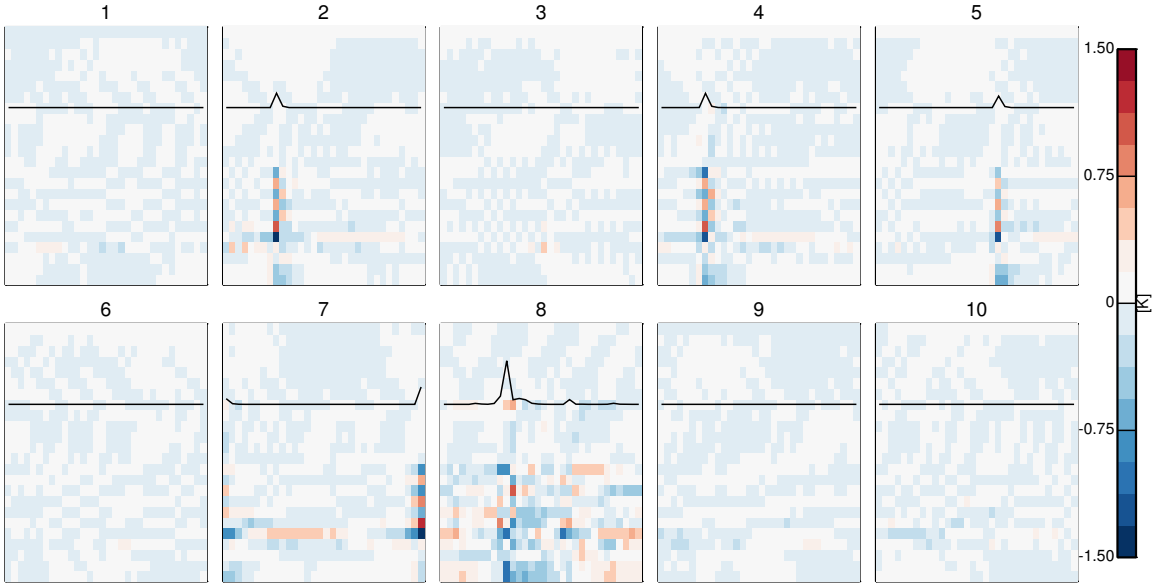

FIGURE 5.7: As in Figure 5.5 but at the point of transition of major precipitation from member 8 to member 2.

Members 2 and 8 are extreme outliers from their companion CPMs in this case, producing intense precipitation from a single organized system. In fact, the convection is so intense that the domain average for members 2 and 8 frequently exceeds 50 mm day^{-1}, allowing the ensemble average to exceed 5 mm day^{-1} (Figures 5.9 and 5.10). 5-10 mm day^{-1} is a fairly common precipitation rate in the high COV region surrounding this point in the MP simulation. Importantly, it is also a fairly common precipitation rate in the same region of the SP simulation. This is disturbing.

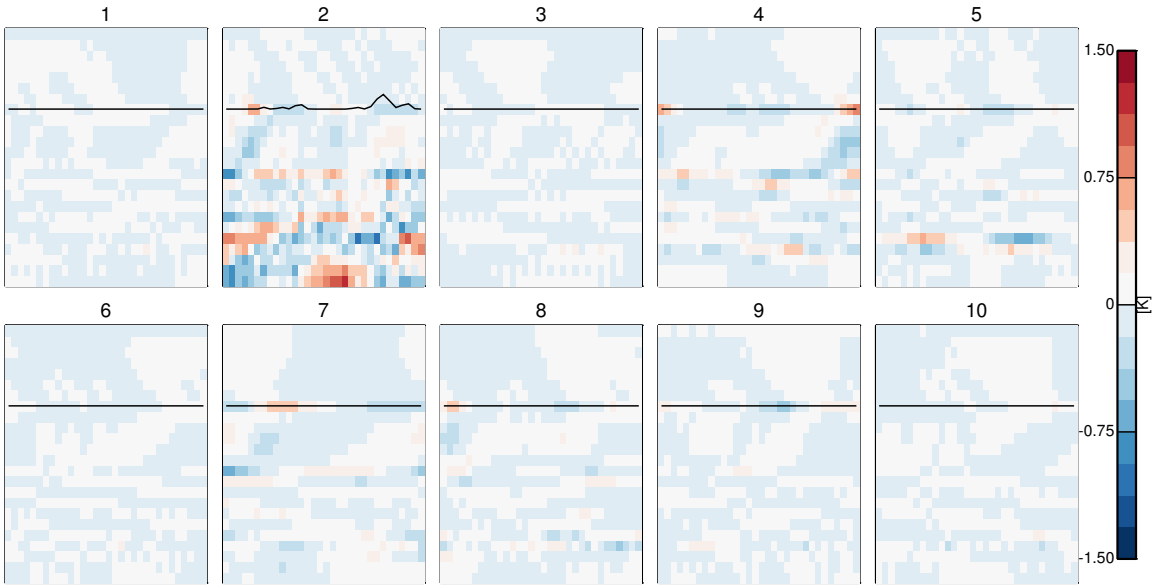

FIGURE 5.8: As in Figure 5.7 but 30 hours later.

In SP, a single CPM curtain in this region is often producing domain-averaged precipitation rates of 5 mm day^{-1}. In MP, under very similar large-scale conditions, the ensemble average returns a similar distribution of precipitation rates, but the members are in odd disagreement such that a single member can produce 50 mm day^{-1} rates over the course of a month or longer, while the nine remaining members produce almost nothing. Energetically, the configurations affect the large-scale in the same way, but the representation on the CPM domain could hardly be more disparate. The time series of the ensemble mean certainly gives no indication as to what is going on under the hood.

Further exploring a sample of locations in this 3-hourly July dataset, Figure 5.11 shows the time series of domain mean precipitation in each CPM at a selection of points, and Table 5.1 provides summary information about these locations, some of which will be addressed later on. The extratropical point, E, is the same as that referenced in Figure 5.3. Again, the close CPM agreement regarding precipitation rate is clear. Point C2 (top right) shows properties similar to the equatorial Pacific point shown for C1 in Figures 5.4 to 5.10. At no time in period shown

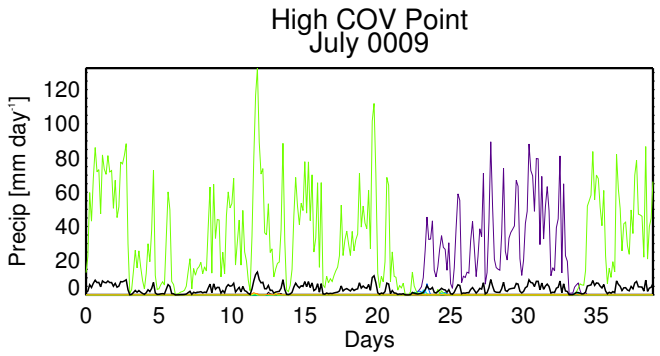

FIGURE 5.9: Time series of domain mean precipitation in each CPM (colors, note many colors long the bottom) and the CPM mean (black) for the month of July of year 9 at a point in the equatorial Pacific (132.5°W, 8.5°S, C1).

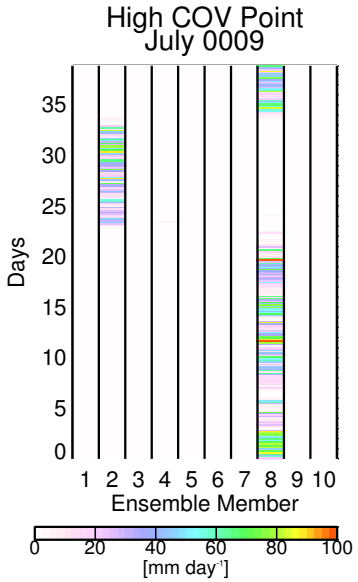

FIGURE 5.10: Time series of domain mean precipitation in each CPM for the month of July of year 9 at a point in the equatorial Pacific (132.5°W, 8.5°S, C1).

do the CPM members ever come particularly close to agreement about the precipitation rate. At a only a handful instances do more than half of the members even agree that there will be precipitation, and often those reporting precipitation do so at rather heavy rates. For most of the period, though, only one or two members report precipitation. It is not, however, a time period of complete disarray. Near days 20, 30, and 37 the members are in agreement about there being zero

precipitation. In further contrast to C1, C2 shows far greater temporal variation in the ensemble mean precipitation rate, ranging from zero to nearly 40 mm day^{-1} (not shown).

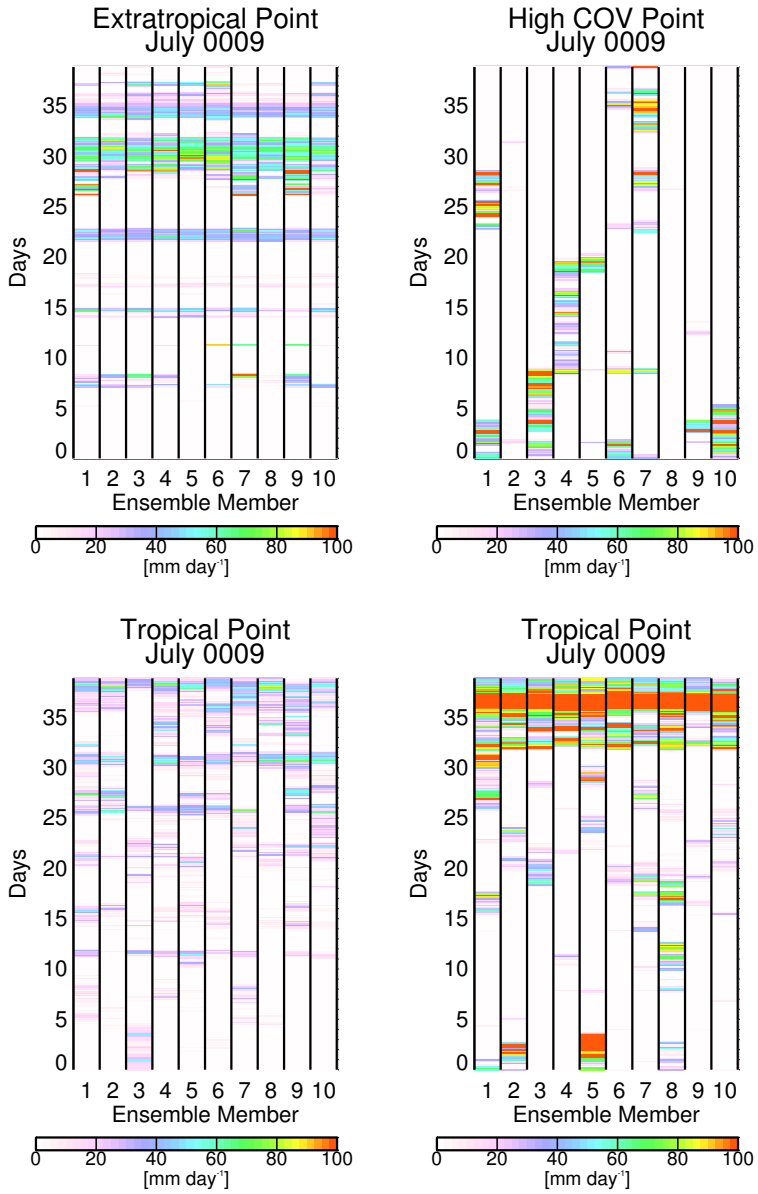

FIGURE 5.11: Time series of domain mean precipitation in each CPM for the month of July during year 9 of the MP simulation at GCM points E (top left, as in Figure 5.3), C2 (top right), T1(bottom left), and T2 (bottom right). More information on these points can be found in Table 5.1.

Figure 5.11 also shows data from two tropical points over the same time period. T1 lies just north of the equator near the coast of Guinea in Western Africa. For this month, the location is

TABLE 5.1: Location, mean precipitation rate, coefficient of variation, and proportional variability of a selection of GCM grid points from MP 3-hourly data obtained for July of year 9.

Map ID	Lon/Lat	Precip	COV	PV
E	130.00°E, 44.53°N	11.3	1.18	0.39
T1	15.00°W, 8.53°N	11.1	1.48	0.74
T2	70.00°E, 2.84°S	20.2	1.75	0.62
C1	132.50°W, 8.53°N	3.5	3.10	0.26
C2	92.5°W, 12.32°N	6.9	2.63	0.37

characterized by moderate rates of precipitation and lies on the eastern border of a local precipitation maximum that stretches westward over the Atlantic Ocean. The CPM patterns are not as nearly as neatly coherent as at point E, but one can at least discern the indication of majority agreement as to whether or not there is some amount of precipitation present. On the other hand, even when the presence of precipitation is agreed, the reported magnitude can show considerable variation (Figure 5.12).

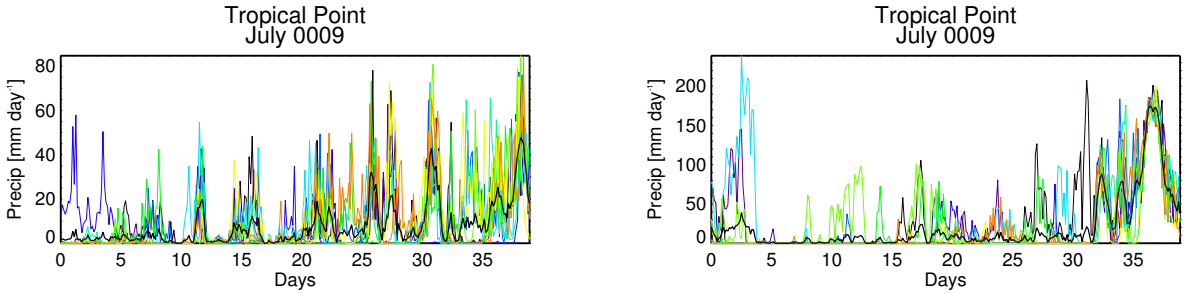

FIGURE 5.12: As in Figure 5.9 but for T1 (left) and T2 (right).

Location T2 is another tropical GCM point, this time in the central Indian Ocean, just south of the equator. In the early days of July (Figure 5.11), we see CPM disagreements reminiscent of those in C2. That is, the members often disagree about the presence of strong precipitation or all agree that there is none. For days 15 through 30 the members show significant disagreement about presence and magnitude of precipitation, which is generally light in the mean. At the end of

this time series, though, the members appear to quickly organize into agreement about the presence of strong precipitation. This feature is associated with the passage of a low pressure trough, a quick rise in precipitable water and a two Kelvin temperature drop (not shown), indicating the passage of a system on the larger scale. Without the presence of strong forcing from the GCM, CPM disagreement at T2 tends to be high. then there is this line

5.2. Reevaluating the Predictability Measure

Understanding the various representations of precipitation at these points, it is interesting to see how their time mean predictability has been rated by the COV. Perhaps expectedly, we see the lowest COV, indicating greatest predictability, for the extratropical point. Most of the time at that point, the CPMs agreed as to timing and magnitude of precipitation. Moving up the COV scale, tropical points, T1 and T2, exhibit larger COVs on account of their mixed levels agreement. C2 COV is considerably higher, at 2.63. In that case, CPM members rarely agreed about the magnitude of precipitation unless they each happened to report zero. Finally, the highest COV was reported in C1, the case where typically only one ensemble member reported some amount of precipitation for the entirety of the period under consideration.

This poses a bit of a potential problem. Is the scenario in C1 typical of high-COV points? Figure 5.13 shows the way CPMs reported daily mean precipitation in July of year 7 where the ensemble mean precipitation exceeded 5 mm day^{-1} and the COV was greater than 3, a value near the maxima reported in Figures 5.1 and 5.2. Contributing events are ranked top to bottom from highest to lowest ensemble mean daily precipitation rate, and ensemble member daily mean precipitation rates are sorted left to right from lowest to highest for each contributing event to visually isolate the outlying member. Based on this information, yes, the scenario in C1 is indeed

typical of the high COV points. Only a few of these events are those in which each member reports some precipitation, and much like the C1 case, the lonely member reporting precipitation is doing so heavily (of course, this is mainly a result of selection bias from the precipitation threshold). It should also be noted that such events are not the norm. They account for less than 0.2% of all potential outcomes.

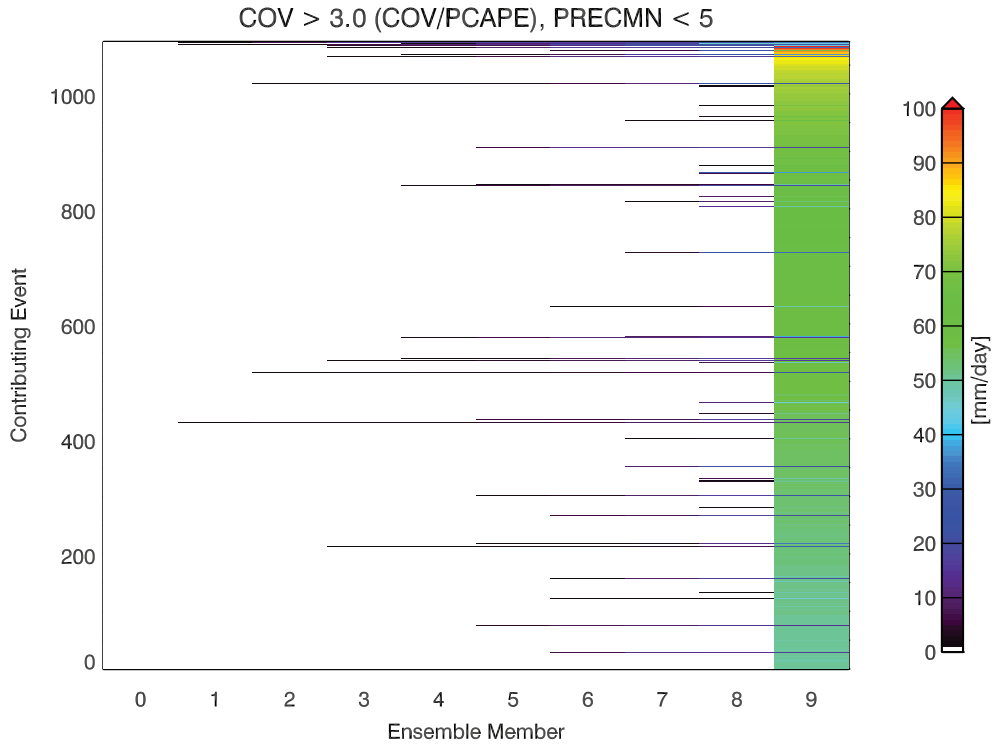

FIGURE 5.13: The daily mean precipitation rate in each ensemble member for points in space and time during July in year 7 of the MP simulation where the ensemble mean daily precipitation rate exceeds 5 mm day^{-1} and the COV exceeds 3.0. Contributing events are ranked top to bottom from highest to lowest ensemble mean daily precipitation rate, and ensemble member daily mean precipitation rates are sorted left to right from lowest to highest to visually isolate the outlying member.

What is particularly worrying about these points is that nine out of the ten ensemble members are often *in exact agreement*. How can an ensemble with members in such close agreement report such poor predictability? Or better yet, how can our measure of predictability indicate poor agreement when the consensus is strong?

For a moment, I must initiate a tangent, but important, discussion. The motivation for this work was the discovery of coherent spatial patterns in the time averaged COV. But more than that, it was the discovery that these patterns showed notable similarity to patterns in CAPE, the indication being that areas commonly exhibiting high potential for convective activity were the same as those where predictability was extremely limited. They had a strong positive correlation. An example of this is shown in Figure 5.14. For points where the ensemble mean precipitation rate is greater than 5 mm day^{-1}, COV and CAPE are correlated at 0.711. It's a tantalizing association.

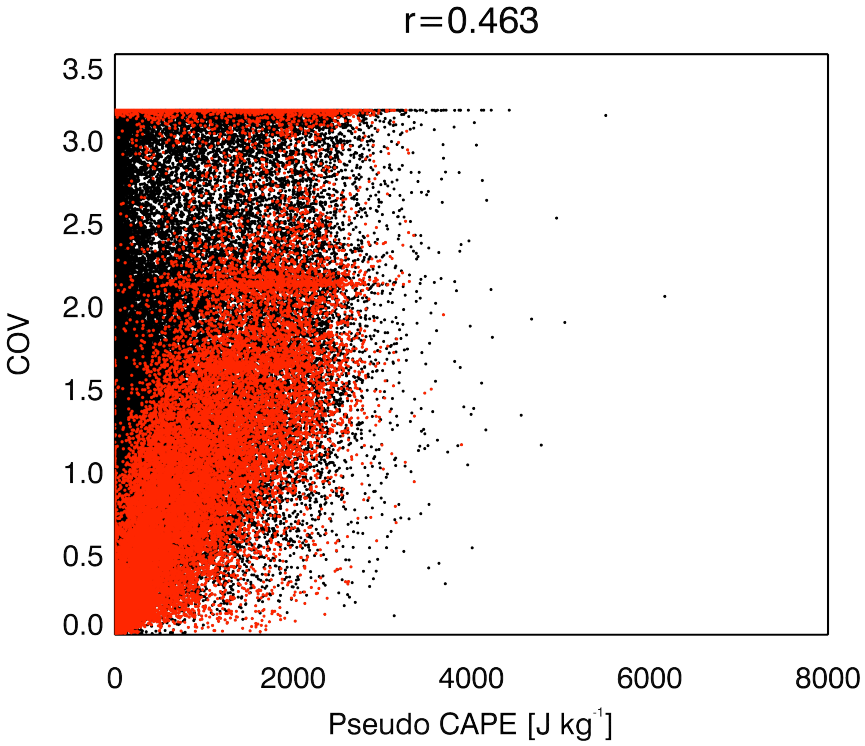

FIGURE 5.14: Scatterplot for all GCM grid points in space and time for the month of July in year 7 of the MP simulation comparing CPM ensemble precipitation COV and pseudoadiabatic CAPE from daily averaged values. Points where the ensemble mean precipitation rate is greater than 5 mm day^{-1} are colored red. The correlation coefficient, r, is for all data points. The correlation coefficient for only the red points is 0.711.

Upon closer inspection of the red points in Figure 5.14, some clustering of particularly high data density at discrete COV points can be seen (Figure 5.15). The red points are analogous to

those instances in Figure 5.13 where usually only one CPM member reports precipitation. The other two areas are new to the discussion, but appear to be just as anomalous, sitting near COV values of 2.1 and 1.6, deviating from what appears to be a reasonable linear relationship in the remaining black points.

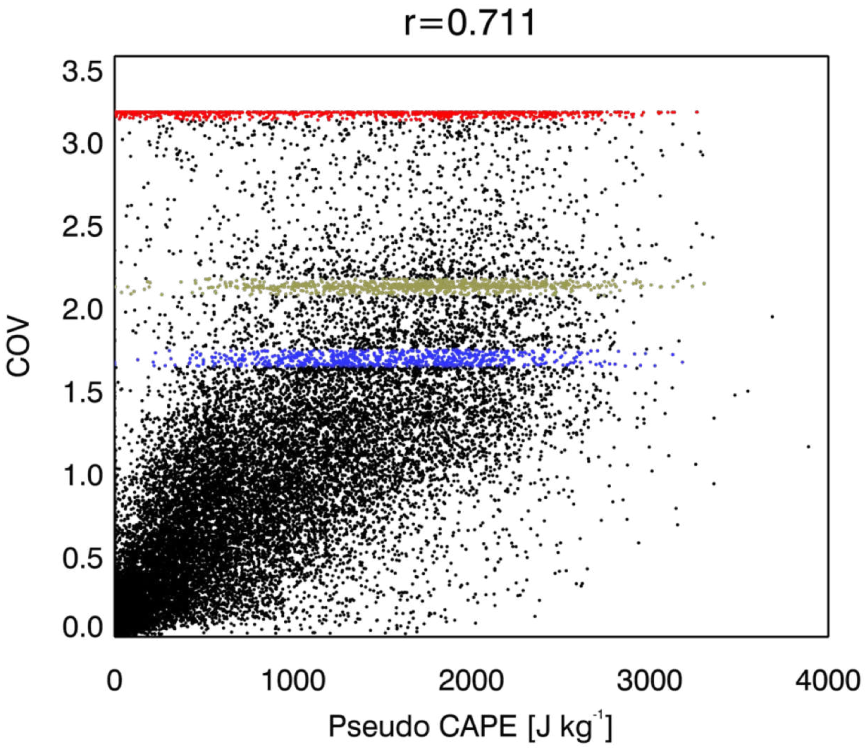

FIGURE 5.15: As in Figure 5.14, but only for points where the ensemble mean precipitation rate is greater than 5 mm day^{-1}. Colored points here highlight clustering of data.

With this information in mind, it is time to revisit the spatial patterns of COV and CAPE. This is shown in Figure 5.16. We see that the two variables do indeed exhibit a similar spatial structure in the long-term mean. Both peak within the tropics and share similar maxima and minima. The pattern of COV seems to follow well with the generalization that may be gleaned from Table 5.1, indicating best predictability in the extratropics. Their annual mean spatial patterns correlate at 0.842, which is particularly strong. However, local correlations in time do not consistently show a positively correlated relationship. In fact, it is in the regions of COV maxima where the temporal

correlations turn negative, clearly at odds with the initial hypothesis. Additionally, the boundaries of high COV are sharp, lacking a smooth gradient; this highlighting of a discontinuity sends up red flags about the presence of a non-physical anomaly.

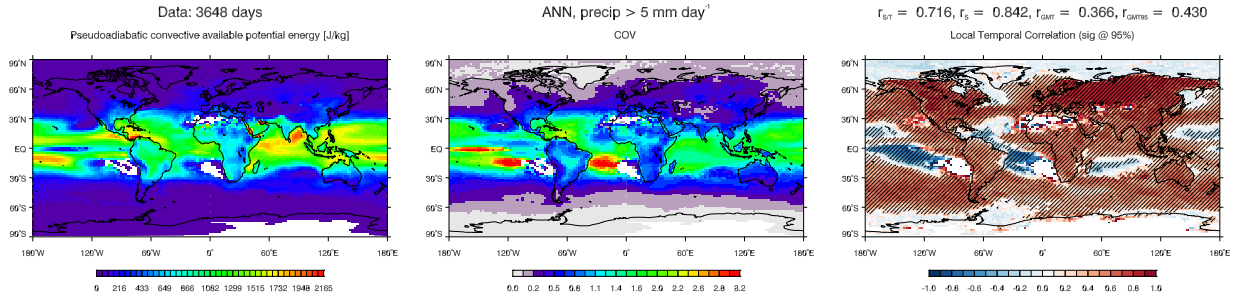

FIGURE 5.16: For points where MP daily precipitation rate exceeds 4 mm day^{-1}, the time averaged daily mean CAPE (left), COV of CPM member daily precipitation rate (center), and the local temporal correlation between the CAPE and COV (right). Shading on the correlation plot indicates significance at the 95% confidence level. $r_{S/T}$ is the correlation coefficient considering all considered points in space and time, r_S is the spatial correlation of the left and center data, r_{GMT} is the global mean of the local temporal correlation coefficients, and r_{GMT95} is the global mean of the significant local temporal correlation coefficients.

A scatterplot of CAPE and COV for the locations where the long term local temporal correlations in Figure 5.16 are less than -0.5 is shown in Figure 5.17. From this figure, it is clear that while the underlying positive association is still present, particularly for COV values less than 2, the weight of the outlying high COV values across the full range of CAPE is causing the correlation to reverse sign.

It would appear that the COV measure is causing the deviation from the assumed relationship, rather than there being a different relationship at only these locations. To prove this, we can consider some hypothetical examples. Consider a CPM ensemble that reports, like the ones we have discussed, nine zero values and one strongly precipitating value. Running the calculation, COV$\approx$3.16. Doing this again for nine zero values and one very weakly precipitating value, again, COV$\approx$3.16. That is simply a bad way to quantify predictability. The differences in the precipitating member should register as a difference in predictability. If instead, we turned the zeros into

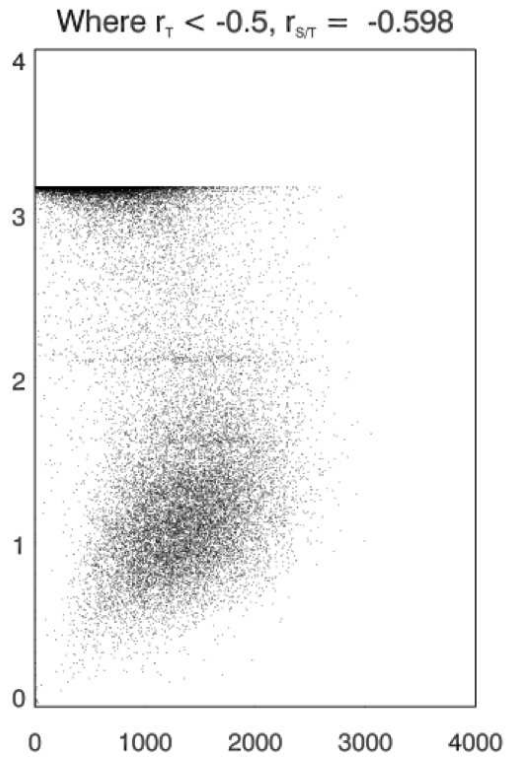

FIGURE 5.17: As in Figure 5.14, but only for locations where the long term local temporal correlations in Figure 5.16 are less than -0.5.

ones (or any other single value) in those two cases, the COV does produce differing values corresponding to the magnitude of the outlier. Therefore, the measure is not all bad, but for a variable like precipitation rate, which can have a high incidence of zero values, it is a poor choice. By experimentation, it was discovered that the COV with one precipitating member is more precisely $\sqrt{10}$. It is an upper limit imposed entirely by the sample size, a statistical artifact. Those with two members precipitating at near equal magnitude produce the next cluster streak in Figure 5.15 at 2.1, those with three are responsible for the clustering at 1.6. This might seem unusual except for the fact that the COV is insensitive to the magnitude of these outliers if they are approximately equal, for instance, three barely-precipitating members.

Interestingly, some of the points that give maximal COV at high CAPE may only be possible in a framework like MP. The C1 case illustrates the reason for this. Points similar to C1 have both

high COV and sometimes large CAPE with only one or two members reporting precipitation. In the climatological average, precipitation at these points is on the low end for the tropics, but when large CAPE is present, it is possible for CAPE to remain large while producing heavy precipitation in a single member. While precipitation generally acts to dissipate the CAPE, the dissipating effects of a single member, which may have by chance overcome some convective inhibition that the remaining members could not, may not be sufficient to turn off its own convection when its physical tendencies are averaged with nine members that are not acting to dissipate the CAPE. Because of this possibility, the COV can be anomalously maximized at high CAPE, which would actually act to slightly enhance the strength of the positive correlation. In a more typical situation, the statistical anomaly occurs for lower precipitation values and low CAPE, which would not be included in analyses like that in Figure 5.16 because of the precipitation threshold. The only reason that these point show up so brightly here is also because of the threshold and the fact that when there is not a strong outlying member, the members tend to agree about zero precipitation.

That is the end of the important tangent discussion, and the conclusion is that a better measure of predictability is required. Many formulations were attempted. It is possible that if the COV were calculated on the model time steps, the majority of the anomalous values may be averaged out, but tests with limited data of this type have not been conclusive. One method that provided some improvement was to calculated the COV from existing values but with bootstrapping to obtain a better estimate. The improvement would likely be better if not for the small sample size. Normalization of the standard deviation by the range of values in the ensemble also showed slight improvement but not enough to warrant continued use.

Exhausting such obvious solutions, I turned to recent literature for a more resilient measure of spread. The winning candidate is a recently developed measure known as proportional variability (hereafter, PV[3]) developed by Heath and Borowski (2013). in developing this measure, the authors draw comparisons to the COV with the aim of finding a measure bounded from zero to one. While COV assumes that the mean is a meaningful benchmark for measuring variation, PV does not. In short, it is the average ratio comparison of all possible combinations of numbers in a set. PV is similar to the COV in a number of respects, including its correlation to standard deviation, but the effects of sample size and zero-valued data is quite reduced, or at least, it is present in a better way. It has the nice property where the 9:1 ratio (while still an anomalous PV value independent of the value of the outlier) is deemed low variability, rather than high variability, congruent with the fact that the majority are in agreement.

As described by Heath and Borowski (2013), for a given dataset of n non-negative numbers, $z_i \geq 0$, there are a combination of $C = n(n-1)/2$ unique pairs, (z_i, z_j), for which the relative difference, $D(z_i, z_j)$ is calculated. PV is then defined:

$$PV = \frac{1}{C} \sum_{combinations} D(z_i, z_j), \tag{5.1}$$

where

$$D(z_i, z_j) = \frac{|z_i - z_j|}{max\,(z_i, z_j)} = 1 - \frac{min\,(z_i, z_j)}{max\,(z_i, z_j)}. \tag{5.2}$$

Used by Adam (2009) for quantifying variability in backscatter measurements from acoustic surveys, the author notes that the measure is "robust to zero-inflated and highly skewed data." That suits precipitation data rather well. Fortunately, it fits our exact needs rather well, too. Because

[3]This is an unfortunate abbreviation to use in atmospheric science considering the importance of potential vorticity.

PV relies on combinations, the calculation can grow rapidly out of hand. The small sample size is a benefit in our case.

Figure 5.18 shows data equivalent data to Figure 5.15 but with PV instead of the COV. On the PV scale, zero indicates zero spread, and one indicates an incredibly high spread. It is actually difficult to obtain values near one. As the PV is measure of ratios, only datasets varying wildly over many orders of magnitude achieve such values. The correlation to CAPE has increased to 0.733, and the red points that were incorrectly placed at poor predictability have been shifted to better predictability values. Both measures of variability have unfortunate features when the data is comprised of zeros. *C'est la vie.*

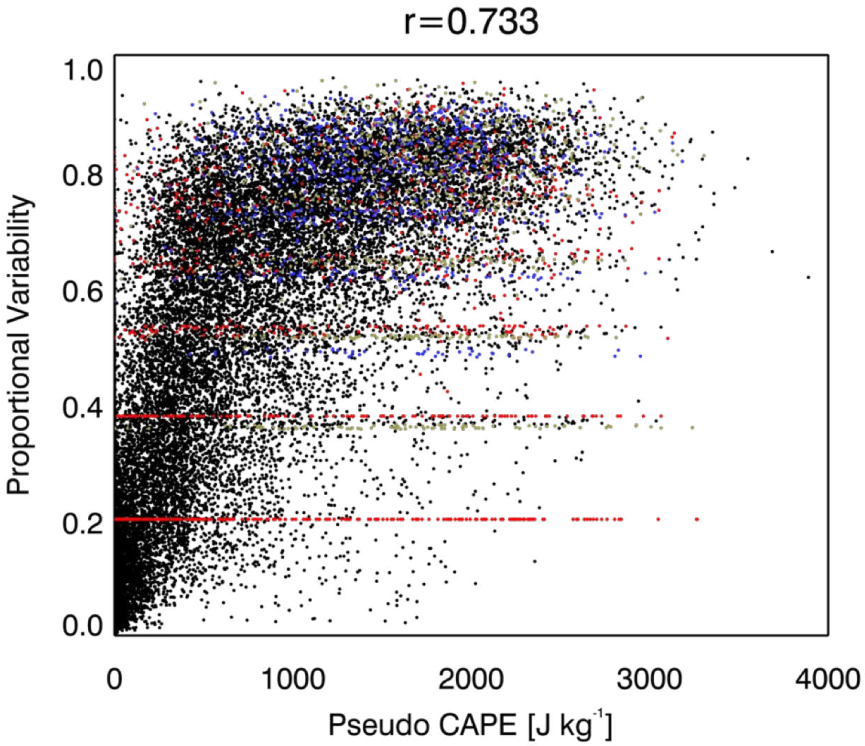

FIGURE 5.18: As in Figure 5.15, but for proportional variability instead of the COV. The colored points are the same in time and space.

The long-term global picture of the CAPE and PV relationship is shown in Figure 5.19. In this case, there are PV minima more often associated with CAPE minima, yielding a long-term

mean spatial correlation of 0.907, considerably higher than in the COV case. The global mean of the local temporal correlations is also increased, owing to near global positive correlations. Overall, we have a stronger association with the PV measure of predictability; CAPE above 1000 J kg^{-1} almost always yields wide CPM precipitation rate spreads. When CAPE is lower than this, PV increases by approximately 0.08 for every 100 J kg^{-1} increase in CAPE. This is our first useful, consistent relationship between a variable derived from the large-scale state and uncertainty in the precipitation rate.

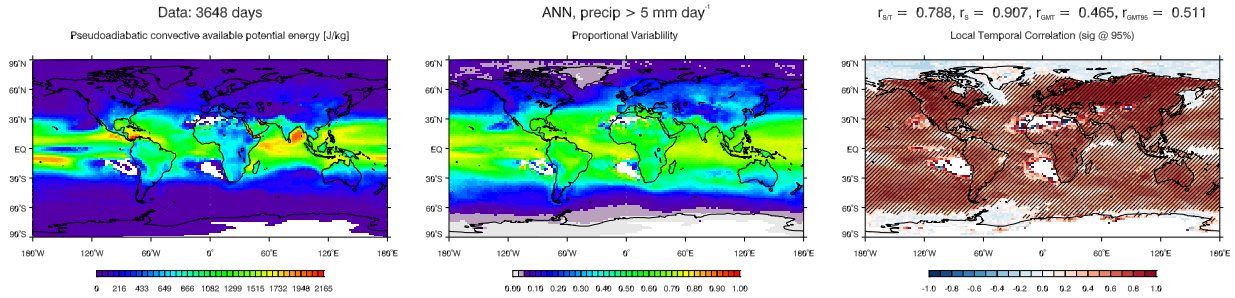

FIGURE 5.19: As in Figure 5.16 but considering PV instead of the COV.

Finally, the COV and PV long-term means are compared in Figure 5.20, conditioned on three minimum daily precipitation rate thresholds. A number of regions show correlative patterns, though the aforementioned problems with COV are clear. Many of the problems with high COV points are removed when the highest precipitation rates are considered, however there is a significantly smaller pool of data at that point. Also, as the threshold increases, the global mean COV tends to decrease, whereas PV tends to be more invariant in that sense. The global scene as it relates to the data at the time of Table 5.1 is shown in Figure 5.21. Even in this short span of time, we can begin to see the association between CAPE and PV. However, this is not universally the case, as the two do not align over the Indian Ocean where precipitation rates were low. COV, on the other hand, tends not to correlate with CAPE in any positive sense over this interval.

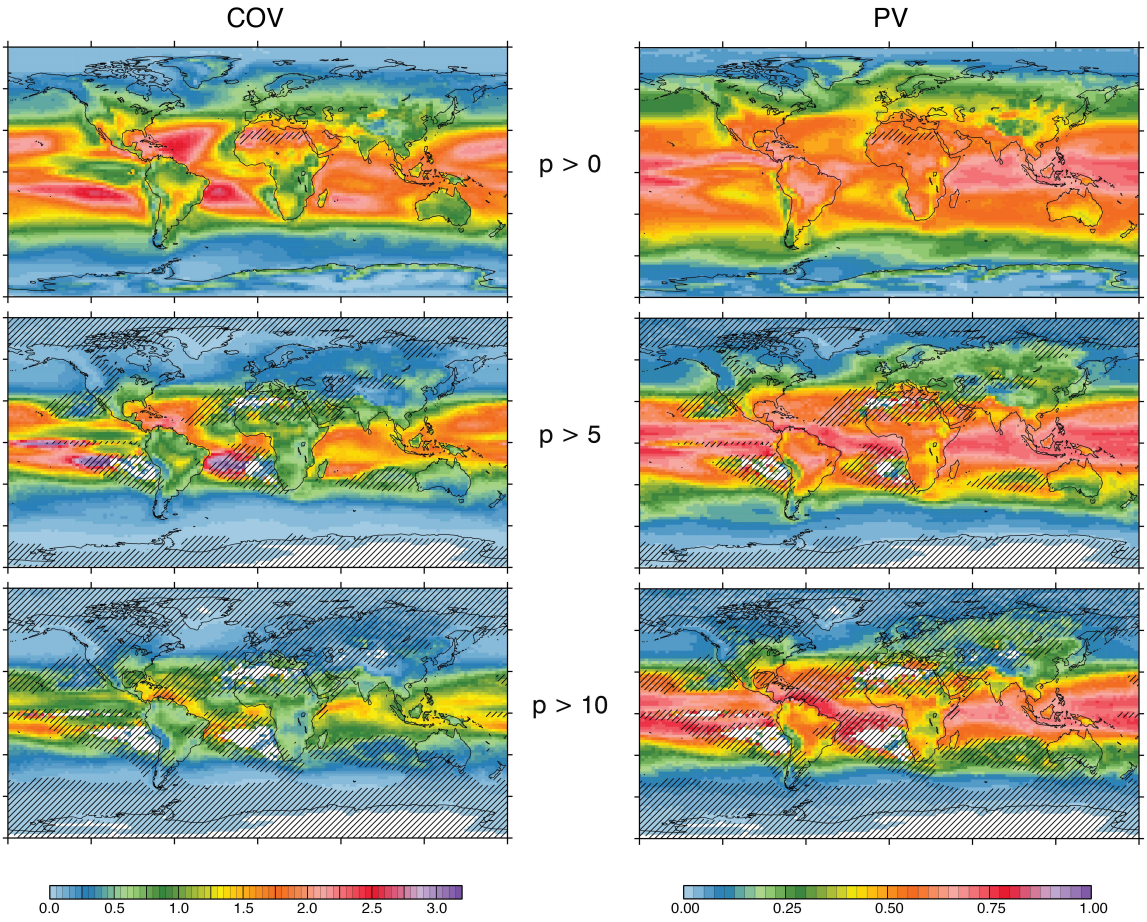

FIGURE 5.20: Time averaged COV (left) and PV (right) for days with precipitation rates greater than 0 (top), 5 (middle), and 10 (bottom) mm day^{-1}. Black diagonal shading indicates where the threshold is met for less than 5% of the available data record.

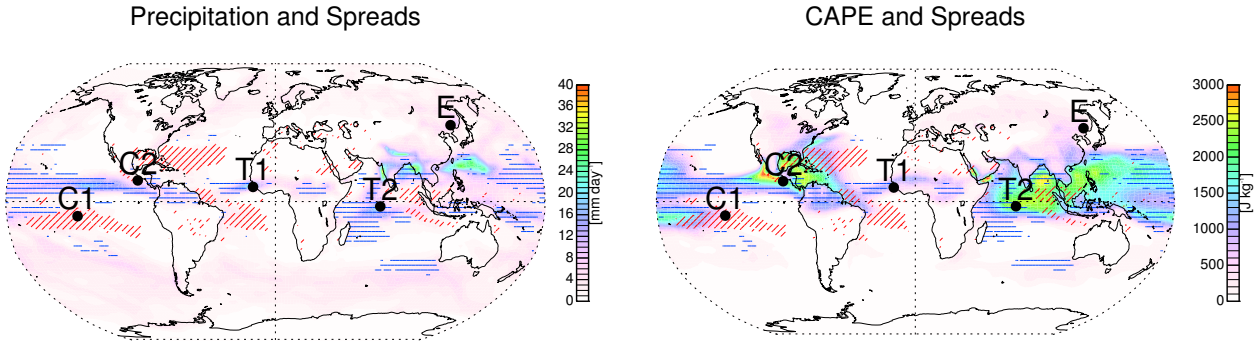

FIGURE 5.21: Time mean precipitation rate (top) and CAPE (bottom) rom MP 3-hourly data obtained for July of year 9 with points marked as in Table 5.1. Red diagonal lines highlight locations where the time mean COV is greater than 2.5, and blue horizontal lines highlight locations where the time mean PV is greater than 0.6.

5.3. PRECIPITATION PREDICTABILITY ASSOCIATIONS

In the search for more associations between the large-scale (or convective-scale as CPM variables were also considered) state and predictability as measured by MP CPM ensemble PV[4], PV correlation analyses like those in Figure 5.19 were performed for each of the daily mean variables in Table 2.2 with consideration of multiple vertical levels in the case of three-dimensional variables. To more rapidly identify features exhibiting strong, statistically significant linear correlations with PV, the global mean of the significant local temporal correlation coefficients, r_{GMT95} in the figures, was the parameter of interest. To more *slowly* identify features exhibiting clear, nonlinear associations with PV, two-dimensional histograms of PV and comparison variables were computed and scanned visually. Additionally, derived variables suggested by information in the literature regarding the variability and/or predictability of precipitation were computed for further comparisons.

We will begin with an easily understandable case. One often cited initiator of convection is forced uplift from topography. Both height above sea level and maximum local topographic slope were considered as potential predictors of PV. In the global sense, mean correlations of these variables are biased by large numbers of points near zero height and slope, whereby only other parameters could be of significant influence. The global spatial pattern correlation between PV and slope, however, was recorded at -0.266, meaning that low (predictable) values of PV are associated with strongly sloped surfaces as expected. Correlations with simple altitude, while also negative everywhere were much weaker except in regions of very high mountains. Being constant features, these associations are good to be aware of but not particularly interesting.

Topping the list of variables from Table 2.2 with strong linear correlations to the PV (aside from the CPM ensemble precipitation standard deviation) were CAPE, as shown previously, in

[4]AKA "predicting predictability."

the positive sense, and cloud fraction at 700 mb in the negative sense. As this is the upper limit of the CAM definition of "low clouds" and because the results are nearly identical, the analysis for low cloud fraction is shown in Figure 5.22. Over most of the globe, local temporal correlations are strongly and significantly negative. This orientation suggests that dense cloud cover points to better predictability, which is likely because dense cloud cover means strong forcing from the large-scale in the form of a spatially large disturbance. Interestingly, we now learn that when the correlations are negative, the PV anomalous values (e.g. 0.2 for the 9:1 no precipitation ratio), skew the correlation results. The same analysis using the COV shows a much more uniformly blue plot in the tropics because the maximum COV outliers in the infrequent and low precipitation regions occur with generally low values of low cloud fraction. Also like the opposite sign COV correlations with CAPE, the anomalous correlations between PV and low cloud fraction vanish when increasing the analysis precipitation threshold to 10 mm day^{-1}. There is little change in the spatial pattern correlation coefficient, as it remains very strong regardless of the precipitation threshold. There is a rapid transition in PV values near low cloud fraction of approximately 0.4 such that most points with low cloud fraction above 0.4 have PV below 0.2, and most points with low cloud fraction below 0.3 have PV near 0.8.

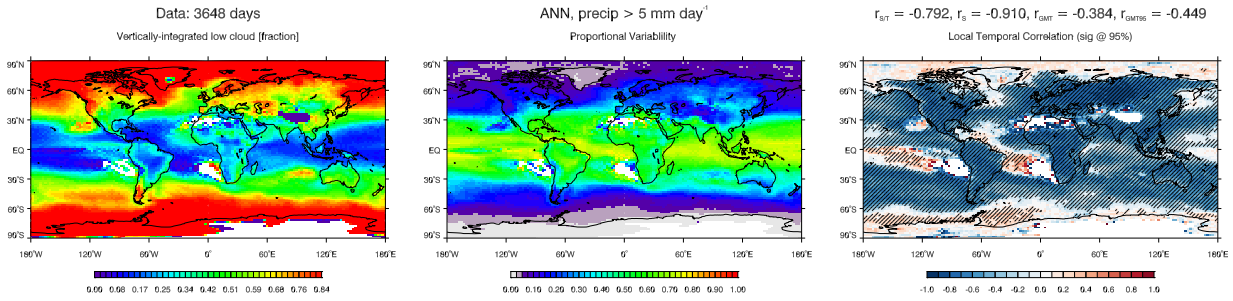

FIGURE 5.22: As in Figure 5.19 for low cloud fraction.

A number of cloud and moisture related variables exhibit strong negative correlations much like the low cloud fraction because they indicate the presence of spatially large disturbances.

These include cloud amounts at all levels, cloud ice and liquid concentrations, precipitation frequency, the precipitation rate itself, relative humidity, and mid-level (but not low or upper-level) specific humidity. A similar idea is found in the correlation to vertical pressure velocity, which is positive by nature of the sign orientation of the variable but indicative of the same type of large disturbance.

Some variables do show differing relationships depending on location. For instance, the sensible (not shown) and latent heat flux (Figure 5.23) and the boundary layer height (Figure 5.24) tend to show positive correlations over land and in the southern extratropics and negative correlations over ocean in the tropics. Global means of the local temporal correlations for these variables tend to be near zero in the annual mean, and they exhibit strong seasonality. Strong positive correlations over land are most prominent in the summer hemisphere, matching the associations with surface temperature and the tendency for sparse convection

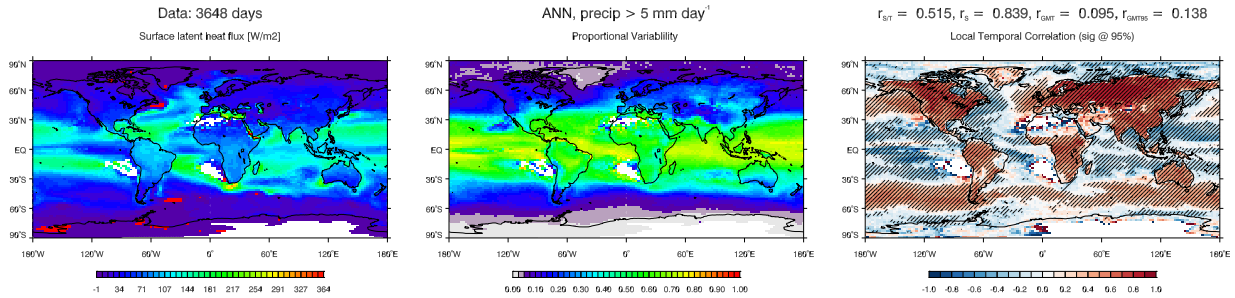

FIGURE 5.23: As in Figure 5.19 for the latent heat flux.

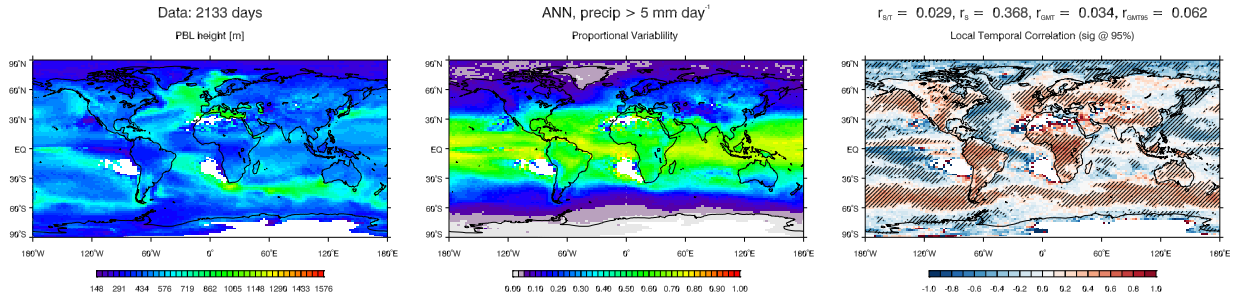

FIGURE 5.24: As in Figure 5.19 for the planetary boundary layer height.

In addition to CAPE, strong positive correlations were found in association with net shortwave radiation at the surface, mid-level drying tendencies from the CPM, low level positive temperature and specific humidity anomalies, and mid-level turbulence kinetic energy and cloud mass flux in the CPM. None of these associations are particularly surprising. They highlight features associated with sparse convection unrelated to large, organized systems. In fact, analysis of the size of the largest precipitation cell within the CPMs shows that smaller cells are very strongly associated with high PV (Figure 5.25). When precipitation cells cover the full CPM they are associated with very low PV values and much greater predictability. This points to greater predictability in domain averaged precipitation rate in the presence of organized systems. It says nothing at all about the predictability of their timing or position on the small scale, however.

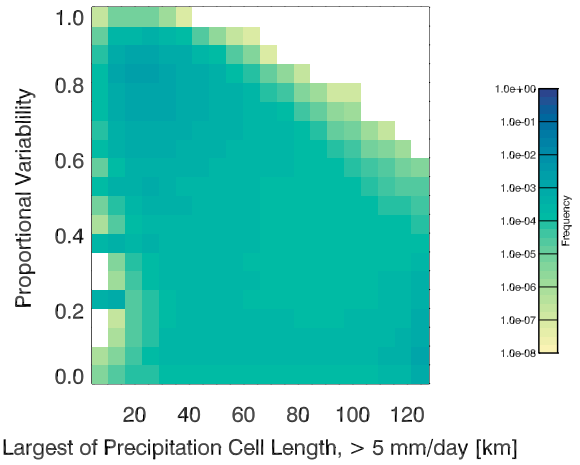

FIGURE 5.25: Two-dimensional histogram relating PV and the size of the largest precipitation cell length inside the CPMs.

A number of associations with organization related parameters support this argument. A negative correlation is present across the globe with vertical wind shear at various heights from the surface. Vertical wind shear tends to organize convection into meso-scale systems since shear tends to displace convective updrafts from precipitation induced downdrafts that may act to kill convection if they were vertically aligned (Liu and Moncrieff 2001). Similarly, an organization

parameter defined as

$$V_{ORG} = \frac{2\overline{w'^2}}{\overline{u'^2} + \overline{v'^2}} \tag{5.3}$$

where each term represents the vertical integral of the variance of the specified wind component within the CRM. Across a full domain, one would expect small values in the presence of organization due to large variance in the horizontal wind speeds. As such, significant global mean correlation coefficients with V_{ORG} are positive at 0.32, indicating greater predictability in the presence of organization. Additionally, the Richardson number, essentially the ratio of CAPE to the vertical wind shear, tends to be large in the presence of pulse storms and small under strong, organized systems. Its significant correlations to PV, which exist nearly exclusively in the storm track regions of the extratropics are all positive, averaging approximately 0.4. The results so far, then, match with the limited analysis of Zawadzki et al. (1994) mentioned in Section 2.2.

With much time spent examining these relationships, it became clear that no single variable seems to directly indicate a level of predictability with great specificity, and one may be concerned that a number of the features could be washed out in the daily average when the life cycles of many convective systems are on timescales much less than a day. While it would be wonderful to examine these relationships at individual GCM time steps, we were not able to produce long enough spans of such data to compute significant statistics due to data storage limitations. As a compromise, I focus the remaining analyses on 3-hourly data produced for years 21 through 23 of the MP simulation. This coincidentally provides roughly the same number of points in time as the 24 year daily dataset.

While there was little correlation between CIN and PV, there is reason to believe that its presence in association with CAPE may have some bearing on the predictability of precipitation. Computing the average value of PV in bins of CAPE and CIN produces the data displayed in Figure 5.26. Viewing the data in this way, we can now see that there is a tendency for PV to

maximize near CAPE values of 1000 J kg^{-1} when CIN is below 20 J kg^{-1} and near 500 J kg^{-1} when CIN is above 40 J kg^{-1}. We also see that PV tends to be higher for large values of CIN when CAPE is low. These combinations indicate lower predictability in the presence of strong convective limitations, such that convection is possible but unlikely because something like a strong inversion cap needs to be overcome in order to produce precipitation. Since this is difficult and may only happen by chance variations in the CPM fields, ensemble members are likely to disagree. Also notice that the PV becomes lower for the highest CAPE values when CIN is low. In those situations, instabilities are realized more effectively and regularly, leading to more likely agreement in the ensemble members.

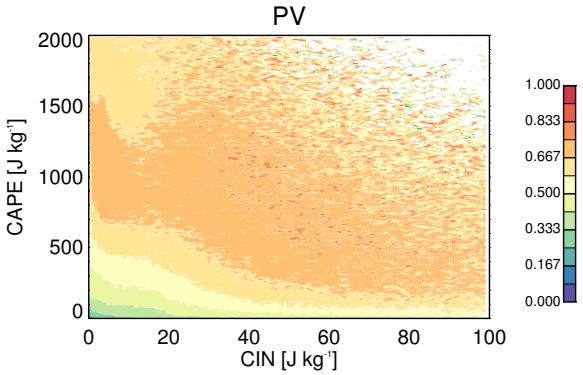

FIGURE 5.26: Mean PV in bins of CAPE and CIN for the full 3-hourly dataset of MP years 21-23.

The amount of precipitable water also shows PV dependence (Figure 5.27). Precipitation rate is a very strong function of precipitable water, with maximum values occurring for precipitable water greater than 60 kg m^{-2} and a very quick transition to extreme precipitation rates near that value following that transition. Almost regardless of CAPE, PV is also maximized along that transition. This relationship brings to mind the results of Neelin et al. (2009) shown in Figure 3.2. One of the conclusions of their work was that precipitation variance is maximized at a critical value of precipitable water, w_c, which in turn is a function of vertically averaged temperature, $\hat{T}$ in the troposphere.

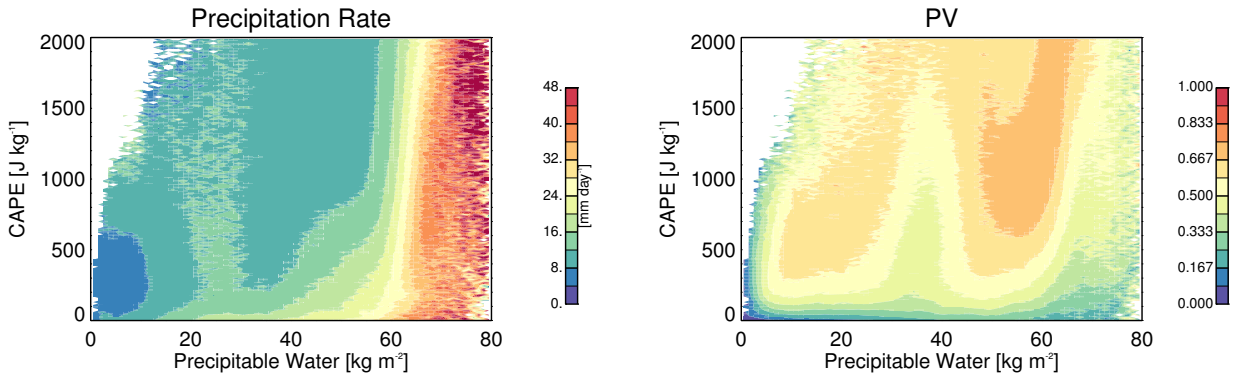

FIGURE 5.27: As in Figure 5.26 but for CAPE and precipitable water, showing mean precipitation (left) and mean PV (right).

While one can repeat the analysis to derive w_c as a function of precipitation, vertically averaged temperature, and precipitable water though a complex system of curve fitting, I find that their solutions are robust enough to derive a simple linear functional relationship to compute w_c based on the data reported in their paper, such that

$$w_c = 2.3714\hat{T} - 579.3, \tag{5.4}$$

where temperature is in Kelvin and w_c is then in kg m^{-2}. This is true even though their analyses were performed on 6-hourly data exclusively over the tropical oceans. Limiting the analysis to the Tropics as defined by $\pm 20^{\circ}$ latitude, Figure 5.26 shows mean precipitation and PV for bins of CAPE and the ratio w/w_c. When w/w_c equals one, precipitation variance should be maximized by the arguments of self-organizing criticality near the transition to strong precipitation, whatever that critical value is for a given location. With rather striking similarity, we see that PV also has a maximum when the critical ratio is equal to one and just above one. This fits quite well with Figure 5.29 taken from Neelin et al. (2008), which plots precipitation variance as a function of the same ratio. In the view of Neelin et al. (2008), this is behavior native to chaotic systems at points of quasi-equilibrium. Since we have empirically tested for predictability through PV, the match between these two methods lends confidence to its significance and truth. It should be noted that

COV does not capture this relationship well at all, putting high values at low precipitable water critical ratios.

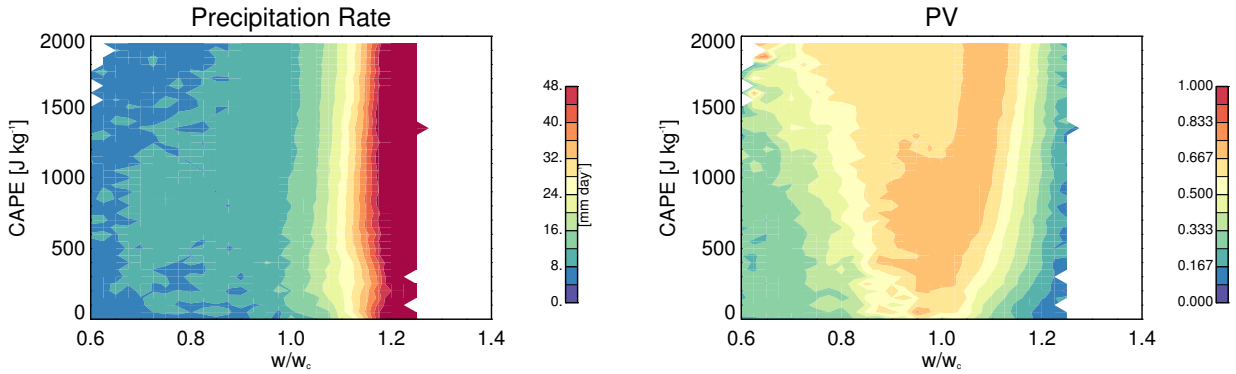

FIGURE 5.28: As in Figure 5.26 but for CAPE and critical precipitable water ratio, w/w_c, showing mean precipitation (left) and mean PV (right) for data over the tropics only.

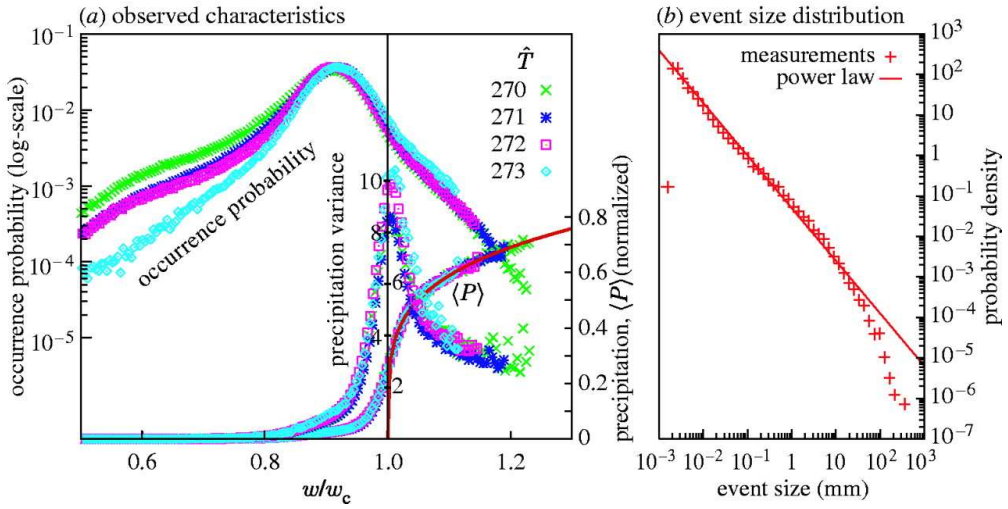

FIGURE 5.29: Caption as in Neelin et al. (2008): (a) Western Pacific observed characteristics from TMI data as a function of column water vapour normalized by the critical value w_c for each value of $\hat{T}$: probability density function of w for precipitating points (four upper curves), precipitation variance conditioned on w (four middle curves) and precipitation pickup curve (non-dimensionalized by amplitude a from (4.1) for each $\hat{T}$). (b) The precipitation event-size distribution for the Nauru ARM site time series.

Not to rest on our laurels with that remarkable result, we continue to investigate other possible relationships. It was proposed in Section 2.2 that some dependency of precipitation may be found along certain critical values of convective triggers. The right panels of Figure 4.70 indicate

that this is not necessarily the case for potential thresholds of relative humidity and vertical velocity. However, results spanning the entirety of the tropics indicate a tendency for peak PV values isolated near 500 mb pressure velocities of -0.25 with little dependence on the coincident relative humidity values (not shown). CAPE, which is often used as part of a triggering mechanism in conventional convective parameterizations, though has been shown to have some PV dependence. Another avenue of investigation is severe weather indices. The total totals index is used to predict the likelihood and nature of thunderstorms based on vertical temperature and dewpoint structure. Similar indices, the modified K-index, and the lifted index, are also moist-thermodynamic stability indices used to indicate convective potential. An additional instability index, named simply the "instability index" by Raymond et al. (2015), which is based on vertical differences in low and mid-level vertically averaged layers of saturated moist entropy. Any of these may present thresholds that correspond to low predictability.

Figure 5.30 shows the mean PV values for bins of these stability indices and CAPE. In operational meteorology, the total totals index purports to indicate likely isolated thunderstorms for values above 44, becoming progressively more intense and organized with increasing values.

$$TT = T_{850} + T_{d850} - 2T_{500} \tag{5.5}$$

Our results show PV maximizing mainly as the index approaches 45 regardless of CAPE values (the maxima near 20 is based on very few values), and then PV decreases again as the index increases, tending toward more organized systems. Operationally, the modified K-index is expected to indicate high convective potential for values above 40.

$$KI = (T_{\overline{sfc-850}} - T_{500}) + T_{\overline{dsfc-850}} - (T_{700} - T_{d700}) \tag{5.6}$$

Perhaps at this point, it is not surprising that PV peaks at and above 40. There is more of a dependence on CAPE with this index and a broadening of the high-PV modified K-index range with increasing CAPE. This is consistent with precipitation variability shown by Davies et al. (2013) in data near Darwin, Australia previously presented in Figure 3.3.

The lifted index indicates extreme instability for values less than -8, which is where we see a sharp maxima in PV at all CAPE values.

$$LI = T_{500} - T_{parcel500} \tag{5.7}$$

Higher values of the lifted index show more cape dependence, and the PV maximum at the lifted index of 20 tends to occur at a number of points in the tropics, particularly on the northern and southern edges in the Pacific. These results support those of Zhang et al. (2003a) who show such low lifted index values at locations of strong model error growth in the fifth-generation mesoscale model (MM5). The last index, the instability index is conditioned about zero, where positive values indicate greater instability. Climatologically, the instability index has strong maxima over land, where high PV values are less prevalent. Though PV is large at high values of the instability index, its maximum is located near the stability threshold on the stable side. Each of these is coincident with the edge of the precipitation maximum in a manner similar to the ratio w/w_c and these indices show appropriate local temporal correlations that agree with the relationships shown.

A number of other parameters and combinations of parameters were tested, as well, but the relationships discussed in this section are the most consistent and significant among those that are easily calculated from the GCM state. Others 3-hourly data of note include surface fluxes in conjunction with wind shear, CAPE in conjunction with wind shear (like the Richardson number),

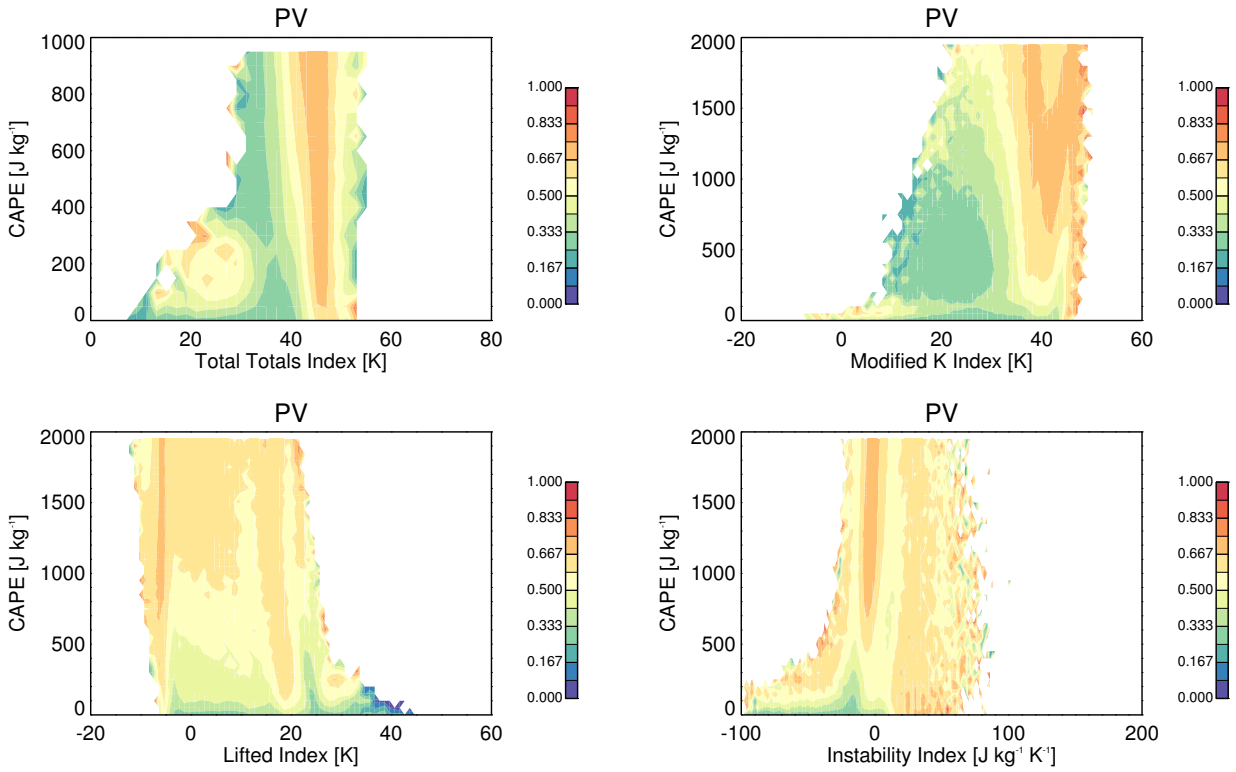

FIGURE 5.30: As in Figure 5.26 but CAPE and the total totals index (upper left), modified K-index (upper right), lifted index (lower left), and instability index (lower right), showing mean PV (right) for data over the tropics only.

and column saturation fraction. While a few basic variables show some association with precipitation predictability as measured by the PV of CPM ensemble precipitation rates, namely positive correlations with CAPE and negative correlations with moisture and cloud conditions indicative of large-scale disturbances, the most direct associations are those relating to critical phenomena. These include critical precipitable water and a variety of moist-thermodynamic stability indices. Even the indices show peak PV coincident with the critical transition to strong precipitation. Based on the information analyzed here, those are the parameters for which, to leading order, precipitation is least predictable.

CHAPTER 6 – CONCLUSIONS

The efforts cataloged herein describe the use of a novel modeling technique to uncover statistical relationships between the predictability of precipitation and characteristics of the large-scale atmosphere that can be resolved on a GCM grid. By modifying the concept of superparameterization to simultaneously run 10 CPMs we can analyze multiple realizations that explore possible precipitative outcomes of a single large-scale state. At the same time, the design of the model was appropriate to test the performance of a deterministic climate model, made so by averaging the physical tendencies produced by the 10 CPMs.

It was the initial hope that the new, more deterministic MP framework would still produce a good representation of the mean state climate and intraseasonal variability in the form of the MJO. For the most part, these goals were achieved. A variety of metrics show the more deterministic nature of the MP-CAM. This was not achieved to the level that one might theorize because the averaging of the CPM tendencies does not happen in a vacuum. Dynamic interactions with the multiple CPMs of the MP framework with the host GCM did alter the mean state climate in some significant ways, particularly with respect to the distributions of high and low clouds due to feedbacks to the mean CPM tendencies. This further caused enhancement of the convective mass flux inside tropical CPMs, resulting in unexpected changes in high clouds and OLR. Specifically, the fraction of high clouds increased, OLR decreased, and global mean precipitation was made to follow suit. The changes to variability in the convective fields did cause a slight degradation in the MJO representation, specifically with regard to its propagation out of the source region and a loss of spectral power at MJO wavenumbers and frequencies. In that sense, the MP framework moved the SP representation closer to that of the standard CAM, which is rather poor. As

a climate model, MP-CAM is not an improvement on the spatially and temporally jagged and stochastic convective scale tendencies of SP-CAM.

In Chapter 5 we tackled the analysis of predictability in the MP framework. There were a number of surprises along the way regarding the specific ways in which the CPMs sometimes handle the generation of precipitation and the methods one can use to reliably quantify predictability given an ensemble of realizations with limited sample size. It was determined that the proportional variability, used to provide a relative, scale-aware measure of ensemble spread, is a reasonable choice for small samples of precipitation data that are often inundated with zero values. Even with its noted faults, PV is a conceptually superior measure compared to the COV.

By comparing the PV to a large variety of large-scale parameters, it was determined that the predictability of precipitation is modulated by a number of environmental factors. Nearly every parameter tested had some significant correlation to the PV, either in the global mean or at specific locations at specific times of the year. Strong surface forcing tends to indicate poor predictability in summer months, and strong forcing from the GCM tends to indicate better predictability. This was evidenced by relationships with features indicating the widespread presence of cloudiness or strong moisture anomalies. Chief among the basic indicators of poor predictability was the large-scale potential for convective activity, CAPE. When CAPE is large, there is at least the possibility that convection can be strong if it happens to be initiated. Indicators of potential mesoscale organization within the CPM domain, whether inferred from GCM parameters or by investigating the state of the CPMs on their own grid, were weakly correlated with better predictability. Since most organization of convection derives from the state of the environment, like vertical wind shear, and because organization has an element of self-sufficiency once it is initiated, the likelihood for CPM ensemble member agreement is increased on average. The relationship is probably not stronger due the barriers to initiating convection that is organized or

convection in general; it is very likely that crossing the threshold to organization will occur by way of chance variations on the CPM scale in the absence of clear, sustained direction from the GCM. Crossing thresholds of certain parameters, including the ratio of critical column water vapor to the actual GCM column water vapor and certain values of a number of commonly used convective instability indices, was the most reliable indicator of poor predictability. This makes sense intuitively, as critical change phenomena are, by their nature, confined to a limited parameter space. Falling on one side of the value or the other can yield vastly different results within an ensemble of possibilities, and therefore large values of PV.

Coming off of these results, one can proceed in multiple different directions. There is a lot of room to make modifications to the MP framework. One could envision employing a larger number of ensemble members to develop even better predictability statistics or to arrive at more consistent expected values for the purposes of a more deterministic model. However, the ways in which such an ensemble splits up the duties of reducing convective instabilities remains uncertain, and the possibilities shown here were not always encouraging. Because of that one may try a different formulation for the tendencies from the CPM ensemble. For instance, since simple averages can be biased for skewed data, we might be better off applying some formulation of the median CPM result. This could, however, prove inconsistent considering the vertical component of the tendencies and the subsequent possibility of an incoherent tendency profile.

With regard to determining predictability relationships, there are many more variables to be tested. There are probably on the order of 100 different stability indices, and new ones are perpetually being devised. Beyond that, checking various combinations of parameters seems like a fruitful pursuit, such as how moisture convergence or upper-level dynamical forcing pairs with the stability indices. I would particularly like to explore the distribution of PV values for the different ISSCP cloud regimes, as there is so much similarity in the structures of those fields. Going

in a different direction, there is still much that can be explored on the CPM level. Whatever the choice, there remains much to be discovered in these areas, and further enhancements to model design and continued research into areas of uncertain precipitation will continue to improve our understanding and forecasting abilities.

REFERENCES

Adam, P., 2009: Quantifying spatial and temporal variability of distribution patterns in acoustic backscatter density with synoptic airborne LIDAR. M.S. thesis, University of Washington.

Ahmed, F., and C. Schumacher, 2015: Convective and stratiform components of the precipitation-moisture relationship. *Geophys. Res. Lett.*, **42 (23)**, 10,453–10,462, doi:10.1002/2015GL066957.

Anber, U., S. Wang, and A. Sobel, 2014: Response of atmospheric convection to vertical wind shear: Cloud-system-resolving simulations with parameterized large-scale circulation. part i: Specified radiative cooling. *J. Atmos. Sci.*, **71 (8)**, 2976–2993, doi:10.1175/JAS-D-13-0320.1.

Anderson, B. T., D. Gianotti, G. Salvucci, and J. Furtado, 2016: Dominant timescales of potentially predictable precipitation variations across the continental United States. *J. Climate*, doi:10.1175/JCLI-D-15-0635.1.

Arakawa, A., 2004: The cumulus parameterization problem: Past, present, and future. *J. Climate*, **17 (13)**, 2493–2525, doi:10.1175/1520-0442(2004)017⟨2493:RATCPP⟩2.0.CO;2.

Arakawa, A., and W. H. Schubert, 1974: Interaction of a cumulus cloud ensemble with the large-scale environment, Part I. *J. Atmos. Sci.*, **31 (3)**, 674–701, doi:10.1175/1520-0469(1974)031⟨0674:IOACCE⟩2.0.CO;2.

Bauer, P., A. Thorpe, and G. Brunet, 2015: The quiet revolution of numerical weather prediction. *Nature*, **525 (7567)**, 47–55, doi:10.1038/nature14956.

Bechtold, P., 2008: Convection parametrization. *Proc. Seminar on Parametrization of Subgrid Physical Processes, 1-4 September 2008*, Shinfield Park, Reading, UK, ECMWF, 63–85, [Available online at http://www.ecmwf.int/sites/default/files/elibrary/2009/8008-convection-parametrization.pdf].

Bechtold, P., M. Köhler, T. Jung, F. Doblas-Reyes, M. Leutbecher, M. J. Rodwell, F. Vitart, and G. Balsamo, 2008: Advances in simulating atmospheric variability with the ECMWF model: From synoptic to decadal time-scales. *Quart. J. R. Meteorol. Soc.*, **134 (634)**, 1337–1351, doi: 10.1002/qj.289.

Bechtold, P., N. Semane, P. Lopez, J.-P. Chaboureau, A. Beljaars, and N. Bormann, 2013: Representing equilibrium and nonequilibrium convection in large-scale models. *Journal of the Atmospheric Sciences*, **71 (2)**, 734–753, doi:10.1175/JAS-D-13-0163.1, URL http://dx.doi.org/10.1175/JAS-D-13-0163.1.

Benedict, J. J., and D. A. Randall, 2007: Observed characteristics of the MJO relative to maximum rainfall. *J. Atmos. Sci.*, **64 (7)**, 2332–2354, doi:10.1175/JAS3968.1.

Berner, J., K. R. Fossell, S. Y. Ha, J. P. Hacker, and C. Snyder, 2015: Increasing the skill of probabilistic forecasts: Understanding performance improvements from model-error representations. *Mon. Wea. Rev.*, **143 (4)**, 1295–1320, doi:10.1175/MWR-D-14-00091.1.

Berner, J., T. Jung, and T. N. Palmer, 2012: Systematic model error: The impact of increased horizontal resolution versus improved stochastic and deterministic parameterizations. *J. Climate*, **25 (14)**, 4946–4962, doi:10.1175/JCLI-D-11-00297.1.

Berner, J., G. J. Shutts, M. Leutbecher, and T. N. Palmer, 2009: A spectral stochastic kinetic energy backscatter scheme and its impact on flow-dependent predictability in the ECMWF Ensemble Prediction System. *J. Atmos. Sci.*, **66 (3)**, 603–626, doi:10.1175/2008JAS2677.1.

Bluestein, H. B., and M. H. Jain, 1985: Formation of mesoscale lines of pirecipitation: Severe squall lines in Oklahoma during the spring. *J. Atmos. Sci.*, **42 (16)**, 1711–1732, doi:10.1175/1520-0469(1985)042⟨1711:FOMLOP⟩2.0.CO;2.

Bluestein, H. B., G. T. Marx, and M. H. Jain, 1987: Formation of mesoscale lines of precipitation: Nonsevere squall lines in Oklahoma during the spring. *Mon. Wea. Rev.*, **115 (11)**, 2719–2727, doi:10.1175/1520-0493(1987)115⟨2719:FOMLOP⟩2.0.CO;2.

Bowler, N. E., A. Arribas, S. E. Beare, K. R. Mylne, and G. J. Shutts, 2009: The local ETKF and SKEB: Upgrades to the MOGREPS short-range ensemble prediction system. *Q.J.R. Meteorol. Soc.*, **135 (640)**, 767–776, doi:10.1002/qj.394.

Bretherton, C. S., J. R. McCaa, and H. Grenier, 2004a: A new parameterization for shallow cumulus convection and its application to marine subtropical cloud-topped boundary layers. Part I: description and 1D results. *Mon. Wea. Rev.*, **132 (4)**, 864–882, doi:10.1175/1520-0493(2004)132⟨0864:ANPFSC⟩2.0.CO;2.

Bretherton, C. S., M. E. Peters, and L. E. Back, 2004b: Relationships between water vapor path and precipitation over the tropical oceans. *J. Climate*, **17 (7)**, 1517–1528, doi:10.1175/1520-0442(2004)017⟨1517:RBWVPA⟩2.0.CO;2.

Bretherton, C. S., M. Widmann, V. P. Dymnikov, J. M. Wallace, and I. Bladé, 1999: The effective number of spatial degrees of freedom of a time-varying field. *J. Climate*, **12 (7)**, 1990–2009, doi:10.1175/1520-0442(1999)012⟨1990:TENOSD⟩2.0.CO;2.

Bright, D. R., and S. L. Mullen, 2002: Short-range ensemble forecasts of precipitation during the southwest monsoon. *Wea. Forecasting*, **17 (5)**, 1080–1100, doi:10.1175/1520-0434(2002)017⟨1080:SREFOP⟩2.0.CO;2.

Brousseau, P., Y. Seity, D. Ricard, and J. Léger, 2016: Improvement of the forecast of convective activity from the AROME-France system. *Q.J.R. Meteorol. Soc.*, n/a–n/a, doi:10.1002/qj.2822.

Buizza, R., M. Miller, and T. N. Palmer, 1999: Stochastic representation of model uncertainties in the ecmwf ensemble prediction system. *Q.J.R. Meteorol. Soc.*, **125 (560)**, 2887–2908, doi: 10.1002/qj.49712556006.

Charron, M., G. Pellerin, L. Spacek, P. L. Houtekamer, N. Gagnon, H. L. Mitchell, and L. Michelin, 2010: Toward random sampling of model error in the Canadian Ensemble Prediction System. *Mon. Wea. Rev.*, **138 (5)**, 1877–1901, doi:10.1175/2009MWR3187.1.

Chen, B., J. Li, and R. Ding, 2006: Nonlinear local Lyapunov exponent and atmospheric predictability research. *Science in China Series D: Earth Sciences*, **49 (10)**, 1111–1120, doi: 10.1007/s11430-006-1111-0.

Chikira, M., and M. Sugiyama, 2010: A cumulus parameterization with state-dependent entrainment rate. Part I: Description and sensitivity to temperature and humidity profiles. *J. Atmos. Sci.*, **67 (7)**, 2171–2193, doi:10.1175/2010JAS3316.1.

Cho, H.-R., 1993: A mechanism causing mesoscale organizations of precipitation in midlatitude cyclones. *J. Appl. Meteor.*, **32 (2)**, 155–160, doi:10.1175/1520-0450(1993)032⟨0155:AMCMOO⟩ 2.0.CO;2.

Clark, A. J., W. A. Gallus, M. Xue, and F. Kong, 2009: A comparison of precipitation forecast skill between small convection-allowing and large convection-parameterizing ensembles. *Wea. Forecasting*, **24 (4)**, 1121–1140, doi:10.1175/2009WAF2222222.1.

Clark, A. J., W. A. Gallus, M. Xue, and F. Kong, 2010a: Growth of spread in convection-allowing and convection-parameterizing ensembles. *Wea. Forecasting*, **25 (2)**, 594–612, doi:10.1175/ 2009WAF2222318.1.

Clark, A. J., W. A. Gallus, M. Xue, and F. Kong, 2010b: Convection-allowing and convection-parameterizing ensemble forecasts of a mesoscale convective vortex and associated severe weather environment. *Wea. Forecasting*, **25 (4)**, 1052–1081, doi:10.1175/2010WAF2222390.1.

Cohen, B. G., and G. C. Craig, 2006: Fluctuations in an equilibrium convective ensemble. Part II: Numerical experiments. *J. Atmos. Sci.*, **63 (8)**, 2005–2015, doi:10.1175/JAS3710.1.

Couvreux, F., and Coauthors, 2015: Representation of daytime moist convection over the semi-arid Tropics by parametrizations used in climate and meteorological models. *Q.J.R. Meteorol. Soc*, **141 (691)**, 2220–2236, doi:10.1002/qj.2517.

Dai, A., 2006: Precipitation characteristics in eighteen coupled climate models. *Journal of Climate*, **19 (18)**, 4605–4630, doi:10.1175/JCLI3884.1, URL http://dx.doi.org/10.1175/JCLI3884.1.

Davies, L., C. Jakob, P. May, V. V. Kumar, and S. Xie, 2013: Relationships between the large-scale atmosphere and the small-scale convective state for Darwin, Australia. *J. Geophys. Res. Atmos.*, **118 (20)**, 11,534–11,545, doi:10.1002/jgrd.50645.

Del Genio, A. D., and W. Kovari, 2002: Climatic properties of tropical precipitating convection under varying environmental conditions. *J. Climate*, **15 (18)**, 2597–2615, doi:10.1175/1520-0442(2002)015⟨2597:CPOTPC⟩2.0.CO;2.

Del Genio, A. D., J. Wu, and Y. Chen, 2012: Characteristics of mesoscale organization in WRF simulations of convection during TWP-ICE. *J. Climate*, **25 (17)**, 5666–5688, doi:10.1175/JCLI-D-11-00422.1.

DeMott, C. A., D. A. Randall, and M. Khairoutdinov, 2007: Convective precipitation variability as a tool for general circulation model analysis. *J. Climate*, **20 (1)**, 91–112, doi:10.1175/JCLI3991.1.

DeMott, C. A., C. Stan, D. A. Randall, J. L. Kinter, and M. Khairoutdinov, 2011: The Asian monsoon in the superparameterized CCSM and its relationship to tropical wave activity. *J. Climate*, **24 (19)**, 5134–5156, doi:10.1175/2011JCLI4202.1.

Ding, R., J. Li, and K.-J. Ha, 2008: Trends and interdecadal changes of weather predictability during 1950s–1990s. *J. Geophys. Res.*, **113 (D24)**, n/a–n/a, doi:10.1029/2008JD010404.

Done, J. M., G. C. Craig, S. L. Gray, P. A. Clark, and M. E. B. Gray, 2006: Mesoscale simulations of organized convection: Importance of convective equilibrium. *Q.J.R. Meteorol. Soc.*, **132 (616)**, 737–756, doi:10.1256/qj.04.84.

Donner, L. J., 1993: A cumulus parameterization including mass fluxes, vertical momentum dynamics, and mesoscale effects. *J. Atmos. Sci.*, **50 (6)**, 889–906, doi:10.1175/1520-0469(1993)050⟨0889:ACPIMF⟩2.0.CO;2.

Donner, L. J., and V. T. Phillips, 2003: Boundary layer control on convective available potential energy: Implications for cumulus parameterization. *J. Geophys. Res. Atmos.*, **108 (D22)**, doi:10.1029/2003JD003773.

Donner, L. J., C. J. Seman, R. S. Hemler, and S. Fan, 2001: A cumulus parameterization including mass fluxes, convective vertical velocities, and mesoscale effects: Thermodynamic and hydrological aspects in a general circulation model. *J. Climate*, **14 (16)**, 3444–3463, doi:10.1175/1520-0442(2001)014⟨3444:ACPIMF⟩2.0.CO;2.

Epstein, E. S., 1969: Stochastic dynamic prediction. *Tellus*, **21 (6)**, 739–759, doi:10.1111/j.2153-3490.1969.tb00483.x.

Feng, Z., S. Hagos, A. K. Rowe, C. D. Burleyson, M. N. Martini, and S. P. de Szoeke, 2015: Mechanisms of convective cloud organization by cold pools over tropical warm ocean during the AMIE/DYNAMO field campaign. *J. Adv. Model. Earth Syst.*, **7 (2)**, 357–381, doi:10.1002/2014MS000384.

Flato, G., and Coauthors, 2013: Evaluation of climate models. *Climate Change 2013: The Physical Science Basis. Contribution of Working Group I to the Fifth Assessment Report of the Intergovernmental Panel on Climate Change*, T. Stocker, D. Qin, G.-K. Plattner, M. Tignor, S. Allen, J. Boschung, A. Nauels, Y. Xia, V. Bex, and P. Midgley, Eds., Cambridge University Press, Cambridge, United Kingdom and New York, NY, USA, book section 9, 741–866, doi:10.1017/CBO9781107415324.020.

Garcia-Carreras, L., A. J. Challinor, B. J. Parkes, C. E. Birch, K. J. Nicklin, and D. J. Parker, 2015: The impact of parameterized convection on the simulation of crop processes. *J. Appl. Meteor. Climatol.*, **54 (6)**, 1283–1296, doi:10.1175/JAMC-D-14-0226.1.

Gehne, M., T. M. Hamill, G. N. Kiladis, and K. E. Trenberth, 2016: Comparison of global precipitation estimates across a range of temporal and spatial scales. *J. Climate*, doi:10.1175/JCLI-D-15-0618.1.

Gottwald, G. A., K. Peters, and L. Davies, 2016: A data-driven method for the stochastic parametrisation of subgrid-scale tropical convective area fraction. *Q.J.R. Meteorol. Soc.*, **142 (694)**, 349–359, doi:10.1002/qj.2655.

Grabowski, W. W., 2001: Coupling cloud processes with the large-scale dynamics using the Cloud-Resolving Convection Parameterization (CRCP). *J. Atmos. Sci.*, **58 (9)**, 978–997, doi:10.1175/1520-0469(2001)058⟨0978:CCPWTL⟩2.0.CO;2.

Grabowski, W. W., and M. W. Moncrieff, 2004: Moisture–convection feedback in the tropics. *Q.J.R. Meteorol. Soc.*, **130 (604)**, 3081–3104, doi:10.1256/qj.03.135.

Grabowski, W. W., and P. K. Smolarkiewicz, 1999: CRCP: a Cloud Resolving Convection Parameterization for modeling the tropical convecting atmosphere. *Physica D*, **133 (1–4)**, 171–178, doi:http://dx.doi.org/10.1016/S0167-2789(99)00104-9, URL http://www.sciencedirect.com/science/article/pii/S0167278999001049.

Grandpeix, J.-Y., and J.-P. Lafore, 2010: A density current parameterization coupled with Emanuel's convection scheme. Part I: The models. *J. Atmos. Sci.*, **67 (4)**, 881–897, doi:10.1175/2009JAS3044.1.

Grassberger, P., and I. Procaccia, 1983: Characterization of strange attractors. *Phys. Rev. Lett.*, **50 (5)**, 346–349.

Gregory, D., R. Kershaw, and P. M. Inness, 1997: Parametrization of momentum transport by convection. II: Tests in single-column and general circulation models. *Q.J.R. Meteorol. Soc.*, **123 (541)**, 1153–1183, doi:10.1002/qj.49712354103.

Gregory, D., and P. R. Rowntree, 1990: A mass flux convection scheme with representation of cloud ensemble characteristics and stability-dependent closure. *Mon. Wea. Rev.*, **118 (7)**, 1483–1506, doi:10.1175/1520-0493(1990)118⟨1483:AMFCSW⟩2.0.CO;2.

Groenemeijer, P., and G. C. Craig, 2012: Ensemble forecasting with a stochastic convective parametrization based on equilibrium statistics. *Atmos. Chem. Phys.*, **12 (10)**, 4555–4565, doi:10.5194/acp-12-4555-2012.

Hack, J. J., 1994: Parameterization of moist convection in the National Center for Atmospheric Research community climate model (CCM2). *J. Geophys. Res.*, **99 (D3)**, 5551–5568, doi:10.1029/93JD03478.

Haiden, T., M. J. Rodwell, D. S. Richardson, A. Okagaki, T. Robinson, and T. Hewson, 2012: Intercomparison of global model precipitation forecast skill in 2010/11 using the SEEPS score. *Mon. Wea. Rev.*, **140 (8)**, 2720–2733, doi:10.1175/MWR-D-11-00301.1.

Harnisch, F., and C. Keil, 2015: Initial conditions for convective-scale ensemble forecasting provided by ensemble data assimilation. *Mon. Wea. Rev.*, **143 (5)**, 1583–1600, doi:10.1175/MWR-D-14-00209.1.

Hasselmann, K., 1976: Stochastic climate models Part I. Theory. *Tellus*, **28 (6)**, 473–485, doi:10.1111/j.2153-3490.1976.tb00696.x.

Heath, J. P., and P. Borowski, 2013: Quantifying proportional variability. *PLoS ONE*, **8 (12)**, e84 074, doi:doi:10.1371/journal.pone.0084074.

Hohenegger, C., D. Lüthi, and C. Schär, 2006: Predictability mysteries in cloud-resolving models. *Mon. Wea. Rev.*, **134 (8)**, 2095–2107, doi:10.1175/MWR3176.1.

Hohenegger, C., and C. Schär, 2007: Atmospheric predictability at synoptic versus cloud-resolving scales. *Bull. Amer. Meteor. Soc.*, **88 (11)**, 1783–1793, doi:10.1175/BAMS-88-11-1783.

Holloway, C. E., and J. D. Neelin, 2009: Moisture vertical structure, column water vapor, and tropical deep convection. *J. Atmos. Sci.*, **66 (6)**, 1665–1683, doi:10.1175/2008JAS2806.1.

Horinouchi, T., and Coauthors, 2003: Tropical cumulus convection and upward-propagating waves in middle-atmospheric GCMs. *J. Atmos. Sci.*, **60 (22)**, 2765–2782, doi:10.1175/1520-0469(2003)060⟨2765:TCCAUW⟩2.0.CO;2.

Hottovy, S., and S. Stechmann, 2015: Threshold models for rainfall and convection: Deterministic versus stochastic triggers. *SIAM J. Appl. Math.*, **75 (2)**, 861–884, doi:10.1137/140980788.

Houston, A. L., and R. B. Wilhelmson, 2011: The dependence of storm longevity on the pattern of deep convection initiation in a low-shear environment. *Mon. Wea. Rev.*, **139 (10)**, 3125–3138, doi:10.1175/MWR-D-10-05036.1.

Huffman, G. J., R. F. Adler, M. M. Morrissey, D. T. Bolvin, S. Curtis, R. Joyce, B. McGavock, and J. Susskind, 2001: Global precipitation at one-degree daily resolution from multisatellite observations. *J. Hydrometeor.*, **2 (1)**, 36–50, doi:10.1175/1525-7541(2001)002⟨0036:GPAODD⟩2.0.CO;2.

Huffman, G. J., and Coauthors, 2007: The TRMM multisatellite precipitation analysis (TMPA): Quasi-global, multiyear, combined-sensor precipitation estimates at fine scales. *J. Hydrometeor.*, **8 (1)**, 38–55, doi:10.1175/JHM560.1.

Jakob, C., 2014: Going back to basics. *Nature Clim. Change*, **4 (12)**, 1042–1045, doi:10.1038/nclimate2445.

Jakob, C., and G. Tselioudis, 2003: Objective identification of cloud regimes in the Tropical Western Pacific. *Geophys. Res. Lett.*, **30 (21)**, n/a–n/a, doi:10.1029/2003GL018367.

Jankov, I., and W. A. Gallus, 2004: MCS rainfall forecast accuracy as a function of large-scale forcing. *Wea. Forecasting*, **19 (2)**, 428–439, doi:10.1175/1520-0434(2004)019⟨0428:MRFAAA⟩2.0.CO;2.

Jin, D., L. Oreopoulos, and D. Lee, 2016a: Regime-based evaluation of cloudiness in CMIP5 models. *Climate Dyn.*, 1–24, doi:10.1007/s00382-016-3064-0.

Jin, D., L. Oreopoulos, and D. Lee, 2016b: Simplified ISCCP cloud regimes for evaluating cloudiness in CMIP5 models. *Climate Dyn.*, 1–18, doi:10.1007/s00382-016-3107-6.

Johnson, R. H., T. M. Rickenbach, S. A. Rutledge, P. E. Ciesielski, and W. H. Schubert, 1999: Trimodal characteristics of tropical convection. *J. Climate*, **12 (8)**, 2397–2418, doi:10.1175/1520-0442(1999)012⟨2397:TCOTC⟩2.0.CO;2.

Jones, C. R., C. S. Bretherton, and M. S. Pritchard, 2015: Mean-state acceleration of cloud-resolving models and large eddy simulations. *J. Adv. Model. Earth Syst.*, **7 (4)**, 1643–1660, doi:10.1002/2015MS000488.

Jones, P. W., 1999: First- and second-order conservative remapping schemes for grids in spherical coordinates. *Mon. Wea. Rev.*, **127 (9)**, 2204–2210, doi:10.1175/1520-0493(1999)127⟨2204:FASOCR⟩2.0.CO;2.

Jones, T. R., and D. A. Randall, 2011: Quantifying the limits of convective parameterizations. *J. Geophys. Res. Atmos.*, **116 (D8)**, doi:10.1029/2010JD014913.

Jung, T., 2005: Systematic errors of the atmospheric circulation in the ECMWF forecasting system. *Q.J.R. Meteorol. Soc.*, **131 (607)**, 1045–1073, doi:10.1256/qj.04.93.

Kain, J. S., and J. M. Fritsch, 1989: A one-dimensional entraining/detraining plume model and its application in convective parameterization. *J. Atmos. Sci.*, **47 (23)**, 2784–2802, doi:10.1175/1520-0469(1990)047⟨2784:AODEPM⟩2.0.CO;2.

Keane, R. J., R. S. Plant, and W. J. Tennant, 2016: Evaluation of the Plant–Craig stochastic convection scheme (v2.0) in the ensemble forecasting system MOGREPS-R (24 km) based on the Unified Model (v7.3). *Geosci. Model Dev.*, **9 (5)**, 1921–1935, doi:10.5194/gmd-9-1921-2016.

Keil, C., F. Heinlein, and G. C. Craig, 2014: The convective adjustment time-scale as indicator of predictability of convective precipitation. *Q.J.R. Meteorol. Soc.*, **140 (679)**, 480–490, doi: 10.1002/qj.2143.

Khairoutdinov, M., D. Randall, and C. DeMott, 2005: Simulations of the atmospheric general circulation using a cloud-resolving model as a superparameterization of physical processes. *J. Atmos. Sci.*, **62 (7)**, 2136–2154, doi:10.1175/JAS3453.1.

Khairoutdinov, M., and X. Zhou, 2015: Changes in sub-daily precipitation extremes in a global climate model with super-parameterization under CO2 warming. *EGU General Assembly Conference Abstracts*, EGU General Assembly Conference Abstracts, Vol. 17, 7931.

Khairoutdinov, M. F., and D. A. Randall, 2001: A cloud resolving model as a cloud parameterization in the NCAR Community Climate System Model: Preliminary results. *Geophys. Res. Lett.*, **28 (18)**, 3617–3620, doi:10.1029/2001GL013552.

Khairoutdinov, M. F., and D. A. Randall, 2003: Cloud resolving modeling of the arm summer 1997 iop: Model formulation, results, uncertainties, and sensitivities. *Journal of the Atmospheric Sciences*, **60 (4)**, 607–625, doi:10.1175/1520-0469(2003)060⟨0607:CRMOTA⟩2.0.CO;2, URL http://dx.doi.org/10.1175/1520-0469(2003)060⟨0607:CRMOTA⟩2.0.CO;2.

Kim, D., and Coauthors, 2009: Application of MJO simulation diagnostics to climate models. *J. Climate*, **22 (23)**, 6413–6436, doi:10.1175/2009JCLI3063.1.

Kober, K., and G. C. Craig, 2016: Physically-based stochastic perturbations (PSP) in the boundary layer to represent uncertainty in convective initiation. *J. Atmos. Sci.*, doi:10.1175/JAS-D-15-0144.1.

Kooperman, G. J., M. S. Pritchard, M. A. Burt, M. D. Branson, and D. A. Randall, 2016: Robust effects of cloud superparameterization on simulated daily rainfall intensity statistics across multiple versions of the Community Earth System Model. *J. Adv. Model. Earth Syst.*, **8 (1)**, 140–165, doi:10.1002/2015MS000574.

Kuo, H. L., 1974: Further studies of the parameterization of the influence of cumulus convection on large-scale flow. *J. Atmos. Sci.*, **31 (5)**, 1232–1240, doi:10.1175/1520-0469(1974)031⟨1232:FSOTPO⟩2.0.CO;2.

Lazo, J. K., R. E. Morss, and J. L. Demuth, 2009: 300 billion served. *Bull. Amer. Meteor. Soc.*, **90 (6)**, 785–798, doi:10.1175/2008BAMS2604.1.

Leith, C. E., 1974: Theoretical skill of Monte Carlo forecasts. *Mon. Wea. Rev.*, **102 (6)**, 409–418, doi:10.1175/1520-0493(1974)102⟨0409:TSOMCF⟩2.0.CO;2.

Li, F., D. Rosa, W. D. Collins, and M. F. Wehner, 2012: "Super-parameterization": A better way to simulate regional extreme precipitation? *J. Adv. Model. Earth Syst.*, **4 (2)**, doi:10.1029/2011MS000106.

Liebmann, B., and C. A. Smith, 1996: Description of a complete (interpolated) outgoing longwave radiation dataset. *Bull. Amer. Meteor. Soc.*, **77 (6)**, 1275–1277.

Lima, M. A., and J. W. Wilson, 2008: Convective storm initiation in a moist tropical environment. *Mon. Wea. Rev.*, **136 (6)**, 1847–1864, doi:10.1175/2007MWR2279.1.

Lin, J.-L., T. Qian, T. Shinoda, and S. Li, 2015: Is the tropical atmosphere in convective quasi-equilibrium? *J. Climate*, **28 (11)**, 4357–4372, doi:10.1175/JCLI-D-14-00681.1.

Lin, J.-L., and Coauthors, 2006: Tropical intraseasonal variability in 14 IPCC AR4 climate models. Part I: Convective signals. *J. Climate*, **19 (12)**, 2665–2690, doi:10.1175/JCLI3735.1.

Lin, J. W.-B., and J. D. Neelin, 2002: Considerations for stochastic convective parameterization. *J. Atmos. Sci.*, **59 (5)**, 959–975, doi:10.1175/1520-0469(2002)059⟨0959:CFSCP⟩2.0.CO;2.

Lin, J. W.-B., and J. D. Neelin, 2003: Toward stochastic deep convective parameterization in general circulation models. *Geophys. Res. Lett.*, **30 (4)**, doi:10.1029/2002GL016203.

Liu, C., and M. W. Moncrieff, 2001: Cumulus ensembles in shear: Implications for parameterization. *J. Atmos. Sci.*, **58 (18)**, 2832–2842, doi:10.1175/1520-0469(2001)058⟨2832:CEISIF⟩2.0.CO;2.

Liu, J., W. Li, L. Chen, J. Zuo, and P. Zhang, 2016: Estimation of the monthly precipitation predictability limit in China using the nonlinear local Lyapunov exponent. *Journal of Meteorological Research*, **30 (1)**, 93–102, doi:10.1007/s13351-015-5049-z.

Liu, Z., A. Mehran, T. Phillips, and A. AghaKouchak, 2014: Seasonal and regional biases in CMIP5 precipitation simulations. *Clim. Res.*, **60 (1)**, 35–50.

López, R. E., 1977: The lognormal distribution and cumulus cloud populations. *Mon. Wea. Rev.*, **105 (7)**, 865–872, doi:10.1175/1520-0493(1977)105⟨0865:TLDACC⟩2.0.CO;2.

Lorenz, E. N., 1969: The predictability of a flow which possesses many scales of motion. *Tellus*, **21 (3)**, 289–307, doi:10.1111/j.2153-3490.1969.tb00444.x.

Ma, H. Y., S. Xie, J. S. Boyle, S. A. Klein, and Y. Zhang, 2012: Metrics and diagnostics for precipitation-related processes in climate model short-range hindcasts. *J. Climate*, **26 (5)**, 1516–1534, doi:10.1175/JCLI-D-12-00235.1.

Malardel, S., and N. P. Wedi, 2016: How does subgrid-scale parametrization influence nonlinear spectral energy fluxes in global NWP models? *J. Geophys. Res. Atmos.*, **121 (10)**, 5395–5410, doi:10.1002/2015JD023970.

Manabe, S., J. Smagorinsky, and R. F. Strickler, 1965: Simulated climatology of a general circulation model with a hydrologic cycle. *Mon. Wea. Rev.*, **93 (12)**, 769–798, doi:10.1175/1520-0493(1965)093⟨0769:SCOAGC⟩2.3.CO;2.

Mapes, B., S. Tulich, J. Lin, and P. Zuidema, 2006: The mesoscale convection life cycle: Building block or prototype for large-scale tropical waves? *Dyn. Atmos. Oceans*, **42 (1–4)**, 3–29, doi:10.1016/j.dynatmoce.2006.03.003.

Mapes, B. E., 1993: Gregarious tropical convection. *J. Atmos. Sci.*, **50 (13)**, 2026–2037, doi:10.1175/1520-0469(1993)050⟨2026:GTC⟩2.0.CO;2.

Masunaga, H., 2012: Short-term versus climatological relationship between precipitation and tropospheric humidity. *J. Climate*, **25 (22)**, 7983–7990, doi:10.1175/JCLI-D-12-00037.1.

McCrary, R. R., D. A. Randall, and C. Stan, 2014: Simulations of the West African Monsoon with a superparameterized climate model. part ii: African Easterly Waves. *J. Climate*, **27 (22)**, 8323–8341, doi:10.1175/JCLI-D-13-00677.1.

Mecikalski, J. R., and K. M. Bedka, 2006: Forecasting convective initiation by monitoring the evolution of moving cumulus in daytime GOES imagery. *Monthly Weather Review*, **134 (1)**, 49–78, doi:10.1175/MWR3062.1.

Mehran, A., A. AghaKouchak, and T. J. Phillips, 2014: Evaluation of CMIP5 continental precipitation simulations relative to satellite-based gauge-adjusted observations. *J. Geophys. Res. Atmos.*, **119 (4)**, 1695–1707, doi:10.1002/2013JD021152.

Mewes, D., 2016: Stochastic parameterization of precipitation in the stochastic parameterization of precipitation in the ECHAM6 general circulation model. M.S. thesis, Leipzig University, 26 pp., [Available online at http://research.uni-leipzig.de/climate/mewes_daniel__masterarbeit__2016.pdf.].

Millán, H., A. Kalauzi, G. Llerena, J. Sucoshañay, and D. Piedra, 2009: Meteorological complexity in the Amazonian area of Ecuador: An approach based on dynamical system theory. *Ecological Complexity*, **6 (3)**, 278–285, doi:http://dx.doi.org/10.1016/j.ecocom.2009.05.004.

Millán, H., J. Rodríguez, B. Ghanbarian-Alavijeh, R. Biondi, and G. Llerena, 2011: Temporal complexity of daily precipitation records from different atmospheric environments: Chaotic and Lévy stable parameters. *Atmos. Res.*, **101 (4)**, 879–892, doi:10.1016/j.atmosres.2011.05.021.

Molinari, J., and M. Dudek, 1992: Parameterization of convective precipitation in mesoscale numerical models: A critical review. *Mon. Wea. Rev.*, **120 (2)**, 326–344, doi:10.1175/1520-0493(1992)120⟨0326:POCPIM⟩2.0.CO;2.

Molteni, F., R. Buizza, T. N. Palmer, and T. Petroliagis, 1996: The ECMWF ensemble prediction system: Methodology and validation. *Q.J.R. Meteorol. Soc.*, **122 (529)**, 73–119, doi:10.1002/qj.49712252905.

Molteni, F., and S. Tibaldi, 1990: Regimes in the wintertime circulation over northern extratropics. II: Consequences for dynamical predictability. *Q.J.R. Meteorol. Soc.*, **116 (496)**, 1263–1288, doi:10.1002/qj.49711649602.

Moncrieff, M. W., 2004: Analytic representation of the large-scale organization of tropical convection. *J. Atmos. Sci.*, **61 (13)**, 1521–1538, doi:10.1175/1520-0469(2004)061⟨1521:AROTLO⟩2.0.CO;2.

Moncrieff, M. W., D. E. Waliser, M. J. Miller, M. A. Shapiro, G. R. Asrar, and J. Caughey, 2012: Multiscale convective organization and the YOTC Virtual Global Field Campaign. *Bull. Amer. Meteor. Soc.*, **93 (8)**, 1171–1187, doi:10.1175/BAMS-D-11-00233.1.

Mullen, S. L., and R. Buizza, 2001: Quantitative precipitation forecasts over the United States by the ECMWF Ensemble Prediction System. *Mon. Wea. Rev.*, **129 (4)**, 638–663, doi:10.1175/1520-0493(2001)129⟨0638:QPFOTU⟩2.0.CO;2.

Mureau, R., F. Molteni, and T. N. Palmer, 1993: Ensemble prediction using dynamically conditioned perturbations. *Q.J.R. Meteorol. Soc.*, **119 (510)**, 299–323, doi:10.1002/qj.49711951005.

National Centers for Environmental Information, cited 2016: Billion-Dollar Weather and Climate Disasters. [Available online at http://www.ncdc.noaa.gov/billions/].

Neale, R. B., J. H. Richter, and M. Jochum, 2008: The impact of convection on ENSO: from a delayed oscillator to a series of events. *J. Climate*, **21 (22)**, 5904–5924, doi:10.1175/2008JCLI2244.1.

Neale, R. B., and Coauthors, 2010: Description of the NCAR Community Atmosphere Model (CAM 4.0). *NCAR Tech. Note*, NCAR/TN-485+STR.

Neale, R. B., and Coauthors, 2012: Description of the NCAR community atmosphere model (CAM 5.0). NCAR technical note NCAR/TN-486+STR, NCAR, Boulder, Colorado, USA Boulder, Colorado, USA.

Neelin, J. D., O. Peters, and K. Hales, 2009: The transition to strong convection. *J. Atmos. Sci.*, **66 (8)**, 2367–2384, doi:10.1175/2009JAS2962.1.

Neelin, J. D., O. Peters, J. W. B. Lin, K. Hales, and C. E. Holloway, 2008: Rethinking convective quasi-equilibrium: Observational constraints for stochastic convective schemes in climate models. *Philos. Trans. R. Soc. A*, **366 (1875)**, 2581–2604, doi:10.1098/rsta.2008.0056.

Palmer, T., R. Buizza, F. Doblas-Reyes, T. Jung, M. Leutbecher, G. Shutts, M. Steinheimer, and A. Weisheimer, 2009: Stochastic parametrization and model uncertainty. ECMWF Tech. Memo. 598, ECMWF, 42 pp. [Available online at https://www2.physics.ox.ac.uk/sites/default/files/2011-08-15/techmemo598_stochphys_2009_pdf_50419.pdf.].

Palmer, T. N., 1996: On parametrizing scales that are only somewhat smaller than the smallest resolved scales with application to convection and orography. *Workshop on New Insights and Approaches to Convective Parametrization, 4-7 November 1996*, Shinfield Park, Reading, U. K., ECMWF, 328–337.

Palmer, T. N., 2000: Predicting uncertainty in forecasts of weather and climate. *Rep. Prog. Phys.*, **63 (2)**, 71–116, doi:10.1088/0034-4885/63/2/201.

Palmer, T. N., F. Molteni, R. Mureau, R. Buizza, P. Chapelet, and J. Tribbia, 1993: Ensemble prediction. *Seminar Proceedings on Validation of models over Europe*, Shinfield Park, Reading, UK, ECMWF, Vol. 1, 285.

Palmer, T. N., G. J. Shutts, R. Hagedorn, F. J. Doblas-Reyes, T. Jung, and M. Leutbecher, 2005: Representing model uncertainty in weather and climate prediction. *Annu. Rev. Earth Planet. Sci.*, **33 (1)**, 163–193, doi:10.1146/annurev.earth.33.092203.122552.

Pan, D.-M., and D. D. A. Randall, 1998: A cumulus parameterization with a prognostic closure. *Q. J. R. Meteorol. Soc.*, **124 (547)**, 949–981, doi:10.1002/qj.49712454714.

Peters, K., C. Jakob, L. Davies, B. Khouider, and A. J. Majda, 2013: Stochastic behavior of tropical convection in observations and a multicloud model. *J. Atmos. Sci.*, **70 (11)**, 3556–3575, doi:10.1175/JAS-D-13-031.1.

Peters, O., and J. D. Neelin, 2006: Critical phenomena in atmospheric precipitation. *Nat. Phys.*, **2 (6)**, 393–396, doi:10.1038/nphys314.

Pincus, R., C. P. Batstone, R. J. P. Hofmann, K. E. Taylor, and P. J. Glecker, 2008: Evaluating the present-day simulation of clouds, precipitation, and radiation in climate models. *J. Geophys. Res. Atmos.*, **113 (D14)**, doi:10.1029/2007JD009334.

Plant, R. S., and G. C. Craig, 2008: A stochastic parameterization for deep convection based on equilibrium statistics. *J. Atmos. Sci.*, **65 (1)**, 87–105, doi:10.1175/2007JAS2263.1.

Posselt, D. J., S. v. d. Heever, G. Stephens, and M. R. Igel, 2012: Changes in the interaction between tropical convection, radiation, and the large-scale circulation in a warming environment. *J. Climate*, **25 (2)**, 557–571, doi:10.1175/2011JCLI4167.1, URL http://dx.doi.org/10.1175/2011JCLI4167.1.

Pritchard, M. S., C. S. Bretherton, and C. A. DeMott, 2014: Restricting 32–128 km horizontal scales hardly affects the MJO in the Superparameterized Community Atmosphere Model v.3.0 but the number of cloud-resolving grid columns constrains vertical mixing. *J. Adv. Model. Earth Syst.*, **6 (3)**, 723–739, doi:10.1002/2014MS000340.

Pritchard, M. S., and R. C. J. Somerville, 2009: Assessing the diurnal cycle of precipitation in a multi-scale climate model. *J. Adv. Model. Earth Syst.*, **1 (4)**, doi:10.3894/JAMES.2009.1.12.

Randall, D., M. Branson, M. Wang, S. Ghan, C. Craig, A. Gettelman, and J. Edwards, 2013: A Community Atmosphere Model with superparameterized clouds. *Eos Trans. AGU*, **94 (25)**, 221–222, doi:10.1002/2013EO250001.

Randall, D., C. DeMott, C. Stan, M. Khairoutdinov, J. Benedict, R. McCrary, K. Thayer-Calder, and M. Branson, 2016: Simulations of the tropical general circulation with a multiscale global model. *Meteor. Monogr.*, **56**, 15.1–15.15, doi:10.1175/AMSMONOGRAPHS-D-15-0016.1.

Randall, D., M. Khairoutdinov, A. Arakawa, and W. Grabowski, 2003: Breaking the cloud parameterization deadlock. *Bull. Amer. Meteor. Soc.*, **84 (11)**, 1547–1564, doi:10.1175/BAMS-84-11-1547.

Randall, D. A., P. Ding, and P. D.-M., 1997: Quasi-equilibrium. *The Physics and Parameterization of Moist Atmospheric Convection*, R. Smith, Ed., Kluwer Academic Publishers, The Netherlands, 359–385.

Randall, D. A., Q. Hu, K. M. Xu, and S. K. Krueger, 1994: Radiative-convective disequilibrium. *Atmos. Res.*, **31 (4)**, 315–327, doi:http://dx.doi.org/10.1016/0169-8095(94)90006-X.

Rasch, P. J., and J. E. Kristjánsson, 1998: A comparison of the CCM3 model climate using diagnosed and predicted condensate parameterizations. *J. Climate*, **11 (7)**, 1587–1614, doi:10.1175/1520-0442(1998)011⟨1587:ACOTCM⟩2.0.CO;2.

Raymond, D., Ž. Fuchs, S. Gjorgjievska, and S. Sessions, 2015: Balanced dynamics and convection in the tropical troposphere. *J. Adv. Model. Earth Syst.*, **7 (3)**, 1093–1116, doi:10.1002/2015MS000467.

Raymond, D. J., and A. M. Blyth, 1992: Extension of the stochastic mixing model to cumulonimbus clouds. *J. Atmos. Sci.*, **49 (21)**, 1968–1983, doi:10.1175/1520-0469(1992)049⟨1968:EOTSMM⟩2.0.CO;2.

Raymond, D. J., and M. J. Herman, 2011: Convective quasi-equilibrium reconsidered. *J. Adv. Model. Earth Syst.*, **3 (3)**, doi:10.1029/2011MS000079.

Raymond, D. J., S. L. Sessions, and Ž. Fuchs, 2007: A theory for the spinup of tropical depressions. *Q.J.R. Meteorol. Soc.*, **133 (628)**, 1743–1754, doi:10.1002/qj.125.

Rémillard, J., and G. Tselioudis, 2015: Cloud regime variability over the Azores and its application to climate model evaluation. *J. Climate*, **28 (24)**, 9707–9720, doi:10.1175/JCLI-D-15-0066.1.

Ricciardulli, L., and R. R. Garcia, 2000: The excitation of equatorial waves by deep convection in the NCAR Community Climate Model (CCM3). *J. Atmos. Sci.*, **57 (21)**, 3461–3487, doi:10.1175/1520-0469(2000)057⟨3461:TEOEWB⟩2.0.CO;2.

Richardson, D. S., 2012: Economic value and skill. *Forecast Verification: A Practitioner's Guide in Atmospheric Science*, I. T. Jolliffe, and D. B. Stephenson, Eds., 2nd ed., John Wiley & Sons, Ltd., 185–201.

Richter, J. H., and P. J. Rasch, 2008: Effects of convective momentum transport on the atmospheric circulation in the Community Atmosphere Model, Version 3. *J. Climate*, **21 (7)**, 1487–1499, doi:10.1175/2007JCLI1789.1.

Roebber, P. J., and L. F. Bosart, 1996: The complex relationship between forecast skill and forecast value: A real-world analysis. *Wea. Forecasting*, **11 (4)**, 544–559, doi:10.1175/1520-0434(1996)011⟨0544:TCRBFS⟩2.0.CO;2.

Roebber, P. J., D. M. Schultz, B. A. Colle, and D. J. Stensrud, 2004: Toward improved prediction: High-resolution and ensemble modeling systems in operations. *Wea. Forecasting*, **19 (5)**, 936–949, doi:10.1175/1520-0434(2004)019⟨0936:TIPHAE⟩2.0.CO;2.

Roehrig, R., D. Bouniol, F. Guichard, F. Hourdin, and J.-L. Redelsperger, 2013: The present and future of the West African Monsoon: A process-oriented assessment of CMIP5 simulations along the AMMA transect. *J. Climate*, **26 (17)**, 6471–6505, doi:10.1175/JCLI-D-12-00505.1.

Romps, D. M., 2016: The Stochastic Parcel Model: A deterministic parameterization of stochastically entraining convection. *J. Adv. Model. Earth Syst.*, **8 (1)**, 319–344, doi:10.1002/2015MS000537.

Rosa, D., and W. D. Collins, 2013: A case study of subdaily simulated and observed continental convective precipitation: CMIP5 and multiscale global climate models comparison. *Geophys. Res. Lett.*, **40 (22)**, 5999–6003, doi:10.1002/2013GL057987.

Rossow, W. B., G. Tselioudis, A. Polak, and C. Jakob, 2005: Tropical climate described as a distribution of weather states indicated by distinct mesoscale cloud property mixtures. *Geophys. Res. Lett.*, **32 (21)**, n/a–n/a, doi:10.1029/2005GL024584.

Rousseau-Rizzi, R., D. J. Kirshbaum, and M. K. Yau, 2016: Initiation of deep convection over an idealized mesoscale convergence line. *J. Atmos. Sci.*, doi:10.1175/JAS-D-16-0221.1.

Roy, S. B., 2009: A quest for the mesoscale spectral gap. *EGU General Assembly Conference Abstracts*, Arabelos, D. N. and Tscherning, C. C., Ed., EGU General Assembly, Vol. 11, 10067.

Schenkman, A. D., M. Xue, A. Shapiro, K. Brewster, and J. Gao, 2011: Impact of CASA radar and Oklahoma Mesonet data assimilation on the analysis and prediction of tornadic mesovortices in an MCS. *Mon. Wea. Rev.*, **139 (11)**, 3422–3445, doi:10.1175/MWR-D-10-05051.1.

Schiro, K. A., J. D. Neelin, D. K. Adams, and B. R. Lintner, 2016: Deep convection and column water vapor over tropical land vs. tropical ocean: A comparison between the Amazon and the Tropical Western Pacific. *J. Atmos. Sci.*, doi:10.1175/JAS-D-16-0119.1.

Scinocca, J. F., and N. A. McFarlane, 2004: The variability of modeled tropical precipitation. *J. Atmos. Sci.*, **61 (16)**, 1993–2015, doi:10.1175/1520-0469(2004)061⟨1993:TVOMTP⟩2.0.CO;2.

Sentić, S., S. L. Sessions, and Ž. Fuchs, 2015: Diagnosing DYNAMO convection with weak temperature gradient simulations. *J. Adv. Model. Earth Syst.*, **7 (4)**, 1849–1871, doi:10.1002/2015MS000531.

Sherwood, S. C., and R. Wahrlich, 1999: Observed evolution of tropical deep convective events and their environment. *Mon. Wea. Rev.*, **127 (8)**, 1777–1795, doi:10.1175/1520-0493(1999)127⟨1777:OEOTDC⟩2.0.CO;2.

Shibata, K., H. Yoshimura, M. Ohizumi, M. Hosaka, and M. Sugi, 1999: A simulation of troposphere, stratosphere and mesosphere with an MRI/JMA98 GCM. *Pap. Meteor. Geophys.*, **50 (1)**, 15–53, doi:10.2467/mripapers.50.15.

Shutts, G. J., and T. N. Palmer, 2007: Convective forcing fluctuations in a cloud-resolving model: Relevance to the stochastic parameterization problem. *J. Climate*, **20 (2)**, 187–202, doi:10.1175/JCLI3954.1.

Sivakumar, B., 2001: Rainfall dynamics at different temporal scales: A chaotic perspective. *Hydrol. Earth Syst. Sci.*, **5 (4)**, 645–652, doi:10.5194/hess-5-645-2001.

Sivakumar, B., 2004: Chaos theory in geophysics: past, present and future. *Chaos, Solitons & Fractals*, **19 (2)**, 441–462, doi:http://dx.doi.org/10.1016/S0960-0779(03)00055-9.

Slingo, J. M., P. M. Inness, and K. R. Sperber, 2005: Modeling. *Intraseasonal Variability in the Atmosphere-Ocean Climate System*, W. K. Lau, and D. E. Waliser, Eds., Praxis-Springer, chap. 11, 361–388.

Slingo, J. M., and Coauthors, 1996: Intraseasonal oscillations in 15 atmospheric general circulation models: results from an AMIP diagnostic subproject. *Climate Dyn.*, **12 (5)**, 325–357, doi:10.1007/BF00231106.

Smith, A. B., and R. W. Katz, 2013: Us billion-dollar weather and climate disasters: data sources, trends, accuracy and biases. *Natural Hazards*, **67 (2)**, 387–410, doi:10.1007/s11069-013-0566-5.

Stan, C., M. Khairoutdinov, C. A. DeMott, V. Krishnamurthy, D. M. Straus, D. A. Randall, J. L. Kinter, and J. Shukla, 2010: An ocean-atmosphere climate simulation with an embedded cloud resolving model. *Geophys. Res. Lett.*, **37 (1)**, doi:10.1029/2009GL040822.

Stechmann, S. N., and J. D. Neelin, 2011: A stochastic model for the transition to strong convection. *J. Atmos. Sci.*, **68 (12)**, 2955–2970, doi:10.1175/JAS-D-11-028.1.

Stechmann, S. N., and J. D. Neelin, 2014: First-passage-time prototypes for precipitation statistics. *J. Atmos. Sci.*, **71 (9)**, 3269–3291, doi:10.1175/JAS-D-13-0268.1.

Stensrud, D. J., J.-W. Bao, and T. T. Warner, 2000: Using initial condition and model physics perturbations in short-range ensemble simulations of mesoscale convective systems. *Mon. Wea. Rev.*, **128 (7)**, 2077–2107, doi:10.1175/1520-0493(2000)128⟨2077:UICAMP⟩2.0.CO;2.

Stensrud, D. J., and J. Gao, 2010: Importance of horizontally inhomogeneous environmental initial conditions to ensemble storm-scale radar data assimilation and very short-range forecasts. *Mon. Wea. Rev.*, **138 (4)**, 1250–1272, doi:10.1175/2009MWR3027.1.

Stephens, G. L., and Coauthors, 2010: Dreary state of precipitation in global models. *J. Geophys. Res. Atmos.*, **115 (D24)**, doi:10.1029/2010JD014532.

Stevens, B., and S. Bony, 2013: What are climate models missing? *Science*, **340 (6136)**, 1053–1054, doi:10.1126/science.1237554.

Subramanian, A. C., T. Palmer, M. Khairoutdinov, F. Vitart, P. Bechtold, and A. Weisheimer, 2015: Stochastic multi-scale modeling for weather and 3 climate prediction. *Poster session presented at Translating Process Understanding to Improve Climate Models*, Princeton, NJ, US Climate Variability and Predictability Program, [Available online at https://usclivar.org/sites/default/files/meetings/2015/cpt-posters/Subramanian-AC-cpt-2015-1_0.pdf.].

Suhas, E., and G. J. Zhang, 2014: Evaluation of trigger functions for convective parameterization schemes using observations. *J. Climate*, **27 (20)**, 7647–7666, doi:10.1175/JCLI-D-13-00718.1.

Sun, J., and Y. Zhang, 2008: Analysis and prediction of a squall line observed during IHOP using multiple WSR-88D observations. *Mon. Wea. Rev.*, **136 (7)**, 2364–2388, doi:10.1175/2007MWR2205.1.

Sun, Y., S. Solomon, A. Dai, and R. W. Portmann, 2007: How often will it rain? *J. Climate*, **20 (19)**, 4801–4818, doi:10.1175/JCLI4263.1.

Sundqvist, H., 1988: Parameterization of condensation and associated clouds in models for weather prediction and general circulation simulation. *Physically-Based Modelling and Simulation of Climate and Climatic Change: Part 1*, M. E. Schlesinger, Ed., Springer Netherlands, Dordrecht, 433–461, doi:10.1007/978-94-009-3041-4{_}10.

Surcel, M., I. Zawadzki, and M. K. Yau, 2015: The case-to-case variability of the predictability of precipitation by a storm-scale ensemble forecasting system. *Mon. Wea. Rev.*, **144 (1)**, 193–212, doi:10.1175/MWR-D-15-0232.1.

Takens, F., 1981: Detecting strange attractors in turbulence. *Dynamical Systems and Turbulence*, 366–381.

Tan, J., C. Jakob, and T. P. Lane, 2013: On the identification of the large-scale properties of tropical convection using cloud regimes. *J. Climate*, **26 (17)**, 6618–6632, doi:10.1175/JCLI-D-12-00624.1.

Taraphdar, S., P. Mukhopadhyay, L. R. Leung, F. Zhang, S. Abhilash, and B. N. Goswami, 2014: The role of moist processes in the intrinsic predictability of Indian Ocean cyclones. *J. Geophys. Res. Atmos.*, **119 (13)**, 8032–8048, doi:10.1002/2013JD021265.

Teixeira, J., and C. A. Reynolds, 2008: Stochastic nature of physical parameterizations in ensemble prediction: A stochastic convection approach. *Monthly Weather Review*, **136 (2)**, 483–496, doi:10.1175/2007MWR1870.1.

Thayer-Calder, K., and D. A. Randall, 2009: The role of convective moistening in the Madden–Julian oscillation. *J. Atmos. Sci.*, **66 (11)**, 3297–3312, doi:10.1175/2009JAS3081.1.

Tiedtke, M., 1989: A comprehensive mass flux scheme for cumulus parameterization in large-scale models. *Mon. Wea. Rev.*, **117 (8)**, 1779–1800, doi:10.1175/1520-0493(1989)117⟨1779:ACMFSF⟩2.0.CO;2.

Toth, Z., and E. Kalnay, 1993: Ensemble forecasting at NMC: The generation of perturbations. *Bull. Amer. Meteor. Soc.*, **74 (12)**, 2317–2330, doi:10.1175/1520-0477(1993)074⟨2317:EFANTG⟩2.0.CO;2.

Toth, Z., and E. Kalnay, 1997: Ensemble forecasting at NCEP and the breeding method. *Mon. Wea. Rev.*, **125 (12)**, 3297–3319, doi:10.1175/1520-0493(1997)125⟨3297:EFANAT⟩2.0.CO;2.

Tracton, M. S., and E. Kalnay, 1993: Operational ensemble prediction at the National Meteorological Center: Practical aspects. *Wea. Forecasting*, **8 (3)**, 379–398, doi:10.1175/1520-0434(1993)008⟨0379:OEPATN⟩2.0.CO;2.

Tselioudis, G., W. Rossow, Y. Zhang, and D. Konsta, 2013: Global weather states and their properties from passive and active satellite cloud retrievals. *J. Climate*, **26 (19)**, 7734–7746, doi:10.1175/JCLI-D-13-00024.1.

Tung, W.-w., M. W. Moncrieff, and J.-B. Gao, 2004: A systemic analysis of multiscale deep convective variability over the tropical Pacific. *J. Climate*, **17 (14)**, 2736–2751, doi:10.1175/1520-0442(2004)017⟨2736:ASAOMD⟩2.0.CO;2.

University Corportation of Atmospheric Research, cited 2016: Mesoscale Meteorology Severe Convection II: Mesoscale Convective Systems. [Available online at http://www.meted.ucar.edu/mesoprim/severe2/index.htm.].

Van der Hoven, I., 1957: Power spectrum of horizontal wind speed in the frequency range from 0.0007 to 900 cycles per hour. *J. Meteor.*, **14 (2)**, 160–164, doi:10.1175/1520-0469(1957)014⟨0160:PSOHWS⟩2.0.CO;2.

Vinnichenko, N. K., 1970: The kinetic energy spectrum in the free atmosphere—1 second to 5 years. *Tellus*, **22 (2)**, 158–166, doi:10.1111/j.2153-3490.1970.tb01517.x.

Wagner, T. M., and H.-F. Graf, 2010: An ensemble cumulus convection parameterization with explicit cloud treatment. *J. Atmos. Sci.*, **67 (12)**, 3854–3869, doi:10.1175/2010JAS3485.1.

WALISER, D., and Coauthors, 2009: Mjo simulation diagnostics. *J. Climate*, **22 (11)**, 3006–3030, doi:10.1175/2008JCLI2731.1.

Walser, A., D. Lüthi, and C. Schär, 2004: Predictability of precipitation in a cloud-resolving model. *Mon. Wea. Rev.*, **132 (2)**, 560–577, doi:10.1175/1520-0493(2004)132⟨0560:POPIAC⟩2.0.CO;2.

Wang, Y., G. J. Zhang, and G. C. Craig, 2016: Stochastic convective parameterization improving the simulation of tropical precipitation variability in the NCAR CAM5. *Geophys. Res. Lett.*, **43 (12)**, 6612–6619, doi:10.1002/2016GL069818.

Watson, P. A. G., H. M. Christensen, and T. N. Palmer, 2014: Does the ECMWF IFS convection parameterization with stochastic physics correctly reproduce relationships between convection and the large-scale state? *J. Atmos. Sci.*, **72 (1)**, 236–242, doi:10.1175/JAS-D-14-0252.1.

Weisheimer, A., S. Corti, T. Palmer, and F. Vitart, 2014: Addressing model error through atmospheric stochastic physical parametrizations: impact on the coupled ECMWF seasonal forecasting system. *Phil. Trans. R. Soc. A*, **372 (2018)**.

Weisman, M. L., C. Davis, W. Wang, K. W. Manning, and J. B. Klemp, 2008: Experiences with 0–36-h explicit convective forecasts with the WRF-ARW model. *Wea. Forecasting*, **23 (3)**, 407–437, doi:10.1175/2007WAF2007005.1.

Weisman, M. L., and Coauthors, 2015: The mesoscale predictability experiment (MPEX). *Bull. Amer. Meteor. Soc.*, **96 (12)**, 2127–2149, doi:10.1175/BAMS-D-13-00281.1.

Wheeler, M., and G. N. Kiladis, 1999: Convectively coupled equatorial waves: Analysis of clouds and temperature in the wavenumber–frequency domain. *J. Atmos. Sci.*, **56 (3)**, 374–399, doi:10.1175/1520-0469(1999)056⟨0374:CCEWAO⟩2.0.CO;2.

Wilks, D. S., 2008: Effects of stochastic parametrization on conceptual climate models. *Phil. Trans. R. Soc. A*, **366 (1875)**, 2475–2488.

Williams, K. D., and M. J. Webb, 2009: A quantitative performance assessment of cloud regimes in climate models. *Climate Dyn.*, **33 (1)**, 141–157, doi:10.1007/s00382-008-0443-1.

Xu, K.-M., A. Arakawa, and S. K. Krueger, 1992: The macroscopic behavior of cumulus ensembles simulated by a cumulus ensemble model. *J. Atmos. Sci.*, **49 (24)**, 2402–2420, doi:10.1175/1520-0469(1992)049⟨2402:TMBOCE⟩2.0.CO;2.

Xu, K.-M., and D. A. Randall, 1998: Influence of large-scale advective cooling and moistening effects on the quasi-equilibrium behavior of explicitly simulated cumulus ensembles. *J. Atmos. Sci.*, **55 (5)**, 896–909, doi:10.1175/1520-0469(1998)055⟨0896:IOLSAC⟩2.0.CO;2.

Yano, J.-I., C. Liu, and M. W. Moncrieff, 2012: Self-organized criticality and homeostasis in atmospheric convective organization. *J. Atmos. Sci.*, **69 (12)**, 3449–3462, doi:10.1175/JAS-D-12-069.1.

Zawadzki, I., J. Morneau, and R. Laprise, 1994: Predictability of precipitation patterns: An operational approach. *J. Appl. Meteor.*, **33 (12)**, 1562–1571, doi:10.1175/1520-0450(1994)033⟨1562:POPPAO⟩2.0.CO;2.

Zeng, X., R. A. Pielke, and R. Eykholt, 1992: Estimating the fractal dimension and the predictability of the atmosphere. *J. Atmos. Sci.*, **49 (8)**, 649–659, doi:10.1175/1520-0469(1992)049⟨0649:ETFDAT⟩2.0.CO;2.

Zhang, F., C. Snyder, and R. Rotunno, 2003a: Effects of moist convection on mesoscale predictability. *J. Atmos. Sci.*, **60 (9)**, 1173–1185, doi:10.1175/1520-0469(2003)060⟨1173:EOMCOM⟩2.0.CO;2.

Zhang, G. J., 2002: Convective quasi-equilibrium in midlatitude continental environment and its effect on convective parameterization. *J. Geophys. Res. Atmos.*, **107 (D14)**, ACL 12–1–ACL 12–16, doi:10.1029/2001JD001005.

Zhang, G. J., and N. A. McFarlane, 1995: Sensitivity of climate simulations to the parameterization of cumulus convection in the Canadian climate centre general circulation model. *Atmos.-Ocean*, **33 (3407–446)**, doi:10.1080/07055900.1995.9649539.

Zhang, M., W. Lin, C. S. Bretherton, J. J. Hack, and P. J. Rasch, 2003b: A modified formulation of fractional stratiform condensation rate in the NCAR Community Atmospheric Model (CAM2). *J. Geophys. Res.*, **108 (D1)**, ACL 10–1–ACL 10–11, doi:10.1029/2002JD002523.

Zhu, H., H. Hendon, and C. Jakob, 2009: Convection in a parameterized and superparameterized model and its role in the representation of the MJO. *J. Atmos. Sci.*, **66 (9)**, 2796–2811, doi:10.1175/2009JAS3097.1.